Geometry Mediated Drag Reduction Using Riblets and Wrinkled Surface Textures

by

Shabnam Raayai Ardakani

B.S., Sharif University of Technology (2011)
S.M., Massachusetts Institute of Technology (2013)

Submitted to the Department of Mechanical Engineering
in partial fulfillment of the requirements for the degree of

Doctorate of Philosophy in Mechanical Engineering

at the

MASSACHUSETTS INSTITUTE OF TECHNOLOGY

February 2018

Author . . . .
Department of Mechanical Engineering
January 15, 2018

Certified by. . . . .
Gareth H. McKinley
School of Engineering Professor of Teaching Innovation
Department of Mechanical Engineering
Thesis Supervisor

Accepted by . . . .
Rohan Abeyaratne
Graduate Officer, Quentin Berg Professor of Mechanics
Chairman, Department Committee on Graduate Students

Geometry Mediated Drag Reduction Using Riblets and Wrinkled Surface Textures

by

Shabnam Raayai Ardakani

Abstract

The surfaces of many plants and animals are covered with a variety of micro-textures such as ribs or 3D tubules which can control surface-mediated properties such as skin friction. Inspired by the drag reducing ability of these natural structures, especially the ribbed features on shark denticles, passive drag reduction strategies such as micro-fabricated riblet surfaces have been developed and studied. Microgroove textures on the surface of objects such as hulls, wings or inner surface of pipes which are aligned in the stream-wise direction have been shown to reduce the wall friction by $4 - 8\%$. The mechanisms suggested for this form of drag reduction are viscous retardation of the flow in the grooves (both laminar and turbulent) and the displacement of vortical structures away from the wall in turbulent flows. Due to their effectiveness in altering the boundary layer structure and reducing the viscous drag force, use of riblets have been banned in various competitions such as the America's Cup. The current thesis work is partly focused on theoretical and numerical modelling (using the open source CFD package OpenFOAM) of the evolution of viscous boundary layers in the presence of various-shaped riblets (V-grooves as well as sinusoidal wrinkled surfaces) in high Reynolds laminar flow. We explore the effect of the dimensionless height to spacing of the grooves (aspect ratio) as well as the length of the wetted surface in the stream-wise direction and how these change the total drag compared with a corresponding flat wall. We show that riblets retard the viscous flow inside the grooves and reduce the shear stress inside the grooves. But for this reduction to result in overall drag reduction, the riblet wall needs to be longer than a critical length. The total drag reduction achieved is a non-monotonic function of the aspect ratio of the riblets, with aspect ratios of order unity offering the largest reduction in the total drag.

To eliminate the role of entrance effects, we additionally investigate the effect of stream-wise aligned riblet structures on fully-developed Taylor-Couette flow. We perform both experimental studies as well as time-dependent numerical simulations in both the laminar Couette and the Taylor vortex regime. We again explore the effect of the size of the riblets with respect to the geometry of the Taylor-Couette cell, as well as the aspect ratio of the riblet grooves and the shape of the grooves

(V-groove, Rectangular, semi-circular, etc.). For the experiments, the cylindrical textured rotors are fabricated using 3D printing techniques and the rest of the Taylor-Couette cell is custom built using CNC machining. The test cell is then aligned and mounted on a stress-controlled rheometer to measure the velocity and the torque on the rotating inner cylinder. The numerical studies are performed using the open source CFD software package OpenFOAM to compare results and understand the physical mechanisms contributing to this drag reduction phenomenon. Again we observe a non-monotonic behavior for the reduction in torque as a function of the aspect ratio of the riblets tested, similar to the trend observed in the boundary layer analysis and we discuss the effect of changing the geometry of the flow as well as the riblet spacing on the changes in the total torque.

When viewed holistically the results of these two studies show that, through careful design, a net reduction in viscous drag force can be robustly realized on micro-textured surfaces in high Reynolds number laminar flows through complex changes in near-wall stream-wise velocity profiles even in the absence of turbulent effects. The understanding of these changes can be effective in guiding the design of internal flows (pipes or ducts) and external flows (such as ship hulls, micro air vehicles or unmanned underwater vehicles) that are tailored and optimized to result in low frictional drag over the entire wetted surface in both laminar and turbulent regions.

Thesis Supervisor: Gareth H. McKinley
Title: School of Engineering Professor of Teaching Innovation
Department of Mechanical Engineering

Acknowledgements

First, I would like to express my sincere gratitude to my advisor Professor Gareth McKinley for his continuous support during my Ph.D. studies and related research, for his patience, motivation, and immense knowledge. His guidance helped me during the entire time of research and writing of this thesis. I could not have imagined having a better advisor and mentor for my Ph.D. studies. Also, I would like to thank the rest of my Ph.D. committee members, professors Mary Boyce, Pierre Lermusiaux, and Pedro Reis for their guidance, comments, and discussions throughout the research.

I also would like to thank my fellow lab-mates in the Non-Newtonian Fluid Mechanics Group (NNF), Hatsopoulos Microfluidics Laboratory (HML), and members of the Boyce Group at MIT, for the stimulating discussions and assistance, and for all the fun we have had in the last few years.

I would like to thank Ms. Leslie Regan and the rest of the academic administration team of the department of mechanical engineering at MIT, as well as the administrative assistants Sean Buhrmester, Juliette Pickering, Elaine Rooney, and Esther Schwartz for all their help.

In addition, I would like to extend my gratitude to my friends and colleagues at Ashdown house, during my time as an officer and serving on the Ashdown House Executive Committee (AHEC) of 2013-2014, for their help and support, and the great times we spent together serving our community. I would like thank our House manager Ms. Denise Lanfranchi for all her help throughout the years. I appreciate all the support from the heads of the house families at Ashdown House, Ann and Terry Orlando, Adam Berinsky and Deirdre Logan, and Katie and Yuri Roman.

I also like to thank the Gradate Student Council Executive Committee and Officer team of 2014-2015 for the amazing year that we had serving the graduate student community at MIT. I am also grateful for all the support and help from different departments and offices that I had the chance to work with during my time as the GSC treasurer: the Office of the Dean of Graduate Education, Division of Student Life, the Ombuds Office, Campus Activities Complex, Students Activities Office,

Contents

THIS PAGE INTENTIONALLY LEFT BLANK

List of Figures

13

14

20

List of Tables

THIS PAGE INTENTIONALLY LEFT BLANK

Chapter 1

Introduction

Over the past century, the field of drag reduction (especially passive drag reduction) has been attracting attention of researchers in various disciplines; reducing the frictional drag in pipe flow, flight vehicles, cars, and marine vehicles directly results in a reduction in energy consumption and can reduce operating costs [1, 2]. Among the various drag reduction methods proposed and investigated, drag reduction using riblet surfaces has shown promising results for both external and internal flows. For example, riblets were even used on the body of the Stars and Stripes racing yacht during the 1987 America's Cup and these riblets are thought to be at least part of the reason for the United States winning the first place in the competition [3, 4]. Similarly in 2010, the BMW Oracle team used 3M adhesive backed riblet films (Figure 1-1) on the yacht surface and the team won the 33rd America's Cup competition [5] (In other years, the use of anything that would alter the boundary layer around the yacht hull has been banned by the rules of the America's Cup competition [6]).
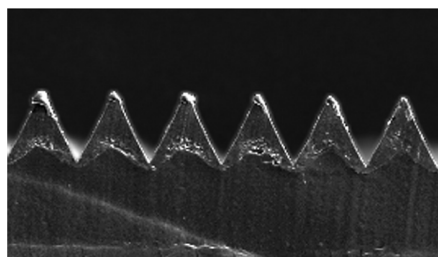
Figure 1-1: SEM image of 3M riblets with amplitude (height) and wavelength (spacing) of 62 μm [7].

Similar to the use of riblets in America's Cup, a range of full scale or partial scale experiments with boats, airplanes, wind turbines, various bodies of revolution, and airfoils using full or partial riblet coverage have been previously performed. For example the Admiralty Research Establishment's (ARE) high speed buoyancy propelled vehicle called MOBY-D (12.6 m long and 3.35 m in diameter, shown in Figure 1-2) was partially (35%) covered with riblets and showed 1% drag reduction. Considering the partial coverage of the riblets, as well as the fact that 80% of the drag in this case is due to skin friction, total skin friction drag reduction in a fully covered case could be estimated to be about 3.4% [8, 9, 10].

Figure 1-2: The Admiralty Research Establishment's (ARE) high speed buoyancy propelled vehicle called MOBY-D used for testing the effect of riblets on drag reduction. This vehicle is 12.6 m long and 3.35 m in diameter [8, 9, 10].

A riblet covered NACA 0012 airfoil has been used for both drag reduction and wake effect studies [11, 12, 13, 14, 15] and a DU (Delft University) 96-W-180 airfoil with riblets of various sizes were tested for drag reduction in wind turbine applications [7]. In terms of flight vehicles, a modified Gates Learjet model 28/29 twin-engine business jet was used by NASA Langley to test the drag reducing ability of a riblet test plate in real flight conditions (pressure altitude of 10,000 - 42,000 feet) and high Mach numbers (0.3-0.7) and observed maximum drag reduction of 6% on the test

plate [16, 17]. Airbus industries also performed a flight test in 1989 using an Airbus 320 (Figure 1-3) with 3M riblets (similar to the one used on the Stars and Stripes yacht). In this test, 700 m^2 of the aircraft's external surfaces were covered with the riblets and a net drag reduction of $1.5 - 2\%$ was measured, which is equivalent to about $4 - 5.3\%$ in skin friction drag reduction [9, 10].
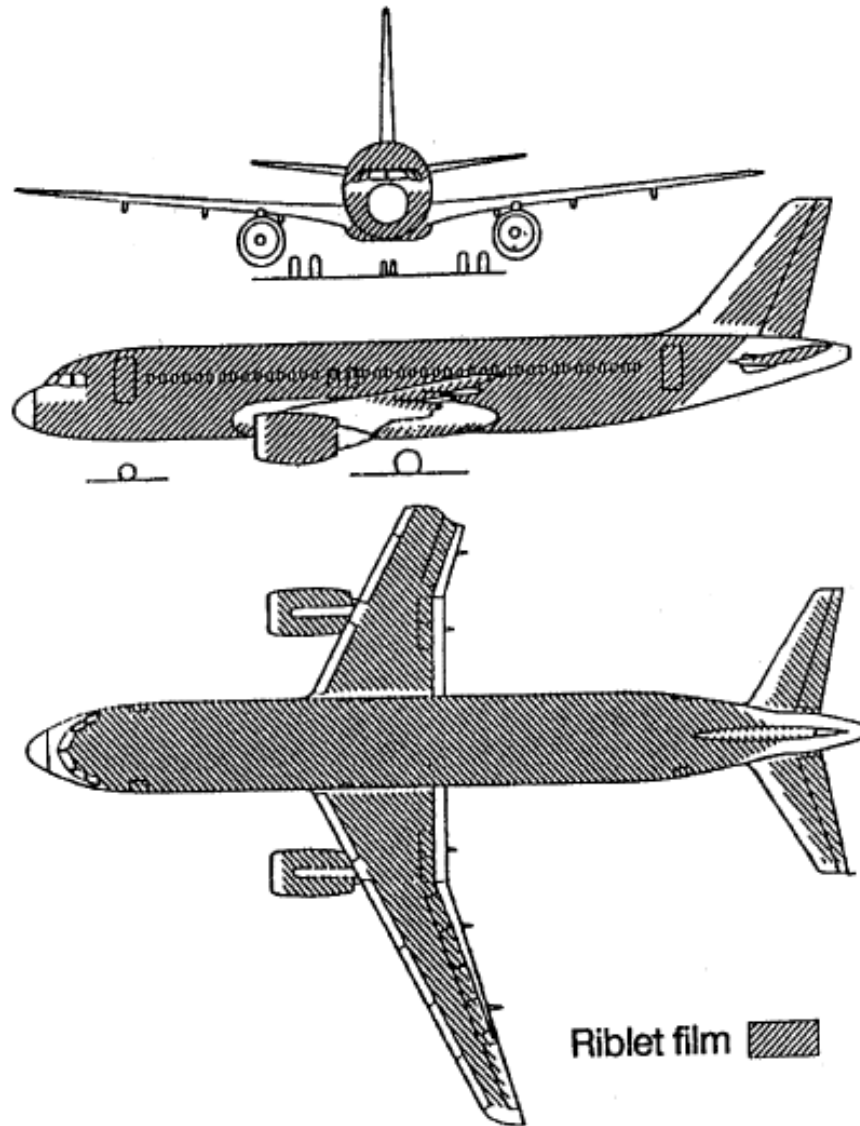
Figure 1-3:   Coverage of the body of an Airbus 320 for the flight test in 1989 [9, 10].

Through a later collaboration, Airbus, Lufthansa, and Cathy Pacific Airways conducted a test to monitor the degradation of the riblets in commercial flights employing the 3M riblet tapes on Airbus 340 aircraft on service. The final results of the tests

suggested that to maintain the drag reduction capacity, the riblet films need to be replaced every 2 to 3 years [10]. Another feasibility study by Lowrey and Harasha has shown that with riblet surfaces that offer 8% drag reduction, industries working with water could save up to $16,720 a year per mile of piping and with natural gas, industries could save up to $23,373 per year per mile of pipes [2].

The method of drag reduction using stream-wise riblets was originally motivated by a few independent ideas. First, inspired by natural surface textures, the observation of fine ridges aligned in the flow direction on the denticles of fast swimming sharks raised the idea of possibly of achieving drag reduction using stream-wise grooves [1, 18, 19, 20]. The body of fast swimming sharks are packed with micro-scale denticles which have between 3-7 parallel ribs on them. Measurements of these micro-scale ribs have shown that the spacing of these ridges vary over a range of $100 - 500$ μm with depth of $10 - 100$ μm. Examples of shark denticles are shown in Figure 1-5. Shark denticles have been the subject of various studies over the years such as in vortex dynamics [21], anti-fouling [22], etc. and these have inspired fabrication of various surface textures such as riblet surfaces, the Sharklet texture by Sharklet Technologies, or graded wrinkling (Figure 1-6) [21, 22, 7, 23] .

Second, it was suggested that riblets or stream-wise grooved textures could constrain the growth of turbulent vortical structures and reduce the Reynolds shear stress (which will be discussed more in section 1.4.3) near the wall by choosing physical rib sizes smaller than the radius of the vortices[1, 25, 26, 27, 28]. Independent DNS calculations and experimental measurements in turbulent boundary layers and channel flows for various Reynolds numbers in the range of $\mathrm{Re}_L \approx 3 \times 10^4 - 8 \times 10^5$ have shown that the diameter of the stream-wise vortical structures near the wall have values of between 10 and 44 ℓ^* and the mean spacing of these structures is about 100 ℓ^* [29, 30, 31]. Here the Reynolds number is a non-dimensional group quantifying the relative importance of dynamic pressure effects in the flow compared to the viscous effects and is defined as

$$\mathrm{Re}_L = \frac{\rho V L}{\mu} \tag{1.1}$$
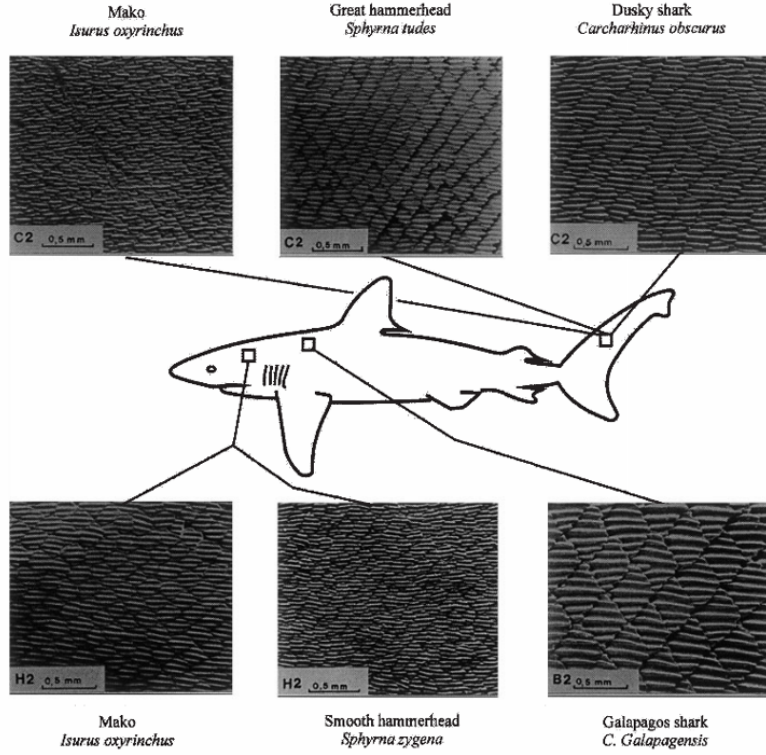
Figure 1-4: Pattern of scales of different sharks at different locations along its body. Note the packing of the denticles on the body and the parallel ribs on each of the denticles. These denticles are claimed to be partially responsible for the fast swimming speed of sharks compared with other marine animals [20].

where ρ and μ are the fluid density and viscosity, V is the characteristic velocity, and L the characteristic length. The viscous length scale ℓ^* is defined as

$$\ell^* = \frac{\nu}{u^*} \tag{1.2}$$

where

$$u^* = \sqrt{\frac{\tau_{\text{wall}}}{\rho}} \tag{1.3}$$

and τ_{wall} is the magnitude of the wall shear stress.

Third, advances in techniques employed to manufacture pipes with straight or spiral fins lead to new experiments in 1970s on the heat transfer of turbulent flows past walls with stream-wise fins, and sharp internal corners (i.e. rectangular ducts and conduits). Experimentally, it has been observed that the secondary flow structures
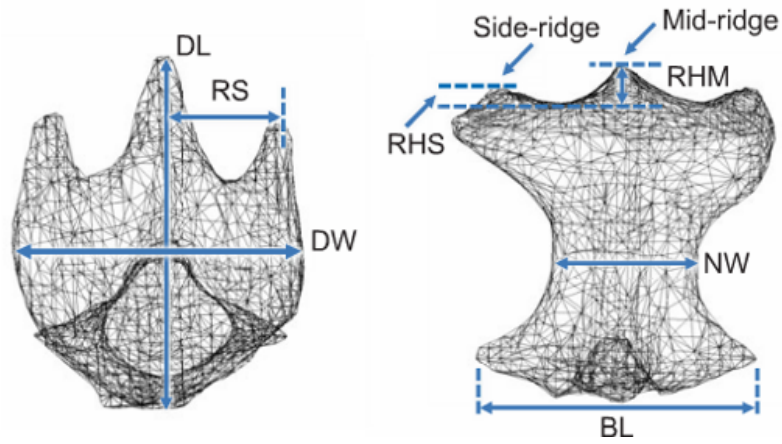
(a)
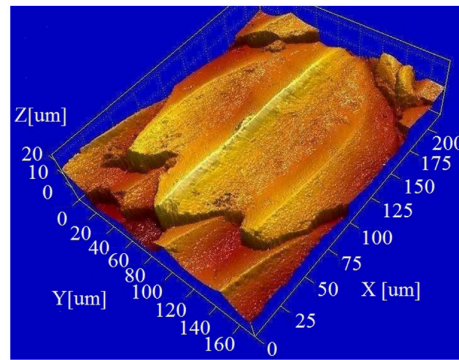
(b)

Figure 1-5: (a) Micro CT scan of a sample shark scale from a shortfin mako shark, here DL = 151 μm, RS = 51 μm, RHM = 21 μm , RHS = 11 μm, BW = 119 μm and NW = 50.9 μm [21]; (b) 3D morphology of a representative shark scale [24].
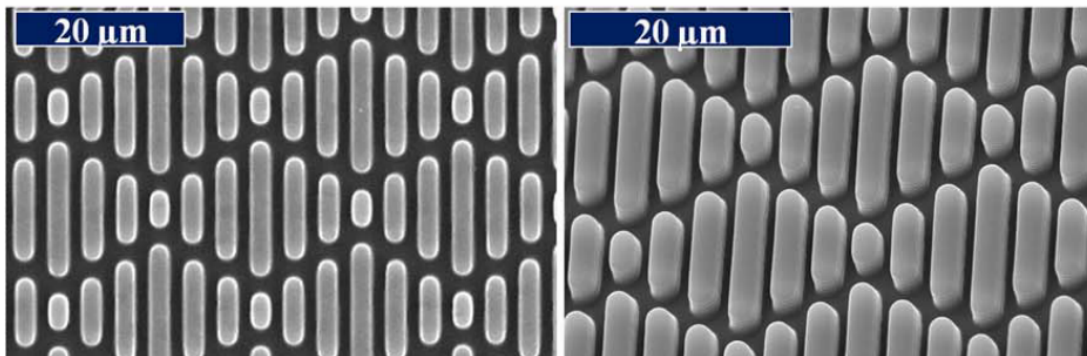
Figure 1-6: SEM images of the Sharklet AF^{TM} with feature width and spacing of 2 μm and height of 3 μm [22].
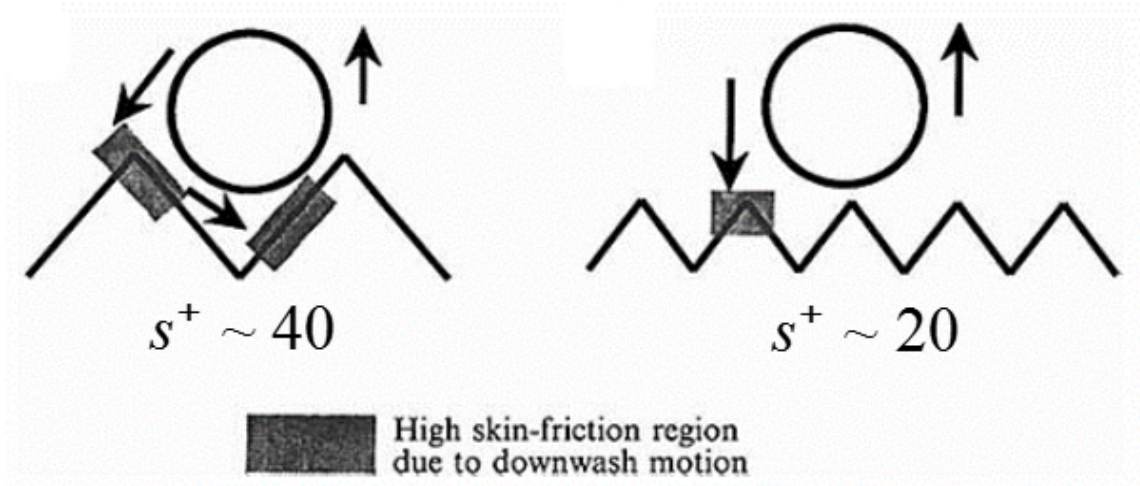
Figure 1-7: Schematic of the mechanism of drag increase and reduction in riblets with wavelength or spacing of 20 (right) and 40 (left) wall units. The circles represent the stream-wise vortical structures in the turbulent flow over riblet surfaces and they have an average diameter of 30 wall units [26].

that develop inside the corners of non-circular ducts, and at the base of the fins (the intersection of the fins with the conduit walls) result in a reduced local shear stress [1, 32, 33]. In addition, it was shown that such corners can weaken the spatial development of the three dimensional flow inside the corner by limiting the span-wise component of the velocity, therefore resulting in a local re-laminarization of flow inside the corners [1, 34]. Thus, it was hypothesised that walls with periodic textures aligned in the stream-wise directions (such as riblets) that contributed a large number of independent corner regions could perform in a similar manner [1, 32, 33, 34].

Therefore, in this chapter, an overview of the riblet surfaces and how they affect the flow behaviour in various conditions is presented. After an introductory summary of the riblet geometry and the flow types used in the previous studies, a review of the definitions of shear stress, drag, and friction coefficient in different settings is presented. Then a short summary of the previous methods (experimental and numerical) used in investigating riblet surfaces and the results of the previous studies are discussed in subsequent sections.

1.1 Geometry and Coordinate Systems

Riblets or stream-wise surface textures are micro- or milli-scale grooves aligned in the direction of the flow. The grooves are periodically aligned parallel to each other and each groove is typically symmetric. Grooves can be manufactured with various cross sectional shapes such as V-grooves, U-grooves, rectangular grooves, sinusoidal wrinkles, or trapezoidal grooves. A few examples of the geometry of the riblets are shown in Figure 1-8(a).

(a)

(b)
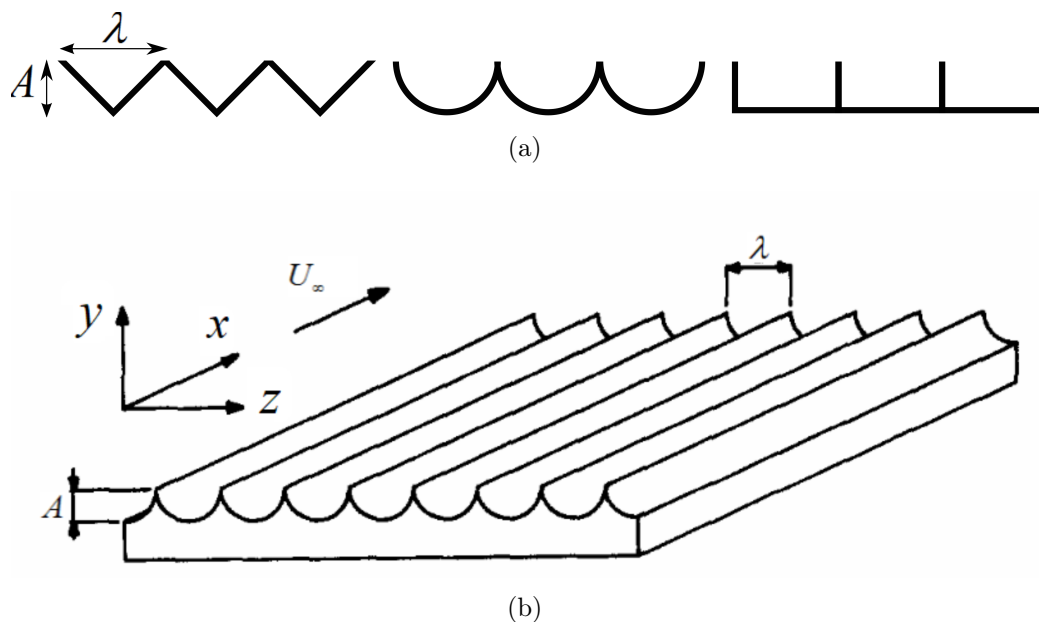
Figure 1-8:   (a) Examples of symmetric riblet geometries, from left to right; V-grooves, U-grooves, and razor blade grooves. Here λ is the wavelength or spacing of the riblets and A is the amplitude or height of the riblets. (b) Schematic of the flow over riblet surfaces and the coordinate system used with it. Here, x is the stream-wise direction, y the normal direction, and z the span-wise direction [35].

In the most general form, the geometry of a symmetric riblet can be defined using the wavelength (λ) or spacing (sometimes denoted by s) and amplitude (A) or height (sometimes shown by h) of each of the riblets. (Various notations can be found in the riblets literature. In this thesis, I will uniformly use λ and A for consistency.) As geometries take more complicated forms, other parameters such as the thickness of the blades in the razor blade grooves (also known as rectangular grooves - see Figure 1-9) or the radius of curvature of the peak or trough of the riblets in V-grooves have

40

been introduced and considered in different investigations [36, 37, 38, 39, 40, 1].
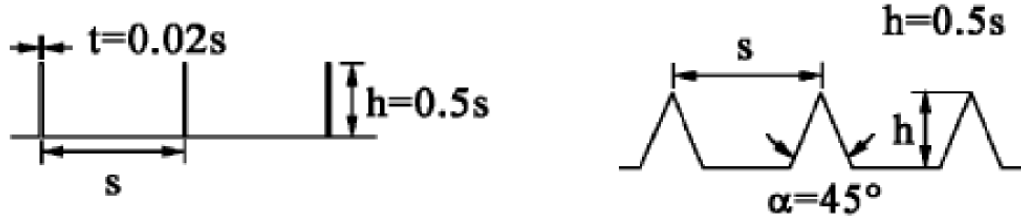
Figure 1-9: Schematic of razor-blade riblets on the left and trapezoidal riblets on the right [40].

To be able to compare the different riblet types, the dimensionless ratio of the height to spacing of the riblets has been frequently used among researchers. This ratio defined as A/λ can be used as a measure of the sharpness of the riblets and one can talk about a flat surface as riblets with $A/\lambda = 0$. In case of V-grooves, $2A/\lambda$ is the tangent of the two angles at the sides of the triangles. Due to the symmetry of the riblets, I use the ratio of the amplitude to half of the wavelength and thus here, Equation 1.4

$$\text{AR} = \frac{2A}{\lambda} = \tan\theta \qquad (1.4)$$

is called the riblet aspect ratio (AR) throughout the thesis. The aspect ratio will be used extensively in the following chapters.
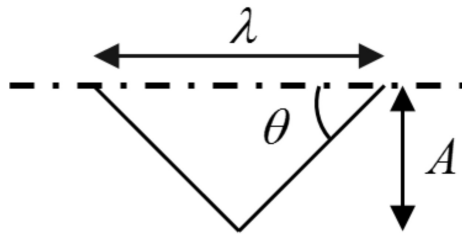
Figure 1-10: Schematic of a V-groove, with wavelength λ, amplitude A and the side angle θ.

The coordinate system used in flows over riblets, is always best described by the

stream-wise direction x which is parallel to the ribs, thus cross sectional plane of the ribs (Figure 1-8(a)) sits perpendicular to the stream-wise direction. In the cross sectional plane, the y direction (wall normal direction) as shown in Figure 1-8(b) is in the direction of the height of the ribs and the z direction (span-wise direction) is in the direction of the wavelength (spacing) of the riblets. This choice of (x, y, z) direction is arbitrary and to avoid confusion, throughout this chapter, the directions are associated with the terms; "stream-wise", "normal" and "span-wise". The same idea can be used in cases where a cylindrical coordinate system is used. In each of the following chapters of this thesis the coordinate system is defined at the beginning of each chapter.

1.2   Shear Stress, Skin Friction, Drag and Friction Factor

In order to investigate the effect of riblets on the frictional drag force on a surface, first I need to define the the frictional drag exerted by the fluid on the solid wall and vice-versa. The stress tensor in an incompressible Newtonian fluid can be calculated using the expression

$$\boldsymbol{\tau} = \mu \left(\nabla \mathbf{u} + (\nabla \mathbf{u})^T \right) \tag{1.5}$$

where $\boldsymbol{\tau}$ is the stress tensor, μ is the dynamic viscosity of the fluid, $\boldsymbol{u}$ is the velocity vector, and $\nabla \mathbf{u}$ and $\nabla \mathbf{u}^T$ are the velocity gradient tensor and its transpose respectively. Therefore, to calculate the traction vector arising from he action of viscous stress on a wall, I have

$$\boldsymbol{\tau}_{\text{wall}} = \boldsymbol{\tau}.\mathbf{n}_{\text{wall}} \tag{1.6}$$

where $\boldsymbol{\tau}_{\text{wall}}$ is the traction vector (force/unit area) at the wall and $\mathbf{n}_{\text{wall}}$ is the vector normal to the surface of the wall. Now, the total force exerted by the fluid on the wall can be calculated by integrating the traction vector over the entire wetted surface

area of the wall

$$\boldsymbol{F} = \int_{A_{\text{wall}}} \boldsymbol{\tau}_{\text{wall}} \, dS_{\text{wall}} = \int_{A_{\text{wall}}} \boldsymbol{\tau} . \mathbf{n}_{\text{wall}} \, dS_{\text{wall}}. \quad (1.7)$$

where $\boldsymbol{F}$ is the total force vector exerted by the fluid on the wall and S_{wall} is the wetted area of the solid surface. The component of the force vector that is in the stream-wise direction is considered to be the frictional drag force on the surface and will be denoted by $D = \boldsymbol{F}.\boldsymbol{e}_x$.

With the non-uniformity of the surface of the riblets, it is important to take extra care to use the appropriate wetted area and obtain the correct wall shear stress and frictional drag force. Depending on whether an internal or external flow is used, the total drag force can be used to calculate a global dimensionless measure such as a friction factor and/or skin friction coefficient.

The study of friction reduction using riblets has been carried out for both internal and external flows, especially boundary layers (external) and channel/pipe flows (internal). Thus, depending on the flow type used, the comparison with smooth surface takes different approaches.

In external flows such as a boundary layer, the no slip boundary condition at the plate results in the formation of a velocity profile which grows along the length of the plate. The shape of the boundary layer profiles over flat plates are self-similar and in laminar flows the thickness of the boundary layer increases proportional to the square root of the distance down the plate in the stream-wise direction. Boundary layers will be discussed in more detail in Chapters 2 and 3. Figure 1-11(a) shows a schematic of the boundary layer growth on a flat wall and Figure 1-11(b) shows a corresponding schematic of the boundary layer growth in the entrance region of a pipe before the formation of a fully developed flow. The shear stress distribution at the flat wall is also a function of the local stream-wise location (denoted x here) along the plate at which the only non-zero component of the shear stress at the wall in the stream-wise direction is $\tau_{yx}(x)$ where y is the direction normal to the surface.

In such flows, the local shear stress can be expressed in a non-dimensionalized
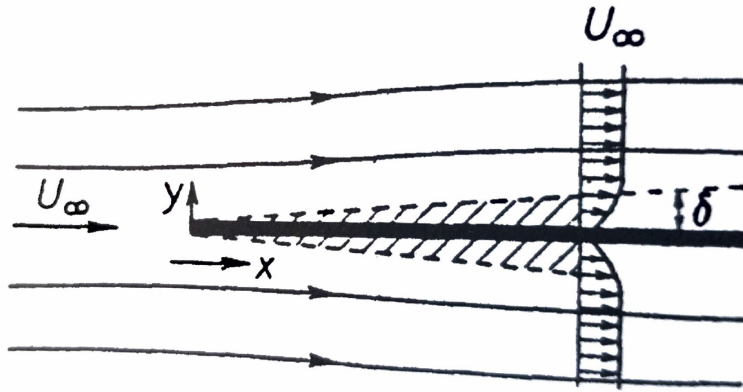
(a)
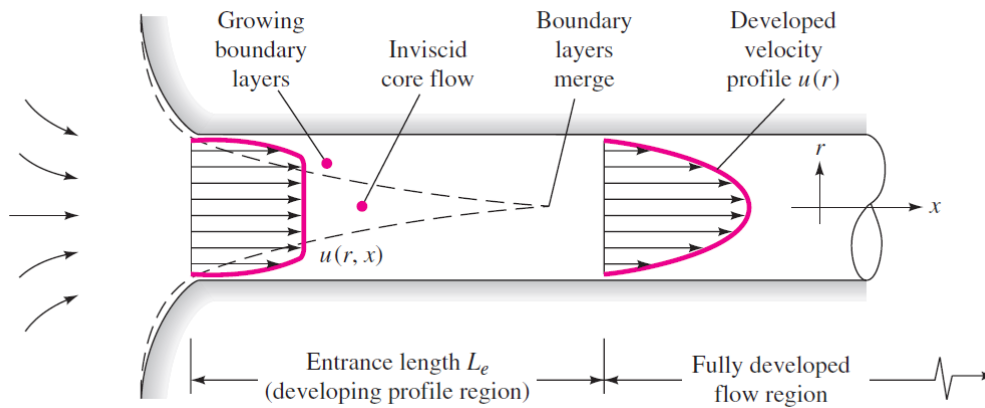
(b)

Figure 1-11: Schematic of growth of boundary layer (a) on a plate (Here U_∞ is the free-stream velocity, and x is the stream-wise direction and y the normal direction, and δ represents the boundary layer thickness [41]) and (b) inside a pipe prior to reaching a fully developed stage (Here x is the stream-wise direction and r is the normal direction, note the cylindrical coordinate system). The velocity profile in the pipe is denoted $u(r)$ and the fully developed velocity profile in the laminar case has a quadratic profile [42].

form using a local skin friction coefficient defined as [41]

$$C_f(x) = \frac{\tau_{yx}(x)}{\frac{1}{2}\rho U_\infty^2} \tag{1.8}$$

where C_f is the local skin friction coefficient, ρ is the density of the fluid, and U_∞ is the free-stream velocity (Figure 1-11(a)). This quantity is local and depends on

the location along the plate. The non-dimensionalized form of the total drag on a plate of total length L and surface area S_{wall} can be expressed in the form of the drag coefficient as

$$C_D = \frac{D}{\frac{1}{2}\rho U_\infty^2 \, S_{\text{wall}}} \qquad (1.9)$$

where C_D is the drag coefficient over the entire surface of the plate of total length L [41]. Equations 1.8 and 1.9 are general expressions and can be used for different types of flow. However, in the case of the flat plate boundary layer theory as developed by Prandtl and Blasius, the local skin friction coefficient and the drag coefficient in a laminar boundary layer (far from the leading edge) can be calculated to be

$$C_f(x) = \frac{0.644}{\text{Re}_x^{\,1/2}} \qquad (1.10)$$

$$C_D = \frac{1.328}{\text{Re}_L^{\,1/2}} \qquad (1.11)$$

where Re_x is the Reynolds number based on the local position in the stream-wise direction and Re_L is the Reynolds number based on the overall length of the plate in the stream-wise direction,

$$\text{Re}_L = \frac{\rho U L}{\mu} \qquad (1.12)$$

where ρ and μ are the fluid density and viscosity, U is the characteristic flow velocity and L is the characteristic length scale of the problem. The velocity and the length can be replaced with the corresponding free-stream velocity and length scale depending on the flow in the problem (hydraulic diameter for internal flows, or stream-wise distance for external flow) [43].

On the other hand, in internal flows, such as channel flow or pipe flow, the fluid is bound by two walls in the normal or span-wise direction, or all around in case of the pipe flow (Figure 1-11(b)) (Most direct numerical simulations bound the flow in the

normal direction and use periodic boundary conditions in the span-wise direction). In either case, at the entrance of the channel, a boundary layer similar to the flat plate boundary layer is formed and as the boundary layer thickness grows on either side of the channel in the stream-wise direction, at some point along the channel the boundary layers meet and from then onwards the flow becomes fully developed. The length from the entrance up to the start of the fully developed velocity profile is known as the entrance length (see Figure 1-11(b)). The entrance length can readily be defined as the required distance along the pipe for the friction factor to decrease to within 5% of its fully developed value. Using boundary layer analysis and laminar flow in a smooth pipe, entrance length can be estimated to be [44]

$$L_\text{e} \approx 0.05 D_\text{H} \text{Re}_{D_\text{H}}. \tag{1.13}$$

with

$$D_\text{H} = \frac{4\text{Area}}{\text{Perimeter}} \tag{1.14}$$

as the hydraulic diameter of the pipe/channel used. Here, Area and Premeter are the area and wetted perimeter of the cross section of the pipe respectively. In fully developed laminar channel flow, the shape of the velocity profile (which is quadratic) stays the same at every cross section along the length of the channel and thus, the shear stress is constant in the stream-wise direction beyond the entrance length. The total drag force in pipe or channel flow can be measured by the pressure drop along the length of the pipe/channel and is presented in the non-dimensional form of a friction factor:

$$f = \frac{\Delta P}{\frac{1}{2}\rho U^2} \frac{D_\text{H}}{L} \tag{1.15}$$

where Δp is the pressure drop along the pipe and L is the length of the pipe and U, the average velocity int he pipe is defined as

$$U = \frac{1}{\pi R^2} \int_0^R u(r) 2\pi r \, dr. \tag{1.16}$$

In laminar channel flow, the friction factor can be calculated analytically to be

$$f = \frac{64}{\mathrm{Re}_{D_\mathrm{H}}} \tag{1.17}$$

where $\mathrm{Re}_{D_\mathrm{H}}$ is the Reynolds number based on the hydraulic diameter of the pipe. For transitional and turbulent flows, various empirical forms (such as Equation 1.18 by Prandtl) and tabulated data (such as the Moody chart) are available [41].

$$f^{-1/2} = 2 \log_{10} \mathrm{Re}_D f^{1/2} - 0.8 \tag{1.18}$$

In addition to the shear stress, friction coefficient, and drag coefficient, the effect of the riblets on the flow can be discussed through comparing additional flow properties such as velocity profiles, boundary layer thickness, vorticity distribution, and in case of turbulent flows, the turbulent statistics, and Reynolds stresses. In turbulent flows close to the wall, independent of the flow type, the friction velocity is defined as in Equation 1.3 and is used to non-dimensionalize the lengths using the wall units as shown in Equation 1.19

$$y^+ = \frac{yu^*}{\nu} = \frac{y}{\tau^*}. \tag{1.19}$$

Turbulent velocity profiles are normally plotted in wall units showing the sub-layer, buffer layer, and the logarithmic layer as indicated in Figure 1-12.

The thickness of the viscous sub-layer is about 5 wall units, the buffer layer is generally between 5 to 30 wall units and the logarithmic layer is between 30 and 300 wall units. Additional details about turbulent flow can be found in the following references [46, 43].
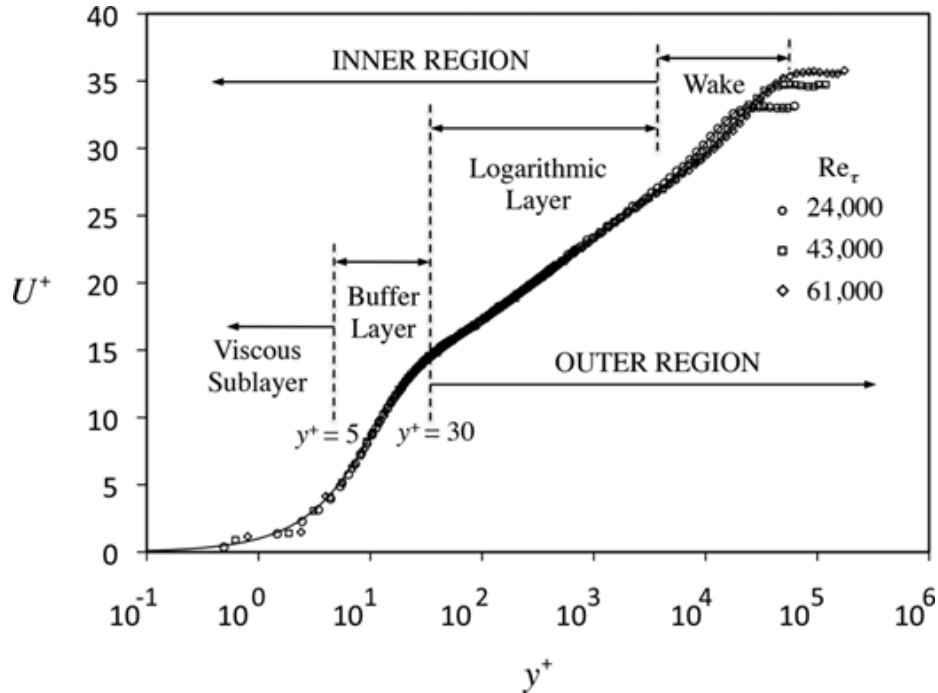
Figure 1-12: Mean velocity profile in a turbulent boundary layer [45].

1.3 Experimental and Numerical Methods

Previous research on the effects of riblets on the frictional drag has been performed using various experimental and numerical methods. For external flows, experimental set-ups such as wind tunnels, water channels, and oil channels have been used to measure the flow properties over riblet walls. For example, Walsh and co-workers [36, 37, 38, 39], Hooshmand and co-workers [47], Vukoslavcevic and co-workers [48], Park and Wallace [49], Choi [50], Lazos and Wilkinson [51], Wang and Jovanovic [52], Caram and Ahmed [12, 13, 14], and Coustols and co-workers [53] used low or high speed wind tunnel to measure various flow properties; Gallagher and Thomas [54], Bacher and Smith [55], Reidy and Anderson [56], and Hou and co-workers [57] used water channels/tunnels and Bechert and co-workers used the Berlin oil channel which was custom designed for the drag reduction measurements [40, 20, 58]. A representative diagram of the wind tunnel set up used by Walsh is shown in Figure 1-13.

Experiments were performed both in boundary layer and channel flow settings. In
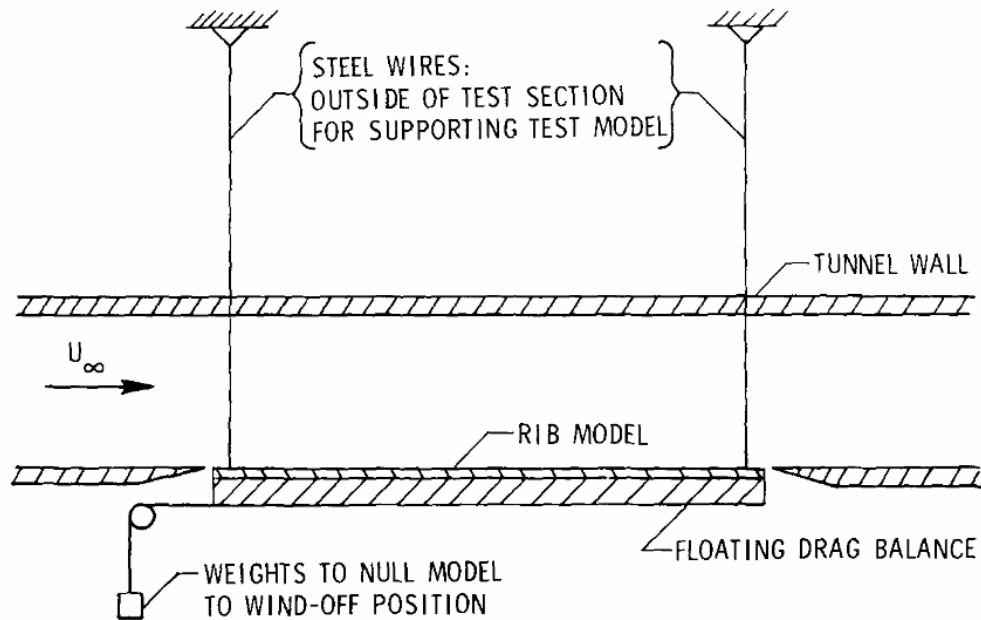
Figure 1-13: Test surface set up in NASA Langley 7"×11" low speed wind tunnel used in riblet drag reduction measurements by Walsh and co-workers. The test section is 91.4 cm long and has a cross section of 17.8×27.4 cm^2. The wind tunnel can be operated up to speeds of 46 m/s [36, 37, 38, 39].

boundary layer experiments, drag measurements have been performed with various direct and indirect methods. Walsh et al. measured the drag force on the test plate by exerting a force in the opposite direction and measuring that force as the total drag on the surface (See Figure 1-13) [36, 37, 38, 39]. Choi has used surface hot wire measurements to measure mean and fluctuating components of skin friction in turbulent flows over both flat and riblet surfaces [59].

Indirect measurements of the drag are based on measurement of the velocity profile at different locations down the flow. Velocity measurements in these cases were performed using methods such as hot wire probes, pitot tubes, and variable reluctance differential pressure transducer [37, 50, 47, 60]. One of the indirect methods of calculating the drag is by post processing the measured velocity profile $u(y, z)$ at the wall. In cases with enough resolution, the velocity profile at specified locations were measured, such as shown in Figure 1-15. In various cases, by considering riblet surfaces as rough surfaces, methods developed for rough walls such as Clauser Methods

has been used to find the velocity gradient at the wall and thus the frictional drag [61, 62, 63]. Analysis of the data in this way, requires a virtual origin for the velocity profile for the normal distance (in the flat plate boundary layer, this origin is on the wall) and introduces uncertainty in the choice of the virtual origin for the riblet surfaces. Hooshmand et al. showed that this uncertainty can result in significant errors in the final results [47]. Gallagher and Thomas showed that simply choosing the peak of the riblets as the origin results in finding $2 - 4\%$ increase in the skin friction and choosing the trough as the origin, shows a drag reduction of the same magnitude [54]. Wallace and Balint have plotted data from various researchers using midway of the peak and valley as the virtual origin and remarked that they obtain more consistent results [64].

To avoid such uncertainty, an alternate indirect method for measuring the drag and skin friction is by using the momentum integral equation and momentum thickness, and the results of this method are not affected by the choice of the origin [37, 47, 54]. This method uses Equation 1.20 (which is a simplified form of the von-Kármán integral equation) to calculate the local skin friction coefficient.

$$\frac{d\theta}{ds} = \frac{C_f}{2} - (H + 2 - M^2)\frac{\theta}{U_e}\frac{dU_e}{ds} \tag{1.20}$$

Here s is the stream-wise direction (not necessarily a straight line), H is the boundary layer shape factor which is the ratio of the displacement thickness δ^* to the momentum thickness θ of the boundary layer (will be discussed in section 1.4.2 as well as in Chapters 2 and 3), M is the Mach number based on the flow at the edge of the boundary layer, and U_e is the velocity profile at the edge of the boundary layer (calculated from potential flow theory for the inviscid flow outside of the boundary layer). In case of a flat plate with $dU_e/ds = 0$, Equation 1.20 reduces to

$$\frac{d\theta}{ds} = \frac{C_f}{2} \tag{1.21}$$

(which will be referred to and discussed in Chapter 2). Also, integration of equation 1.20 over the entire length gives

$$C_D = 2\frac{\theta_\infty}{L} \tag{1.22}$$

for the total drag coefficient, where θ_∞ is the momentum thickness measured in the wake of the plate or airfoil. In case of an airfoil, L is replaced by the chord length. Thus, by measuring the pressure distribution at different locations, the velocity distribution can be measured and then integrated to calculate both displacement thickness δ^* and momentum thickness θ and thus calculate the skin friction and drag coefficients [65].

In the case of internal flows (pipe or channel flow cases), pressure at different locations along the channel is measured and the pressure drop along the length is transformed to the friction factor using appropriate equations and then compared with smooth pipe/channel results [52, 66]. Channel flow set-up is popular in numerical investigations, especially in Direct Numerical Simulation (DNS) of flow over riblet surfaces, with one riblet wall (with various shapes and sizes), one flat wall, and periodic boundary conditions on the other four sides [27, 67, 25, 26]. DNS with Boundary Integral Methods (BIM) and Large Eddy Simulations (LES) have been also used to explore the effect of the rectangular and pointed rectangular riblets in turbulent flow [68, 69].

In multiple cases, simplified versions of the Navier-Stokes equations have been used for numerical calculations; Khan used finite difference discretization of the boundary layer equations with laminar and turbulent flows (to model the turbulence, an algebraic uni-directional Reynolds stress model was used) [70]. Bechert and Bartenwerfer assume that the flow inside the grooves is viscously dominated to simplify the Navier-Stokes equation to the Laplace equation and used the solution over various geometries to calculate a "Protrusion Height" as the virtual origin of the flow in presence of the riblets (This will be discussed further in section 1.5) [71].

51

1.4   Flow Behaviour in Presence of the Riblets

Having discussed the methods employed by earlier researchers for studying the effect of the riblets on the flow behaviour in both boundary layer and channel flow settings, below a summary of the results and observations are listed. The results are presented as a comparison with the corresponding flow over the smooth surface as well as a comparison among the different cases in the literature.

1.4.1   Velocity

The presence of riblets in either boundary layer or channel flow changes the shape of the velocity profiles, thus at each riblet cross section, the velocity distribution is a function of both normal and span-wise directions. This effect is more pronounced inside the groove where the shape of the velocity profile in the normal direction is a function of the span-wise location within each riblet and moving toward the valley of the riblet shows a higher retardation in the local flow profile, while the velocity profile at the peaks are similar to the profiles on a flat plate [72, 26, 25, 27, 73, 68, 12, 74, 75].

The large eddy simulations of Bannier et al. for riblets with $A/\lambda = 0.5$ (AR = 1) also shows that above $y^+ = 10$ the mean velocity profiles at different span-wise locations collapse on the velocity profile above a flat plate. This shows that riblets only have minor effects on the flow outside of the viscous sub-layer [69]. Examples of velocity profiles at 3 different locations inside each riblet in laminar and turbulent channel flow (mean velocity profiles in case of turbulent flow) are shown in Figure 1-14 where y is the wall normal direction. In each of the cases, the flow inside the grooves experiences a substantial retardation in the valley and at the midpoint. Velocity profiles at 3 different locations of riblets in a boundary layer flow are shown in Figure 1-15.

Turbulent velocity profiles can be non-dimensionalized using wall units and plotted in semi-log plots as illustrated in figure 1-16. In wall units, it can be seen that the introduction of the riblets shifts the velocity profiles upward in the y^+ direction (which is the normal direction in wall units). Various researchers have confirmed this shift
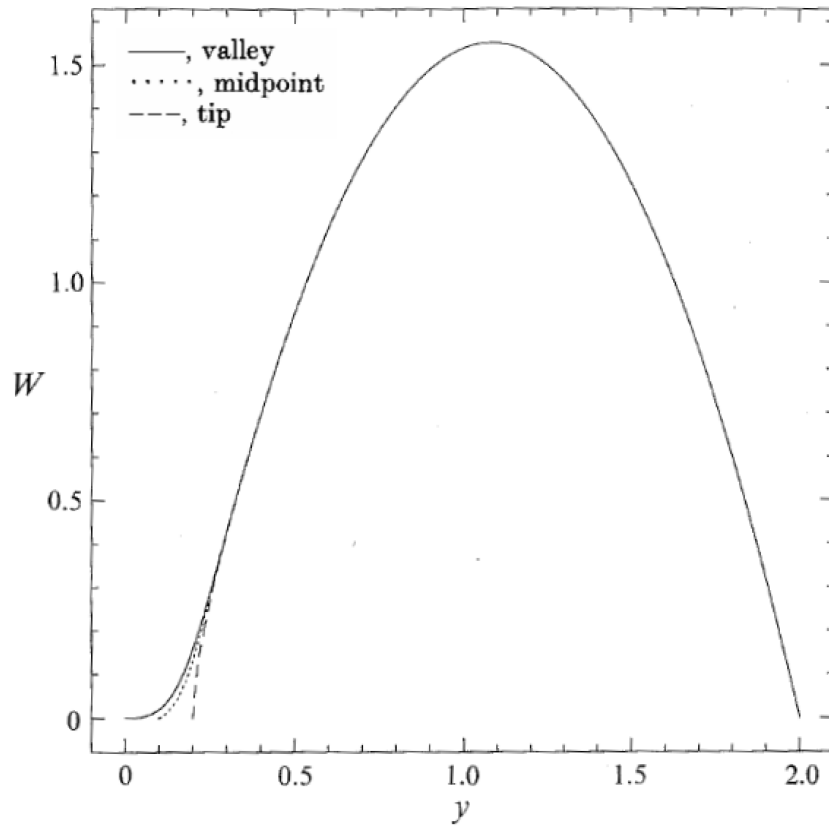
(a)
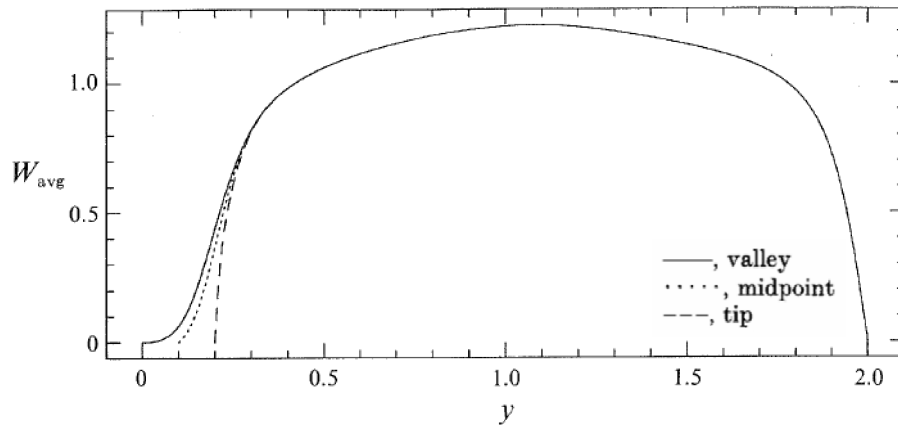
(b)

Figure 1-14: DNS results of (a) the velocity profiles in laminar flow with $Re = 1000$ and (b) the mean velocity profile in turbulent flow with $Re = 3500$ over V-grooves (left wall) and flat wall (right wall) channel flow with riblets of $A = \lambda = 0.1H$ where H is the channel height (AR $= 2$) [25]. Here W is the velocity in the stream-wise direction and $W_{\text{avg}}(y)$ is the temporal average at each local position.
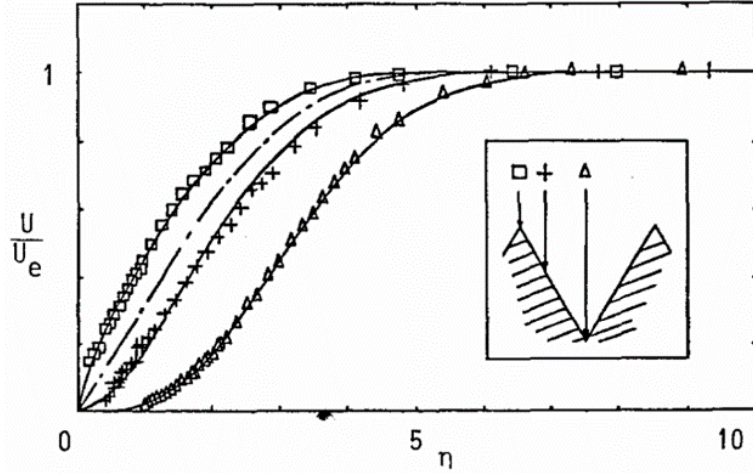
Figure 1-15: Experimental and numerical results for the velocity profiles over V-grooves in a boundary layer flow. The local Reynolds number of this profile is $\mathrm{Re}_x = 99,200$ and the profiles are normalized by the free-stream velocity (U_e) and normal direction is normalized by the boundary layer similarity variable $\eta = y/x\sqrt{\mathrm{Re}_x}$. Solid lines are from the numerical simulations, the dash-dot line represents the Blasius boundary layer and the symbols are the experimental results [73].

through experiments and numerical simulations [47, 64, 68, 57].

1.4.2 Boundary layer thickness

One of the main observations of the effect of riblets on the flow is increasing the thickness of the boundary layer (and displacement thickness). But for the momentum thickness different trends such as increase, no change, or decrease have been reported in the literature [47, 25, 56, 54, 76].

The boundary layer thickness can be defined in various ways. One of the simplest measures of the boundary layer thickness is by defining the distance from the plate where the velocity reaches 99% of its free-stream value, also known as δ_{99}. Other variations of this definition can be found by changing the percentage to other values such as 95% [41, 43]. A more rigorous way of measuring the boundary layer thickness is by using an integral definition for the thickness. The displacement thickness (δ^*) and momentum thickness (θ) are two methods of defining boundary layer thickness which are not dependent on the origin, and are defined in Equations 1.23 and 1.24
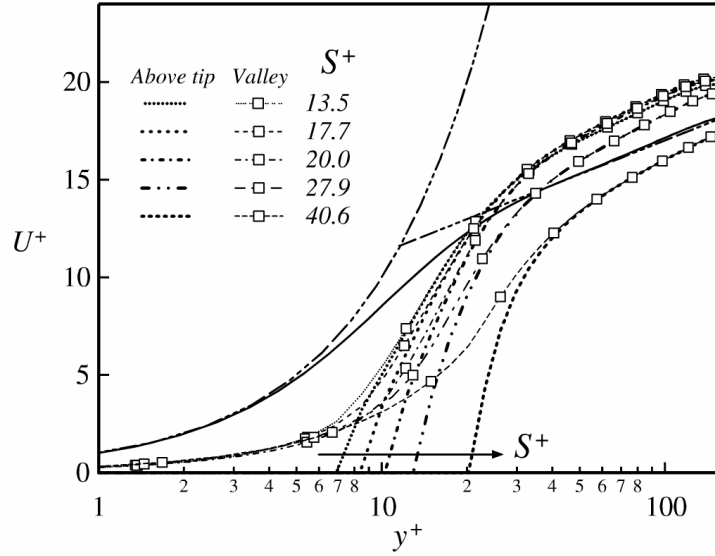
Figure 1-16: Numerical results of the mean stream-wise velocity profiles at the peak and valley of rectangular grooves in a turbulent channel flow using the Boundary Integral Method (BIM). The local Reynolds number of this profile is $Re_H = 5642$ where H is the channel height and velocity and normal direction are normalized by the friction velocity and the wall units respectively. Solid line refers to the flat channel results. All the riblets here have $A/\lambda = 0.5$ corresponding to an aspect ratio (from Equation 1.4 of $AR = 1$ [68].

respectively:

$$\delta^* = \int_0^\infty \left(1 - \frac{u}{U_\infty}\right) dy \qquad (1.23)$$

$$\theta = \int_0^\infty \frac{u}{U_\infty}\left(1 - \frac{u}{U_\infty}\right) dy \qquad (1.24)$$

where $u(y)$ is the velocity profile in the stream-wise direction and y is the direction normal to the surface in the flat plate boundary layer.

In the case of the boundary layer theory and using Blasius solution, the boundary layer thickness, using each of the above definitions can be written as
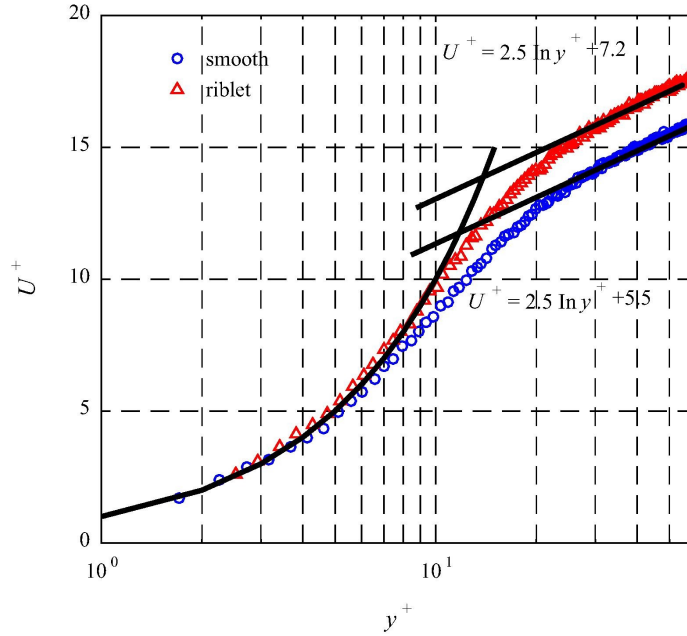
Figure 1-17:   Turbulent velocity profile with smooth and riblet walls measured using microscopic particle tracking velocimetry (μPTV) at $\mathrm{Re}_H = 480$. Riblets have trapezoidal cross section with amplitude of 0.375 mm and wavelength of 0.75 mm [57].
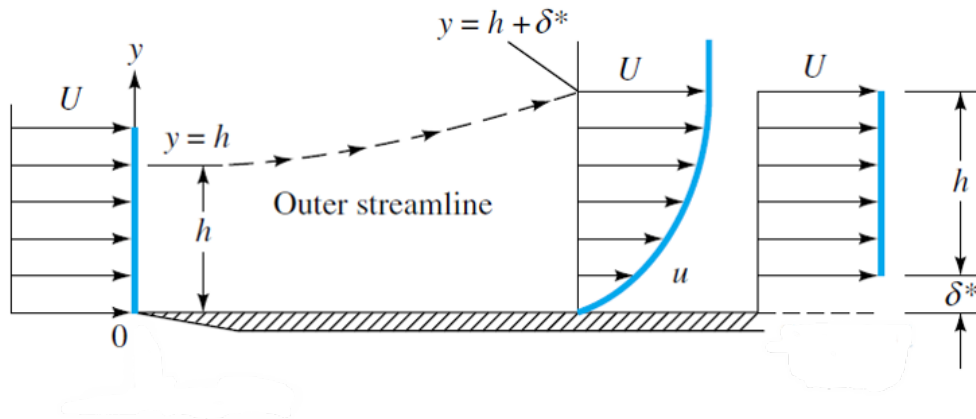
Figure 1-18:   Schematic of the velocity profile in the flat plate boundary layer, the displacement thickness δ^* and the corresponding inviscid flow outside the plate [42].

$$\delta_{99} = \frac{4.99\ x}{\sqrt{\mathrm{Re}_x}} \tag{1.25}$$

$$\delta^* = \frac{1.72 \, x}{\sqrt{\mathrm{Re}_x}} \tag{1.26}$$

$$\theta = \frac{0.664 \, x}{\sqrt{\mathrm{Re}_x}} \tag{1.27}$$

with x the stream-wise direction [41, 43]. The displacement thickness in physical terms is equivalent to the distance away from the plate where it can be assumed that the viscous effects are not significant and the flow is governed by the inviscid flow solution [65, 41, 43]. Also, the displacement thickness can be related to the distance between the wall and the shear layer in the boundary layer while the momentum thickness is related to thickness of the shear layer, especially for flows close to separation or separated flows [65].
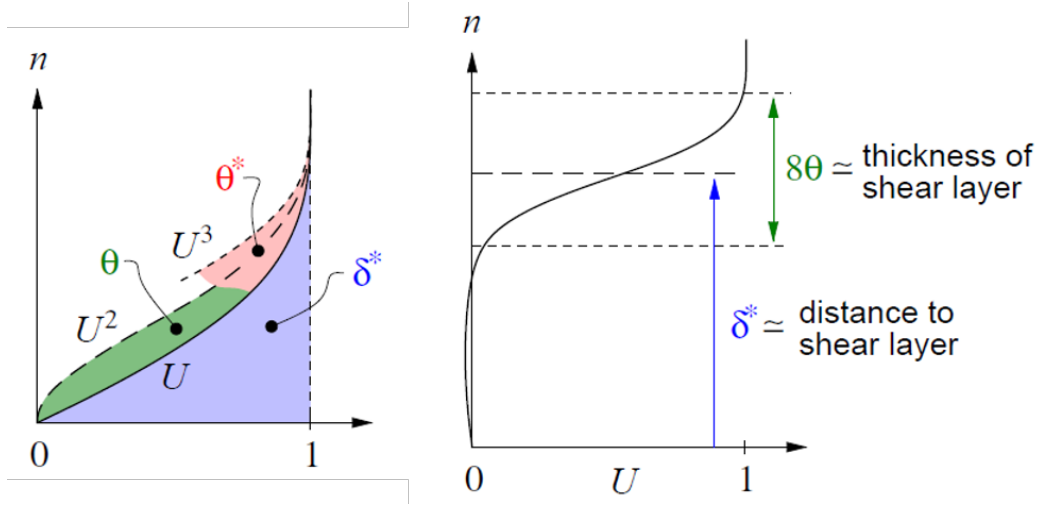
Figure 1-19: Schematic of the mathematical and physical definition of the displacement thickness and momentum thickness in flat plate boundary layer [65].

Experiments at $\mathrm{Re}_x = 2.02 \times 10^6$ with riblets of $A/\lambda = 0.5$ (AR = 1) showed an increase in the thickness of the boundary layer (δ_{99}) from 4.5 inches to 5.25 in (about 16.7% increase) and the displacement thickness (δ^*) was increased by 20.2% [47]. DNS results for a turbulent channel flow of $\mathrm{Re}_H = 3500$ with $A/\lambda = 1$ (AR = 2) showed a 46.4% increase in the displacement thickness for flow over the riblet surface compared with the flat surface, and a corresponding 12.6% increase in the momentum thickness

[25]. Experiments with boundary layer in water at $\text{Re}_x = 122,500$ show a reduction in the momentum thickness at various locations in the span-wise direction of each riblet [56]. Another boundary layer experiment in water channel flow with $A = \lambda$ (AR = 2) reported no changes (or a slight increase) in the momentum thickness along the length of the riblet plate, in this case, the riblets did not show a reduction in the total drag, but local skin friction reduction of 20% was observed [54]. Savill suggests that the observed shifts in the logarithmic velocity profile in turbulent flow over riblet surfaces also means that riblets increase the thickness of viscous sub-layer [76]. Experimental results of Hou et al. using microscopic particle tracking velocimetry (μPTV) also show this shift in the profile of the turbulent flow over riblet surfaces (trapezoidal ribs) compared with a corresponding flat surface as shown in Figure 1-17 [57].

Only a very limited number of papers have reported values for the boundary layer shape factors. The boundary layer shape factor denoted by H is defined as the ratio

$$H = \frac{\delta^*}{\theta} \tag{1.28}$$

and is used as a measure of flow attachment, separation, inflection or reversal [65, 42]. For a laminar boundary layer, using the classical Blasius boundary layer theory, the shape factor has a value of 2.6. A shape factor of $H = 4$ indicates separation and $H > 4$ indicates that flow reversal occurs [65, 42]. In turbulent boundary layer, the shape factor reduces to a value of 2.4 [65, 42]. An increase in shape factor is an indicator of reduction in the local shear stress [65, 77, 78]. All the literature which mention the shape factor have reported an increase in the value of the shape factor. For example, in experiments of Hooshmand et al. with $\text{Re}_x = 2.02 \times 10^6$ where x is the stream-wise direction and $A/\lambda = 0.5$ (AR = 1), shape factor was increased from 1.35 in case of flat wall to 1.37 [47]. DNS results of the turbulent channel flow of $\text{Re}_H = 3500$ with $A/\lambda = 1$(AR = 2) showed an increase from 1.77 for flat wall to 2.3 for the riblet wall [25].

1.4.3 Turbulent Statistics and Reynolds Stresses

In studies of turbulent flow over riblet surfaces, in addition to the mean velocity profile, measurements of the root mean square of fluctuating velocities, turbulence intensity, as well as the Reynolds stresses are used to understand the effect of the riblets.

In turbulent flows, using the well-known Reynolds decomposition, the instantaneous velocity is decomposed into a mean and a fluctuating component so that $\mathbf{U}(\mathbf{x},t) = \overline{\mathbf{U}}(\mathbf{x},t) + \mathbf{u}(\mathbf{x},t)$ [46]. Therefore the root mean square of the components of the fluctuating velocity can be calculated as $(u', v', w') = (\sqrt{<u^2>}, \sqrt{<v^2>}, \sqrt{<w^2>})$ [46]. Substitution of the decomposed velocity in the non-linear convection term in the Reynolds Averaged Navier Stokes equations results in an additional term in the equations known as the Reynolds stress ($<u_i u_j>$ in index notation), which is a symmetric second order tensor [46]. The diagonal components of the Reynolds stresses are also known as root mean square velocity[46] and the turbulent intensity is defined as

$$I = \frac{\sqrt{\frac{1}{3}(u'^2 + v'^2 + w'^2)}}{\sqrt{U^2 + V^2 + W^2}} \tag{1.29}$$

where (U, V, W) are the components of the mean velocity. Contours of the root mean square velocities (u', v', w') as well as Reynolds shear stresses ($<-uv>, <-uw>, <-vw>$), for an example flow over riblets and the equivalent flat plates are shown in Figure 1-20 from Goldstein et al. [67].

Goldstein et al. and Chu and Karniadakis show only a very small (or close to zero) reduction in the peak of the fluctuating velocities over the riblet wall compared to the flat wall [27, 25]. Another DNS study by Choi, Moin, and Kim reports observing a 10% reduction in the maximum root mean square velocity fluctuations in the normal and span-wise directions and a 5% reduction in the stream-wise component in the case of a drag reducing riblet surface ($\lambda^+ = 20$ and $A/\lambda = 0.5, 0.865$ (AR = 1, 1.73)). The drag increasing case ($\lambda^+ = 40$ and $A/\lambda = 0.5, 0.865$ (AR = 1, 1.73)) however, shows
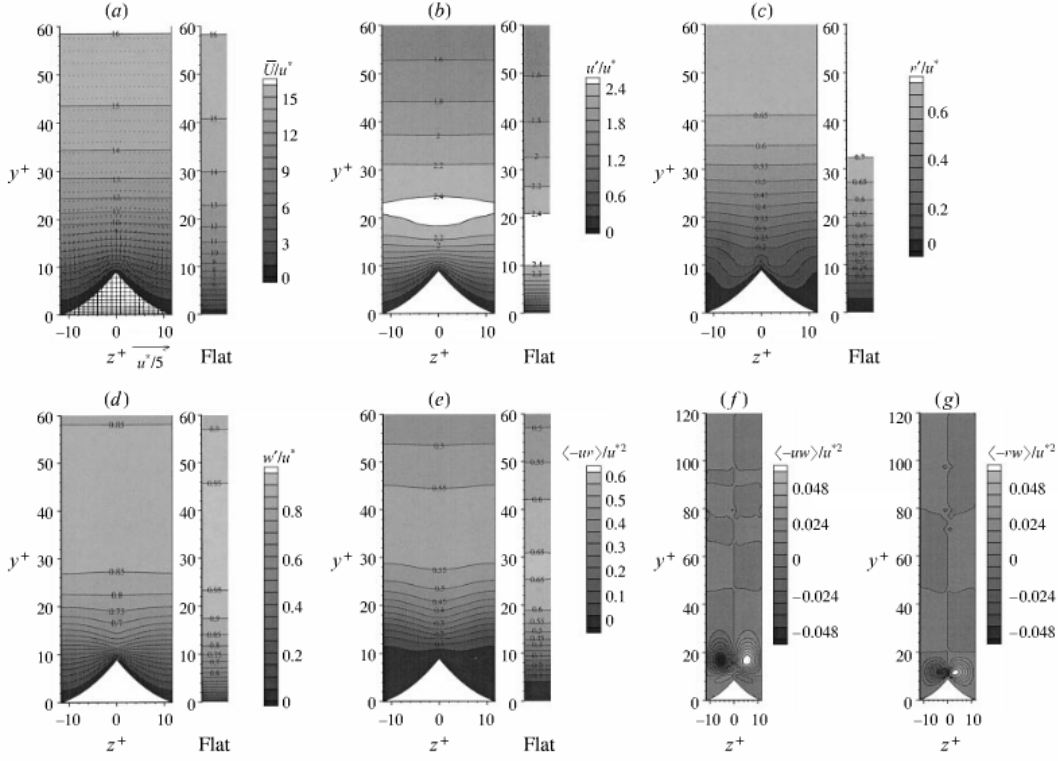
Figure 1-20: Contours of mean and root mean square (rms) velocities and Reynolds stresses in turbulent flow over riblets with $A^+ = 8.7$ and $\lambda^+ = 23$. Here, $\overline{U}$ is the mean velocity in the stream-wise direction and u', v', w' are the root mean square velocity component in stream wise, normal and span-wise direction. The quantities $< -uv >, < -uw >, < -vw >$ are negative of shear components of the Reynolds stress tensor (The negative sign only allows for presenting the color bars in positive values). The flat plate contours for all the cases, except $< -uw >$ and $< -vw >$, are shown on the right hand side of each figure. Note that $< -uw > = < -vw > = 0$ in flat plate. Vector of $u^*/5$ is shown as scale [67].

a 5% increase in the normal and span-wise directions across the entire span, but the stream-wise component shows 5% increase at the riblet peak and 15% reduction above the riblet valley [26]. The numerical study of El-Samni et al. using Boundary Integral Methods also reports an overall reduction in the stream-wise root mean square velocity over the riblet surfaces with an outward shift in the location of the maximum for rectangular grooves of $A/\lambda = 0.5$ (AR $= 1$). This shift is more pronounced in the drag reducing cases where the spacing of the riblets (λ^+) are lower than the diameter of the coherent stream-wise vortices. Also, in drag reducing cases, they

report observing a significant decrease in the stream-wise component of the turbulent intensity inside the grooves [68]. Choi also reports a reduction in the stream-wise turbulence intensity of about 10% for riblets with $A/\lambda \approx 0.64$ (AR = 1.28) with pointed rectangular riblets [50] and Park and Wallace show that for V-grooves of $A/\lambda = 0.5$ (AR = 1) and $\text{Re}_\theta = 1.2 \times 10^3$ (where Re_θ is the Reynolds number based on the momentum thickness), all components of turbulence intensities diminish in the valleys of the riblets and increase when above the peak of the riblets [74].

The experimental studies of Hooshmand et al. also report a significant decrease of about $10 - 15\%$ in the stream-wise turbulent intensity over the riblet surface as compared to the flat surface at a normal distance of less than 0.08 of the boundary layer thickness from the surface, for V-grooves with $A/\lambda = 0.502$ (AR ≈ 1) [47]. Walsh also reports a similar trend of reduction in the stream-wise and normal turbulence intensities compared to flat wall for V-grooves with $A/\lambda = 0.5$ (AR = 1) at normal distances less than 0.5 of the boundary layer thickness [37]. The experimental studies of Caram and Ahmed using a NACA 0012 arifoil with V-groove riblets of $A/\lambda = 1$ (AR = 2) also shows a reduction in the stream-wise turbulence intensity in the wake of the airfoil [12, 14, 13].

In the work of El-Samni et al. the spatial average contours of Reynolds shear stress over rectangular riblets show that in the drag decreasing riblet case ($\lambda^+ = 17.7, A/\lambda = 0.5$), the riblets move the regions of large Reynolds stress away from the wall, while in the drag increasing case ($\lambda^+ = 40.6, A/\lambda = 0.5$), local spots of high Reynolds stress start to penetrate inside the grooves concentrating around the riblet tips (see Figure 1-21). This indicates that drag reducing riblets are able to move the near wall activities and their corresponding turbulent structures away from the wall [68].

1.4.4   Vorticity and Vortical Structures

Various experimental and numerical works have looked into the near wall stream-wise vortices above drag reducing and drag increasing riblet structures. In drag reducing cases with turbulent flow, it has been observed that the size of the stream-wise vortices
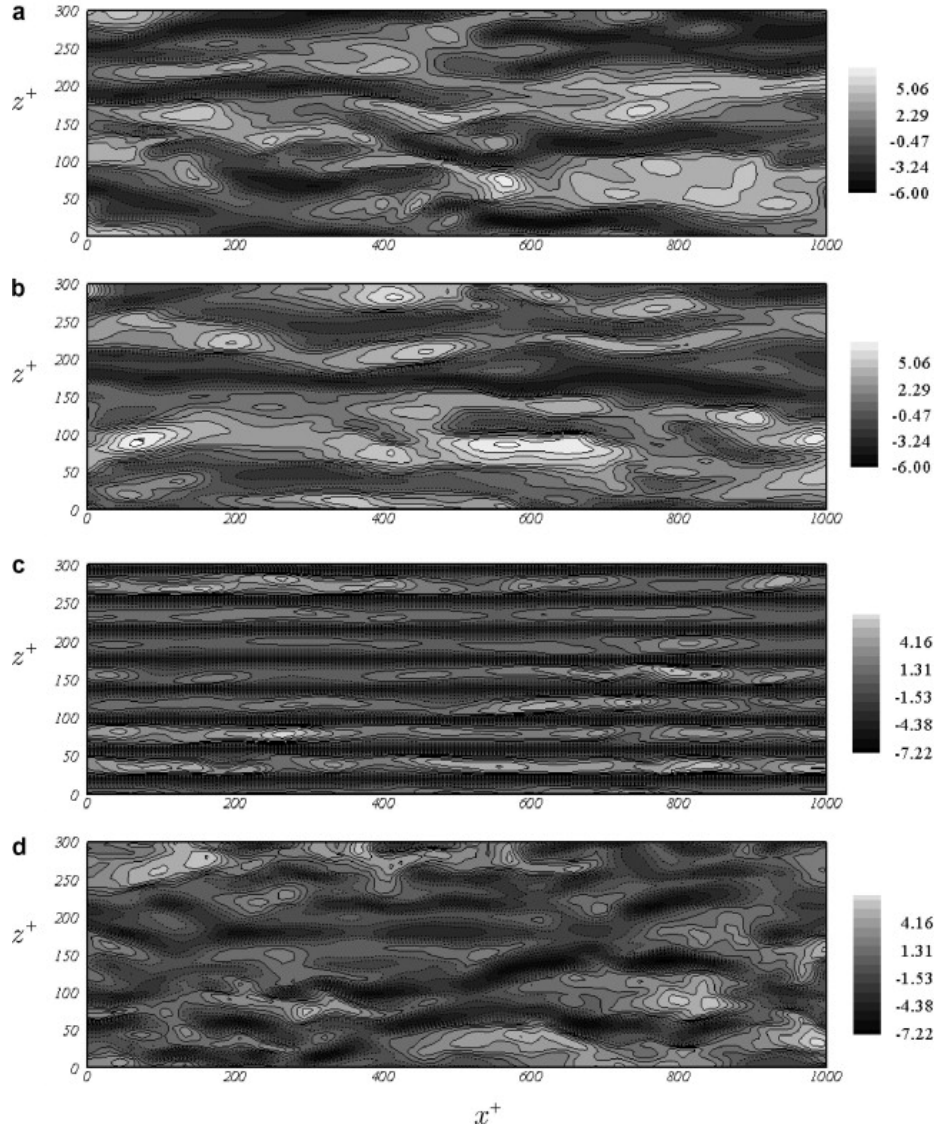
Figure 1-21: Streaky structures: (a) smooth surface at $y^+ \sim 12$; (b) ribbed surface of drag reduction case at $y^+ \sim 21$; (c) ribbed surface of drag increase case at $y^+ \sim 12.5$; (d) ribbed surface of drag increase case at $y^+ \sim 29$ [68].

are larger than the spacing of the riblets and thus the vortices are restricted and stay above the riblets. This has been observed in DNS data of Choi, Kim, and Moin for V-grooves with $\lambda^+ = 20$ and $A/\lambda = 0.5$ (AR = 1), calculations of El-Samni for rectangular grooves with $\lambda^+ = 17.7$ and $A/\lambda = 0.5$ (AR = 1) and experimental data obtained by Lee and Lee for semi-circular grooves (U-grooves) with $\lambda^+ = 20$ and $A/\lambda = 0.5$ (AR = 1) as shown in Figure 1-22 [26, 68, 28]. Contour plots of the distribution of the stream-wise vorticity in the cross section of a channel flow with

one riblet wall are shown in Figure 1-23.

On the other hand in the case of drag increasing riblets, the size of the vortices are smaller than the riblet spacing and thus the vortices are able to penetrate inside the riblets. Examples of such cases can be seen in the data of Choi, Kim, and Moin (V-grooves with $\lambda^+ = 40$ and $A/\lambda = 0.5$), El-Samni et al. (rectangular riblets with $\lambda^+ = 40.6$ and $A/\lambda = 0.5$), and Lee and Lee (semi-circular grooves with $\lambda^+ = 40.6$ and $A/\lambda = 0.5$) [26, 68, 28].

In addition, the diameter of the stream-wise vortices were calculated by Kim et al. to be about 25 ℓ^* in wall units [29], while the measurements of Kim, Kline and Reynolds, as well as those of Simpson, show that the diameter of the vortices are between 10-44 wall units and the transverse spacing between the low speed streaks is about 100 ℓ^* in wall units [30, 31]. Measurements of Bacher and Smith, and Gallagher and Thomas using variable interval time averaging technique (VITA) with hydrogen bubbles and dye injection for visualization show that the presence of the V-groove riblets can increase the streak spacing by about 45% and 15-30% respectively [55, 54].

1.4.5   Local Shear Stress Distribution

As a result of the non-uniform velocity profiles at different locations within one riblet, the shear stress distribution at the wall within each riblet is no longer uniform. DNS of laminar and turbulent channel flow by Chu and Karniadakis with V-grooves of $A/\lambda = 1$ (AR = 2) at $\text{Re}_H = 1000$ and $\text{Re}_H = 3500$ show a shear stress distribution within one riblet, with higher shear stress at the peaks and lower shear stress in the valleys when compared to the equivalent flat channel (Figure 1-24) [25] .

Hooshmand et al. reported that local shear stress at the peaks of the riblets was approximately 10% higher than the equivalent flat plate while the local shear stress in the troughs was 40% less than the flat plate in turbulent boundary layer flow with $\text{Re}_x = 2.02 \times 10^6$ and V-grooves of $A/\lambda = 0.5$ (AR = 1) [47]. Khan's numerical models of V-grooves with $A/\lambda = 0.5$ (AR = 1) for $A^+ = 8.33, 14.4$ and 20.67 also show a shear stress distribution similar to Figure 1-24 with the local shear stress at the peak of the ribs higher than the shear stress on a flat wall and lower shear stresses
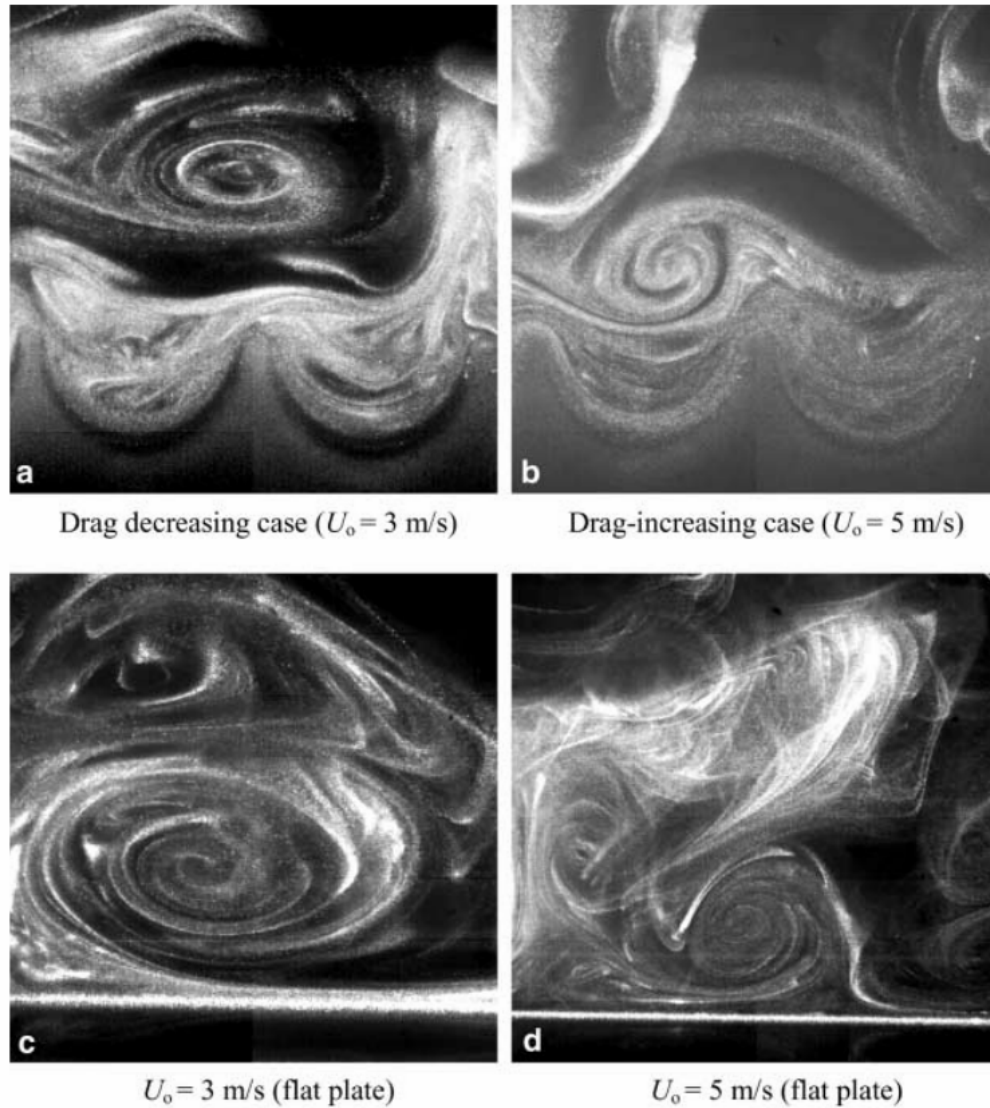
Figure 1-22: Visualization of stream-wise vortices in the normal plane in turbulent flow with, and without, riblets. Riblet spacing in the wall units, in the drag reducing case is $\lambda^+ = 25.2$ ($U_0 = $ 3m/s) and in the drag increasing case is $\lambda^+ = 40.6$ ($U_0 = $ 5 m/s) and in both cases $A/\lambda = 0.5$ (AR = 1). [28]

in the valley of the riblets compared to the flat wall [70]. Vukoslavcevic et al. also report the wall shear stress at the peak of V-grooves with $A/\lambda = 0.5$ (AR = 1) to be about 85% larger than flat plate and a vanishing velocity gradient (almost zero) in the valley of the riblets [48].
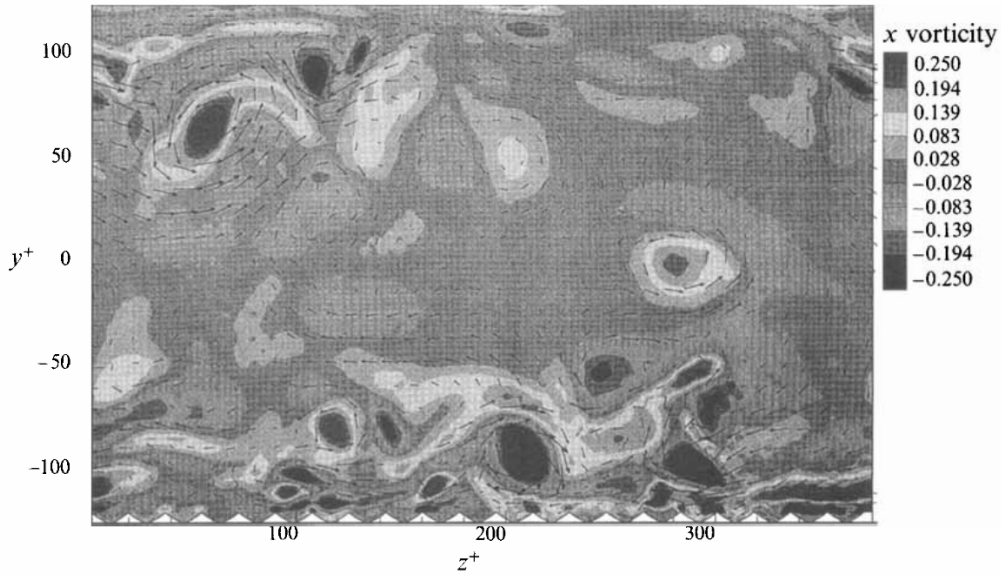
(a)
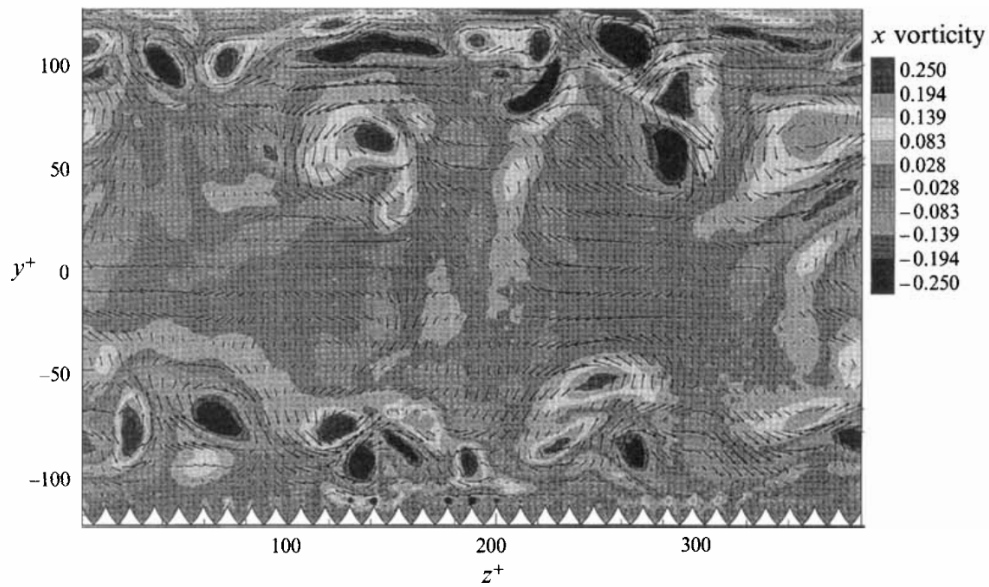
(b)

Figure 1-23:   Contours of stream-wise vorticity in the normal plane from DNS of turbulent flow in a channel with one riblet and one flat wall for $\mathrm{Re}_H = 1000$ (a) for $\lambda^+ = 18$, $A^+ = 5.3$ and (b) for $\lambda^+ = 11.7$, $A^+ = 9.4$ [27].

1.4.6   Friction Factor for Fully Developed Pipe Flows

In pipe/channel flow experiments the drag reduction is measured through the changes in the pressure gradient along the pipe/channel and using equation 1.15 can be translated to a dimensionless friction factor. The measurements of Liu et al. reported a

(a) Re = 1000   (b) Re = 3500
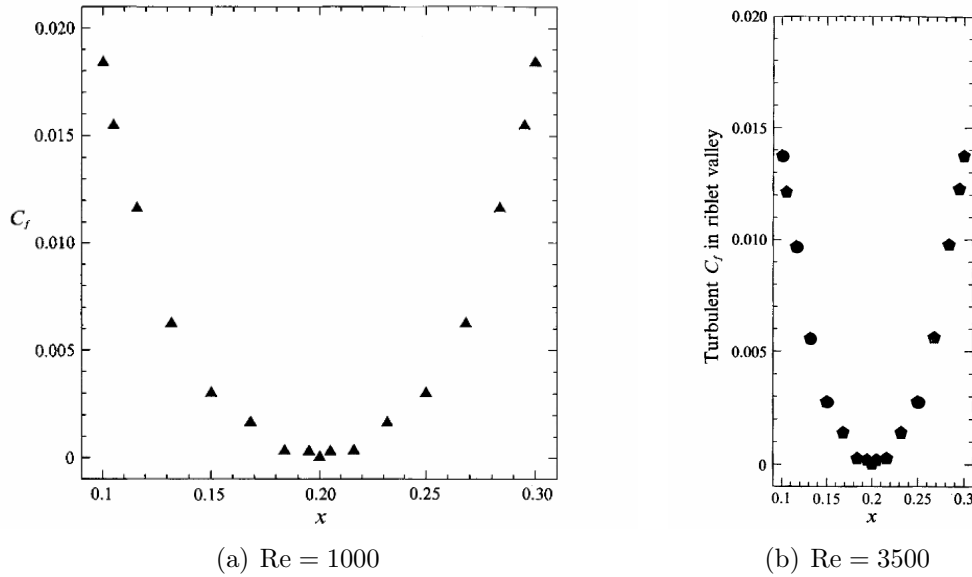
Figure 1-24: Shear stress distribution within one riblet from the laminar and turbulent channel flow DNS by Chu and Karniadakis. Here for $A = \lambda = 0.1H$ where H is the channel height (AR = 2). In the laminar case $C_{f,\text{flat}} = 0.01284$ [25].

$5 - 7\%$ reduction in the friction factor of fully developed turbulent pipe flow over riblets with $A/\lambda = 0.87$ (AR = 1.74) and water using 1 and 2 in diameter pipes. Results for the 1 in diameter pipes are shown in Figure 1-25(a) and the maximum reduction was seen with riblets of $\lambda^+ \approx 11 - 13$ [66]. Nakao's experiments showed a $5 - 7\%$ reduction in the friction factor in pipe flow using V-groove riblets of various aspect ratios and noticed that riblets with $A/\lambda \approx 0.4 - 0.5$ (AR $\approx 0.8 - 1$) showed drag reduction over a wide range of Reynolds numbers compared to others. In addition, maximum reduction observed was for riblets with spacings in the range of $\lambda^+ \approx 15 - 25$ in wall units [79].

Experiments of Rohr et al. showed no reduction in the friction factor for laminar flow with riblets of $A = \lambda$ (AR = 2), but after transition to turbulence, first a drag reduction and then drag increase was observed as the Reynolds number was increased. Additionally, they observed a substantial delay in transition to turbulence when riblets are used as shown in Figure 1-25(b) [60]. Numerical calculations of Launder and Li also showed no reduction using riblets of $A/\lambda = 1$ (AR = 2) and $A/\lambda = 3$ (AR = 6) in laminar flow [72]. The measurements of Wang and Javanovic

66
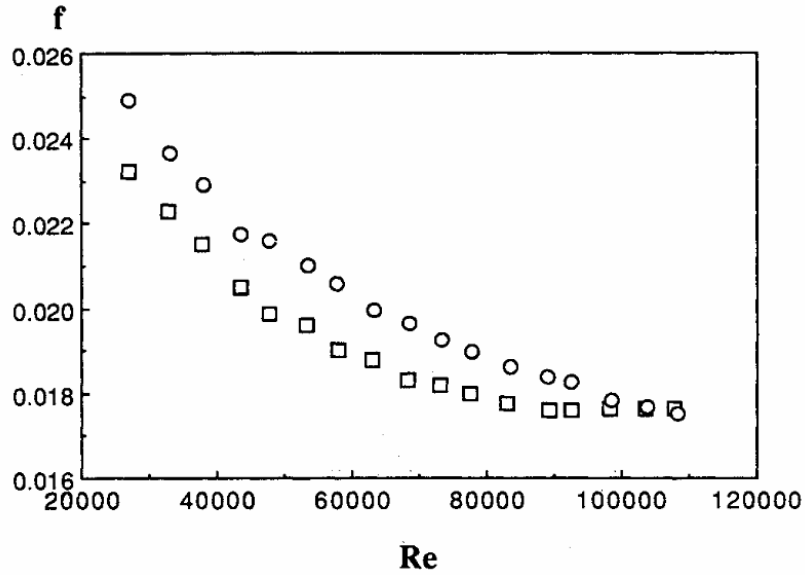
(a)
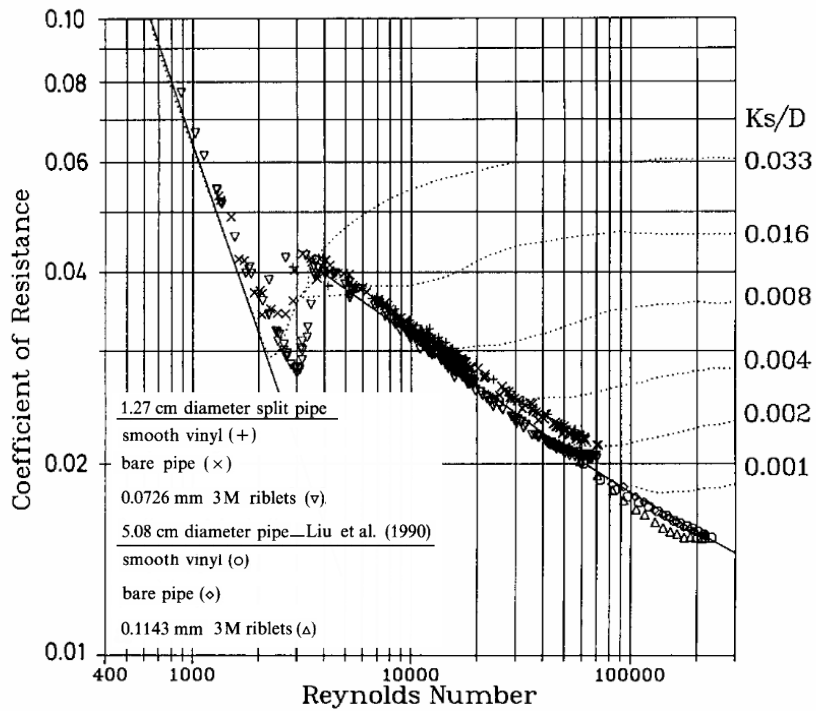
(b)

Figure 1-25: (a) The friction factor coefficient in a pipe of diameter $D = 25.4$ mm with and without V-groove riblets of AR $= 1.67$ with respect to Re$_D$; Open circles correspond to the smooth pipe data and open squares present the riblet results [66]; (b) Friction factor in pipes with and without V-groove riblets with respect to variation of Re$_D$ for various types of riblets [60].

using thin-fin riblet elements (close to rectangular riblet shapes) with $A/\lambda = 1$ (AR = 2) or $A/\lambda = 0.5$ (AR = 1) showed a reduction in the friction factor over a wide range of Reynolds numbers [52].

1.4.7   Total Skin Friction Drag

The ultimate goal of using riblets is to reduce the total frictional drag force on the surfaces. As I noted earlier, the presence of riblets results in a redistribution of the wall shear stress and thus as reported by various researchers, the local skin friction inside the valleys is lower than the corresponding flat surface value while at the peak it is higher. However, when integrated over the entire area, it is possible to not get any reduction in the total drag as the riblets increase the wetted area of the surface. For example, Gallagher and Thomas reported a 20% reduction in the local skin friction coefficient at the end of the test plate used, but they did not observe any reduction in the total drag measured as compared with the flat plate [54]. As seen in the previous section, for different cases of pipe flow, both reduction and increase in the total drag (reported as a dimensionless friction coefficient) were observed. Also, DNS results of a laminar ($\text{Re}_H = 1000$) and turbulent channel flow ($\text{Re}_H = 3500$) with riblets of $\lambda = A$ (AR = 2) showed no drag reduction in the laminar case and a 6% reduction in the turbulent case [25].

The results found in the riblets literature clearly show that the drag reduction (in the turbulent flow) is a function of the spacing of the riblets in the wall units, the ratio of the height to spacing (or equivalently the aspect ratio, AR) of the riblets (even though there is not much discussion offered regarding this parameter in the previous papers), as well as the shape of the riblets. Walsh et al. show that the highest drag reduction achieved is for riblets with spacing of about 15 wall units (Figure 1-26) [37, 38, 39, 1]. Experimental results of Bechert et al. show a clear connection between the reduction achieved and the aspect ratio of the riblets (see Figures 1-26 and 1-27) [40, 20]. In addition the DNS results of Goldstein et al. show drag reduction of 2.2% in case of V-grooves with $\lambda^+ = 18$ and $A/\lambda = 0.29$ (AR = 0.58) and a reduction of 3.3% in case of V-grooves with $\lambda^+ = 11.7$ and $A/\lambda = 0.8$ (AR = 1.6) [27]. Lazos and

Wilkinson present the results of experiments with assembled rectangular riblets and trapezoidal riblet films (Figure 1-28) and as seen from the plot and the accompanying table, riblets with lower aspect ratios, show reductions in the total drag over a wider range of λ^+; especially comparing models 6,8 and 10, as A/λ (or AR) decreases, riblets are able to give reduction in the drag over a wider range of λ^+ or as translated to Reynolds number by re-plotting the same data in Figure 1-29.

Additionally, Bechert and co-workers show that rectangular riblets can perform better than trapezoidal or V-groove riblets [20]. Walsh and Lindermann report that peak curvature does not affect the results, but valley curvature could improve the reduction, but is harder in terms of manufacturing [39]. Additionally, rounding the tips of a blunt riblet peak can enhance the drag reduction, while rounding the tips of sharp riblets has been seen to decrease the maximum level of total drag reduction achieved [6].

1.5   Drag Reduction Mechanism

So far, various mechanisms for the drag reducing capabilities of riblet surfaces have been suggested. As briefly discussed earlier, it is thought that in turbulent flows, riblets smaller than the diameter of the vortices serve to lift the turbulent vortical structures away from the wall and prevent them from penetrating inside the grooves. As I have noted, experiments and simulations show that the diameter of the vortical structures in turbulent flow is typically around 10-30 wall units [29, 30, 80, 31]. The data presented earlier confirm that spacing of drag reducing riblets are within the range of 10-30 wall units, with the maximum drag reduction observed in the range of $\lambda^+ \approx 10 - 20$ [28, 27, 6, 26, 34, 55]. A schematic of the interaction of the turbulent vortices with the riblets of different sizes is shown in Figure 1-30(a). Displacement of the vortices affects the turbulent statistics as well, which in part results in lower Reynolds shear stresses in turbulent flow and thus an overall drag reduction [28, 27, 26].

Additionally, the aspect ratio $(2A/\lambda)$ of the riblets affects the ability of the riblets
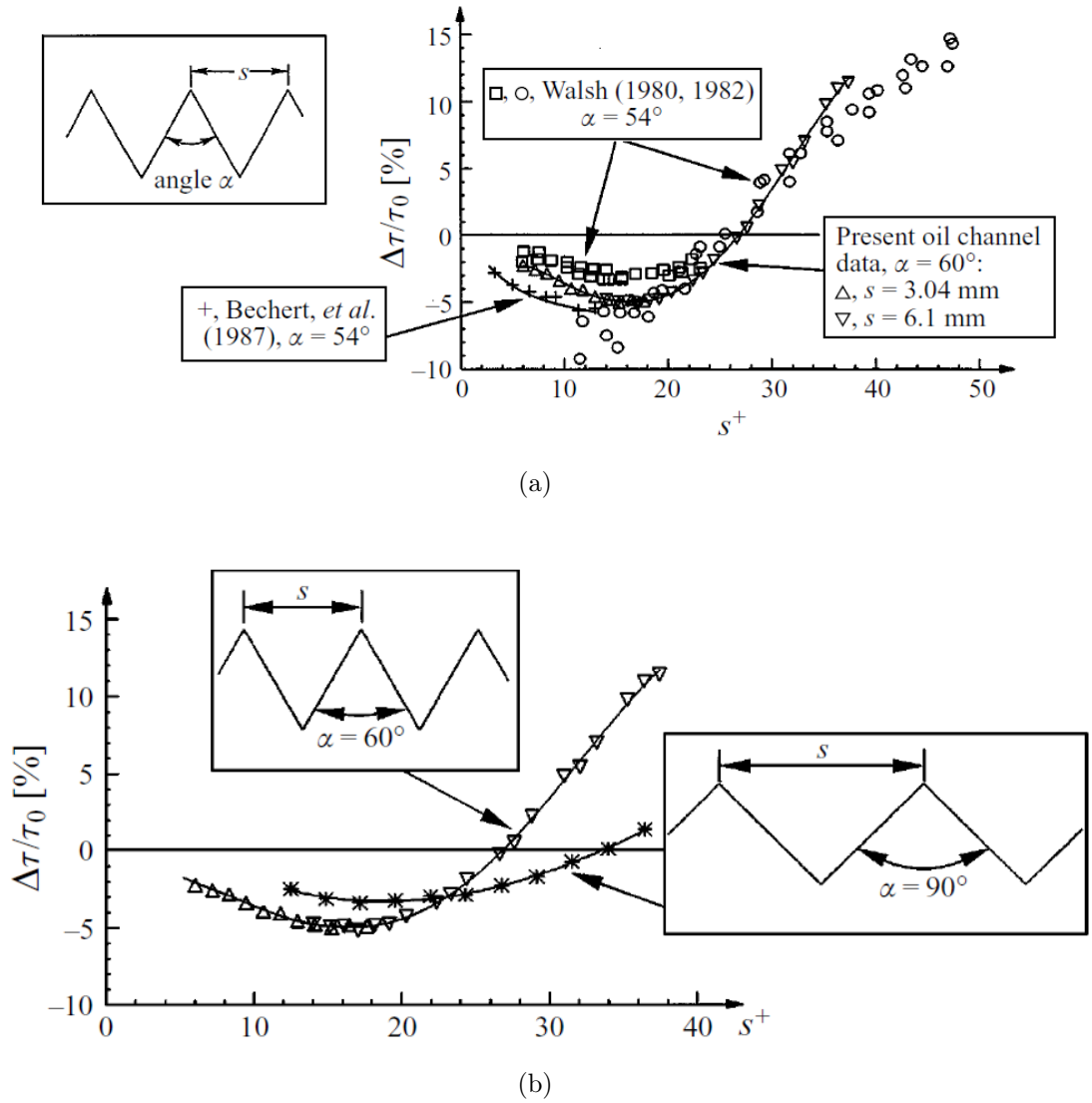
Figure 1-26: Drag reduction curves of various V-grooves from wind tunnel and oil channel experiments performed by Walsh and co-workers, and Bechert and co-workers [40, 37, 38, 39, 1].

to reduce viscous the drag. As indicated in Figure 1-30(a), increasing the aspect ratio of the riblets, results in an increase in the wetted area and could result in an increase in the total drag as seen in Section 1.4.7 [81].

Another mechanism that has been suggested is that riblets cause a retardation of the local flow close to the wall and this retardation (in some literature also called *re-laminarization*) reduces the velocity gradient at the wall which, as seen earlier, creates a span-wise distribution of the wall shear stress with valleys experiencing a
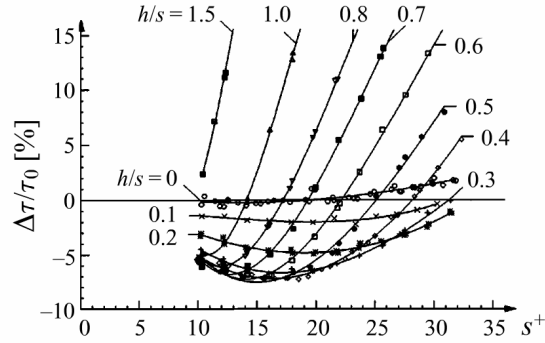
Figure 1-27: Drag reduction curve for rectangular riblets with the same spacing and varying heights (varying aspect ratios). Riblets with aspect ratios of less than 1 ($A/\lambda < 0.5$) show drag reduction over a wider range of λ^+ [40].

Model	Type	h(in.)	s(in.)	Aspect ratio (h/s)
	A	0.010	0.140	0.07
2	A	0.010	0.064	0.16
3	A	0.013	0.080	0.16
4	A	0.020	0.064	0.31
5	F	0.006	0.018	0.33
6	A	0.010	0.025	0.40
7	F	0.006	0.012	0.50
8	A	0.020	0.025	0.80
9	F	0.006	0.006	1.00
10	A	0.025	0.025	1.00

A = assembled model; F = plastic film model.
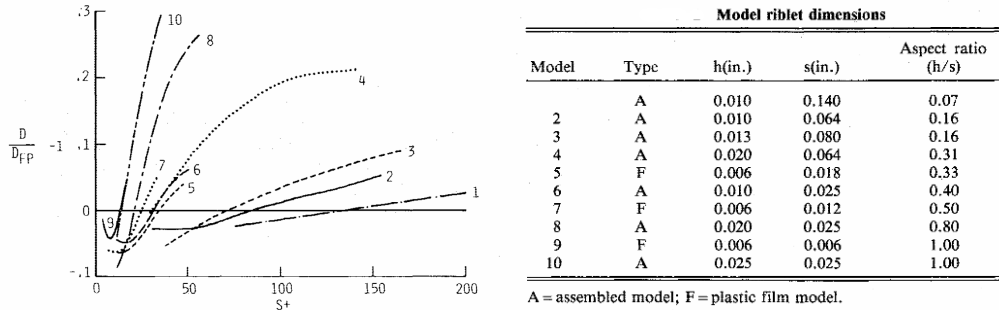
Figure 1-28: Drag reduction plot for rectangular riblets and trapezoidal riblets with various aspect ratios. Numbers on the plot correspond to the numbers in the list of the riblet wall shapes in the accompanying table [51].

(a)
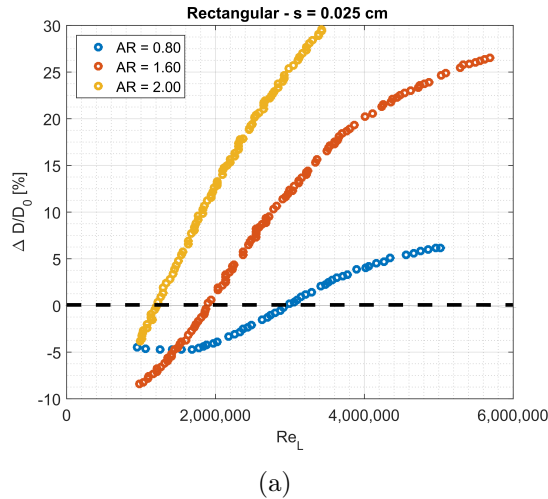
Figure 1-29: Total drag reduction for riblets with various aspect ratios against Reynolds number taken from Figure 1-28 for models 6,8 and 10 [51].

71

(a)

(b)

Figure 1-30: (a) Schematic diagrams showing the interaction of vortices with wall in flat and riblet case [81]. (b) Schematic definition of the *protrusion height* in both stream-wise and span-wise directions [71].

shear stress lower than the corresponding flat surface and thus results in a reduction in the overall drag force [74, 1, 15, 75, 63, 55]. This mechanism holds for both laminar and turbulent flows. Since the data available for laminar drag reduction using riblets is very limited, one cannot conclude definitely that riblets would not be effective in laminar flow.

Bechert and Bartenwerfer use the idea of a retarded flow and with assumption of viscous dominated flow, calculate the "Protrusion Height" for the stream-wise and cross flow [40]. As per their definition, the protrusion height is equivalent to the virtual origin of the flow in both stream-wise and cross flow configurations (as shown in Figure 1-30(b). They argue that drag reduction is dependent on the difference of these two values as a measure of how much the turbulent cross flow close to the wall (especially the span-wise component of the velocity) has been retarded by the riblet structures [40]. Choi, and Suzuki and Kasagi also suggest that suppression of the span-wise velocity component plays an important role in drag reduction using riblets [50, 75]. But it should be noted that these calculations were performed with the assumption of a fully viscous flow inside the riblets, and from their experiments, Vuskoslaveciv et al. mention that they did not observe the assumed linear variation in the velocity profile ($\mathrm{Re}_\theta = 1000$ and $A/\lambda = 0.5$ (AR = 1)) [48].

1.6   Conclusion

In this chapter, an overview of the previous research in the use of riblets to achieve drag reduction is presented. In summary, stream-wise grooves aligned in the flow direction, also known as riblets, have been shown to be able to reduce the skin friction drag by an average of $5-7\%$ compared to the corresponding flat surface. Studies have shown that inside the grooves the flow is retarded in both laminar and turbulent flow and it has been seen that the thickness of the boundary layer increases when riblet structures are introduced on the wall. In wall-bounded turbulent flow, riblets with a lateral spacing size less than the diameter of the natural vortical structures of the flow limit the interaction of the turbulent vortices with the walls, and thus reduce the

Reynolds stresses in turbulent flow. Experimental and numerical results have shown that riblets with spacing $\lambda^+ = 10 - 20$ wall units give the maximum drag reduction.

In terms of viscous shear stress, the grooves result in a shear stress distribution with the local shear stress in the valleys lower than the corresponding flat surface and higher at the peak of the riblets. However, because riblets increase the total wetted area, the integration of this lateral shear stress distribution might or might not offer a net drag reduction. Studies have shown that riblets with aspect ratios of unity and lower result in drag reduction over a wider range of flow conditions.

The main two mechanisms suggested for this form of drag reduction are restriction of the turbulent vortices from penetrating into the riblets and retardation of the local viscous flow inside the grooves. Most of the studies so far have been in turbulent flow regions and limited work has been done under laminar flow conditions. Additional studies focusing on laminar flow could help in understanding the mechanism of this form of drag reduction even more, because it does not require the use of large scale numerical simulation algorithms such as DNS (Direct Numerical Simulations), LES (Large Eddy Simulations), or RANS (Reynolds Averaged Numerical Simulations) as well as allowing me a chance to analyse the equations of motion in great details.

To complement the efforts in the research on drag reduction method using riblet surfaces, in this thesis I will consider the effect of riblets in laminar flows, especially looking at the effect of riblets in flat plate boundary layers as well as in Taylor Couette flows. In Chapter 2, a theoretical model of the boundary layer over V-groove riblets is presented and used to discuss the resulting changes in the total frictional drag force on riblet walls. Then in Chapter 3, using numerical modelling the effect of sinusoidal riblets on the evolving boundary layer flow especially near the leading edge of the plate is presented and later compared with the results presented in Chapter 2. Then in chapters 4 and 5, I will consider the case of using riblet covered rotors in axi-symmetric Taylor-Couette flows and investigate the effect of riblets on the total torque exerted on the inner rotor, using experimental and numerical calculations.

Chapter 2

Extended Three Dimensional Boundary Layer Theory for Periodic Riblet Surfaces

2.1 Introduction

As it was introduced in Chapter 1, inspired by the shape of the ribs on the shark denticles, various approaches to drag reduction using riblet surfaces have been introduced and previously investigated with different riblet shapes such as V-grooves, U-grooves, and rectangular razor blades in turbulent flows [82, 71, 25, 9, 8, 38, 39, 6], laminar flows [72, 73, 83], high Mach number flows [84, 85, 86], and pipe flows [60, 79, 66]. Among the various forms of the external flows, boundary layer flows, especially boundary layers over a flat plate are of great importance due to their application in flight vehicles and marine equipment. Various researchers such as Djenidi and co-workers [73], Hooshmad and co-workers [47], Lee and Lee [28] have discussed some aspects of the turbulent and laminar boundary layer flows over V-grooves and U-grooves riblet surfaces and parts of their work were discussed in Chapter 1.

In boundary layer flows, the fluid with a free-stream velocity W_∞, flows past a solid wall (flat or curved) and due to the no-slip boundary condition at the fluid-solid

interface, the fluid is slowed down close to the wall. However, as I move further and further away (in the normal direction) from the wall, the velocity of the fluid goes back to the free-stream value [41, 43]. Prandtl was the first person to discuss the boundary layers in detail and established the classical boundary layer theory. He simplified the equations of motion to a set of two equations defining the boundary layer flow over the flat plates (shown later in Equations 2.4 and 2.5). He assumed that only within a small region with thickness $\delta \ll L$ (where L is the length of the plate) close to the wall (which is much smaller than the length of the plate, L) the viscous effects are as important as the inertial effects and outside this layer, the flow can be analysed as inviscid. This small region close to the wall is called a boundary layer. Using scaling arguments one can show that in this region both viscous effects and inertial effects are of the same order and hence, even the simplified form of the equations of motion, also known as the classical boundary layer equations are non-linear [41, 43].

Prandtl's graduate student, Blasius was the first person to solve the boundary layer equations using a similarity solution and presented the shape of the boundary layer profile (Figure 2-2) as a function of the similarity variable η defined as [41, 43]

$$\eta = \frac{y}{z}\sqrt{\mathrm{Re}_z} \tag{2.1}$$

where y is the wall normal direction and z is the stream-wise direction, and Re_z is the Reynolds number as a function of the stream-wise location defined as $\rho W_\infty z/\mu$. (ρ and μ are the fluid density and viscosity respectively.)

The Blasius solution to the boundary layer equations (discussed in more details in section 2.2) is shown in Figure 2-2 where the non-dimensional stream-wise velocity w/W_∞ is plotted as a function of the similarity variable η.

While the classical boundary layer theory over flat plate is a two dimensional flow, introducing riblets on the surface of the plates, changes the velocity profile from only being a function of the stream-wise and wall normal direction to a function of all three directions in the Cartesian coordinate system. This results in changes in the velocity profile, the boundary layer thickness, shear stress distribution on the

76

(a)   (b)
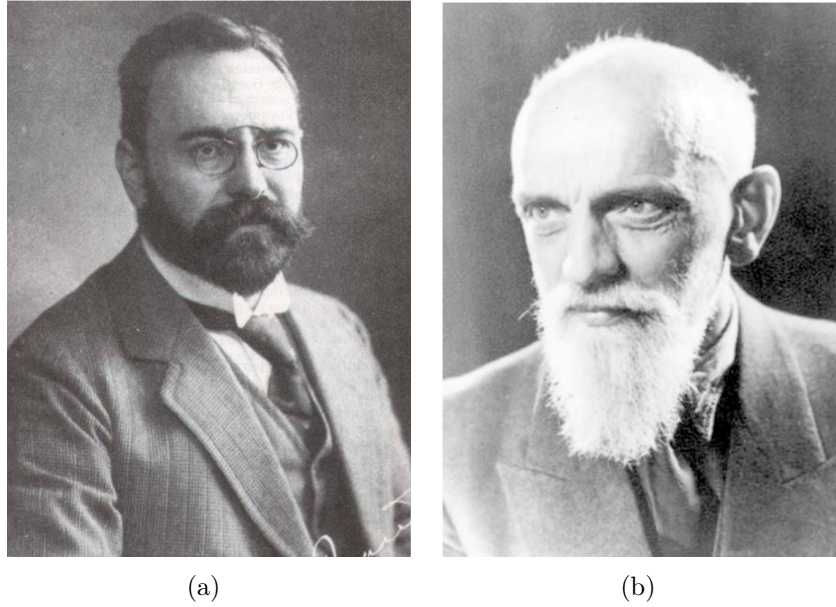
Figure 2-1:   (a) Young Ludwig Prandtl (1875-1953) [87] [87] (b) Paul Richard Heinrich Blasius Prandtl's doctoral student (1883-1970) [88].

wall, and ultimately the total drag force exerted by the fluid on the wetted area of the surface. While these changes have been previously studied in the context of the turbulent flows [47, 1, 73], fewer works have looked at the boundary layer flows over riblet surfaces in the laminar region prior to transition to turbulence. In a boundary layer, close to the leading edge of the plate, the flow initially starts as laminar and evolves along the plate until it naturally transitions to turbulent at a local Reynolds number of $\mathrm{Re}_z \approx 5 \times 10^5$ [41, 43]. Therefore, while it is important to understand the mechanism of drag reduction in the turbulent regime, I also need to understand how riblets behave in the laminar regime and thus be able to tune the shape and size of the riblets for the optimum performance throughout the length of the plate.

High Reynolds number laminar boundary layer is a canonical flow problem and understanding the effect of the change of geometry of the riblet surfaces can be used to understand the geometric and dynamic parameters that define this mode of passive drag reduction (before introducing complicating factors such as turbulence and mixing).

To be able to understand the changes due to riblet surfaces in laminar boundary

(a)

(b)
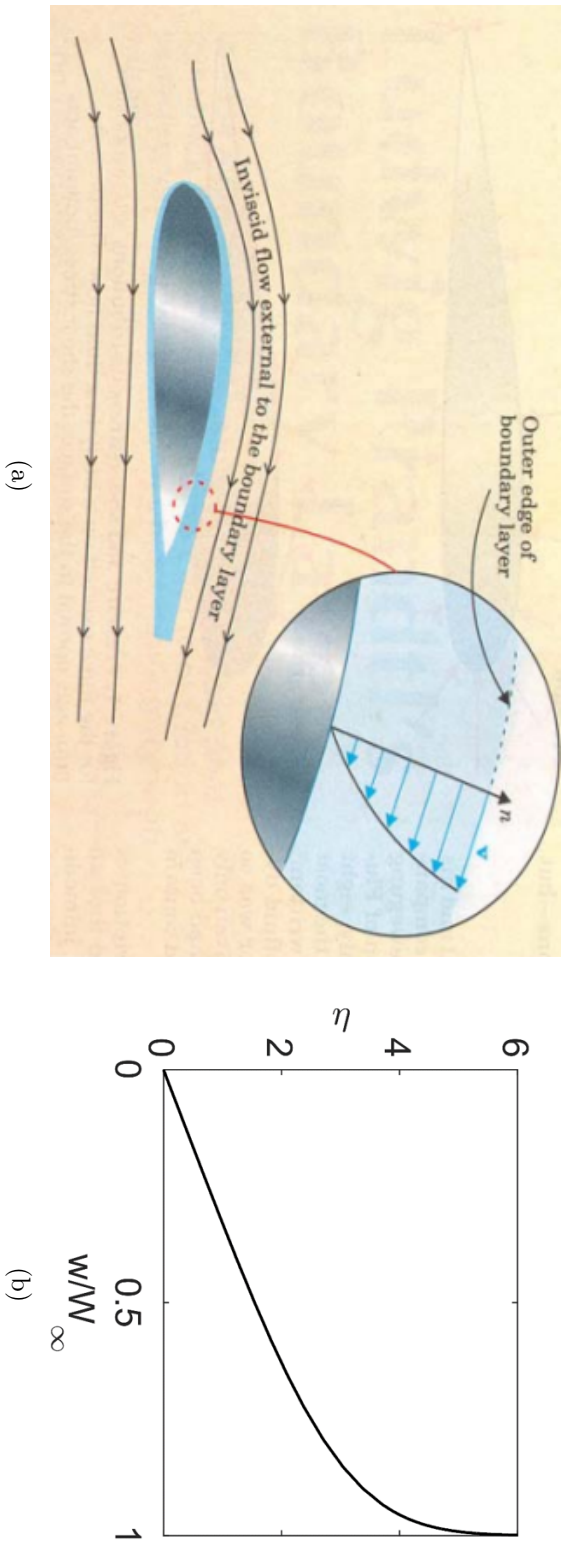
Figure 2-2: (a) Schematic of the boundary layer over the surface of an airfoil [87]. (b) Self-similar profile of the boundary layer over a flat surface as calculated by Blasius. w/W_∞ is the non-dimensional velocity in the stream-wise direction and η is the similarity variable defined as in Equation 2.1.

layer flows in more detail, in this chapter, I will expand the boundary layer theory from two dimensional as put together by Prandtl to three dimensional flow over periodic riblet surfaces with riblets of wavelength λ and amplitude A (the same was as defined in Section 1.1). First by scaling and non-dimensionalizing the equations of motion, I will derive the three dimensional boundary layer equations as discussed in Section 2.2. Then using an appropriate change of coordinate system and employing conformal mapping, I solve the three dimensional boundary layer equations for the simple case of V-groove riblets in Section 2.3. Afterwards in Section 2.4 I discuss the results of the solution by looking at a new mode of self-similarity for flow over riblet surfaces, then calculate the boundary layer thickness, and ultimately use the momentum integral equations to calculate the total drag force over riblet plates of various lengths. Ultimately I discuss the effect of the geometry and dynamics of the flow on the possibility of achieving drag reduction employing riblet surfaces. Lastly, I will compare the results with some of the previous experiments presented in the literature. Finally, I will discuss the limitation of this theory and seek ways to resolve this issue in the future chapters.

2.2   Extension of the Boundary Layer Theory to Three Dimensions

In 1904 Prandtl introduced the concept of the viscous boundary layer, recognizing that in high Reynolds number flows, close to a rigid wall, there is a thin region where the viscous effects are as important as inertial effects of the flow and cannot be neglected; outside this thin layer viscous effects are negligible and flow can be considered to be inviscid and analysed using potential flow.

Assume an incompressible fluid of density ρ and viscosity μ is flowing past a plate of length L with free-stream velocity W_∞ in the stream-wise direction z. The wall normal direction and the vorticity direction into the plane are y and x respectively. Close to the wall a thin boundary layer is formed where the thickness of this boundary

layer (denoted by δ) is scaled as

$$\frac{\delta}{L} \sim \mathrm{Re}_L^{-1/2}, \tag{2.2}$$

where the Reynolds number is defined as

$$\mathrm{Re}_L = \frac{\rho W_\infty L}{\mu}. \tag{2.3}$$

The pressure gradient in all directions is zero , i.e. $\boldsymbol{\nabla} p = \mathbf{0}$ (neglecting gravitational effects). The velocity vector inside the boundary layer is written as (u, v, w) where the span-wise velocity is equal to zero $(u = 0)$ and the stream-wise and wall normal components, w, and v, are found using

$$\frac{\partial v}{\partial y} + \frac{\partial w}{\partial z} = 0 \tag{2.4}$$

$$\rho \left(v \frac{\partial w}{\partial y} + w \frac{\partial w}{\partial z} \right) = \mu \frac{\partial^2 w}{\partial y^2} \tag{2.5}$$

known as flat plate boundary layer equations consisting of the continuity equation and the Navier-Stokes equation in the z direction with all first order terms $(O(1))$. The Navier-Stokes equation in the x direction is identically zero and the Navier-Stokes equation in the y direction has an order of magnitude of $O(\mathrm{Re}_L^{-1})$ compared to the equation of motion in the z direction and is neglected [41].

To extend the classical boundary layer theory over a flat smooth plate to the case of boundary layer theory over flat (as opposed to curved surfaces) periodic riblet surfaces, the case of V-groove textures (triangular riblets) are considered here. Any riblet surface comprises of two main length scales, defining the overall shape of the grooves; one is the wavelength (or spacing) of the riblets, denoted by λ and the other is the amplitude (or height) of the riblets, denoted by A. These two variables correspond to the variables s and h in most of the previous literature on riblet surfaces respectively [71, 38, 39, 6, 82]. For periodic V-groove textures of interest, wavelength (λ) and amplitude (A) are shown in Figure 2-3(b). Note the same general definition

can be extended to other riblet shapes as well.

To extend the boundary layer theory to the case of flat plates with three dimensional periodic riblet surfaces, it is assumed that there are no pressure gradients in the problem and therefore

$$p \approx \text{constant} \quad \implies \quad \boldsymbol{\nabla} p = \mathbf{0}. \tag{2.6}$$

For analysing the high Reynolds number laminar boundary layer flow over periodic riblet surfaces (after the leading edge effects have subsided), I neglect the pressure gradient term in the equations of motion. Additionally, length of the plate along the flow direction is much larger than the spacing of the riblets ($L \gg \lambda$). Similar to the boundary layer theory thickness of the boundary layer is defined as δ and its growth is proportional to

$$\delta \sim \sqrt{\frac{\mu}{\rho}} \tag{2.7}$$

and it is much smaller than the length of the plate ($\delta \ll L$).

From experimental measurements near textured surfaces by Hooshmand and co-workers [47], I expect that the thickness of the boundary layer is of the same order as the spacing of the riblets. Hence

$$\frac{\delta}{\lambda} \sim 1. \tag{2.8}$$

So, to non-dimensionalize the Navier-Stokes equations for the stream-wise and the normal direction,

$$z^* = \frac{z}{L} \quad \& \quad y^* = \frac{y}{\delta} \tag{2.9}$$

are used respectively; while for the x direction it it appropriate to introduce

$$x^* = \frac{x}{\lambda} \tag{2.10}$$

for non-diemsionalizing the equations. Note that this group is added due to the

presence of the riblets and it does not exist in the classical boundary layer theory. In addition, velocities u, v and w can be scaled by U, V, and W_∞. Hence

$$u^* = \frac{u}{U} \quad \& \quad v^* = \frac{v}{V} \quad \& \quad w^* = \frac{w}{W_\infty} \tag{2.11}$$

where the relative scales of U and V can be found using the continuity equation:

$$\frac{\partial u}{\partial x} + \frac{\partial v}{\partial y} + \frac{\partial w}{\partial z} = 0 \tag{2.12}$$

$$\frac{U}{\lambda} \sim \frac{V}{\delta} \sim \frac{W_\infty}{L} \tag{2.13}$$

Therefore, non-dimensional steady state Navier-Stokes equation in the span-wise direction x is written as

$$\left(\frac{\lambda}{L}\right)^2 \left(u^* \frac{\partial u^*}{\partial x^*} + v^* \frac{\partial u^*}{\partial y^*} + w^* \frac{\partial u^*}{\partial z^*}\right) = \frac{1}{\mathrm{Re}_L} \left(\frac{\partial^2 u^*}{\partial x^{*2}} + \left(\frac{\lambda}{\delta}\right)^2 \frac{\partial^2 u^*}{\partial y^{*2}} + \left(\frac{\lambda}{L}\right)^2 \frac{\partial^2 u^*}{\partial z^{*2}}\right). \tag{2.14}$$

On the left hand side of Equation 2.14 I have

$$u^* \frac{\partial u^*}{\partial x^*} \sim v^* \frac{\partial u^*}{\partial y^*} \sim w^* \frac{\partial u^*}{\partial z^*} \sim O(1) \tag{2.15}$$

$$\left(\frac{\lambda}{L}\right)^2 \sim \left(\frac{\delta}{L}\right)^2 \sim \frac{1}{\mathrm{Re}_L} \sim O(\mathrm{Re}_L^{-1}) \tag{2.16}$$

and on the right hand side of the Equation 2.14, similarly I can write
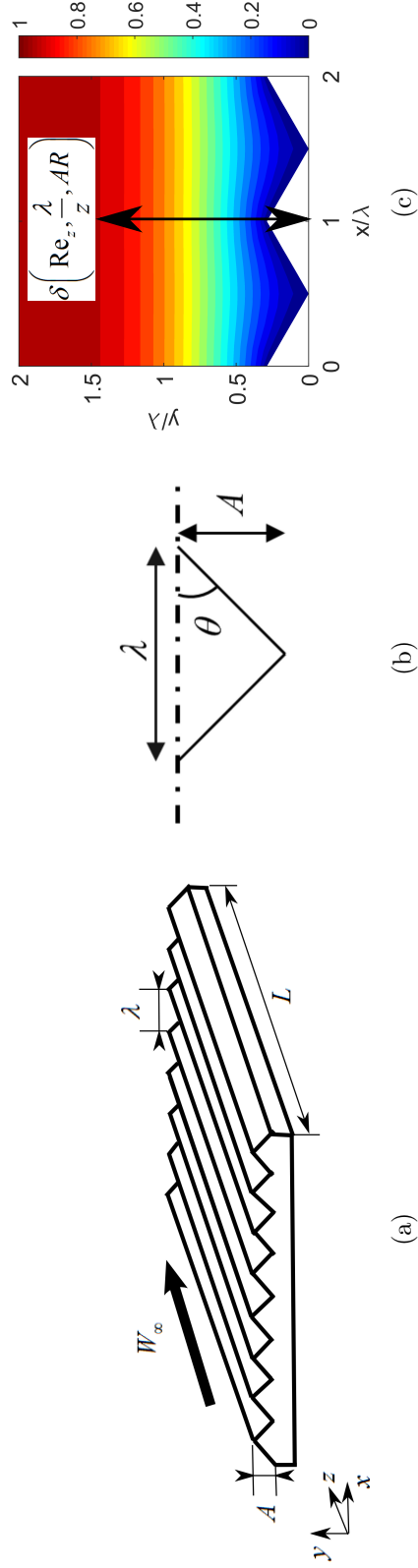
Figure 2-3: (a) Schematic of three dimensional flow over V-groove riblet surfaces and the geometry of the V-groove riblets with wavelength (spacing) of λ (in x direction) and amplitude A (in y direction). The length of the plate in the flow direction z is L and the free-stream velocity of W_∞. (b) Cross sectional view of each riblet with spacing λ and amplitude A. (c) The velocity contours at $\text{Re}_L = 1000$ and $\lambda/L = 0.1$ for boundary layer over 3D riblets of $AR = 0.58$ and schematic of boundary layer thickness.

$$\frac{1}{\mathrm{Re}_L}\frac{\partial^2 u^*}{\partial x^{*2}} \sim \frac{1}{\mathrm{Re}_L}\left(\frac{\lambda}{\delta}\right)^2 \frac{\partial^2 u^*}{\partial y^{*2}} \sim O(\mathrm{Re}_L^{-1}) \tag{2.17}$$

$$\frac{1}{\mathrm{Re}_L}\left(\frac{\lambda}{L}\right)^2 \frac{\partial^2 u^*}{\partial z^{*2}} \sim O(\mathrm{Re}_L^{-2}). \tag{2.18}$$

Therefore, it shows that the Navier-Stokes equation in the span-wise (x) direction is of the order of $O(\mathrm{Re}_L^{-1})$. Now, for the normal direction (y) I have

$$\left(\frac{\delta}{L}\right)^2 \left(u^*\frac{\partial v^*}{\partial x^*} + v^*\frac{\partial v^*}{\partial y^*} + w^*\frac{\partial v^*}{\partial z^*}\right) = \frac{1}{\mathrm{Re}_L}\left(\left(\frac{\delta}{\lambda}\right)^2\frac{\partial^2 v^*}{\partial x^{*2}} + \frac{\partial^2 v^*}{\partial y^{*2}} + \left(\frac{\delta}{L}\right)^2\frac{\partial^2 v^*}{\partial z^{*2}}\right) \tag{2.19}$$

where on the left hand side

$$u^*\frac{\partial v^*}{\partial x^*} \sim v^*\frac{\partial v^*}{\partial y^*} \sim w^*\frac{\partial v^*}{\partial z^*} \sim O(1) \tag{2.20}$$

$$\left(\frac{\delta}{L}\right)^2 \sim \frac{1}{\mathrm{Re}_L} \sim O(\mathrm{Re}_L^{-1}) \tag{2.21}$$

and on the right hand side

$$\frac{1}{\mathrm{Re}_L}\left(\frac{\delta}{\lambda}\right)^2\frac{\partial^2 v^*}{\partial x^{*2}} \sim O(\mathrm{Re}_L^{-1}) \tag{2.22}$$

$$\frac{1}{\mathrm{Re}_L}\frac{\partial^2 v^*}{\partial y^{*2}} \sim O(\mathrm{Re}_L^{-1}) \tag{2.23}$$

$$\frac{1}{\mathrm{Re}_L}\left(\frac{\delta}{L}\right)^2\frac{\partial^2 v^*}{\partial z^{*2}} \sim O(\mathrm{Re}_L^{-2}). \tag{2.24}$$

84

Thus, again resulting in the Navier-Stokes equation in the normal direction (y) to be of order of $O(\mathrm{Re}_L^{-1})$. On the other hand, the Navier-Stokes equation in the stream-wise (z) direction is non-dimensionalized as

$$\left(u^* \frac{\partial w^*}{\partial x^*} + v^* \frac{\partial w^*}{\partial y^*} + w^* \frac{\partial w^*}{\partial z^*} \right) = \frac{1}{\mathrm{Re}_L} \left(\left(\frac{L}{\lambda} \right)^2 \frac{\partial^2 w^*}{\partial x^{*2}} + \left(\frac{L}{\delta} \right)^2 \frac{\partial^2 w^*}{\partial y^{*2}} + \frac{\partial^2 w^*}{\partial z^{*2}} \right)$$
(2.25)

which on the left hand side

$$u^* \frac{\partial w^*}{\partial x^*} \sim v^* \frac{\partial w^*}{\partial y^*} \sim w^* \frac{\partial w^*}{\partial z^*} \sim O(1)$$
(2.26)

and the right hand side

$$\frac{1}{\mathrm{Re}_L} \left(\frac{L}{\lambda} \right)^2 \frac{\partial^2 w^*}{\partial x^{*2}} \sim O(1)$$
(2.27)

$$\frac{1}{\mathrm{Re}_L} \left(\frac{L}{\delta} \right)^2 \frac{\partial^2 w^*}{\partial y^{*2}} \sim O(1)$$
(2.28)

$$\frac{1}{\mathrm{Re}_L} \frac{\partial^2 w^*}{\partial z^{*2}} \sim O(\mathrm{Re}_L^{-1}).$$
(2.29)

Thus, resulting in the Navier-Stokes equation in the stream-wise direction (z) to be of order $O(1)$. Neglecting all the terms that are of orders $O(\mathrm{Re}_L^{-1})$ or lower, the boundary layer equations for three dimensional periodic steam-wise riblets surfaces can be simplified into

$$\frac{\partial u^*}{\partial x^*} + \frac{\partial v^*}{\partial y} + \frac{\partial w^*}{\partial z^*} = 0 \tag{2.30}$$

$$\tag{2.31}$$

$$\mathrm{Re}_L \left(\frac{\lambda}{L} \right)^2 \left(u^* \frac{\partial w^*}{\partial x^*} + v^* \frac{\partial w^*}{\partial y^*} + w^* \frac{\partial w^*}{\partial z^*} \right) = \left(\frac{\partial^2 w^*}{\partial x^{*2}} + \left(\frac{\lambda}{\delta} \right)^2 \frac{\partial^2 w^*}{\partial y^{*2}} \right) \tag{2.32}$$

and in the dimensional form

$$\frac{\partial u}{\partial x} + \frac{\partial v}{\partial y} + \frac{\partial w}{\partial z} = 0 \tag{2.33}$$

$$\rho \left(u \frac{\partial w}{\partial x} + v \frac{\partial w}{\partial y} + w \frac{\partial w}{\partial z} \right) = \mu \left(\frac{\partial^2 w}{\partial x^2} + \frac{\partial^2 w}{\partial y^2} \right). \tag{2.34}$$

Instead of only depending on the Reynolds number (Re_L) and the boundary layer thickness δ/L as in the Prandtl boundary layer theory, an additional dependence on the dimensionless variable λ/L (or locally λ/z) comparing the wavelength of the riblets to the overall length of the plate (or the location in the stream-wise direction z), is also present in the equations. In the limit $\lambda \ll \delta \ll L$ (i.e. when the boundary layer has diffused normally away from the plate large distances compared to the wavelength of the riblet texture), these expressions, outside the grooves, reduce to the classical 2D boundary layer equations.

The physical important of the parameter λ/z can be discussed by comparing two scenarios: In the first case, as the boundary layer is evolving, the boundary layer thickness is still smaller than the wavelength of the riblets and therefore the velocity profiles at every point are different for different locations, x, within one riblet. However, as the boundary layer evolves (i.e. grows), the thickness of the boundary layer increases and when $\delta > \lambda$ then the velocity profiles follow the same shape outside of the wrinkled grooves, while only inside the riblet grooves the profiles take different shapes. Therefore, at this stage of the boundary layer evolution one

can think of the solution to this problem in terms of an inner and outer solution. The inner solution, which is dependent on all three spatial directions, is valid inside the grooves. On the other hand, the outer solution is only a function of (y, z) and the equations governing that flow return back to the classical two dimensional boundary layer problem.

In the boundary layer flow, I assume that the diffusion of vorticity is always perpendicular to the surface of the wall and in the case of the riblets, it is perpendicular to the surface of the riblets which have a profile of (x_s, y_s) with λ as the characteristic length scale within the riblet groove. So, the boundary layer thickness (locally normal to the wall) at each point can be estimated using the classical scaling

$$\delta \sim \frac{z}{\mathrm{Re}_z^{1/2}}. \tag{2.35}$$

However, this scaling is valid as long as the δ is smaller than the length scale of the riblets, λ. Therefore, to compare the two length scales, the boundary layer thickness and the wavelength of the riblets (for riblets of similar AR), I have

$$\frac{\delta}{\lambda} \sim \left(\frac{1}{\mathrm{Re}_z^{1/2}} \right) \left(\frac{z}{\lambda} \right) \tag{2.36}$$

and thus

$$\left(\frac{\delta}{\lambda} \right)^2 \sim \left(\mathrm{Re}_z \left(\frac{\lambda}{z} \right)^2 \right)^{-1} = \left(\mathrm{Re}_\lambda \left(\frac{\lambda}{z} \right) \right)^{-1} \tag{2.37}$$

which is a combination of both the Reynolds number and λ/z and can be used to explain the evolution of the boundary layer over riblet surfaces. Note that this combination, here denoted as a re-scaled form the of Reynolds number, is the same group as the dimensionless group on the right hand side of Equation (2.32) and will be discussed more in the upcoming sections. It should also be noted that the scaled Reynolds number can also be written in the form of the Reynolds number based on the wavelength of the riblets Re_λ times λ/z as shown above.

On the other hand, in these new boundary layer equations extended to the case

of periodic riblets, the boundary layer thickness, δ, (a measure that needs to be calculated after the boundary layer equations are solved) is also a function of the shape and sharpness of the riblets. Here, I assume that δ is a function of Re_L, the dimensionless wavelength λ/L as well as the aspect ratio of the riblets defined as $\mathrm{AR} = 2A/\lambda$ (a measure of how sharp the riblets). In case of the V-grooves, $\mathrm{AR} = \tan\theta$ as shown in Figure 2-3(b).

Therefore, with the introduction of the riblets, the boundary layer thickness is also a function of the local Reynolds number, Re_z, the dimensionless wavelength, λ/z, as well as the aspect ratio of the riblets AR. Hence, the main non-dimensional groups in this problem are Re_z, λ/z as well as AR. These boundary layer equations (Equations 2.33 and 2.34) are to be solved subject to boundary conditions as below: at the plane of $z = 0$, the velocity is the same as the free-stream velocity and thus

$$\boldsymbol{v}(x, y, z = 0) = (0, 0, W_\infty). \tag{2.38}$$

At the riblet wall $(x_\mathrm{s}, y_\mathrm{s}, z)$, defined as

$$0 \leq x_\mathrm{s} \leq \frac{\lambda}{2} \quad : \quad y_\mathrm{s} = \frac{\lambda}{2}\mathrm{AR}\left(1 - \frac{2x_\mathrm{s}}{\lambda}\right) \tag{2.39}$$

$$\frac{\lambda}{2} \leq x_\mathrm{s} \leq \lambda \quad : \quad y_\mathrm{s} = \frac{\lambda}{2}\mathrm{AR}\left(\frac{2x_\mathrm{s}}{\lambda} - 1\right) \tag{2.40}$$

I have the no-slip boundary condition

$$\boldsymbol{v}(x_\mathrm{s}, y_\mathrm{s}, z) = \boldsymbol{0}. \tag{2.41}$$

Lastly, as the y direction goes to infinity, then the velocity profile returns to the free-stream velocity

$$\boldsymbol{v}(x, y \to \infty, z) = (0, 0, W_\infty). \tag{2.42}$$

2.3   Solving the Extended Boundary Layer Equation

The set of extended boundary layer equations is more difficult to solve compared to the Prandtl boundary layer equations, since all three components of the velocity field (u, v, w) are involved in the equations 2.33 and 2.34 and are each a function of the three spatial directions (x, y, z). In addition, the equations include derivatives in all three directions adding to the complexity. Since the growth of the boundary layer is dependent on the diffusion normal to the surface of the riblets, it is desirable to transform the coordinate system where one of the directions is perpendicular to the surface of the riblets at the wall. Therefore, I seek a coordinate transformation from (x, y, z) to a curvilinear orthogonal coordinate system (α, β, z) where one of the directions is perpendicular to the riblet surface at every point $(x_\mathrm{s}, y_\mathrm{s})$. If I denote the local wall normal coordinate β, then in the other direction (which I denote α) I expect to have no diffusion of vorticity and thus

$$u_\alpha = 0 \tag{2.43}$$

and

$$\frac{\partial^2 w}{\partial \alpha^2} = 0 \tag{2.44}$$

where u_α is the velocity components in the new direction α, and w is the stream-wise velocity as before. In other words, transforming the original Cartesian coordinate system (x, y, z) to (α, β, z) results in the velocity field being transformed from (u, v, w) to $(u_\alpha = 0, v_\beta, w)$ as shown schematically in Figures 2-4(a) and 2-4(b).

Such a transformation changes the extended boundary layer equations from Equations 2.33 and 2.34 to

$$\frac{\partial v_\beta}{\partial \beta} + \frac{\partial w}{\partial z} = 0 \tag{2.45}$$

$$\rho \left(v_\beta \frac{\partial w}{\partial \beta} + w \frac{\partial w}{\partial z} \right) = \mu \left(\frac{\partial^2 w}{\partial \beta^2} \right) \tag{2.46}$$

89
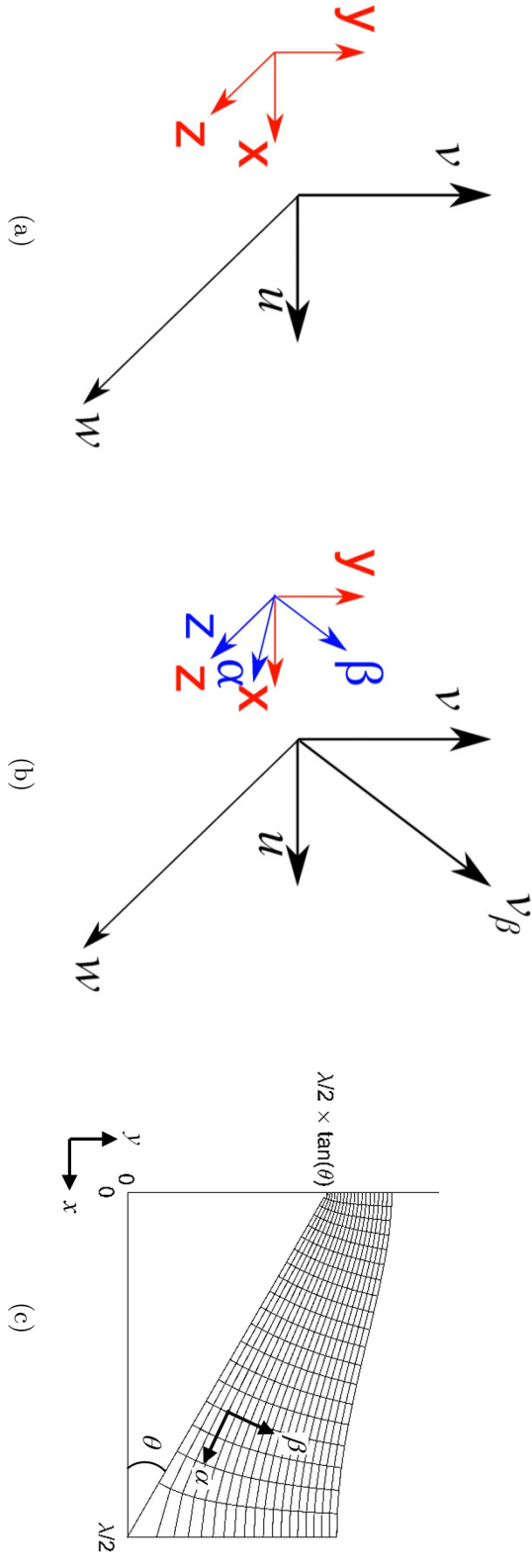
Figure 2-4: Schematic of coordinate transformation from (x, y, z) to (α, β, z) coordinate system, resulting in the velocity profile to transform from (u, v, w) to $(0, v_\beta, w)$. (a) x, y, z coordinate system; (b) x, y, z and α, β, z coordinate systems; (c) Ortho-normal curvilinear coordinate system for riblet surfaces with x, y and α, β.

which are identical to the original boundary layer equations (2.4) and (2.5) that were solved by Blasius [88, 41]. Thus the classical Blasius solution combined with the appropriate coordinate transformation can be used together to solve the extended boundary layer equations, giving the solution for the evolution in the velocity profile both tangential and normal to the textured plate as a function of β and z, $(0, v_\beta(\beta, z), w(\beta, z))$.

2.3.1 Coordinate Transformation

To find the transformed coordinate system with the desired properties as above, the method of conformal mapping is employed for transformation from (x, y) to (α, β) and the reverse, at each z cross section. Here, I use the Schwarz-Christoffel method, which transforms a half space into a simple open or closed polygon [89]. Conformal mapping is an angle preserving transformation. Therefore, while the map preserves the orthogonality of the Cartesian coordinate system, it gives a map that is perpendicular to surface of the riblets. Previously Bechert and Bartenwerfer [71] have used a similar method to solve the Laplace equation for the velocity inside the grooves. They use the idea of a retarded flow inside the grooves and with assumption of viscous dominated flow, calculate the "Protrusion Height" for the stream-wise and cross flow which is equivalent to the virtual origin of the flow in both stream-wise and cross flow configurations and they argue that drag reduction is dependent on the difference of these two values as a measure of how much the turbulent cross flow close to the wall (especially the span-wise component of the velocity) has been retarded by the riblet structures.

Here, it is considered that half of a V-groove riblet $(0 \leq x \leq \lambda/2)$ is formed from the 3 sides of an open polygon, where the two vertices of the polygon in non-dimensional form are given by $0 + i\text{AR}$ and $1 + i0$ in the complex plane and the angle at the first vertex is $\gamma_1 = \pi/2 - \tan\theta$ (where $\tan\theta = \text{AR}$) and at the second vertex is $\gamma_2 = \pi - \gamma_1 = \pi/2 + \theta$ (Figure 2-5(c)).

Using the Schwarz-Christoffel theorem, a rectangular grid (X_1, Y_1) with two vertices corresponding to $(-\pi/2, 0)$ and $(\pi/2, 0)$ (Figure 2-5(a)) is transformed into a
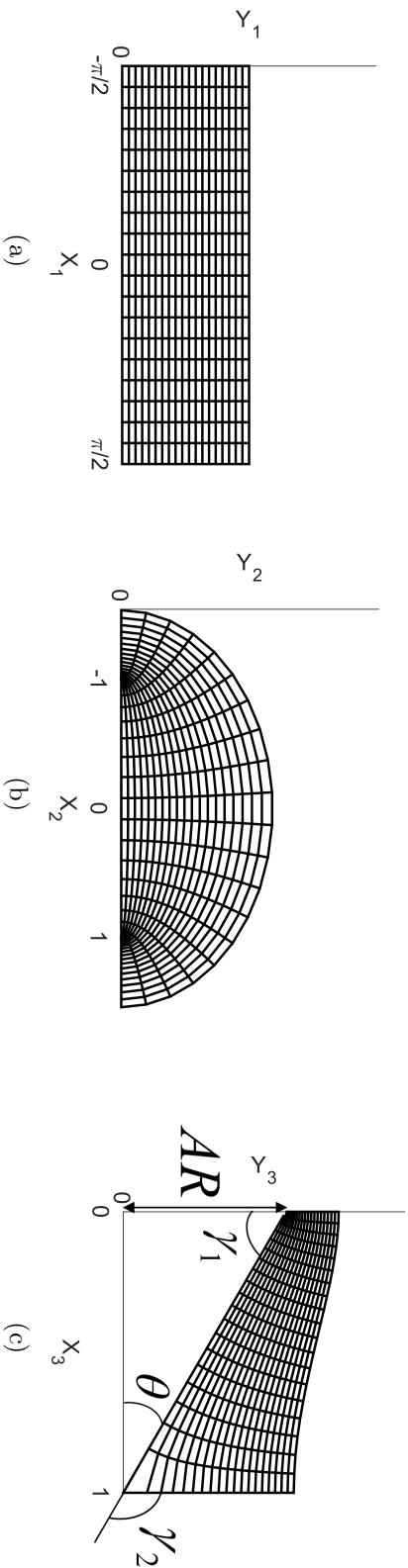
Figure 2-5: Steps used in conformal mapping from a Cartesian coordinate system to a curvy-linear locally orthonormal coordinate system for half of a V-groove riblet surface. (a) $\chi_1 = X_1 + iY_1$; (b) $\chi_2 = X_2 + iY_2$; (c) $\chi_3 = X_3 + iY_3$.

half-space (X_2, Y_2) with vertices $(-1, 0)$ and $(1, 0)$ respectively (Figure 2-5(b)). Using complex variables to transform from $\chi_1 = X_1 + iY_1$ $(-\pi/2 < X_1 < \pi/2$ and $Y_1 > 0)$ to $\chi_2 = X_2 + iY_2$ I have

$$\chi_2 = X_2 + iY_2 = \sin(\chi_1) = \sin(X_1 + iY_1). \tag{2.47}$$

Then the half space χ_2 is transformed to half of a V-groove (X_3, Y_3) where two vertices $(-1, 0)$ and $(1, 0)$ corresponding to $0 + i\text{AR}$ and $1 + i0$. Using the Schwarz-Christoffel method

$$\frac{d\chi_3}{d\chi_2} = \frac{i}{\pi} \frac{1}{(\chi_2 + 1)^{\gamma_1/\pi}(\chi_2 - 1)^{(1-\gamma_2/\pi)}}. \tag{2.48}$$

Equation 2.48 needs to be integrated with respect to χ_2 to find the final conformal map for half of the V-groove riblet boundary. To simplify the integration for the transformation from $\chi_2 = X_2 + iY_2$ to $\chi_3 = X_3 + iY_3$, two intermediate variables (n and ξ) are introduced as follows

$$\frac{1}{n} = \frac{\pi}{2} - \frac{\pi}{\theta} = \frac{\pi}{\gamma_1}, \tag{2.49}$$

$$\xi = \left(\frac{\chi_2 - 1}{\chi_2 + 1}\right)^{\frac{1}{n}}. \tag{2.50}$$

Here n can take any real value larger or equal to 2. The case of $n = 2$ or $\gamma_1 = \pi/2$ returns the results of the flat plate boundary layer $(\text{AR} = 0)$. When substituted back into Equation (2.48) integration gives

$$\chi_3 = X_3 + iY_3 = 1 + n\frac{i}{\pi} \int \frac{d\xi}{1 - \xi^n}. \tag{2.51}$$

Equation 2.51 can also be represented in a simplified form using a generalized hypergeometric function $(_2F_1)$ and written in the form

$$\chi_3 = X_3 + iY_3 = 1 + n\frac{i}{\pi}\xi \, _2F_1\left(\frac{1}{n}, 1, 1 + \frac{1}{n}, \xi^n\right). \tag{2.52}$$

Here χ_1, and χ_3 are non-dimensional complex variables (employed in the conformal map) and are related to the Cartesian (x, y) and the transformed variables along and normal to the wall (α, β) as

$$\chi_1 = X_1 + iY_1 = \frac{2\pi}{\lambda}(\alpha + i\beta) \tag{2.53}$$

$$\chi_3 = X_3 + iY_3 = \frac{2}{\lambda}(x + iy). \tag{2.54}$$

Hence, even though the boundary layer equations (2.45) and (2.45) are the same as the classical boundary layer equations solved by Blasius, the coordinate transformation emphasizes the effect of the riblet shape in the problem through the spacing of the riblets λ and the aspect ratio AR of the riblets in the mapping.

Equation 2.49 connects the variable n to the angle θ or the aspect ratio of the riblets $(\mathrm{AR} = \tan\theta)$ and equation 2.54 involves the wavelength; therefore, for any given wavelength and aspect ratio of V-groove shaped riblets, the above set of equations can be used to find a transformation between (x, y) and (α, β) for one half of the riblet. Due to symmetry of the riblets, it is sufficient to find the map for only half of a riblet.

To solve the extended boundary layer equations, first I use the coordinate transformations (from (x, y) to (α, β) at each cross section with constant z), to transform Equation (2.34) to equation (2.46). Then equation 2.46 is solved using the Blasius solution [41] in the (α, β, z) coordinate system. Using equation (2.53) and the Blasius solution, the similarity variable η for the new boundary layer problem can be defined as

$$\eta = \frac{\lambda/2}{\pi}\frac{Y_1}{z}\sqrt{\mathrm{Re}_z} = \frac{\beta}{z}\sqrt{\mathrm{Re}_z} \tag{2.55}$$

and thus $w(\beta, z)/W_\infty$ is calculated as a function of η from the Blasius solution. Then, using the conformal mapping steps introduced earlier in reverse, (α, β) (or $\chi_1 = X_1 + iY_1$) can be transformed back into the physical domain of the riblets (x, y)
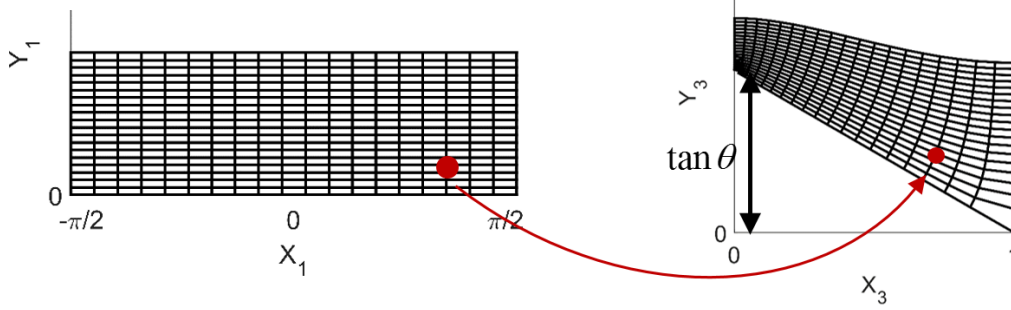
Figure 2-6: Schematic of the transformation between a point on the Cartesian coordinate system and the corresponding point on the curvy-linear orthogonal coordinate system used for solving the boundary layer flow equations over riblet surfaces. Cartesian coordinate system on the left is used to solve the classical boundary layer equations using Blasius solution and then transformed to the riblet coordinate system shown on the right.

(or in dimensionless form of $\chi_3 = X_3 + iY_3$) as a function of the spacing of the riblets (λ) and the aspect ratio of the riblets AR through the value of parameter $n \geq 2$, where AR $= \tan(\pi/2 - \pi/n)$. Note that using $n = 2$ returns the results of two-dimensional boundary layer and n can taken any real value larger than 2.

To solve the extended boundary layer equation: I employ the above transformation, particularly using X_1 and Y_1, I define the generalized similarity variable η as equation 2.55 and calculate the w/W_∞ as a function of η using the Blasius solution. This method is used to calculate the velocity distribution for any V-groove riblet with wavelength of λ and aspect ratio of AR for the rest of this work.

2.4   Results

The transformed boundary layer equations 2.45 and 2.46 employing the transformation introduced in section 2.3.1, were solved for riblet surfaces of various spacing (λ) and aspect ratios (AR) using Matlab and the results are discussed below in the form of the evolution in the velocity contours, the boundary layer thickness along the plate, and the total drag on the textured surfaces. The results are presented as a function of the dimensionless position along the plate z or the Reynolds number of the flow Re_z, ratio of spacing of the riblets to the location along the flow direction (λ/z), as

well as the aspect ratio (AR) of the riblets. In global coordinates, local position z is replaced with the length of the plate L in the above dimensionless groups.

2.4.1 Velocity Profiles and Self-Similarity

The evolution of the velocity profiles are plotted as contour plots as a function of Re_z, λ/z, and AR. First, I keep the shape and size of the riblets constant (by keeping the wavelength, λ, and aspect ratio, AR constant) and present the velocity contours at different local positions z (i.e. as a function of Re_z and λ/z). The results for riblets with AR = 1 and $\{\text{Re}_z = 100, \ \lambda/z = 1\}$, $\{\text{Re}_z = 500, \ \lambda/z = 0.2\}$, and $\{\text{Re}_z = 1000, \ \lambda/z = 0.1\}$ are plotted in Figure 2-7. Similar to the evolution of the boundary layer over a flat plate, an increase in the Reynolds number results in the diffusion of vorticity further away from the wall and thus an increase in the thickness of the boundary layer. However, as it can be seen in Figure 2-7(a), at lower Reynolds numbers, the velocity contours is partially mimicking the shape of the riblets (as seen in the iso-velocity color stripes), but as I move along the plate (i.e. increase the Reynolds number and decrease λ/z), then the velocity contours start to forget the shape of the riblets, especially outside the grooves and the variations inside the grooves stay within 25% of the free-stream velocity. Additionally, as Re_z increases, the velocity inside the grooves becomes more retarded and as seen in Figure 2-7(c) for $\text{Re}_z = 1000$, the velocity inside the groove is less than 25% of the free stream value W_∞. Other researchers have reported this phenomenon numerically and experimentally [73, 83, 25, 72].

On the other hand, the results can be discussed for when the Reynolds number and λ/z are kept constant and only the shape of the riblets are changed by changing the aspect ratio, AR. For example, for a constant $\{\text{Re}_z = 200, \lambda/z = 0.5\}$, velocity contours are plotted as a function of the aspect ratio, AR, of the V-groove in Figure 2-8. The figures qualitatively show that at a fixed Reynolds number, or fixed position along the plate, the introduction of riblets causes an increase in the thickness of the boundary layer compared to the corresponding flat plate and as the aspect ratio, AR, increases, thickness of the viscous boundary layer also increases. Additionally it can
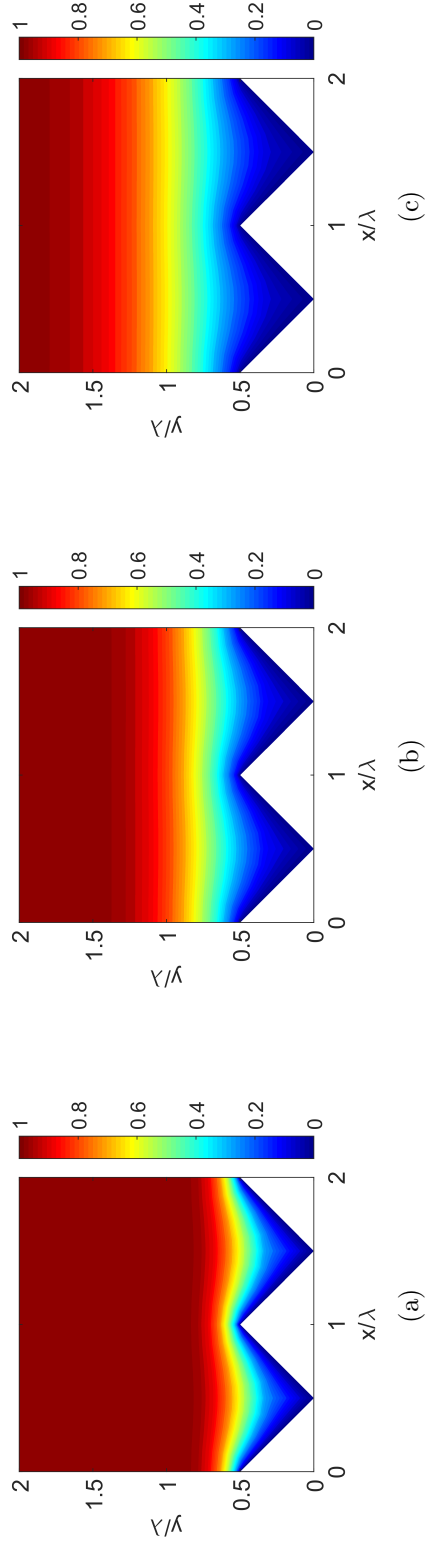
Figure 2-7: Velocity contours for boundary layer over riblet plates with $AR = 1$ at (a) {$\mathrm{Re}_z = 100$, $\lambda/z = 1.0$}, and $\mathrm{Re}_z(\lambda/z)^2 = 100$; (b) {$\mathrm{Re}_z = 500$, $\lambda/z = 0.2$} and $\mathrm{Re}_z(\lambda/z)^2 = 20$; (c) {$\mathrm{Re}_z = 1000$, $\lambda/z = 0.1$} and $\mathrm{Re}_z(\lambda/z)^2 = 10$.
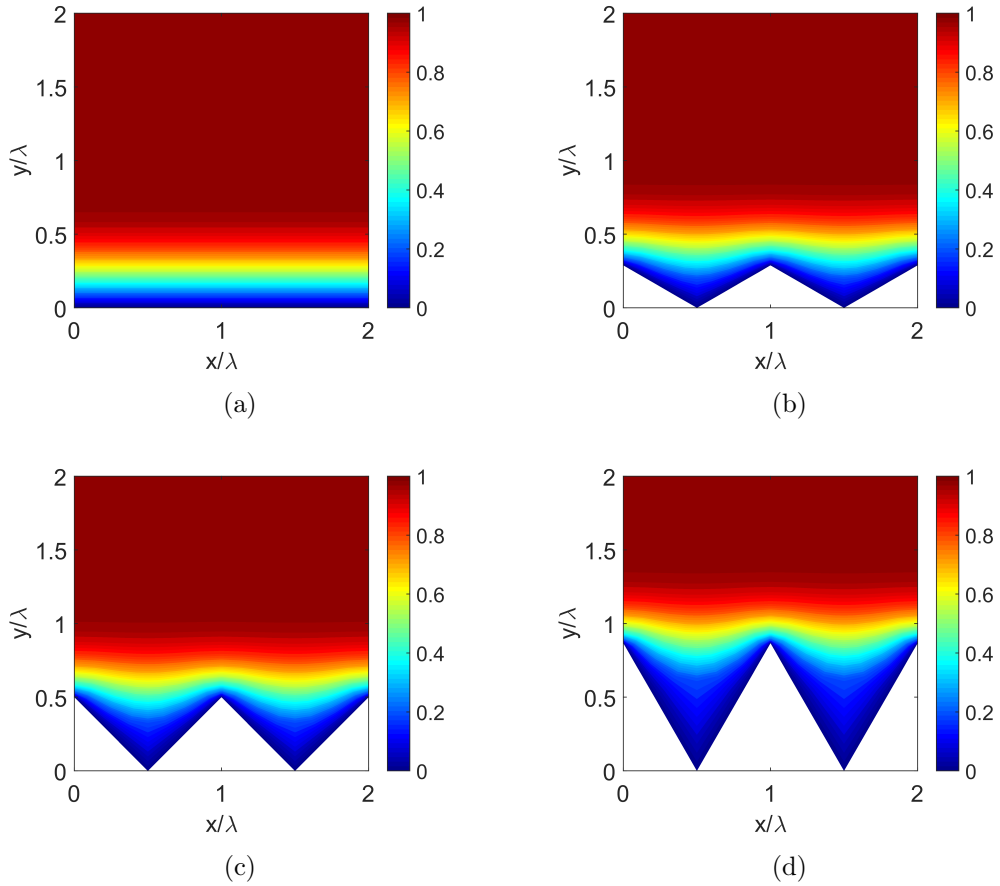
Figure 2-8: Velocity contours for boundary layer over riblet plates with $\{\mathrm{Re}_z = 200, \lambda/z = 0.5\}$ at (a) AR = 0; (b) AR = 0.58; (c) AR = 1.00; (d) AR = 1.73.

be seen that the introduction of the riblets results in the flow inside the grooves becoming progressively more retarded. As the AR of the riblets is increased at constant Reynolds number, a larger area of slowly moving fluid is seen inside the grooves and thus a thicker cushion of slow moving fluid inside the grooves.

Changing the spacing of the riblets changes the shape of the boundary layer and thus the boundary layer thickness δ/λ will have a different behaviour depending on λ/z. As it was discussed in Section 2.2, when the boundary layer thickness, δ, is larger than the wavelength of the riblet, λ, the flow outside the grooves forgets about the shape of the wall and all the variations are inside the grooves, while when the boundary layer thickness is smaller than the wavelength, the velocity contours mimic the shape of the grooves. On the other hand, it was shown earlier that the ratio of

boundary layer thickness to the wavelength δ/λ is directly dependent on a re-scaled Reynolds number as in Equations 2.37 and 2.32. Therefore, changing the wavelength will directly result in a change in δ/λ and the velocity profiles. However, one can see that boundary layers that develop over riblets with the same aspect ratio but different spacing, are self similar as long as the combination of $\mathrm{Re}_z(\lambda/z)^2$ is the same between the cases. The comparison can be seen in Figures 2-7 and 2-9 where the spacing of the riblets in Figure 2-9 is two times the spacing of riblets in Figure 2-7: while Figure 2-7(a) and 2-9(a) correspond to different positions along the plate (thus different Reynolds numbers and different λ/z), they have the same values of $\mathrm{Re}_z(\lambda/z)^2 = 100$ and the same velocity profile as seen in the figures. The same similarity can also be seen by comparing Figures 2-7(b) and 2-9(b) as well as Figures 2-7(c) and 2-9(c).

In other words, one can see that the development of the velocity profile over three dimensional periodic riblet surfaces are effectively dependent on the Reynolds number based on the wavelength of the riblets which can also be seen using the scaling in section 2.2 and shown in Equations 2.32 and 2.37. On the other hand, this re-scaled form of the Reynolds number, $\mathrm{Re}_z(\lambda/z)^2 = \mathrm{Re}_\lambda(\lambda/z)$, combines the effect of the flow along the plate as well as the effect of the size of the riblets; therefore, it can serve as a meaningful dimensionless group for design purposes as it combines the fluid properties, velocity, as well as the lateral size of the riblets (in form of the wavelength). Hence, with this form of the self-similarity, it is possible to discuss the results as only a function of two variables, $\mathrm{Re}_z(\lambda/z)^2$, and the aspect ratio, AR, instead of the three dimensionless variables originally introduced.

The re-scaled dynamical variable $\mathrm{Re}_z(\lambda/z)^2$ has a slightly different behaviour compared with the classical variable Re_z. Firstly, when all the aspects of geometry are kept constant, increasing the free-stream velocity results in a linear increase in the value of $\mathrm{Re}_z(\lambda/z)^2$ (since $\mathrm{Re}_z(\lambda/z)^2 \sim W_\infty$). Similarly, keeping the free-stream velocity constant and increasing the spacing of the riblets results in quadratic increases in the scaled Reynolds number ($\mathrm{Re}_z(\lambda/z)^2 \sim \lambda^2$). In global form, when the Reynolds number is defined based on the length of the plate (i.e. $z_{\mathrm{max}} = L$), then all the above relations are re-written in terms of L instead of local position z. However, unlike Re_z,
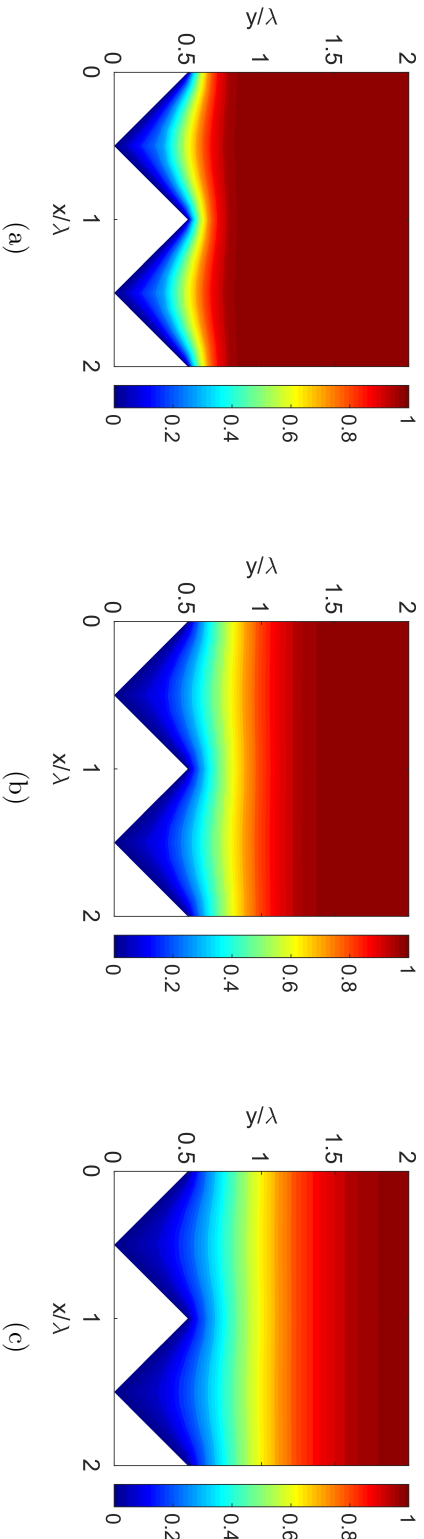
Figure 2-9: Velocity contours for the evolution in the viscous boundary layer over riblet plates with AR = 1 at (a) {Re$_z$ = 400, λ/z = 2.0} and Re$_z(\lambda/z)^2$ = 100; (b) {Re$_z$ = 2000, λ/z = 0.4} and Re$_z(\lambda/z)^2$ = 20; (c) {Re$_z$ = 4000, λ/z = 0.2} and Re$_z(\lambda/z)^2$ = 10.

increasing z or in other words moving along the length of the plate results in a decrease in the scaled Reynolds number since $\text{Re}_z(\lambda/z)^2 = \text{Re}_\lambda(\lambda/z) \sim z^{-1}$. Therefore, for constant velocity and riblet spacing, while keeping fluid properties the same, increasing the total length of the plate will result in an increase in the maximum Reynolds number Re_L but decreases the minimum scaled Reynolds number $\text{Re}_L(\lambda/L)^2$.

2.4.2 Measures of Boundary Layer Thickness

As it was shown in Figure 2-8, at constant Reynolds number (i.e. flow dynamics) and at the same local position along the plate, for riblets with the same wavelength, changing the aspect ratio of the riblets results in a change in the boundary layer thickness qualitatively and increasing the aspect ratio increases the boundary layer thickness compared to the case of a flat plate boundary layer. Note that as it was mentioned earlier, using the same mapping and same transformed equations, one can re-create the results of the velocity profiles from the Blasius solution by setting $n = 2$ (corresponding to AR $= 0$, thus $\chi_3 = \chi_1/\pi$ where Equation 2.55 turns back into the similarity variable used in the Blasius solution). However, these figures are only qualitative and I need to define the boundary layer thickness in a quantitative way.

Boundary layer thickness in this work is calculated using an integral definition similar to the displacement thickness and momentum thickness as in the flat plate boundary layer. To extend the definition of the boundary layer thickness from two-dimensional to three-dimensional, the classical definition of displacement thickness and momentum thickness are extended to displacement area and momentum area using Equations 2.56 and 2.57 below. By analogy to displacement thickness, the displacement area is a measure of the portion of the cross sectional area (with its normal parallel to the stream-wise direction) that the inviscid outer flow has been displaced by the presence of the wall and the formation of the viscous boundary layer [41, 65]. Therefore the displacement area and momentum area are defined as

$$\Delta^* = \int_S \left(1 - \frac{w}{W_\infty}\right) dS \tag{2.56}$$

$$\Theta = \int_S \frac{w}{W_\infty} \left(1 - \frac{w}{W_\infty}\right) dS \tag{2.57}$$

where S is the cross sectional area normal to the flow direction at constant z (its normal is parallel to the x direction, similar to the cross section in Figures 2-7, 2-8, and 2-9) where for one of the periodic riblets the (x, y) of the points on each of these surfaces have $0 < x < \lambda$ and $y_s < y < \infty$. In Section 2.2, the square of the boundary layer thickness (δ^2) in Equation 2.32 is non-dimensionalized by λ^2. However, since the displacement area and momentum area both are of dimensions of square of length, therefore, the integral measure Δ^*/λ^2 can substitute $(\delta/\lambda)^2$ in the scaling analysis.

The results of the displacement area for riblets of the same wavelength (i.e. λ) are plotted as a function of the Reynolds number and aspect ratio in Figure 2-10. As it can be seen in Figure 2-10(a) the presence of the riblets results in an increase in the boundary layer thickness or displacement area compared to a flat plate (AR $= 0$) and increasing the aspect ratio results in an increase in the displacement area. Similar behaviour was qualitatively observed in Figures 2-8, 2-7, and 2-9.

At lower Reynolds numbers the increasing trend of displacement area as a function of the aspect ratio AR) is clearly seen, but as the value of Re$_z$ increases (corresponding to greater distances, $z/(\nu/W_\infty)$, down the plate), the difference between the calculated displacement areas for various aspect ratios becomes less visible.

On the other hand, momentum area follows a slightly different behaviour. At lower Reynolds number, (i.e. shorter distances along the plate) as seen in Figure 2-10(b), increasing the aspect ratio of the riblets, results in an increasing trend in the momentum area. However, as the Reynolds number is increased, after a certain point, the momentum area of the riblet surfaces cross over to values smaller than the momentum area of a the case of the flat plate (i.e. AR $= 0$). This trend is discussed in more detail in Section 2.4.3.

Next, to investigate the effect of the spacing of the riblets (λ) on the displacement
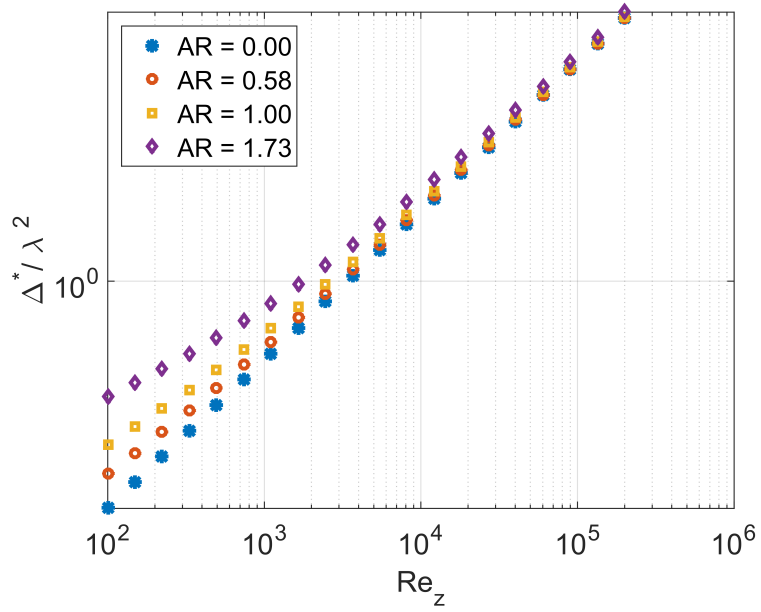
(a)
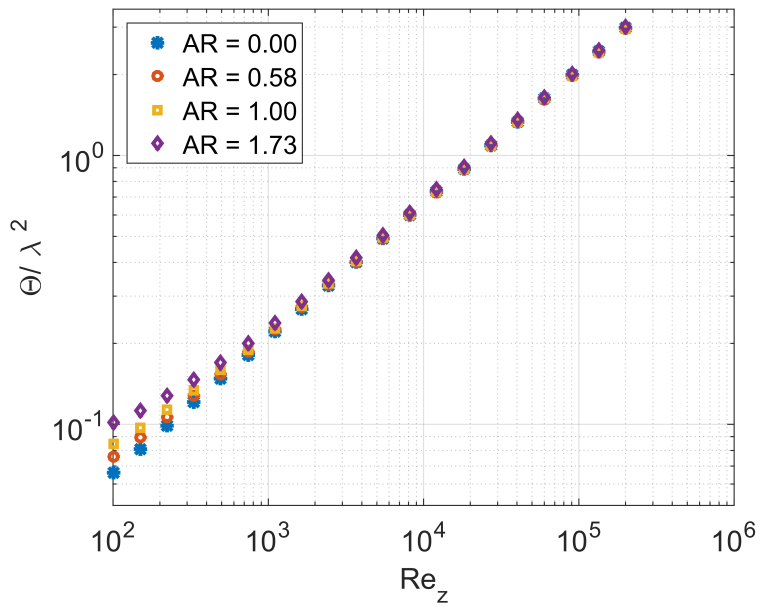
(b)

Figure 2-10: (a) Displacement area (Δ^*) and (b) momentum area (Θ) of boundary layer flow over the riblets as a function of the Reynolds number and various aspect ratios. The spacing of the riblets has been kept constant for all the cases here.

area, the results of the displacement area for riblets with various spacings, λ/z, are plotted as a function of the aspect ratio, AR, at three Reynolds numbers (Re_z), 10^4, 4×10^4, and 9×10^4 in Figures 2-11(a), 2-11(b) and 2-11(c). Again it can be seen that increasing the aspect ratio (AR) results in a slight increase in the displacement area for all the cases shown in the figures. In all three figures increasing the spacing of the riblets results in a decrease in the displacement area at the same Re_z and the difference is more pronounced as the Reynolds number increases.

However, again the self-similarity of the velocity profiles with the scaled Reynolds number (Equation 2.37) can be used to collapse the results of the displacement area as well. The data shown with star symbols in Figure 2-11(a) for $\{\mathrm{Re}_z = 10^4,\ \lambda/z = 0.01\}$, the data shown with circle symbols in Figure 2-11(b) for $\{\mathrm{Re}_z = 4 \times 10^4,\ \lambda/z = 0.005\}$, and the data shown with diamond symbols in Figure 2-11(c) for $\{\mathrm{Re}_z = 9 \times 10^4,\ \lambda/z = 0.0033\}$ show the same trend in displacement area for the different aspect ratios and all the cases have the same value of the scaled Reynolds number of $\mathrm{Re}_z(\lambda/z)^2 = 1$. These three sets of results are overlaid on each other in Figure 2.4.2, again confirming the earlier observation that using the scaled Reynolds number $\mathrm{Re}_z(\lambda/z)^2$ captures the self-similarity in the structure of the boundary layer along riblets of the same aspect ratio and different spacing (λ).

Similar behaviour is observed for the momentum area as a function of the scaled Reynolds number and aspect ratio and thus, for the rest of this work, both displacement and momentum area are written as a function of the scaled Reynolds number $\mathrm{Re}_z(\lambda/z)^2$ and aspect ratio (AR) of the riblets instead of the three dimensionless groups introduced in section 2.2.

2.4.3 Momentum Area and Total Drag

In the previous section the boundary layer equations are all solved in the *differential form* to calculated the velocity distribution $w(x, y)$ at each cross section (constant z or Re_z). In a different view, Navier Stokes equation in the z direction can be written in the *integral form* (also known as the momentum integral equation) as below
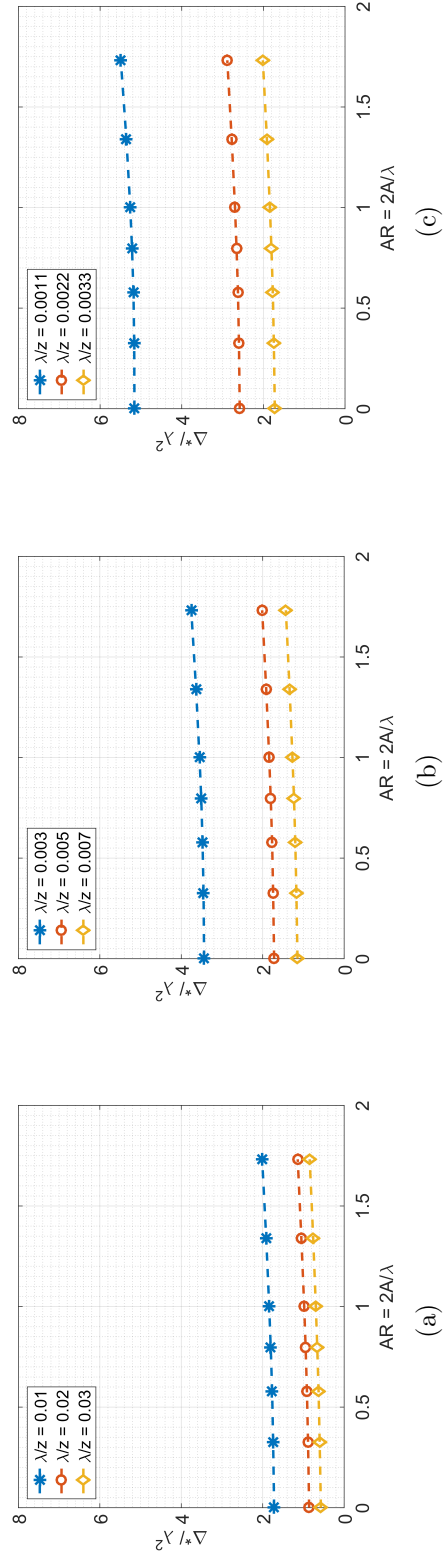
Figure 2-11: Displacement area as a function of aspect ratio of the riblets and different λ/z for cases of (a) $\mathrm{Re}_z = 10000$, (b) $\mathrm{Re}_z = 40000$ and (c) $\mathrm{Re}_z = 90000$.
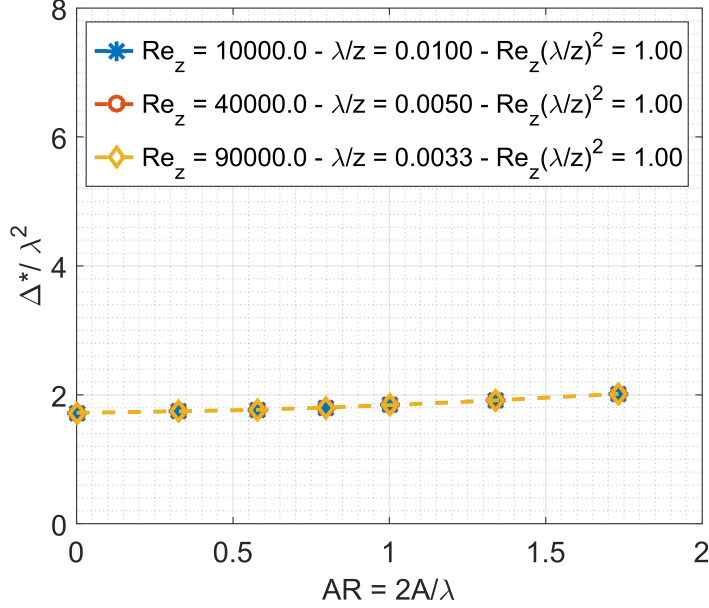
Figure 2-12: Collapse of the results of Displacement area as a function of aspect ratio of the riblets with different λ/z for $\{\mathrm{Re}_z = 10000, \lambda/z = 0.01\}$, $\{\mathrm{Re}_z = 40000, \lambda/z = 0.02\}$, and $\{\mathrm{Re}_z = 90000, \lambda/z = 0.03\}$ as a function of aspect ratio of the riblets. The three cases have $\mathrm{Re}_z(\lambda/z)^2 = 1$.

$$\int_S \frac{\partial}{\partial z}\left(w\left(W_\infty - w\right)\right) dS + \frac{dW_\infty}{dz}\int_S \left(W_\infty - w\right) dS = \frac{1}{\rho}\int_\ell \boldsymbol{\tau}_\mathrm{w}.\boldsymbol{d\ell} \qquad (2.58)$$

where S is the cross sectional area at each constant z in the $x-y$ plane (similar area as the one in the definition of displacement area and momentum area in Equations 2.56 and 2.57), $\boldsymbol{\tau}_\mathrm{w}$ is the traction vector on the wall ($\boldsymbol{\tau}_\mathrm{w} = \boldsymbol{\tau} \cdot \boldsymbol{n}_\mathrm{w}$ where $\boldsymbol{\tau}$ is the shear stress tensor and $\boldsymbol{n}_\mathrm{w}$ is the normal vector to the riblet wall), $\boldsymbol{\ell}$ is the local tangential vector along the contour of the riblets. Equation 2.58 is simplified as

$$\frac{\partial}{\partial z}\left(\rho W_\infty^2 \Theta\right) + \rho W_\infty \frac{dW_\infty}{dz}\Delta^* = \int_l \boldsymbol{\tau}_\mathrm{w}.\boldsymbol{d\ell} \qquad (2.59)$$

where Δ^* and Θ are the displacement area and momentum area as defined in equations 2.56 and 2.57 respectively. With the assumption of no pressure gradient (i.e. $dp/dz = 0$), using Euler's equation for the inviscid flow outside the boundary layer,

$$\rho W_\infty \frac{dW_\infty}{dz} = -\frac{dp}{dz} = 0 \qquad (2.60)$$

therefore, Equation 2.59 is simplified more to relate the traction vector on the wall to the momentum area in the form of an ordinary differential equation as

$$\frac{\partial}{\partial z}\left(\rho W_\infty^2 \Theta\right) = \int_l \boldsymbol{\tau}_{\text{w}}.\boldsymbol{d\ell} \tag{2.61}$$

Then, integrating equation 2.61 along the z direction of a plate from 0 to L, gives

$$\rho W_\infty^2 \Theta(L) = \int_0^L \int_l \boldsymbol{\tau}_{\text{w}}.\boldsymbol{d\ell} = D \tag{2.62}$$

where the integral of the wall traction vector ($\boldsymbol{\tau}_{\text{w}}$) along the riblet contour (ℓ) and then along the length (L) of the plate results in the total drag, D, over the riblet surface (note that $\Theta(0) = 0$). Therefore, calculating the momentum thickness is sufficient for finding the total drag on the surface instead of calculating the shear stress distribution on the surface. Therefore, to explore the effect of the riblets on the total drag, the reduction in drag is found by calculating

$$\frac{D - D_{\text{flat}}}{D_{\text{flat}}} = \frac{\Theta - \Theta_{\text{flat}}}{\Theta_{\text{flat}}} \tag{2.63}$$

where D_{flat} is the drag on a flat surface (or AR $= 0$) and Θ_{flat} is the momentum area of the flat surface.

As it was discussed at length in the earlier section, the boundary layer flow over riblet surfaces exhibits another level of self-similarity, as long as the scaled Reynolds number $\text{Re}_z(\lambda/z)^2$ is used instead of the classical Reynolds number. Due to this self-similarity in the velocity profiles of riblets with different scales and at different stream-wise locations, I presented the displacement area as a function of only $\text{Re}_L(\lambda/L)^2$ (in the global form as I am interested in the total drag, calculated by the integral over the entire surface of the riblets) and the aspect ratio (AR). Similar behaviour is observed in momentum area as well and thus, the results of the total drag (equation 2.63) is presented as a function of $\text{Re}_L(\lambda/L)^2$ and AR in Figure 2-13.

The first key point presented in the contour plot is that riblets can both increase or reduce the total drag force on the plate and it depends on the size of the riblets, the dynamics of the flow, and the aspect ratio of the riblets. This visual presentation

confirms the experimental and numerical observations of previous literature where both drag reduction and increase have been reported.

The second point is that at a constant aspect ratio, (AR), decreasing the scaled Reynolds number $(\mathrm{Re}_L(\lambda/L)^2)$ results in a decrease in the total drag on the surface and to achieve drag reduction with the riblet surface, the scaled Reynolds number needs to be lower than a threshold. This threshold depends on the aspect ratio of the riblets, AR and the threshold line for all the cases as calculated in this theory is shown with the white continuous line in Figure 2-13. Therefore, for the same flow velocity, fluid properties, and riblet geometry, to achieve drag reduction, the length of the plate should be larger than a minimum length corresponding to the threshold scaled Reynolds number. On the other hand, with the same plate length, constant fluid properties, and riblet size, the velocity needs to be lower than a maximum velocity (again corresponding to the threshold scaled Reynolds number) for the riblets to be drag reducing. Similar trend was observed by Walsh [37] as well where increasing the velocity for the same fluid and geometry resulted in an increasing trend in the drag measured on the surfaces for V-grooves as well as other types of riblets tested.

On the other hand, at a constant scaled Reynolds number, possibility of achieving drag reduction with riblets is dependent on the aspect ratio of the riblets; at each scaled Reynolds number, total drag on the surface depicts a non-monotonic behaviour as a function of the aspect ratio; it first decreases with the increase in the aspect ratio of the riblets and then takes as increasing trend after crossing a minimum. Therefore at each $\mathrm{Re}_L(\lambda/L)^2$ there is an aspect ratio resulting in the highest drag reduction. This optimum aspect ratio depends on the scaled Reynolds number of the flow. Also, it can be seen that riblets with aspect ratios greater than a threshold (here AR $\gtrsim 1.4$) are no longer drag reducing.

Experimental results by Walsh [37] also shows that in similar flow conditions, riblets with AR $= 1$ reduce the drag over a wider range of velocities compared to the V-grooves with AR $= 2$. Additional results from Walsh and co-workers [38, 39] also show similar non-monotonic trends when riblets of the same spacing, and different aspect ratios were used in the same flow conditions and for $10 < s^+ < 20$, maximum
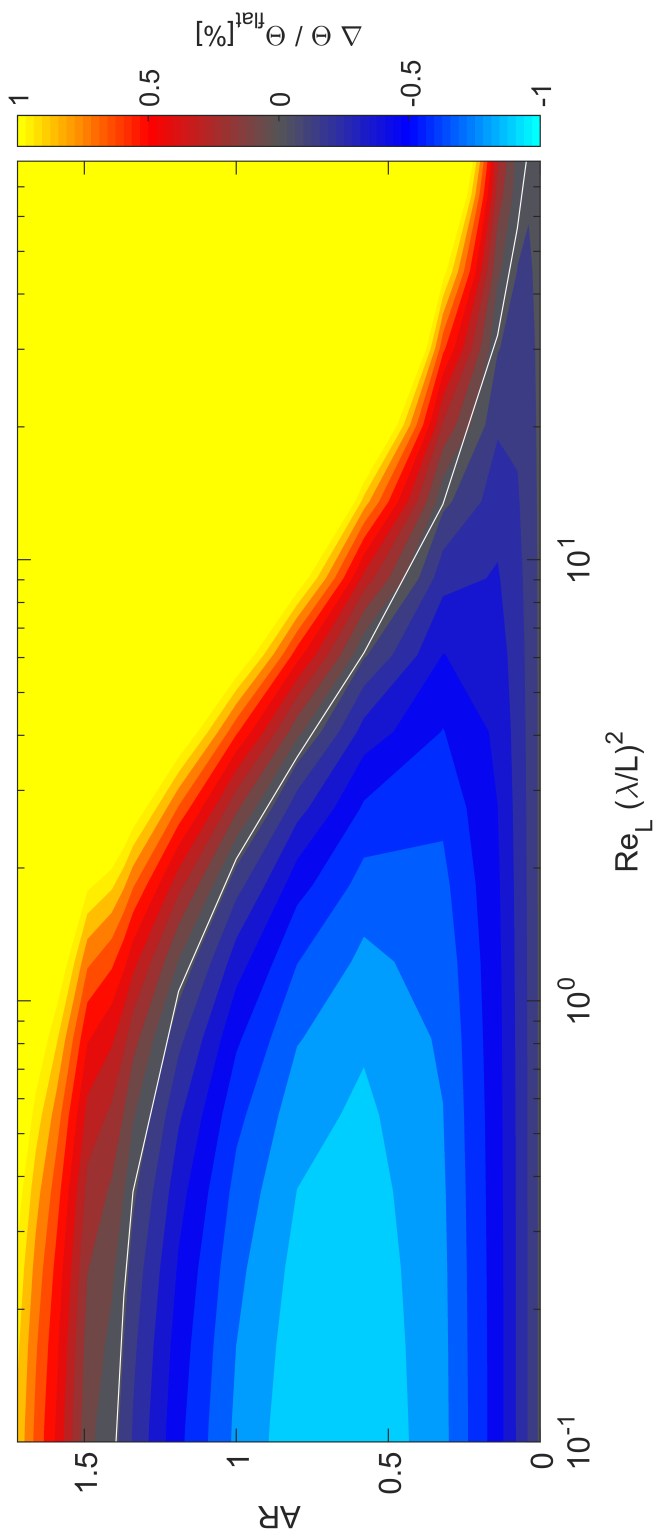
Figure 2-13: Reduction in total drag shown in form of the reduction in the momentum area of plates as a function of the aspect ratio AR of the riblets and the scaled Reynolds number $\mathrm{Re}_L(\lambda/L)^2$.

reduction is achieved using AR ≈ 1.6 and drag has a non-monotonic trend with AR as predicted by this theory. Results of experiments with rectangular (razor-blade) riblets by Lazos and co-workers [51] also show a similar trend with AR for riblets with spacing of $0.025''$ and aspect ratios of 0.8, 1.6 and 2 in a range of s^+, AR = 1.6 provides the highest reduction, while in another range of s^+, AR = 0.8 results in the highest reduction and AR = 1.6 and AR = 2 causes drag increase. Similar trends can also be seen in the experiments of Bechert and co-workers [20] for trapezoidal and rectangular grooves where riblets with AR $\approx 0.6 - 0.8$ offered the highest reduction over a wide range of flow dynamics.

On the other hand, in Figure 1-27 shown in Chapter 1, the data presented by Bechert and co-workers shows that as AR increases, the cross over from drag increasing to drag reducing state happens at lower and lower values of s^+. This can be qualitatively compared with the scaled Reynolds number introduced earlier in this chapter. From the definition of s^+ or equivalently using the notation of this thesis λ^+ I know

$$\lambda^+ = \frac{\lambda}{\nu} u^* \tag{2.64}$$

and

$$u^* = \sqrt{\frac{\tau}{\rho}} \tag{2.65}$$

For different types of flows one can write the wall shear stress in the form of a drag/friction coefficient C_f multiplied by $1/2\rho U^2$. If I assume that this drag/friction coefficient is a function of the Reynolds number of the flow in the form of a power law, Re_L^{-m}, where Re_L is Reynolds number based on the characteristic length scale of the problem with $0 < m \leq 1$, then one can find a scale for Equation 2.64 as

$$\lambda^+ \sim \frac{\lambda}{L}\frac{UL}{\nu}\sqrt{\mathrm{Re}_L^{-m}} \sim \frac{\lambda}{L}\mathrm{Re}_L^{1-\frac{m}{2}} \tag{2.66}$$

Therefore, while s^+ or λ^+ is not exactly the same as the scaled Reynolds number, it

has a similar functional form and follows similar increasing/decreasing trends with Reynolds number and the riblet wavelength (spacing). Therefore for a flow to be drag reducing, the s^+ (or λ^+) should be smaller than a threshold as demonstrated in Figure 1-27 by Bechert and co-workers which is comparable to the trend in the drag reduction and the scaled Reynolds number explained earlier. Note that to return to the scaled Reynolds number as in Equation 2.37, then $m = 1$. This figure also confirms the non-monotonic behaviour of the drag reduction as a function of the aspect ratio and at each s^+ there is one intermediate aspect ratio offering the largest reduction in the frictional drag.

2.5   Shark Skin and Boundary Layer Theory over Riblet Surfaces

The extended boundary layer theory introduced here can also be used to give an insight into the geometrical features of the ribs on shark skin and their potential for being able to reduce the skin friction drag. Using the reported values for the average spacing and heights of the ribs of various types of shark denticles by Bechert and co-workers [82], Wen and co-workers [90], and Luo and coworkers [91], it can be seen that on average, the spacing of the ribs of the shark scales is $\lambda \approx 35 - 105$ μm and the heights are in the range of $A \approx 20 - 30$ μm, giving an aspect ratio of AR $\approx 0.4 - 0.8$.

So, assuming that the ribs on the shark skin create a long continuous groove with AR $\approx 0.4 - 0.8$, and sharks of $L \approx 2$ m swim at an average speed of 5 m/s, the flow over the shark skin will have a scaled Reynolds number of $\mathrm{Re}_L (\lambda/L)^2 \approx 0.05$ in water with $\mathrm{Re}_L \approx 10^7$ which falls in the drag reducing region in Figure 2-13. Since $\mathrm{Re}_L \approx 10^7$ is in the turbulent flow regimes, assuming the transition to turbulence happening at $\mathrm{Re}_L \approx 5 \times 10^5$, the location of the transition is at $L \approx 0.5$ m corresponding to $\mathrm{Re}_L (\lambda/L)^2 \approx 0.02$ which also falls into the drag reducing region in Figure 2-13.

Therefore, this simple theoretical argument and the corresponding drag reduction contour plot (Figure 2-13) shows that ribs on the shark skin have the potential of

being drag reducing and their geometrical parameters, especially the aspect ratio of the ribs falls in the region with the optimum drag reduction.

2.6 Limitations of the Theory

The theoretical modelling of laminar boundary layer flow over riblet surfaces presented so far is a simplified model of the three dimensional flow and captures the trends in the effect of riblet surfaces on the flow as well as the total drag on the surfaces and it is able to predict the drag-reducing effect of the riblet surfaces.

However, similar to the boundary layer theory, this theoretical modelling fails to capture the effect of the pressure gradient close to the leading edge of the plate which enhances the ability of riblets in reducing the total drag using riblet surfaces (will be discussed in more detail in Chapter 3). Looking back at Equation 2.59, if the pressure gradient is non-zero, then the second term in the equation involving the effect of the displacement area will be non-zero and will affect the calculation of total drag. Previous experimental and numerical works discussed in Chapter 1 have shown reductions up to 8% in various flow conditions including the boundary layer experiments performed by Walsh and co-workers while the results of the theory showed earlier can capture up to 1% reduction [37, 39, 38].

On the other hand, using the this theory, I can calculate the velocity profiles for V-grooves of various sizes; for example, for $\mathrm{Re}_L = 99200$ with $\lambda/L = 7.81 \times 10^{-3}$ and AR $= 1.72$, the velocity profiles at three span-wise locations $x/\lambda = 0$, $x/\lambda = 0.25$, and $x/\lambda = 0.5$ are plotted in Figure 2-14. The results shown here correspond to the experimental and numerical data presented by Djenidi et. al at the same Reynolds number and similar riblet sizes (Figure 1-15). Comparing their results to the figure below, one can see that qualitatively the velocity profiles at these three stream-wise locations are similar especially as I move away from the riblets. However, inside the grooves at the wall, one can see that the results of this theory cannot predict the nearly zero velocity gradient that is visible in Figure 1-15 which results in a higher shear stress inside the grooves and hence the total drag reduction predicted is smaller
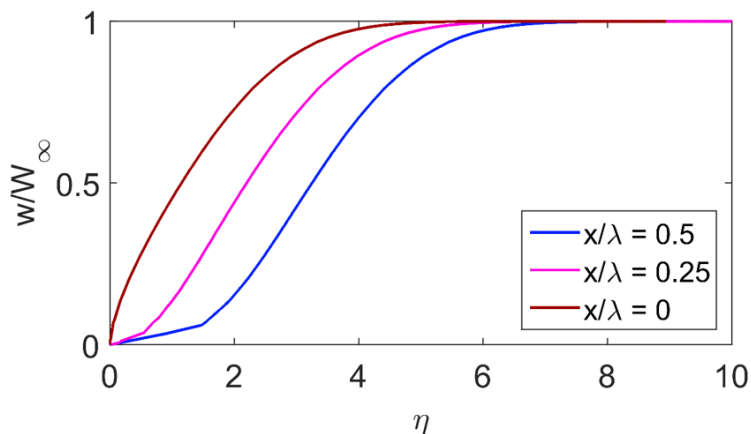
Figure 2-14: Calculated velocity profiles for boundary layer flow over V-groove riblet surfaces with $\text{Re}_L = 99200$, $\lambda/L = 7.81 \times 10^{-3}$ and $\text{AR} = 1.72$ corresponding to the data presented by Djenidi et al. [73].

than the reported values.

To be able to take the effect of the leading edge into account, the complete set of the Navier-Stokes should be solved for the problem over the riblets of different aspect ratios and sizes. In Chapter 3, I will use full three dimensional numerical simulation of the boundary layer flow over riblet surfaces to complement the analysis presented so far and understand how the leading edge and the pressure gradients can help enhance the total reduction in the frictional drag force.

2.7 Conclusion

In this chapter, using an extension of the boundary layer theory, I showed that boundary layer over three dimensional periodic riblets can be described using three non-dimensional variables; Reynolds number of the flow Re_L, the ratio of the spacing of the riblets to the length of the plate λ/L, and the aspect ratio of the riblets $\text{AR} = 2A/\lambda$. Scaling of the equations show that the results of the boundary layer calculations can be presented in a self-similar manner, using a scaled form of the Reynolds number $\text{Re}_L(\lambda/L)^2$ and the aspect ratio of the riblets AR.

The boundary layer equations were solved using coordinate transformation and conformal mapping to find the relations between the Cartesian and curvy-linear riblet

coordinate systems. Boundary layer over riblet surfaces is seen to have a thickness larger than the flat plate and as the aspect ratio of the riblets increases the thickness, presented in the form of displacement area. Additionally, increasing the aspect ratio of the riblets results in a larger area of flow retardation inside the grooves.

Using the momentum integral equations the momentum area calculated for each of the riblets can be used to calculate the total drag on the entire plate and the results are presented in the form of a contour plot of the total reduction in frictional torque as a function of the scaled Reynolds number and the aspect ratio of the riblets. The results show that at each constant aspect ratio, scaled Reynolds number of the flow should be lower than a maximum threshold for the riblet surface to be drag reducing. On the other hand at each constant scaled Reynolds number, there is an aspect ratio corresponding to the highest drag reduction. This theory can also be used to explain that ribs on the shark denticles have optimum feature size to act as a drag reducing surface.

As discussed in the chapter, the results of the this theory can capture the trends presented previously in the literature and offers an explanation for the conflicting results presented in terms of the effectiveness of riblets as a passive drag reduction method. With the non-monotonic behaviour of the drag reduction as a function of the aspect ratio, the choice of the aspect ratio, as well as the size of the riblets, in any dynamic condition can result in situations where the riblets are able to reduce or not reduce the total drag.

Lastly, one can see that while capturing the trends in the total drag, this theory fails to predict the magnitude of the reduction achieved compared to the ranges from previous experimental and numerical efforts. To mitigate this limitation, one needs to remove the simplifying assumptions made earlier in the chapter, especially in terms of neglecting the pressure gradient and the leading edge effects. To do that, one needs to use the full three dimensional form of the Navier-Stokes equations which is achievable employing various numerical simulation methods available. In the next chapter I will perform the full three dimensional simulations of the steady state boundary layer flow over sinusoidal riblet surfaces and discuss the effects of the leading edge on

the dynamics of the flow and the total frictional drag reduction using riblet covered surfaces.

THIS PAGE INTENTIONALLY LEFT BLANK

Chapter 3

Numerical Modelling of Boundary Layer over Sinusoidal Riblet (Wrinkled) Surfaces

3.1   Introduction

In the previous chapter, I discussed the boundary layer flow over V-groove riblet surfaces by extending the two dimensional boundary layer theory to three dimensions for periodic riblet surfaces. I showed that viscous boundary layer flow over riblet surfaces can be discussed using two dimensionless groups, the scaled Reynolds number $\text{Re}_L(\lambda/L)^2$, and the aspect ratio of the riblets $\text{AR} = 2A/\lambda$. First, it was demonstrated that for riblets with the same AR, the flow is self similar as long as the scaled Reynolds number is kept constant between different cases. Then using the definition of the momentum thickness and momentum integral equations, I showed that riblet surfaces can offer a level of drag reduction compared to smooth walls, and for a surface to

be drag reducing the flow near the surface needs to have a scaled Reynolds number lower than a critical aspect ratio-dependent threshold. In addition, at a constant scaled Reynolds number, it was seen that there is always one aspect ratio that offers the optimum drag reduction and the change in the total frictional drag force for riblet surfaces (compared to smooth surfaces) has a non-monotonic behaviour with the aspect ratio of the riblets.

While this theoretical modelling allows me to understand and predict the trend in the changes in drag as a function of the flow and the geometry, it cannot quantitatively capture the magnitude of the drag reduction that has been previously reported in literature as it was shown previously in Chapter 1. The calculations presented in Chapter 2 were only able to show a maximum of 1% reduction in the total drag, while in the previous experimental and computational literature reductions up to 8% have been reported [38, 39, 1, 40, 59].

As I constructed the three dimensional extension to the boundary layer theory, similar to the classical boundary layer theory, the dynamics of the leading edge of the plate plus the resulting pressure gradients induced in the local flow near the edge were neglected. Therefore, the total integrated frictional drag force calculated for both riblet and smooth surfaces neglected all effects of the leading edge and hence a lower percentage drag reduction is predicted. Thus to reintroduce the hydrodynamic effect of the leading edge back into the problem, one needs to solve the full three dimensional Navier-Stokes equations with the continuity equation without any geometric simplifications, which is possible using steady-state numerical simulations of the boundary layer over riblet surfaces.

In the previous chapter the three-dimensional boundary layer theory was developed quite generally for any riblet surface, but was solved specifically for V-grooves since I could find an analytical solution for the conformal map between the Cartesian (x, y, z) coordinate system and the curvy linear ortho-normal coordinate system (α, β, z). Similar conformal maps can be found for other riblet surfaces, however, they might not have a closed form analytical solution and thus require numerical calculations using the Laplace equation [89]. To expand my investigation of riblet surfaces,

in the present chapter I will use numerical simulations of steady three-dimensional boundary layer flow over sinusoidal riblet surfaces (also known as wrinkled surfaces) to evaluate more accurately the level of drag reduction that can be expected in real applications using textured substrates.

Wrinkled surfaces have been capturing the attention of the mechanics world for a number of years now. In recent decades, new developments in soft materials research have demonstrated the possibility of creating surfaces with various types of wrinkled textures in the forms of sinusoidal periodic and non-periodic wrinkles and herringbone patterns using hyper-elastic materials [92, 93, 23]. With the advances in the understanding of the tunability of the wavelength and amplitude of textured surfaces with geometric, dynamic and material parameters, it is also of interest to investigate the possibility of using such surfaces for applications such as smart adhesion [94], and flow control. Terwagne et al. have recently used dimpling patterns of wavelength of 4.37 mm and average dimple depth of between $0 - 0.8$ mm on spherical surfaces of 20 mm radius and showed the potential of dynamically controlling the total drag for Reynolds numbers between $5 \times 10^3 - 10^5$ [95].

In order, to understand the integrated effect of the riblets on the structure of an evolving viscous boundary layer, it is important to first systematically unravel how the laminar boundary layer spatially develops over riblet textured surfaces prior to the transition to turbulence, and whether changes in the corresponding laminar flow evolution could lead to an increase or reduction in the total drag force on the surface compared to a flat plate. In this chapter, I explore the changes induced by periodic sinusoidal wrinkles on a spatially developing laminar viscous boundary layer flow. I study the systematic changes in velocity profiles, pressure distribution, and the resulting local changes in the boundary layer thickness and the shear stress distribution along the length and breadth of the textured plate. By understanding each of these local kinematic and dynamical changes I can then ultimately evaluate the effect of the riblets on the total integrated viscous drag force. In general, unperturbed boundary layers over plates remain laminar up to Reynolds numbers close to 5×10^5 and then naturally transition to turbulence [41]. Note I also recognize that boundary layers

can be tripped to transition at earlier Reynolds numbers, resulting in an increase in the total frictional drag force, however this is not the focus of this study [96, 55].

This chapter is organized as follows: in Sections 3.2, 3.3, and 3.4, I discuss the numerical method used in the research combined with a grid resolution and benchmark study of flat plate boundary layer. Then in Section 3.5, the primary results of the numerical study are presented; first I discuss the evolution of the velocity profiles along the boundary layer that develops over periodic riblet surfaces as well as the pressure distribution in the stream-wise direction. Then I discuss the effect of wrinkles of various aspect ratio on the thickness of the boundary layer, and lastly in Section 3.5.3, I explore the effect of the riblets on changes in the local shear stress distribution along the length of the plate as well as on the total integrated frictional drag over riblet surfaces with various aspect ratios.

3.2   Numerical Method

My goal is to solve the full steady state Navier-Stokes equations for the three velocity components (u, v, w) and the pressure (p) distribution in the laminar viscous boundary layer that develops over different textured plate geometries. In the present study the numerical simulations are carried out using the finite volume method, with the SIMPLE algorithm (Semi Implicit Method for Pressure Linked Equations) [97]. The SIMPLE algorithm is widely used for steady state problems with velocity and pressure coupling and was first introduced by Patankar and Spalding in 1972 [98]; in this algorithm initial guesses for the velocity and pressure components are provided at the beginning of each step of the iteration, then the discretized momentum equation is solved leading to corrections for the velocity components and lastly the pressure correction equation is solved, correcting the initial pressure estimate. The algorithm then checks for convergence and either terminates the procedure at the desired convergence criteria or continues to the next iteration step [97, 99]. The SIMPLE algorithm is already implemented in the open source CFD package OpenFOAM$^{\circledR}$ for three dimensional laminar viscous flows and this implementation was utilized throughout

the present study [100].

A schematic of the geometry and the coordinate system used is shown in Figure 3-1(a). Stream-wise wrinkles (sinusoidal riblets) are aligned in the direction parallel to the flow (z-direction) and are fully defined by two geometric parameters, the wavelength (λ) or spacing of the riblets and the amplitude (A), here defined as the distance between the peak and the trough of a wave as shown in Figure 3-1(b). Velocities in x, y, z direction are denoted by u, v, w respectively and the total length of the plate along the flow direction is denoted by L. To compare simulations with different riblet geometries, two dimensionless groups are used: the aspect ratio $AR = 2A/\lambda$ of the riblets provides a measure of the local sharpness of the ribbed texture and λ/L (global) provides a measure of the size of the plate riblets with respect to the size of the plate. Because the flow also evolves in the stream-wise direction, it is also helpful in my analysis to compare the ridge wavelength to local position suing a local scaled variable z/λ. The lines $y = 0$ and $y = -A$ are chosen to be at the peak and trough of the wrinkles respectively and the surface of the riblets can be defined as

$$y_{\mathrm{s}} = -\frac{A}{2} + \frac{A}{2}\cos\left(\frac{2\pi}{\lambda}x\right) \tag{3.1}$$

where x is the cross-stream direction.

The scale of the wrinkles simulated in this work were chosen based on the physical riblet sizes reported previously to show drag reduction [38, 39, 1, 40, 59]; the wavelength has been kept constant at $\lambda = 2\pi/3 \times 10^{-4}$ m $\approx 200\ \mu$m and the length of the domain ($0 < L/\lambda < 191$) and amplitude ($AR = 0.48, 0.72, 0.95, 1.43, 1.91$) have been varied to investigate the effect of geometric changes on the level of drag reduction that can be achieved. To ensure the flow is laminar, the Reynolds number of all the cases simulated were limited to $\mathrm{Re}_L < 5 \times 10^5$, which is the conventional criterion for transition to turbulence on a flat plate [41].

The appropriate Reynolds number that parametrizes the relative importance of inertial and viscous effects in this spatially developing flow, is defined using the flow direction (z) as the length scale (similar to the classical boundary layer theory) and

(a)

(b)
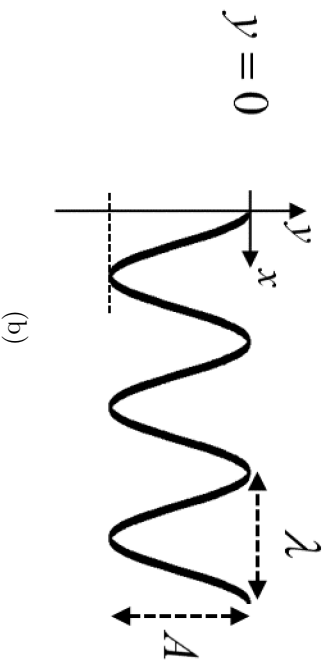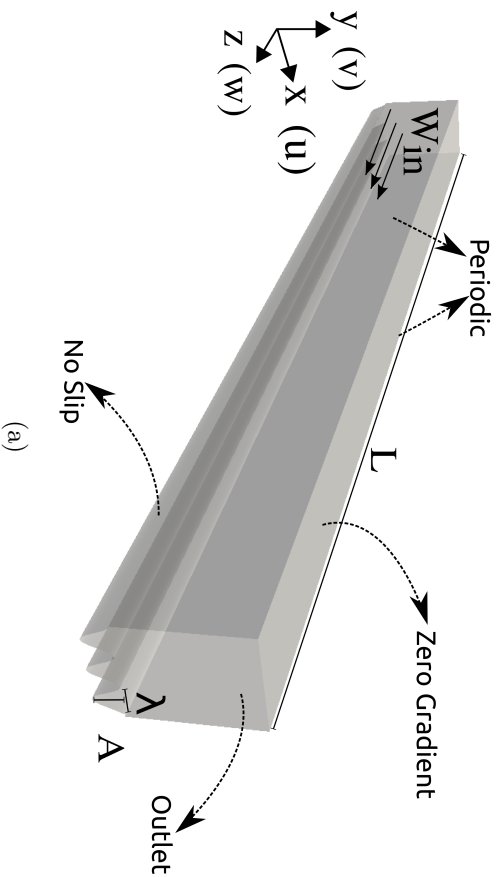
Figure 3-1: (a) Schematic of the 3D geometry of the wrinkled surfaces used in OpenFOAM simulations; (b) The cross section of a wrinkled surface ($x - y$ plane).

122

the maximum velocity of the stream along the plate (W_∞) which is determined after the simulations are carried out. The local Reynolds number can thus be written as $\mathrm{Re}_z = W_\infty z/\nu$, where $\nu = \mu/\rho$ is the kinematic viscosity of the fluid, μ is the dynamic viscosity and ρ is the density of the fluid.

The boundary conditions of this problem shown schematically in Figure 3-1(a) are similar to the case of a conventional boundary layer problem [41]. At the inlet (plane of $z = 0$), flow enters the domain uniformly with uniform velocity W_{in}, over the computational domain the wrinkled surface on the bottom is non-permeable and acts as a no-slip wall, the upper surface has a zero pressure and no velocity gradient across it and the outlet (plane of $z = L$) has zero velocity gradient across it and zero pressure. The two side walls have periodic boundary conditions. Note that due to leading edge effects, the maximum velocity in the simulations is up to 30% larger than the inlet velocity and the maximum velocity calculated for each case is used as W_∞ throughout the chapter.

3.3 Grid Resolution Study

The dimensions of the mesh elements used in this finite volume study have been kept similar for all the cases with an average size of $0.08 \times \lambda$. (The average size is calculated as the cubic root of average cell volume $V^{1/3}$). The smallest mesh element is located close to the wall at the leading edge with an average size of $0.05 \times \lambda$ and the largest mesh element is at the top boundary at $z = L$ has a length scale in the stream-wise direction of $0.1 \times \lambda$. AS a illustrative example of the problem size to simulate the cases of $L/\lambda = 95.5$ with 3 wrinkles, $N = 6.72 \times 10^6$ mesh elements were used. For longer/shorter geometries, the number of mesh elements were proportionally increased/decreased.

I first take two models with AR $= 1.91$ and AR $= 0$ (flat plate), $L/\lambda = 23.87$ and $\mathrm{Re}_L = 6650$ and use these to investigate the effect of the spatial resolution by changing the number of cells (or changing the average size of the elements). The results are presented in Fig. 3-2 in terms of the change in the overall integral drag

coefficient on the plate as the number of elements N in the simulation is incremented or as the size of the mesh element is reduced. The drag coefficient on the plate is defined as

$$C_D = \frac{D}{\rho W_\infty^2 A_{\mathrm{w}}} = \frac{1}{\rho W_\infty^2 A_{\mathrm{w}}} \int_{A_{\mathrm{w}}} (\boldsymbol{\tau}_{\mathrm{w}}.\boldsymbol{n}_{\mathbf{w}}).\mathbf{e}_z dA_{\mathrm{w}} \qquad (3.2)$$

where D is the total drag force on the wall, A_{w} is the wetted area of the wall, $\mathbf{n}_{\mathrm{w}}$ is the local normal to the surface of the wall, $\boldsymbol{\tau}_{\mathrm{w}}$ is the shear stress tensor evaluated at the wall. The total drag coefficient calculated using the Blasius solution $C_D = 1.328/\sqrt{\mathrm{Re}_L}$ is also shown in Figs. 3-2 with dashed line. Due to the leading edge effects present for plates with low Reynolds number (lower than 10^4) such as $\mathrm{Re}_L = 6650$ the calculated results for the flat plate is about 20% higher than the theory. This difference can be captured using the higher order theory where the drag coefficient includes an additional term and can be written as $C_D = 1.328/\sqrt{\mathrm{Re}_L} + 2.67/\mathrm{Re}_L^{7/8}$ [41].

Results show that increasing the number of cells from from 1.22×10^6 to 1.68×10^6 (equivalently, changing the average cell size from 0.09λ to 0.08λ) changes the drag coefficient by only 0.1% and thus using the later cell size gives sufficient resolution for the simulations. A similar mesh size as the $N = 1.68 \times 10^6$ ($V^{1/3}/\lambda = 0.08$) for $L/\lambda = 23.7$ has been used throughout this study where for $L/\lambda = 47.75$ and $L/\lambda = 95.5$, $N = 3.36 \times 10^6$ and $N = 6.72 \times 10^6$ cells are used respectively.

3.4   Benchmark

As an initial benchmark, the problem of a flat plate boundary layer has been solved with the method explained in Section 3.2; for this the same geometry as Figure 3-1(a) has been used with a flat no-slip wall instead of the wrinkled one at $y = 0$. The rest of the boundary conditions are the same as explained. Water has been chosen as the working fluid with $\nu = 10^{-6}$ m^2/s and the inlet velocity is $W_{\mathrm{in}} = 6$ m/s. The corresponding maximum free-stream velocity is found to be $W_\infty = 6.56$ m/s and the Reynolds number based on the length is $\mathrm{Re}_L = 31550$, corresponding to a flat plate

(a)

(b)
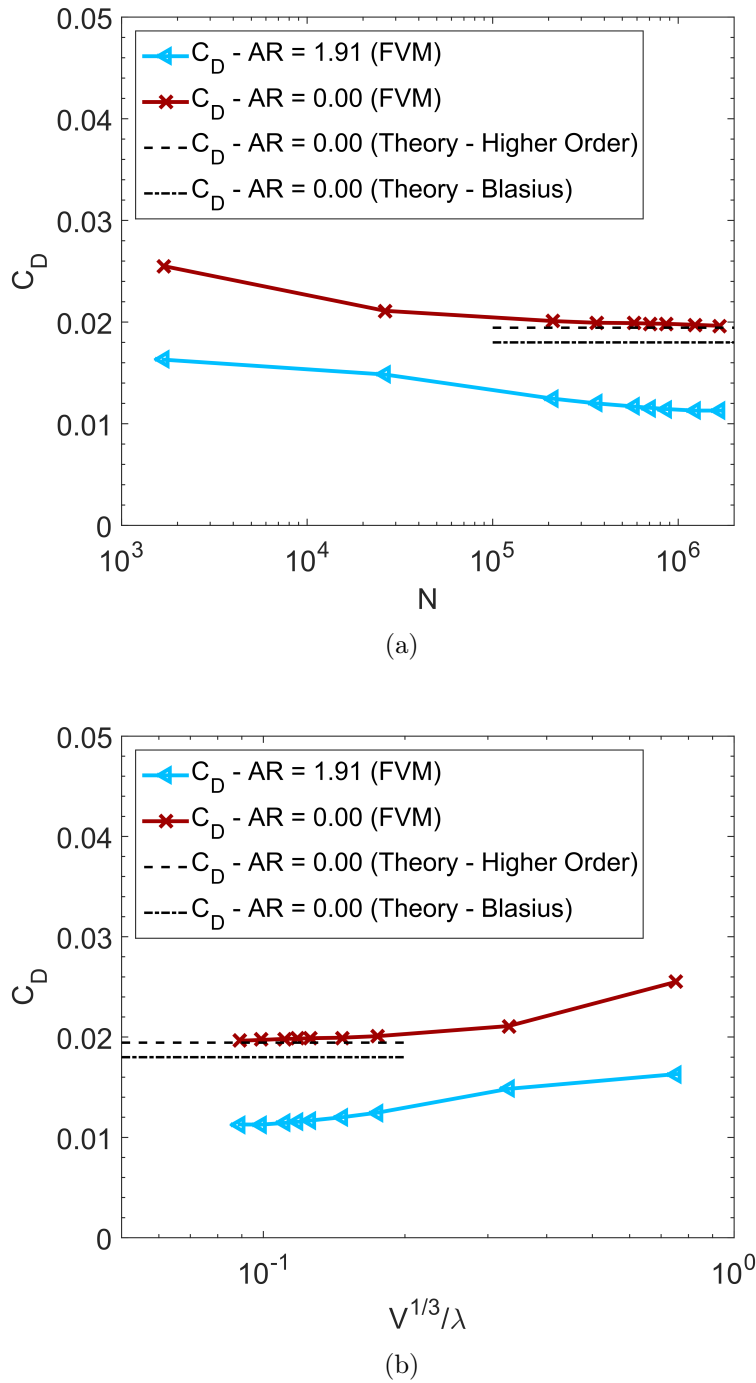
Figure 3-2: Effect of (a) the number of mesh elements and (b) the average size of the mesh elements on the study of flow over sinusoidal riblets. The results are presented for the calculated drag coefficient on the riblet walls for a geometry with AR = 1.91 and AR = 0 (flat plate), $\mathrm{Re}_L = 6650$ and $L/\lambda = 23.87$. The theoretical results for a corresponding flat plate is shown with dashed line.

of length $L = 0.1$ m.

In order to validate the solution, the results from the numerical simulations are compared with the boundary layer theory. Based on the Blasius solution for the laminar boundary layer flow over a flat plate under zero pressure gradient, the velocity profiles along the length of the flat plate are self-similar when expressed in terms of a similarity variable η defined as $\eta = y/z\sqrt{\text{Re}_z}$. Using η and non-dimensionalizing the velocity with the free-stream velocity w/W_∞, the velocity profiles collapse on each other, having a form as shown with a solid line in Figure 3-3(a) as calculated by Blasius in 1907 [88, 41]. The calculated velocity profile w/W_∞ at the end of the plate, $z = L$ (at $\text{Re}_L = 31550$) as scaled using the definition of $\eta = y/L\sqrt{\text{Re}_L}$ are shown on Figure 3-3(a) by the points. As shown, the results of the theory and the numerical simulation match very well.

Additionally, the computed values of the skin frictional shear stress along the plate are compared with the Blasius boundary layer theory. According to the Blasius solution for the flat plate boundary layer, the shear stress at each point along the plates is given in the form of a non-dimensional local skin friction coefficient C_f at each point on the flat wall and is given as [41]

$$C_f(z) = \frac{\tau_{yz}(y = 0, z)}{\frac{1}{2}\rho W_\infty^2} = \frac{0.664}{\sqrt{\text{Re}_z}}. \tag{3.3}$$

The local skin friction distribution at the wall $\tau_{yz}(y = 0, z)$ is also extracted from the simulations, scaled with $1/2\ \rho W_\infty^2$ and plotted versus the local Reynolds number Re_z, next to the theoretical line (solid line) in Figure 3-3(b). It is clear that good agreement with the Blasius result is obtained

3.5 Results

Having established the fidelity and convergence of the simulation technique I now proceed to use the finite volume code to investigate how the presence and shape of the sinusoidal riblet structures influence the development of the boundary layer flow. I first investigate the evolution of velocity profiles in the stream-wise and span-wise

(a)

(b)
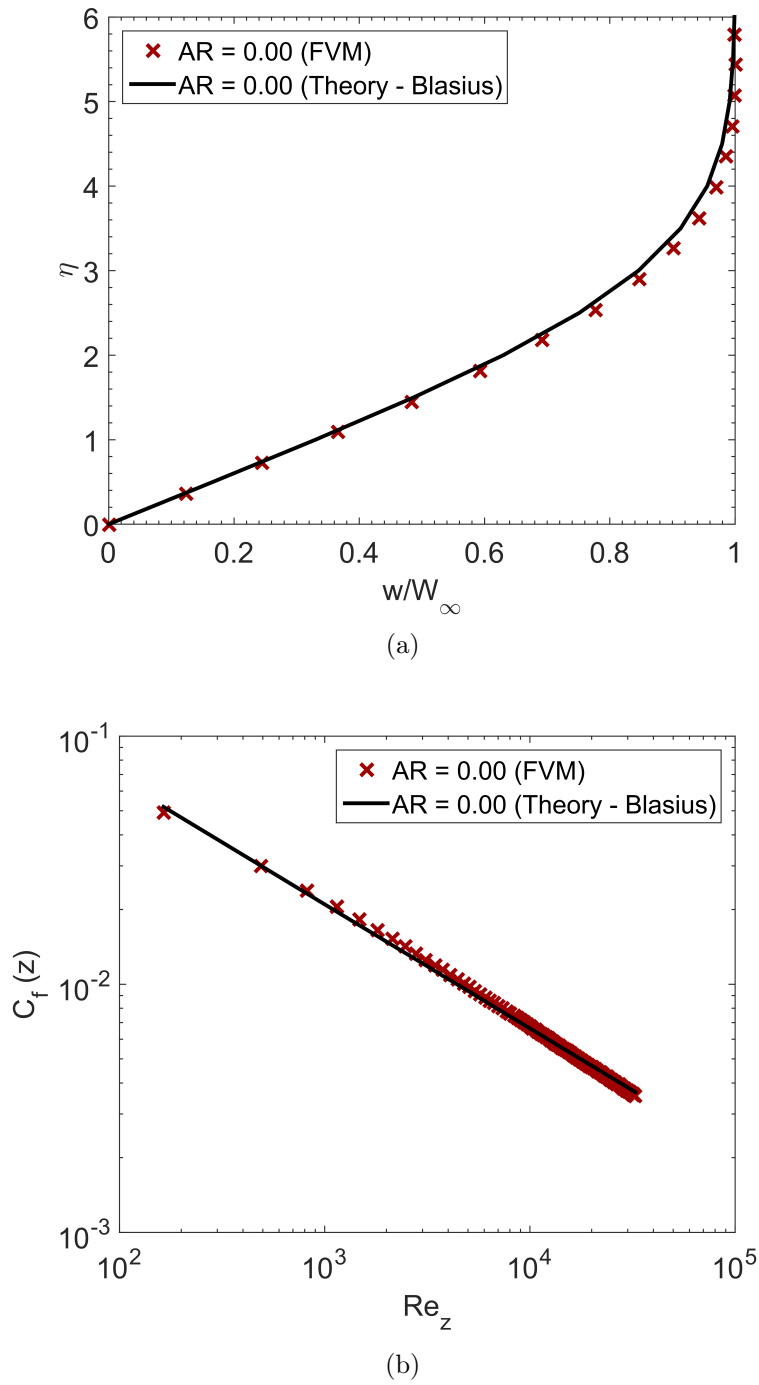
Figure 3-3: Results of flat plate boundary layer calculation using OpenFOAM and boundary layer theory for a flat plate with $\mathrm{Re}_L = 31550$; (a) Velocity profiles as a function of the similarity variable $\eta = y/z\sqrt{\mathrm{Re}_z}$ at $z = L$. Maximum difference between the numerical calculations and theory is 2.7%. (b) Distribution of skin friction coefficient $C_f(z)$ along the plate as a function of the local Reynolds number Re_z.

direction as well as the pressure distribution along the flow direction in Section 3.5.1. Then I discuss different measures used to calculate the boundary layer thickness and how the riblets affect the evolution in the boundary layer thickness in Section 3.5.2. Lastly, I examine the effect of the riblets on the shear stress distribution along the length of the plate as well as the total viscous drag acting on the surface in Section 3.5.3 and conclude whether drag reducing behaviour can be observed.

3.5.1 Evolution of Velocity and Pressure Field

In contrast to the flat plate boundary layer, with a textured plate the velocity profile takes various shapes at each cross section depending on the span-wise (x-direction) location across the plate. As an example, the velocity profiles at 7 equi-spaced distances across a single sinusoidal wrinkle with AR = 1.91 at Re_L = 13300 and L/λ = 47.75 are presented in Figure 3-4. Similar shaped velocity profiles have been previously reported in both experimental and numerical simulations by Djenidi et al. [83, 73] as previously shown in Figure 1-15. They reported velocity profiles, further away from the leading edge at a Reynolds number of $\text{Re}_L = 7.13 \times 10^4$ for a plate of $L/\lambda = 92$ featuring V-shaped grooves with AR = 1.72. Their profiles were comparable with the key features reported here, showing a retarded (nearly stagnant) flow inside the grooves (with a local velocity less than 20% of the free-stream velocity) while outside of the riblets all velocity profiles collapsed onto the same universal profile. Similar flow retardation and mean velocity profiles have been reported for turbulent flow over thin rectangular riblets as well as V-groove and U-groove textures of different sizes [68, 74, 27].

Because the differences in the shape of the velocity profiles vary systematically with the cross sectional position (x), the velocity profiles at the peak ($x = \lambda$) and in the trough ($x = \lambda/2$) of the wrinkles are chosen as the representative profiles to be discussed further as they present the two extrema of the problem. To illustrate qualitatively the three-dimensional evolution in the flow, contours of the dimensionless velocity distribution (w/W_∞) at the peak and trough for ribbed plates at Re_L = 13300, L/λ = 47.75 and AR = 1.9 are shown in Figures 3-5(a) and 3-5(b) respectively.

128
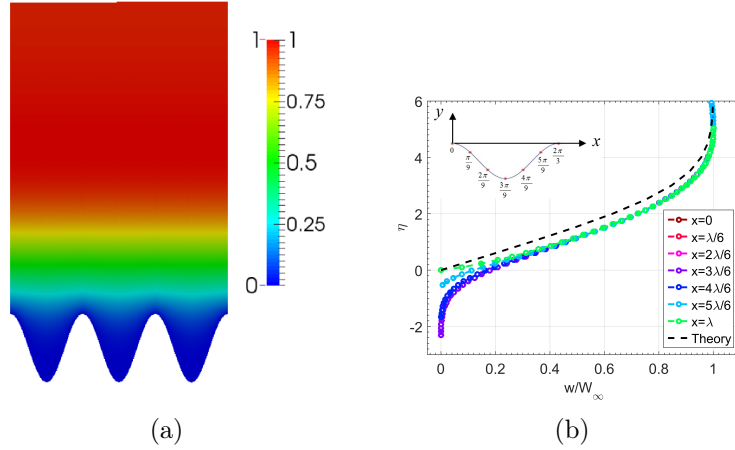
Figure 3-4:   (a) Contours of dimensionless velocity and (b) velocity profiles $w(x,y)/W_\infty$ at 7 different locations of $x = i\lambda/6$ and $0 \leq i \leq 6$, within a single groove of a wrinkled plate with AR = 1.91 and $L/\lambda = 47.75$ at $\text{Re}_L = 13300$; Here $\eta = y/L\sqrt{\text{Re}_L}$ which is the same definition as used in the flat plate boundary layer theory. The dashed line denotes the theoretical profile from the Blasius solution to boundary layer equation for a flat plate (AR = 0).

Qualitatively the velocity contours at the peak appear very similar to the evolution observed along a flat plate boundary layer while the contour distribution in the trough differs from the peak and depict a thicker boundary layer for which most of the region inside the groove has velocities lower than 25% of the free-stream velocity.

The evolution in the velocity distributions can be studied more quantitatively by plotting the spatial changes of the velocity profiles in the flow direction, as shown in Figures 3-6 and 3-7. Here I non-dimensionalize the position along the plate using a characteristic diffusive scale ν/W_∞ so that the dimensionless position corresponds to a local Reynolds number $\text{Re}_z = W_\infty z/\nu$. Although the wrinkles (sinusoidal riblets) result in different velocity profiles at different locations, the main features and the local differences induced by the riblets can be effectively contrasted by comparing the velocity profiles at the peak and trough of a single riblet. Figures 3-6 and 3-7 present the velocity profiles at the peak and trough respectively (corresponding to the velocity contours in Figure 3-5). As I have noted, the stream-wise profiles at the peak, $w(x = \lambda, y)$ closely resemble the profiles of flat plate boundary layer theory. In the trough, the profiles $w(x = \lambda/2, y)$ look markedly different and reveal a thicker
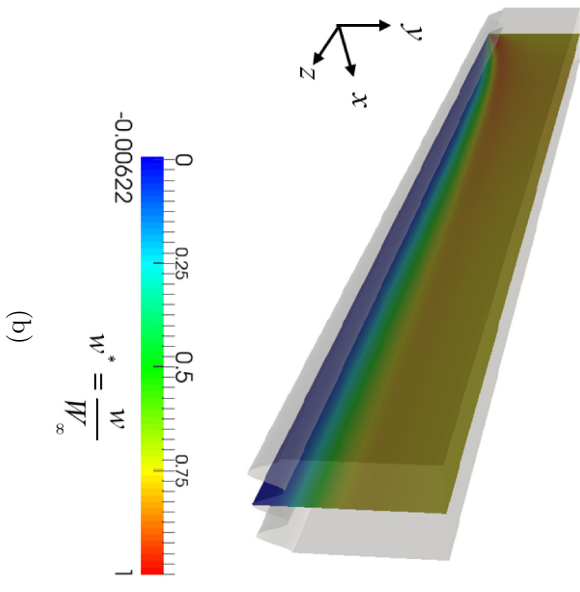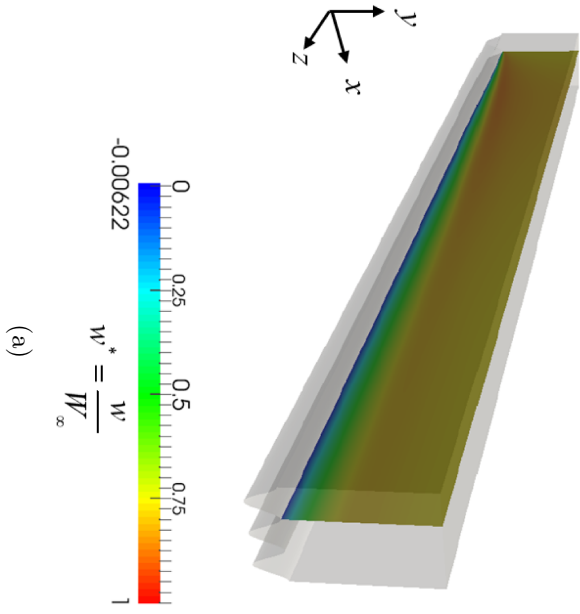
Figure 3-5: Schematic of the evolution in the boundary layer at (a) the peak ($x = \lambda$, $y_{\min} = 0$) and (b) the trough ($x = \lambda/2$, $y_{\min} = -A$) of a sinusoidal riblet surface with $\mathrm{Re}_L = 13300$, $L/\lambda = 47.75$ and AR $= 1.91$.
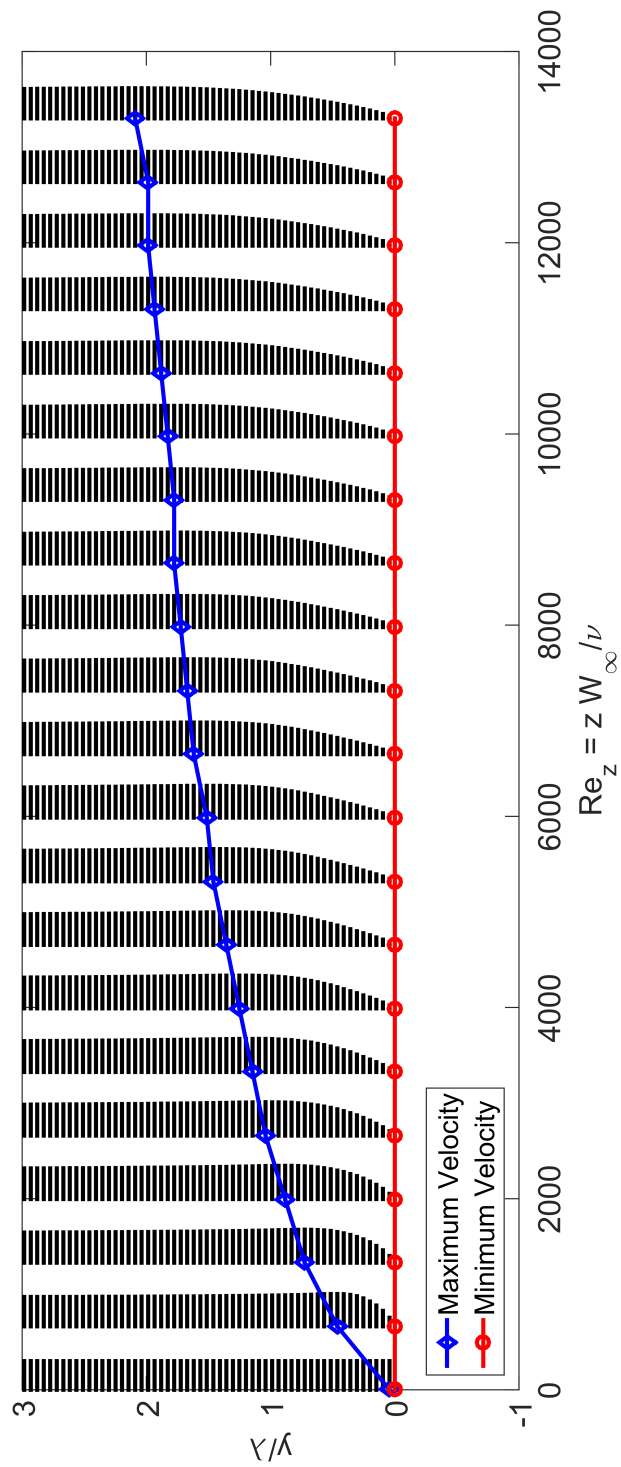
Figure 3-6: Evolution of stream-wise velocity profiles $w(x, y, z)$ in the flow direction along (a) a peak $x = \lambda$ and $y_{\min} = 0$ of a surface with sinusoidal riblets with $L/\lambda = 47.75$ and AR $= 1.91$ at $\mathrm{Re}_L = 13300$.

131
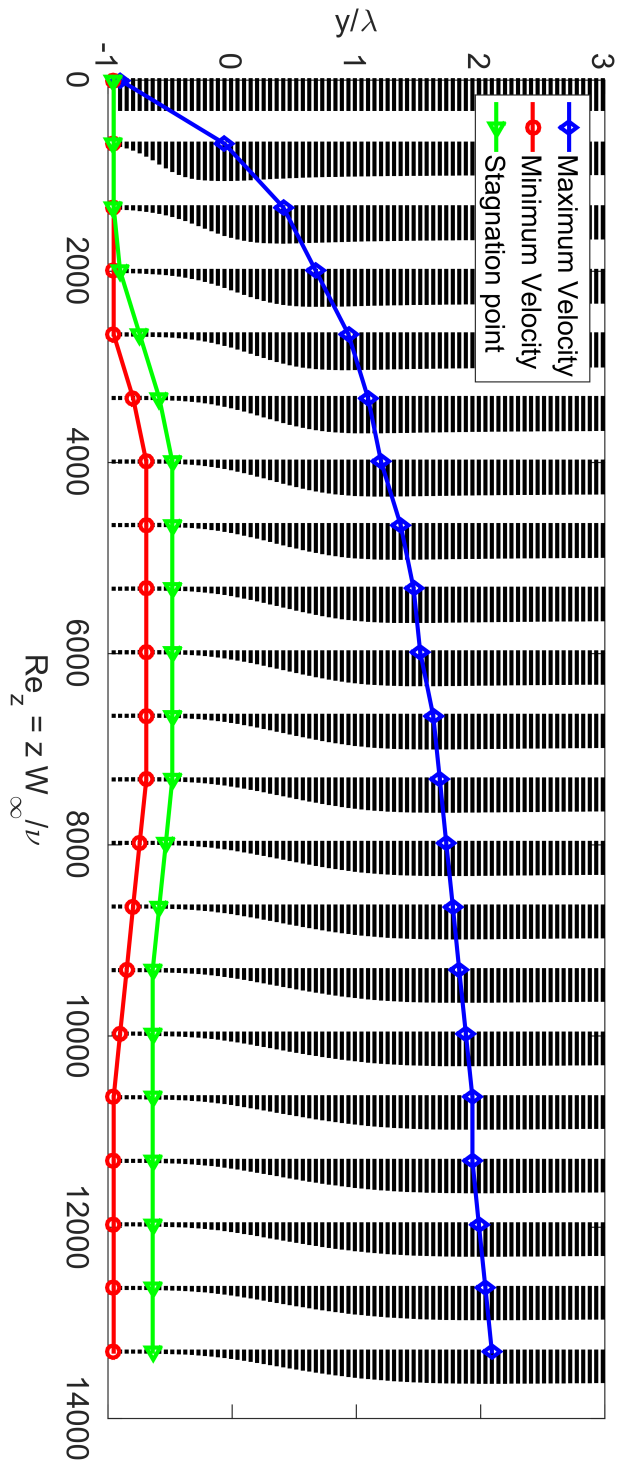
Figure 3-7: Evolution of stream-wise velocity profiles $u(x, y, z)$ in the flow direction along a trough $x = \lambda/2$ and $y_{min} = -A$ of a surface with sinusoidal riblets with $L/\lambda = 47.75$ and AR $= 1.91$ at $Re_L = 13300$.

boundary layer, with the velocity inside the groove ($y < 0$) much lower than the free-stream velocity. For this case with AR $= 1.91$ the minimum velocity observed in each profile i.e. $w_{\min} = \min(w(x = \lambda/2, y))$ is not always zero (as it is for the velocity profiles at the peak $x = \lambda$), but can in fact become negative and within a region between about $2500 < \text{Re}_z < 10500$, a local *re-circulation* is observed. The location of the minimum velocity at each position z along the plate is shown in Figures 3-6 and 3-7 by the red circles joined by a line. If there is a *re-circulation* present, then the line of minimum velocity is displaced from the wall inside the groove. As a consequence above this line of points, a stagnation line is also formed inside the grooves and shown in each figure by the solid green line and triangular symbols.

At three representative local positions (corresponding to local Reynolds numbers of $\text{Re}_z = 4000,\ 8000$ and 12000) velocity profiles are extracted and plotted as shown in Figures 3-8. For $\text{Re}_z = 4000$ and $\text{Re}_z = 8000$ the trough profiles show a region of weak re-circulation inside the grooves ($y < 0$) whereas outside the groove, the velocity profiles at the peak and at the trough collapse on each other and evolve in similar fashion toward the outer inviscid flow far from the plate. Further along the plate at $\text{Re}_z = 12000$, the recirculating region ends, and thereafter the fluid inside the groove is in an essentially stagnant condition with zero velocity. Outside the groove the two velocity profiles meet and grow similarly to reach the free-stream velocity.

The detailed computations of the velocity field in the vicinity of the sinusoidal texture reveal that due to the presence of the wrinkles the flow inside the grooves feels a strong retardation that ultimately results in this local re-circulating region. Eventually, as the frictional effects of the walls diffuse further outwards, the recirculating region ends and the fluid in the groove becomes almost stagnant inside the grooves. This stagnant fluid acts like a "cushion" of fluid on which the fluid outside of the grooves can slide. Similar behaviour is observed for cases with higher Reynolds numbers and longer lengths (achieved by changing the inlet velocity and the length of the plate). For example, for riblets of AR $= 1.91$ with global Reynolds number of $\text{Re}_L = 120600$ and $L/\lambda = 95.5$, velocity profiles in the trough are presented in Figure 3-9 and as it can be seen the re-circulation starts at a later position (i.e. a higher
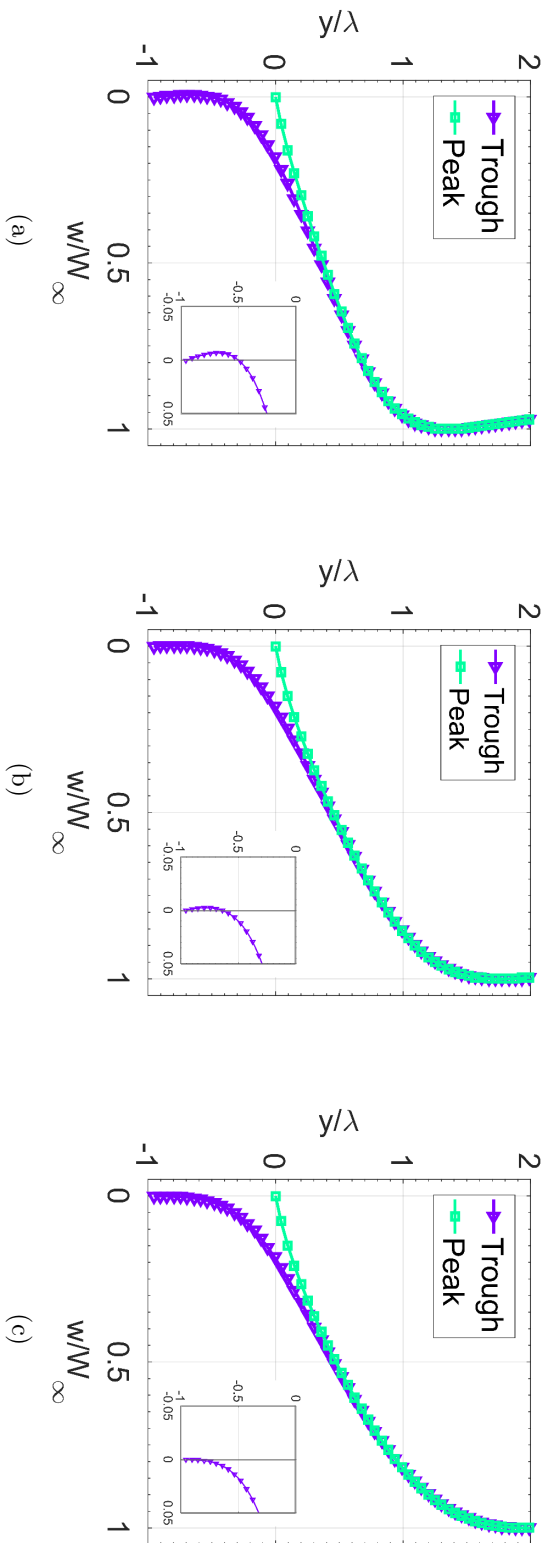
Figure 3-8: Normalized velocity profiles at peak and trough at different locations (a)$\mathrm{Re}_z = 4000$, $z/\lambda = 14.32$, (b)$\mathrm{Re}_z = 8000$, $z/\lambda = 28.65$ and (c)$\mathrm{Re}_z = 12000$, $z/\lambda = 42.97$ along the flow direction for a riblet surface with AR = 1.91 and $L/\lambda = 47.75$.

local Re_z) and it extends to a larger distance downstream.

However, the aspect ratio AR of the wrinkles also has an effect on whether a re-circulating region is created or not. The progression of local velocity profiles for a wrinkled texture with global Reynolds number $\text{Re}_L = 13300$ and $L/\lambda = 47.75$ with a lower aspect ratio of AR $= 0.95$ (compared to AR $= 1.91$ in Figure 3-7) is presented in Figure 3-10. Again one can see flow retardation inside the grooves with a stagnant layer of fluid and a bounding stagnation line, shown with a green line with triangular symbols. However for this shallower riblet geometry the minimum velocity is zero and located at the wall (shown by red line with circular symbols) and thus no re-circulation develops in the groove ($y < 0$).

This local re-circulation in the grooves can also be identified by using other vortex identification methods such as the scalar measure Q defined as [101]

$$Q = \boldsymbol{\Omega} : \boldsymbol{\Omega} - \boldsymbol{S} : \boldsymbol{S}. \tag{3.4}$$

This measure based on the the second invariant of the velocity gradient tensor, compares the rotation rate in the fluid (the anti-symmetric part of the velocity gradient tensor $\boldsymbol{\Omega} = \frac{1}{2}(\nabla\boldsymbol{u} - \nabla\boldsymbol{u}^T)$) with the irrotational straining (symmetric part of the velocity gradient tensor $\boldsymbol{S} = \frac{1}{2}(\nabla\boldsymbol{u} + \nabla\boldsymbol{u}^T)$)) in the fluid [101]. For example for $\text{Re}_L = 13300$ and $L/\lambda = 47.75$ the iso-Q surfaces of $Q = 1206.5 < \omega_{z,\text{w}} >^2$ are shown in Figure 3-11 where ω_z is the z component of the vorticity vector and $< \omega_{z,\text{w}} >$ is the magnitude of the mean z component of vorticity evaluated at the wall. The observed vortical structures develop in the same region within the grooves as the local flow re-circulation that was observed in Figure 3-7.

Close to the leading edge of the plate, the effects of stream-wise pressure gradients are not negligible and this results in velocity profiles with a higher maximum velocity than the bulk fluid velocity W_{in} at the inlet [41, 102]. To evaluate the effects of this local acceleration near the leading edge, the stream-wise pressure distribution above one of the troughs ($x = \lambda/2$) at $y = 0$ is shown in Figure 3-12. Figure 3-12(a) shows the dimensionless pressure distribution p^* (scaled as $p^* = p/\frac{1}{2}\rho W_\infty^2$) as a function
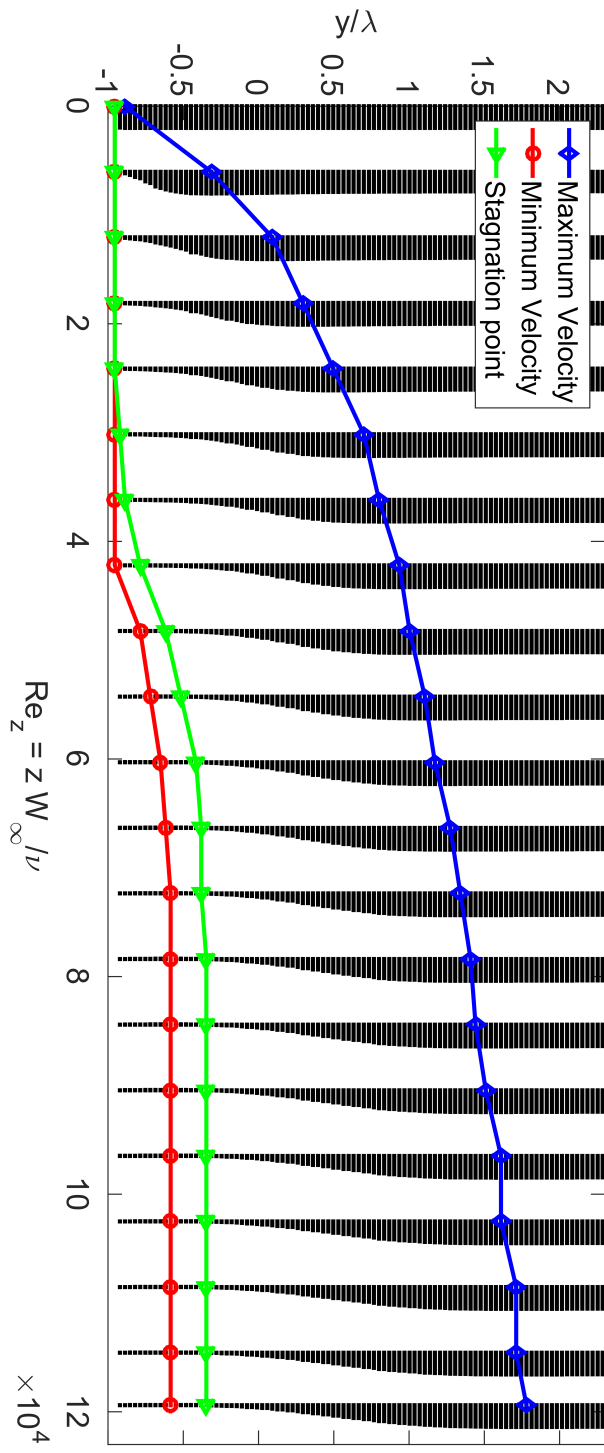
Figure 3-9: Normalized velocity profiles along the flow direction in the trough of a wrinkle for $Re_L = 120600$, $L/\lambda = 95.5$ and $AR = 1.91$.
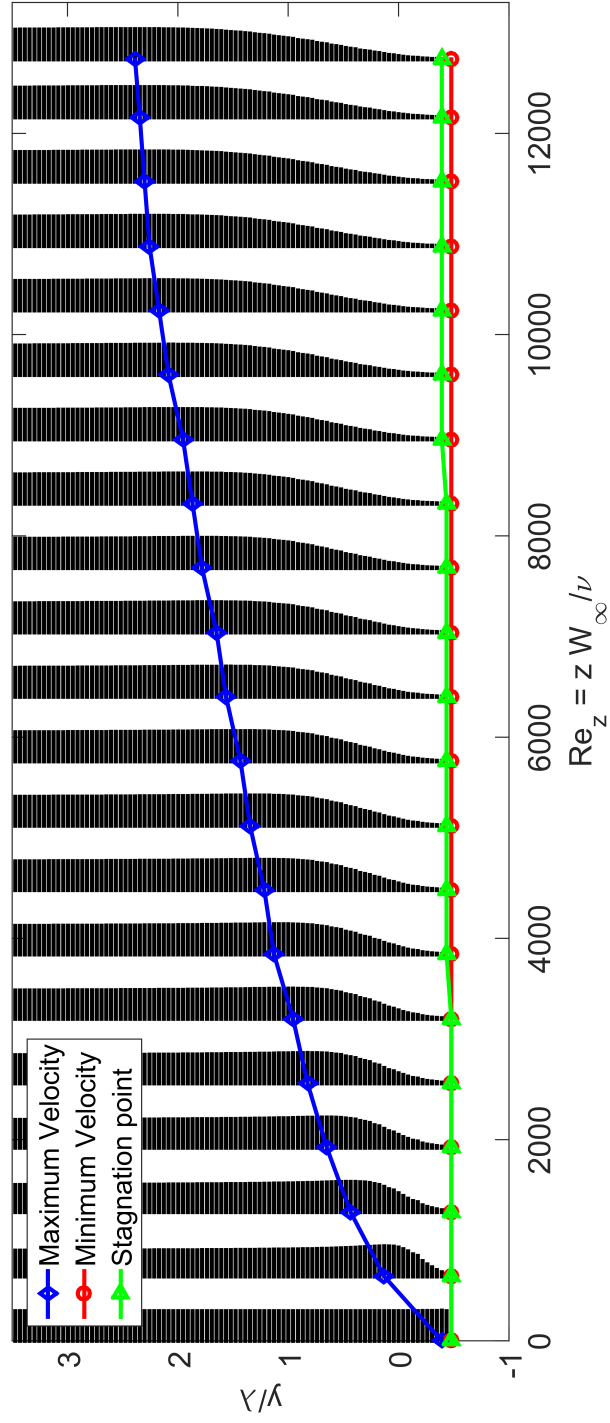
Figure 3-10: Normalized velocity profiles along the flow direction in the trough of a wrinkle for $\text{Re}_L = 13300$, $L/\lambda = 47.75$ and $AR = 0.95$.
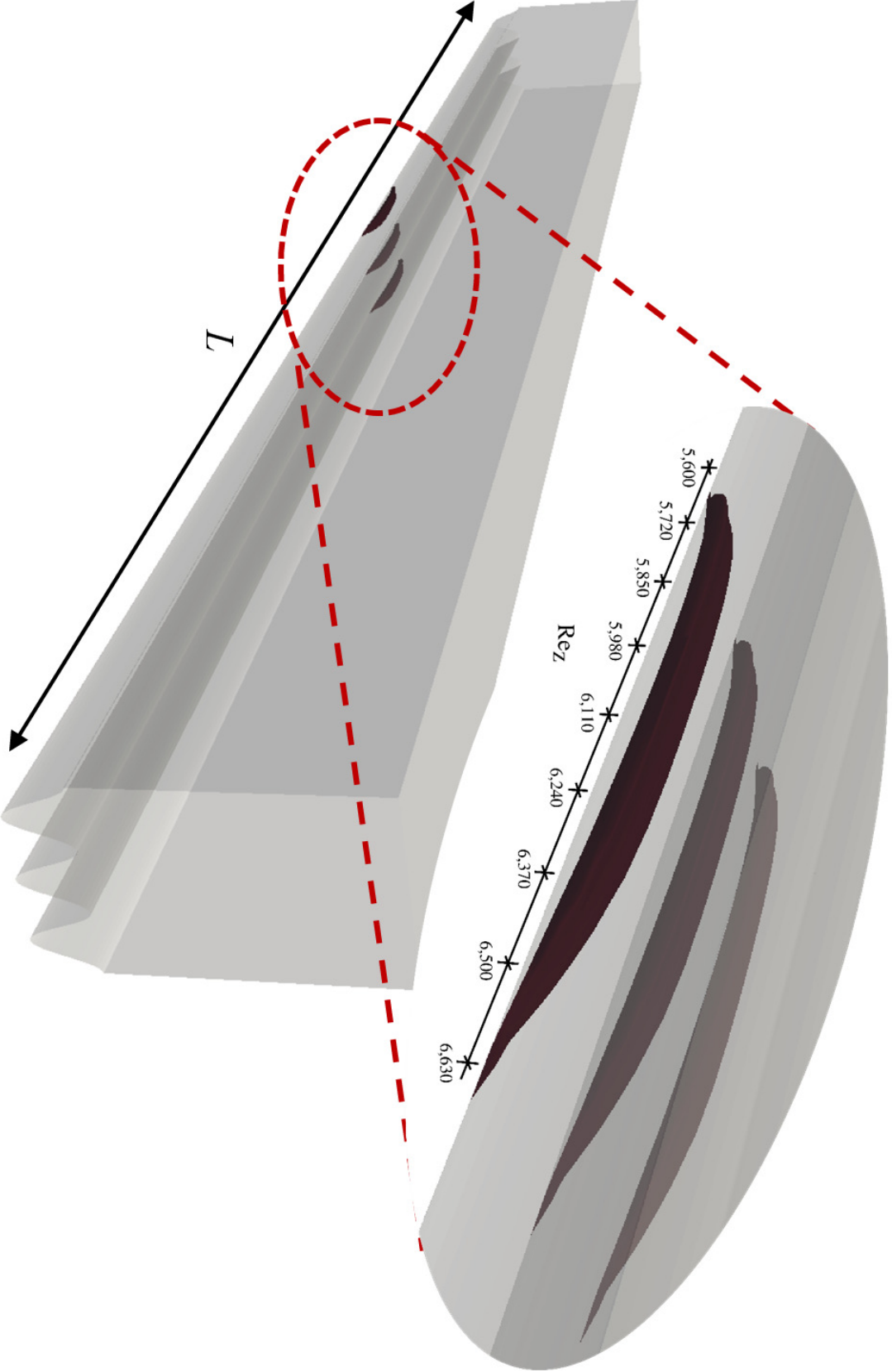
Figure 3-11: Vortical structures in the grooves of a wrinkled surface for $Re_L = 13300$, $L/\lambda = 47.75$ and AR = 1.91 revealed by an iso-Q surface with $Q = 1206.5 < \omega_{z,w} >^2$; As seen in the figure the vortical structures are located in the middle of the re-circulating region identified in Figure 3-7.

138

of the local position along the plate (or local Reynolds number, Re_z) for a series of different aspect ratio wrinkles, keeping the inlet velocity constant. As seen in the figure, close to the leading edge a favourable pressure gradient (pressure decrease) is observed. However at an intermediate location along the plate this turns into an adverse pressure gradient (local stream-wise pressure increase) and ultimately the pressure increases to an asymptotic value of zero (set by the exit boundary condition).

In the case of the boundary layer over a flat plate ($\text{AR} = 0$), the changes in pressure disappear after $\text{Re}_z \approx 15000$, and from there onwards, the classical flat plate boundary layer approximation of $\frac{\partial P}{\partial z} \approx 0$ is a valid assumption to simplify the equations of motion. However, in the presence of the riblets, the region of favourable pressure gradient is extended and the pressure decreases to progressively lower values as the riblet aspect ratio increases. This results in the need for a larger pressure recovery in the adverse pressure gradient region, and this contributes to the establishment of local flow re-circulation. Comparing the case of $\text{AR} = 1.91$ from Figures 3-12(a) and 3-7 one can observe that the location of the minimum pressure is consistent with the location of the start of the re-circulation inside the grooves. In addition the local region corresponding to the adverse pressure gradient ($\frac{\partial P}{\partial z} > 0$) corresponds to the entire recirculating region inside grooves. As the pressure gradient driving this re-circulating flow slowly decays away down the plate, a cushion of stagnant fluid is formed, which can be observed in the grooves in Figure 3-7. The computations in Figure 3-12(a) for different aspect ratios show that the pressure distribution in case of riblets with $\text{AR} \leq 0.95$ is only slightly different from $\text{AR} = 0$ (flat) case and thus results in only a very thin stagnant cushion of fluid. For this configuration this textured plate does not exhibit any re-circulation in the grooves (cf. Figure 3-9). However, for aspect ratios of $\text{AR} \gtrsim 0.95$ the magnitude of the local adverse pressure gradient is notably enhanced and the recirculating region shown in Figures 3-7 and 3-9 develops.

The evolution of similar pressure distribution can be calculated for the case of $\text{AR} = 1.91$ and $L/\lambda = 95.5$, and different global Reynolds numbers of 2.5×10^4, 5.1×10^4 and 2.5×10^5 (by changing the inlet velocity) and are presented as a function
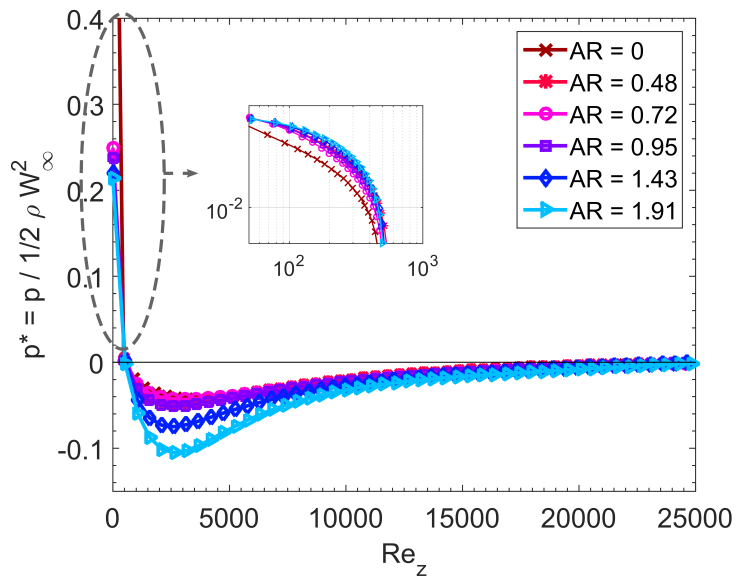
(a)
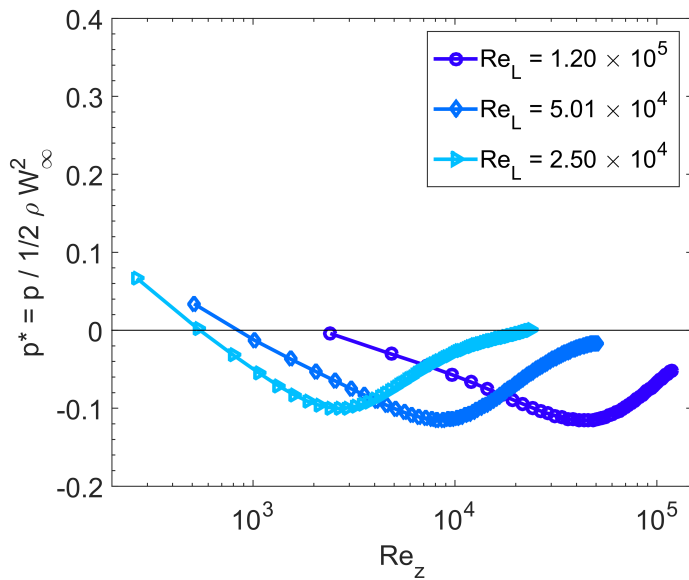
(b)

Figure 3-12: (a) Stream-wise pressure distribution at $x = \lambda/2$ and $y = 0$ (above a trough) as a function of the local Reynolds number down the plate for different aspect ratio riblets, keeping the inlet velocity constant ($\mathrm{Re}_L = 25000$ and $L/\lambda = 95.5$). Inset shows additional details for small values of $\mathrm{Re}_z < 10^3$ on a logarithmic scale. (b) Pressure distribution along the direction of flow on top of a groove at $y = 0$ for various inlet velocities (and different global Reynolds numbers) and $L/\lambda = 95.5$.

140

of the position or local Reynolds number in Figure 3-12(b). Comparing the three cases shows that the location of the minimum pressure (which coincides with the start of the recirculating region in the case of AR = 1.91) evolves with changes in the inlet velocity while the magnitude of the minimum dimensionless pressure stays nearly constant. I denote the location of the minimum pressure as L_c and seek to find a scaling for L_c as the flow geometry changes. Since the flow in the boundary layer close to the leading edge is quasi-steady and inertial pressure effects balance viscous stresses one expects that the pressure drop is of the same order as the divergence of the shear stress tensor in the z direction inside the grooves. A scaling estimate for the pressure gradient in this region gives

$$\frac{\partial p}{\partial z} \sim \frac{\rho W_\infty^2}{L_c} \tag{3.5}$$

and the divergence of the shear stress tensor in the z direction for the viscous flow inside the grooves (with characteristic groove length scale λ) can be expressed as

$$(\nabla . \boldsymbol{\tau})_z \sim \frac{1}{\lambda}\left(\frac{\mu W_\infty}{\lambda}\right). \tag{3.6}$$

Therefore for the pressure gradient to balance with the shear stress gradient inside the grooves, it requires

$$\frac{\partial p}{\partial z} \sim (\nabla . \boldsymbol{\tau})_z \tag{3.7}$$

$$\frac{\rho W_\infty^2}{L_c} \sim \frac{1}{\lambda}\left(\frac{\mu W_\infty}{\lambda}\right) \tag{3.8}$$

$$L_c \sim \frac{\rho W_\infty \lambda^2}{\mu} \tag{3.9}$$

or in dimensionless form

$$\frac{L_c}{\lambda} \sim \frac{\rho W_\infty \lambda}{\mu} = \mathrm{Re}_\lambda. \tag{3.10}$$

Therefore, the location of the minimum pressure along the plate is expected to

increase linearly with increases in the inlet velocity. Figure 3-13 shows the calculated location of the minimum pressure for cases with inlet velocities $0.5 \leq W_{in} \leq 7$ m/s (and calculated maximum velocities of $0.6 \leq W_\infty \leq 8.2$ m/s, respectively) for wrinkles with AR = 1.91 plotted as a function of $\rho W_\infty \lambda / \mu$. It can be seen from the figure that the calculated location scales linearly with the Reynolds number based on the wrinkle length scale (λ) $Re_\lambda = \rho W_\infty \lambda / \mu$ as predicted using the scaling above. Additional computations indicate that keeping the inlet velocity constant and varying the wavelength at a constant aspect ratio of AR = 1.9 results in the same scaling as Equation 3.10 and in Figure 3-13.
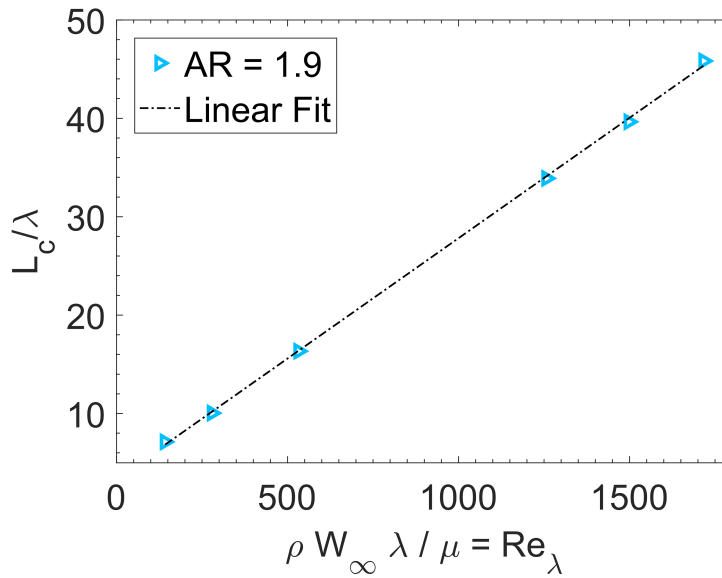
Figure 3-13: Location of the minimum pressure for flow over textured surfaces with various inlet velocities $0.5 \leq W_{in} \leq 7$ m/s and the calculated maximum velocities of $0.6 \leq W_\infty \leq 8.2$ for AR = 1.91.

A principal goal of the present study is to investigate the source of friction reduction arising from variations in the texture of the surface. The local shear stress acting on the surface is directly proportional to the velocity gradient at the wall. Furthermore, as was seen earlier, the presence of the wrinkled topography provides a method to alter the curvature of the velocity profiles near the plate, especially inside the grooves, thus resulting in lower velocity gradients at the walls (for example, compare the peak and trough profiles in Figures 3-8). This results in a lower local

142

wall shear stress inside the grooves compared with an equivalent flat plate and thus can result in a net reduction in the local average shear stress. This is especially seen in the recirculating region and stagnant areas where there is a cushion of almost stationary fluid. In these regions the velocity gradient is small or close to zero (as seen in Figure 3-7). However, conversely, the total surface area of a grooved or ridged surface over which the shear stress is acting increases with the ridge scales and this can potentially offset or even overwhelm the local friction reduction. I therefore now proceed to carefully evaluate each contribution to the total skin friction on a wrinkled surface.

3.5.2   Boundary Layer Thickness and Velocity Decomposition

I have shown qualitatively in Figures 3-6 and 3-7, 3-9 and 3-10, that the presence of stream-wise sinusoidal riblets along the surface increases the overall thickness of the boundary layer. To quantify this, I need to develop an appropriate definition of the boundary layer thickness for flow over riblet surfaces. To do this I generalize the definition of displacement thickness for a two dimensional flat plate boundary layer to the integral form shown below [41, 65]

$$\frac{\Delta^*}{z\ \alpha\lambda} = \frac{1}{z\ \alpha\lambda} \int_S \left(1 - \frac{w}{W_\infty}\right) dS \tag{3.11}$$

where Δ^* is now a *displacement area*, α is the number of wrinkles modelled in the simulation, z is the local stream-wise location and S is the cross sectional area of the flow in the $x - y$ plane. This expression for $\Delta^*(z)$ is defined locally but the equation can be extended to a global definition by replacing the position z with the total plate length L. The boundary layer thickness for a flat plate (AR = 0) and three different wrinkle textures of AR = 0.48, AR = 0.95, and AR = 1.91 are calculated for cases with various inlet velocities and a fixed $L/\lambda = 47.75$ and plotted on double logarithmic axes versus the global Reynolds number $\mathrm{Re}_L = \rho W_\infty L/\mu$ in Figure 3-14. From the figure, it is clearly seen that increasing the aspect ratio of the riblets (AR) results in an increase in the thickness of the boundary layer, as expected from the

velocity contours shown in Figures 3-6 and 3-7.

At higher Reynolds numbers $\mathrm{Re}_L > 10^4$ when the initial pressure gradient is negligible, the flat plate results extracted from the computations follow the $\mathrm{Re}_L^{-0.5}$ scaling as calculated by Blasius. However, for lower Reynolds numbers, where the effects of the initial pressure gradient are non-negligible along the entire length of the plate, the data follows the scaling found from the higher order boundary layer theory results presented by van de Vooren and Dijkstra [103], which can be fitted to a power law proportional to $\mathrm{Re}_L^{-0.44}$.
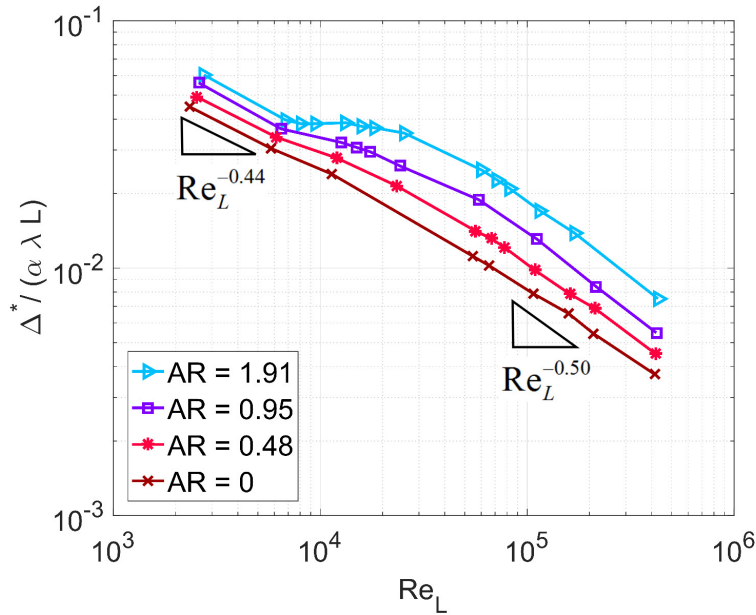
Figure 3-14:   Boundary layer thickness for different Re_L and different wrinkle aspect ratios; in all cases $L/\lambda = 47.75$ and for each profile the change in the Reynolds number is due to systematically changing the inlet velocity W_{in} which results in changes of the calculated maximum velocity W_∞.

In addition to the displacement area, a momentum area (the equivalent of the classical momentum thickness for a boundary layer that now varies in both x and y) can be calculated using the following expression [41, 65]

$$\frac{\Theta}{z\,\alpha\lambda} = \frac{1}{z\,\alpha\lambda} \int_S \frac{w}{W_\infty}\left(1 - \frac{w}{W_\infty}\right) dS. \tag{3.12}$$

Similar to displacement area, the above definition is local and it can be extended to

a global definition by replacing the position z with the length of the plate L.

Keeping the inlet velocity constant, the variation of the displacement area (Δ^*) and momentum area (Θ) locally along the flow direction (z) are plotted in Figure 3-15 for wrinkles with various aspect ratios, showing an increase in the local displacement area of the boundary layer as AR increases. For all wrinkled cases studied this value is larger than for a flat plate with AR = 0 but the results slowly converge as Re_z increases beyond 10^4. This provides a clear indication that the effects of the wrinkled texture on the boundary layer size decay away as the flow progresses along the plate. In the case of the momentum area, again the local value of the momentum area for wrinkled walls is always larger than the flat wall, but as Re_z increases beyond 10^4, the data once again converges to the flat plate results.

The shape factor $H = \Delta^*/\Theta$, is used frequently in aerodynamics as an indicator of boundary layer separation and re-circulation [41, 104, 65]. For flow over a flat plate in the laminar regime, $H < 2.65$ and at higher Reynolds numbers it reaches the value of $H = 2.65$ as given by the Blasius solution. The shape factor of the evolving boundary layer profiles along the length of the plates are shown in Figure 3-16 for wrinkles with different aspect ratios as a function of the local Reynolds number Re_z (corresponding to Figure 3-15). The introduction of stream-wise wrinkles results in an increase in the local shape factor of the viscous boundary layer and as the aspect ratio of the wrinkles progressively increases the shape factor H increases. This indicates a retardation in the local velocity close to the wall compared with the flat wall ($H < 4$) [65], but no re-circulation for $0 < AR < 1.5$. For the case with the highest aspect ratio (AR = 1.91), the shape factor reaches a peak value of $H = 4.5$ at $Re_z \sim 4000$ and then as the flow progresses along the plate H monotonically decays to a nearly constant value. The region with local Reynolds number of $3000 \leqslant Re_z \leqslant 8000$ where the shape factor goes through an increase and then a decrease corresponds to the re-circulation region documented earlier in Figure 3-7. At distances further down the plate the amplified value of the shape factor ($H > 2.65$) is a quantitative indication of fluid flowing over a cushion of stagnant fluid.

It is of interest to understand the differences between the calculated velocity pro-

145

(a)

(b)
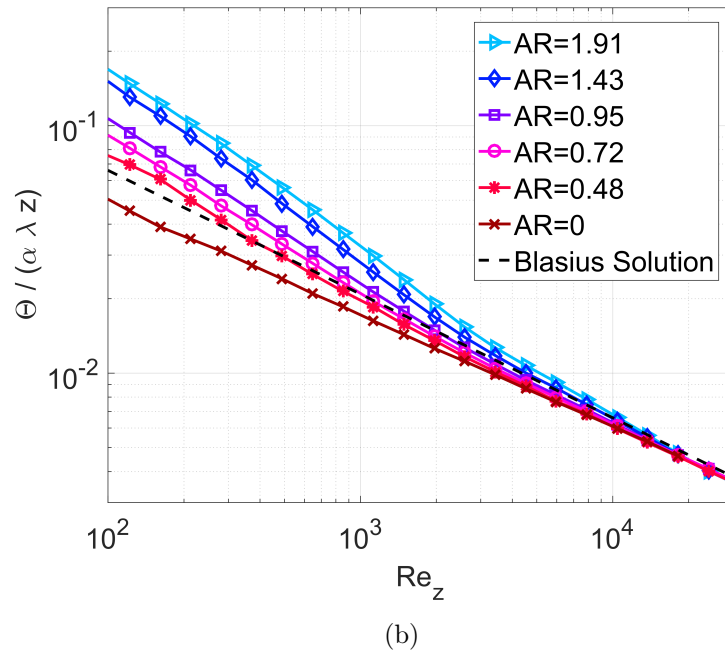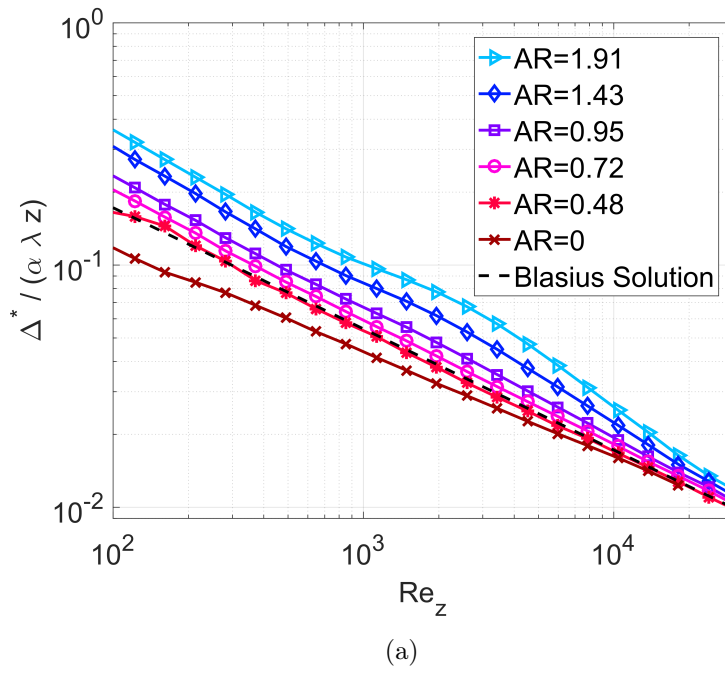
Figure 3-15: Evolution of (a) the local displacement area (Δ^*) and (b) the local momentum area (Θ) along the plate (plotted in the form of a local Reynolds number Re_z) for wrinkles with different aspect ratios $0 < \mathrm{AR} < 2$ keeping the length ($L/\lambda = 191$) and inlet velocity constant $W_{\mathrm{in}} = 1$ m/s. For these conditions, calculations for a flat plate (AR $= 0$) give $W_\infty = 1.33$ m/s.
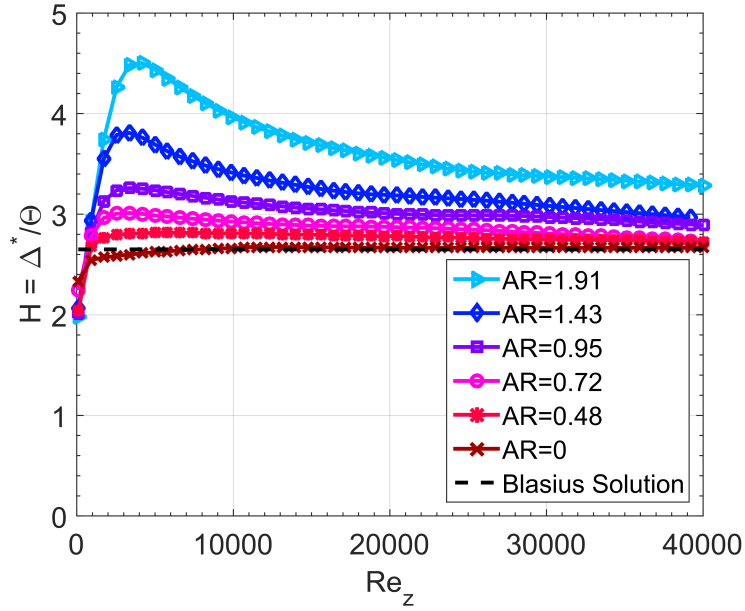
Figure 3-16: Shape factor ($H = \Delta^*/\Theta$) of the velocity profile in a viscous boundary layer for different aspect ratio wrinkles corresponding to Figure 3-15.

files obtained for flow over wrinkled surfaces with different aspect ratios and the corresponding Blasius solution for the flat plate at every location of the riblet cross section. As seen earlier, far from the surface of the riblets, the velocity profiles at different cross sectional locations collapse onto the same profile and behave similarly to the Blasius solution (Figure 3-4). Additionally, as one moves further down the plate, the effects of the riblets on the velocity profile are confined to the creation of a cushion of stagnant fluid inside the grooves and are barely noticeable outside the grooves. In order to examine the difference between the classical two dimensional boundary layer and the current computations, the velocity contours at each cross section are decomposed into two additive contributions; the first contribution assumes the flat plate boundary layer solution of Blasius holds at every location in the cross section and is here denoted by $w_{\text{BL}}(x,y)$. The second contribution is obtained from the difference between the actual velocity profile $w(x,y)$ and the flat plate boundary layer solution at every cross sectional location, denoted by $\Delta w(x,y) = w(x,y) - w_{\text{BL}}(x,y)$; therefore:

$$\frac{w(x,y)}{W_\infty} = \frac{w_{\mathrm{BL}}(x,y)}{W_\infty} + \frac{\Delta w(x,y)}{W_\infty}. \tag{3.13}$$

The velocity gradient and the shear stress (proportional to the velocity gradient at the wall or $n = 0$) can thus also be decomposed into two parts:

$$\frac{\partial w}{\partial n} = \frac{\partial w_{\mathrm{BL}}}{\partial n} + \frac{\partial \Delta w}{\partial n} \quad \rightarrow \quad \tau = \tau_{\mathrm{BL}} + \mu \frac{\partial \Delta w}{\partial n} \tag{3.14}$$

where τ_{BL} is the wall shear stress on the wrinkled wall, assuming the flat plate boundary layer solution holds at every location. This decomposition can be used to understand the increase or reduction in the local shear stress due to the periodic texture of the wall and illustrative examples of this decomposition are presented in Figures 3-17, 3-18 and 3-19. If the flat plate solution was the solution everywhere to the velocity field (w_{BL}), then the gradient of the velocity field normal to the wall (n) evaluated at the wall $(n = 0$ or $y = y_\mathrm{s})$ could be found from the expression

$$\left.\frac{\partial w_{\mathrm{BL}}}{\partial n}\right|_{n=0} = \sqrt{1 + \left(\frac{\pi A}{\lambda}\sin\left(\frac{2\pi}{\lambda}x\right)\right)^2}\ \left.\frac{\partial w_{\mathrm{BL,f}}}{\partial y}\right|_{y=y_\mathrm{s}} \tag{3.15}$$

where $w_{\mathrm{BL,f}}$ is the Blasius solution on the flat plate. The shear stress at the wall is defined as $\tau = \mu\ \partial w/\partial n|_{n=0}$, thus

$$\tau_{\mathrm{BL}} = \sqrt{1 + \left(\frac{\pi A}{\lambda}\sin\left(\frac{2\pi}{\lambda}x\right)\right)^2}\ \tau_{\mathrm{BL,f}} \tag{3.16}$$

where $\tau_{\mathrm{BL,f}}$ is the wall shear stress for the flat wall as calculated by the Blasius solution. Since the first trigonometric term in the expression in Equation 3.16 is always larger than or equal to unity, the shear stress at the wall of a textured surface (in this case a sinusoidally wrinkled surface) would be higher than that of the flat plate if the Blasius solution were to hold everywhere for flow over a riblet surfaces $(\tau_{\mathrm{BL}} > \tau_{\mathrm{BL,f}})$. Therefore, any local decrease in the shear stress on the wrinkled plate (compared with the flat plate) will be dependent on the sign of the last term in Equation 3.14. This decomposition can be used to explain how wrinkle size affects changes in the viscous shear stress compared to the stress distribution above a flat plate at the same local
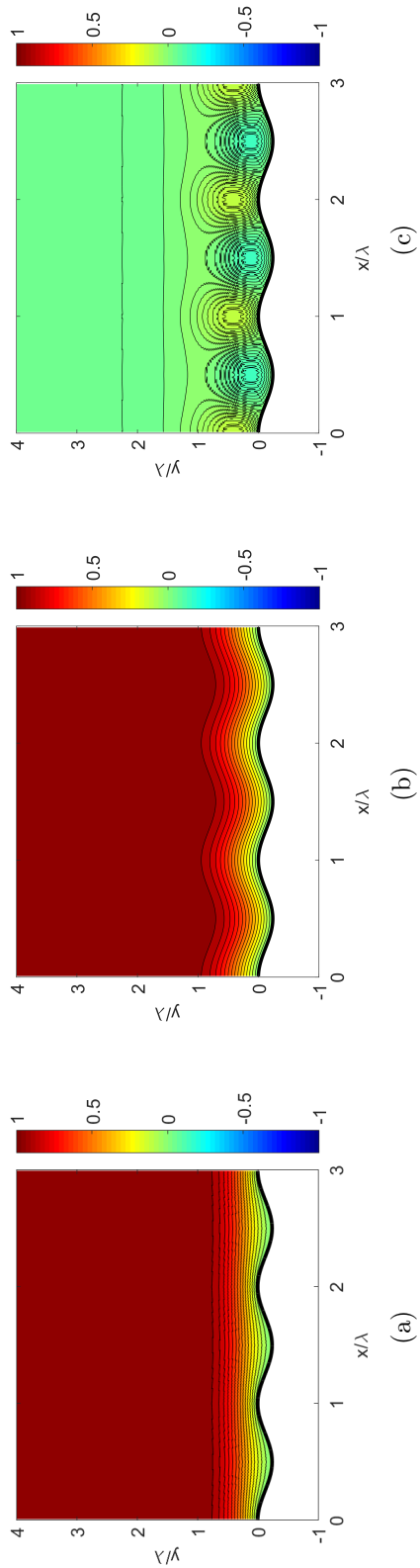
Figure 3-17: Decomposition of the full computed velocity profile (w/W_∞) shown in (a) into two pieces; the first one shown in (b) is based on the flat plate boundary layer w_{BL}/W_∞ plus a velocity defect ($\Delta w/W_\infty$) shown in (c). Figures above shown for $\mathrm{Re}_z = 4000$ and $z/\lambda = 14.32$ with AR $= 0.48$.
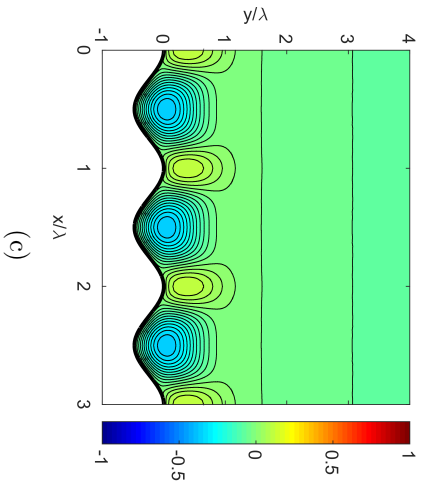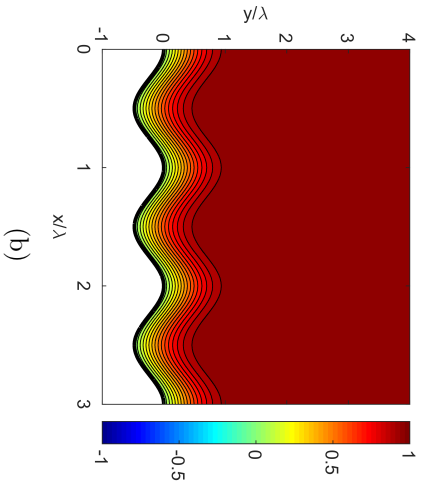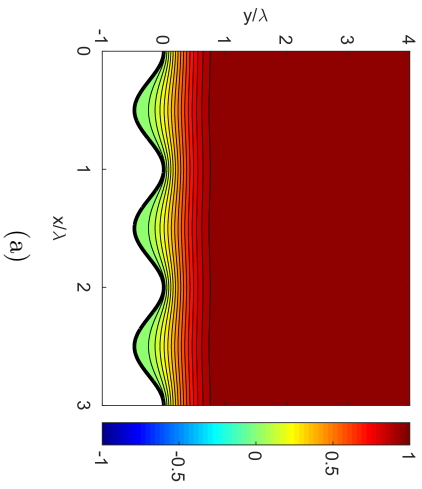
Figure 3-18: Decomposition of the full computed velocity profile (w/W_∞) shown in (a) into two pieces; the first one shown in (b) is based on the flat plate boundary layer $w_{\mathrm{BL}}/\mathrm{W}_\infty$ plus a velocity defect ($\Delta w/\mathrm{W}_\infty$) shown in (c). Figures above are for $\mathrm{Re}_z = 4000$ and $z/\lambda = 14.32$ with AR $= 0.95$.
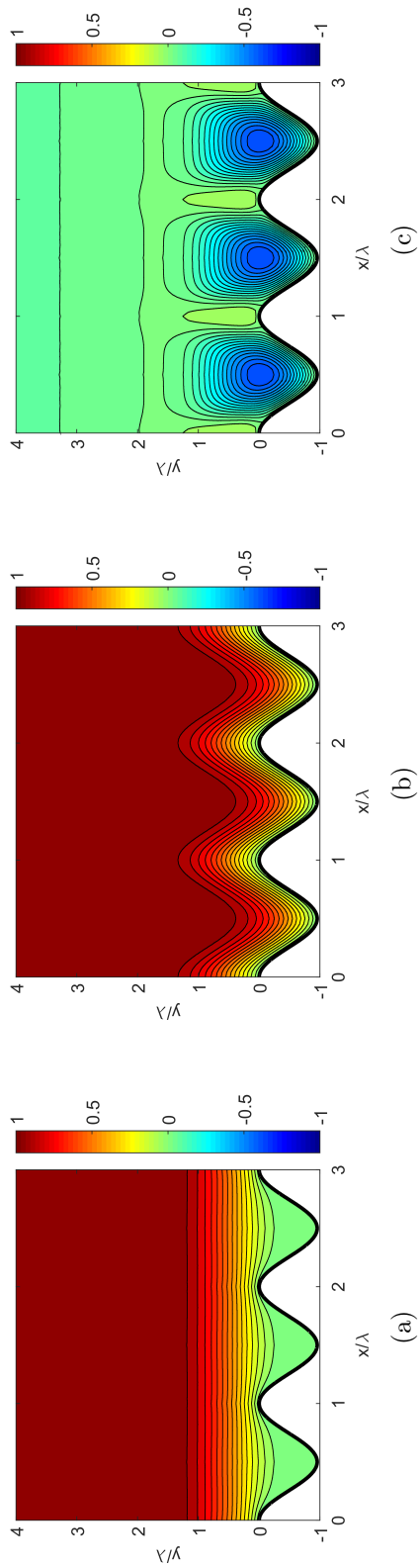
Figure 3-19: Decomposition of the full computed velocity profile (w/W_∞) shown in (a) into two pieces; the first one shown in (b) is based on the flat plate boundary layer w_{BL}/W_∞ plus a velocity defect ($\Delta w/W_\infty$) shown in (c). Figures above are for $Re_z = 4000$ and $z/\lambda = 14.32$ with AR = 1.91.

Reynolds number Re_z. For example the cross sectional velocity contours for three different wrinkle sizes (AR = 0.48, AR = 0.95, and AR = 1.91) with $\mathrm{Re}_z = 4000$ and $z/\lambda = 14.32$ are shown in Figures 3-17, 3-18 and 3-19. In each case the wrinkles have the same wavelength while only the amplitude of the wrinkles is changed. In all the figures, the y direction is normalized with the constant wavelength (λ) of the wrinkle.

The most prominent differences between the actual velocity profiles shown in Figures 3-17(a), 3-18(a) and 3-19(a) and the locally-shifted form of the Blasius solution w_{BL} (Figures 3-17(b), 3-18(b) and 3-19(b)) is inside the grooves where the velocity boundary layer is thicker and the flow is almost stagnant close to the wall (as was also demonstrated earlier). Therefore, the velocity defect Δw (shown in Figures 3-17(c), 3-18(c) and 3-19(c)) shows non-zero and negative values which results in a lower velocity gradient in the grooves compared with $\partial w_{\mathrm{BL}}/\partial n|_{n=0}$ inside the grooves. Another region of difference is at the peak of the riblets. Here the difference is not as clearly discernible, but is clearly non-zero and yields positive values of the velocity defect Δw (with magnitudes lower than those observed inside the grooves). This results in a slightly higher velocity gradient at the peak of the riblets compared to $\partial w_{\mathrm{BL}}/\partial n$. The combination of these features results in a substantially lower local shear stress inside the grooves, plus a slightly higher shear stress at the peak of the riblets. Similar conclusions have been reported previously (through DNS results as well as experiments) indicating that the velocity gradients, and thus local shear stress, observed at the peaks and troughs of riblet structures are higher and lower respectively than the results for the flat plate [25, 70, 47].

Based on Equation 3.16 an increase in the aspect ratio (AR $= 2A/\lambda$) of the wrinkles would result in an increase in the wall shear stress calculated by using just the Blasius solution for the riblets (τ_{BL}) without correction. However when examining the actual velocity defect structure in Figures 3-18(c), 3-17(c), and 3-19(c) one sees a stronger negative velocity gradient inside the grooves which, from Equation 3.14, can result in a reduction in the net local shear stress evaluated at each cross section along the plate.

3.5.3   Wall Shear Stress and Drag

Finally, I investigate the ability of the riblets to reduce the total drag force exerted on the wall. To do this I evaluate the average skin friction coefficient C_f (Figure 3-20(a)) and the total integrated drag force D (Figure 3-20(b)) with respect to the flat surface. I consider cases with different aspect ratios $(0 < \text{AR} < 2)$ and constant $L/\lambda = 47.75$, as a function of the global Reynolds number Re_L (by using different inlet velocities W_{in} and computing the maximum calculated velocity W_∞) for each case. If the stress tensor at the wall and local wall normal vector evaluated at a position $x_{\text{s}}, y_{\text{s}}$ on the riblet surface are defined as $\boldsymbol{\tau}_{\text{w}}(x_{\text{s}}, y_{\text{s}}; z)$ and $\boldsymbol{n}_{\text{w}}(x_{\text{s}}, y_{\text{s}}; z)$ respectively (where $y_{\text{s}} = -\frac{A}{2} + \frac{A}{2}\cos(\frac{2\pi}{\lambda}x_{\text{s}})$), then the total drag force on a plate of length L and the average skin friction coefficient are defined as

$$D = \int_0^L [\ \boldsymbol{\tau}_{\text{w}}(x_{\text{s}}, y_{\text{s}}; z).\boldsymbol{n}_{\text{w}}(x_{\text{s}}, y_{\text{s}}; z)\ ].\boldsymbol{e}_z\ dA_w \qquad (3.17)$$

and

$$C_f = \frac{D}{\frac{1}{2}\rho W_\infty^2\ A_{\text{w}}} \qquad (3.18)$$

respectively, where A_w is the wetted area of the riblet wall. A reduction in the skin friction coefficient is defined as $\Delta C_f = C_f - C_{f,0}$ where $C_{f,0}$ is the skin friction coefficient of a flat plate and the reduction in total drag is defined as $\Delta D = D - D_0$ where D_0 is the total drag on the flat surface. Note that negative values in both plots correspond to skin friction coefficient reduction and drag reduction respectively. The results in Figure 3-20 show that the presence of the riblets reduces the average skin friction coefficient on the wall in nearly all of the riblet cases considered. At the same value of the global Reynolds number (Re_L) increasing the aspect ratio (AR) results in a progressively larger decrease in the average skin friction coefficient. This also confirms the observations based on consideration of the velocity decomposition that the negative velocity defect observed inside the grooves (Figures 3-17(c), 3-18(c) and 3-19(c)) results in a reduction in the average shear stress compared to the flat plate. As the aspect ratio of the wrinkles increases, the increase in the magnitude of the negative velocity defect $\Delta w < 0$ results in a higher reduction in the average skin

friction coefficient.
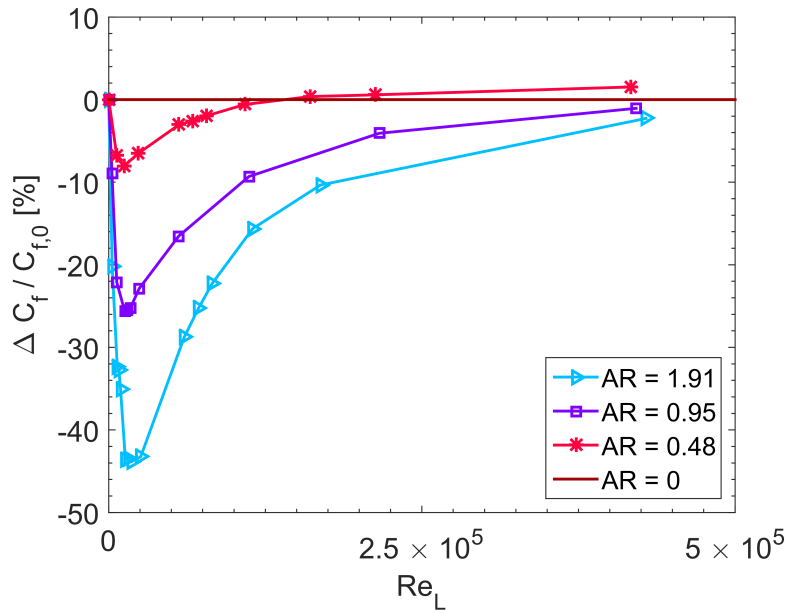
(a)
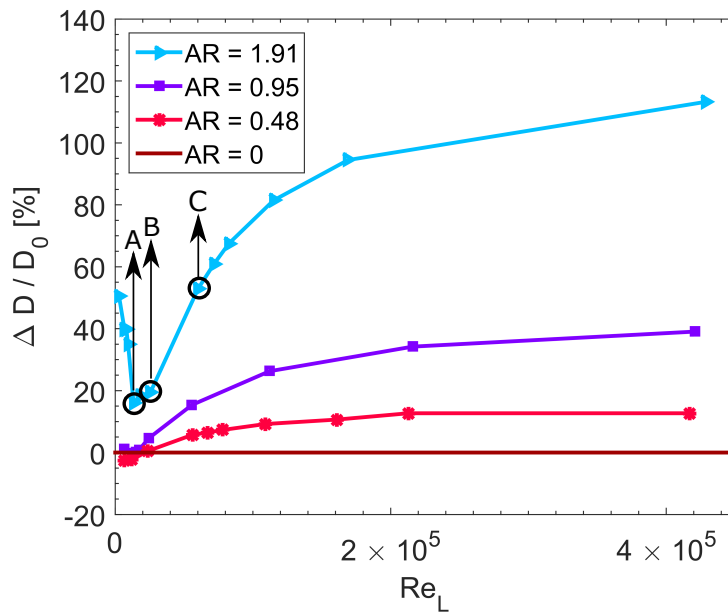
(b)

Figure 3-20: Reduction in (a) the skin friction coefficient (C_f) and (b) changes in the total drag (D) for wrinkles of different aspect ratios, fixed plate length $L/\lambda = 47.75$ and different Re_L (varying the inlet velocity). Points A, B and C correspond to the same points shown below in Figure 3-23.

154

However, reduction of the average skin friction coefficient alone cannot define whether a textured riblet surface is drag reducing or not because the total area of the wetted surface is also increased through the presence of the wrinkles. The total wetted surface area of the textured plate is larger than a flat surface and increases with AR; thus for a textured surface to be drag reducing the reduction in the skin friction coefficient due to the riblets must more than offset the increasing wetted area. For the results shown in Figure 3-20(b) at $L/\lambda = 47.75$ the only cases that appear to show a net drag reduction are the cases with aspect ratios of AR $= 0.48$ and AR $= 0.95$ and global Reynolds number of $\mathrm{Re}_L = 13300$. The rest of the cases show substantial increase in the total drag when compared to an equivalent flat surface.

To better understand these drag reducing cases and how changes in the length of the plate (Re_L) and aspect ratio (AR) interact to affect the total drag, I consider the following situations: I keep the inlet velocity constant (thus keeping W_∞ constant) and extend the calculations to plates of longer total lengths than those used in the computations presented in Figure 3-20. I consider a maximum plate length of $L/\lambda = 191$ and an inlet velocity of $W_{\mathrm{in}} = 1$ m/s (thus corresponding to a maximum global Reynolds number of $\mathrm{Re}_L = 5 \times 10^4$) for 5 different aspect ratios of $0 < \mathrm{AR} < 2$. The results are shown in Figure 3-21. I first consider the distribution of the wall shear stress on the wall as a function of different aspect ratios at different positions z along the length of the plate corresponding to different values of the local Reynolds number, Re_z. From steady two-dimensional boundary layer theory I know that the local shear stress on the wall decreases along the plate as $\tau_{\mathrm{BL}} \sim \mathrm{Re}_z^{-1/2}$ (Equation 3.3). For reference, I plot this result as the black dashed line in Figure 3-21(a). For a ribbed plate, the wall shear stress is now a function of lateral position $x_{\mathrm{s}}, y_{\mathrm{s}}$ on the surface as well as distance down the plate. I therefore define the dimensionless local average shear stress distribution at any distance z along the plate as

$$\tau^*(z) = \frac{1}{\frac{1}{2}\rho W_\infty^2} \frac{1}{\ell_{\mathrm{C}}} \int_{\mathrm{C}} \boldsymbol{\tau}_{\mathrm{w}}(x_{\mathrm{s}}, y_{\mathrm{s}}; z).\boldsymbol{n}_{\mathrm{w}}(x_{\mathrm{s}}, y_{\mathrm{s}}; z).\boldsymbol{e}_z \; d\ell \qquad (3.19)$$

where C is the riblet contour at each stream-wise cross section, ℓ_{C} is the total length

of the riblet contour ($\ell_{\mathrm{C}} = \int_{\mathrm{C}} d\ell$) and $d\ell$ is the line element along the rib transverse to the flow direction. In Figure 3-21(a) I show the evolution in the local average shear stress along the length of the plate for wrinkled cases with $0 < \mathrm{AR} < 2$ and plates with $\mathrm{Re}_L = 4 \times 10^4$ and $L/\lambda = 191$ compared with the shear stress on the flat plate. It is clear that the presence of the wrinkles changes the evolution in the shear stress distribution along the flow direction. As seen in this figure, close to the leading edge of the plate, the presence of wrinkles does not reduce the large initial shear stress that results from the sudden generation of vorticity at the leading edge. However as the local Reynolds number Re_z increases along the plate, the wrinkles retard the flow in the grooves and thus reduce the local average shear stress at the wall. The case of $\mathrm{AR} = 1.91$ shows a region with almost constant average shear stress between $5000 < \mathrm{Re}_z < 12000$ which also corresponds with the re-circulation region presented earlier in Figure 3-7. Smaller aspect ratios do not show any re-circulation and thus there is no region with constant shear stress distribution.

At lower local Reynolds numbers $\mathrm{Re}_z \leqslant 10^3$ (close to the leading edge), the local average shear stress for all the riblet cases is nearly the same as the shear stress distribution on the flat plate. However, as established above, increasing the aspect ratio of the riblets results in an increase in the wetted area and therefore this results in a substantial increase in the total drag for plates with $\mathrm{AR} > 0.48$ and global Reynolds numbers of $\mathrm{Re}_L < 8000$ (and nearly no change in the total drag for the case of $\mathrm{AR} = 0.48$). However, further down the plate, as the cushion of stagnant fluid starts to form inside the grooves, the reduction in the local shear stress can offset the increase in the wetted area and this results in a net reduction of the total drag.

As I show in Figure 3-21(b) it becomes clear that riblets have the potential of reducing drag provided the plate is *longer* than a minimum critical length $\mathrm{Re}_{L,\mathrm{c}}(\mathrm{AR})$ (which can be determined from where each of the curves cross the value of zero on the ordinate axis). Secondly, the sharpness of the riblets plays an important role in controlling the extent of total drag reduction achieved. Higher aspect ratio wrinkles provide greater local shear stress reduction but this is offset by the large increase in wetted area for very high aspect ratios. For the range of global Reynolds number Re_L
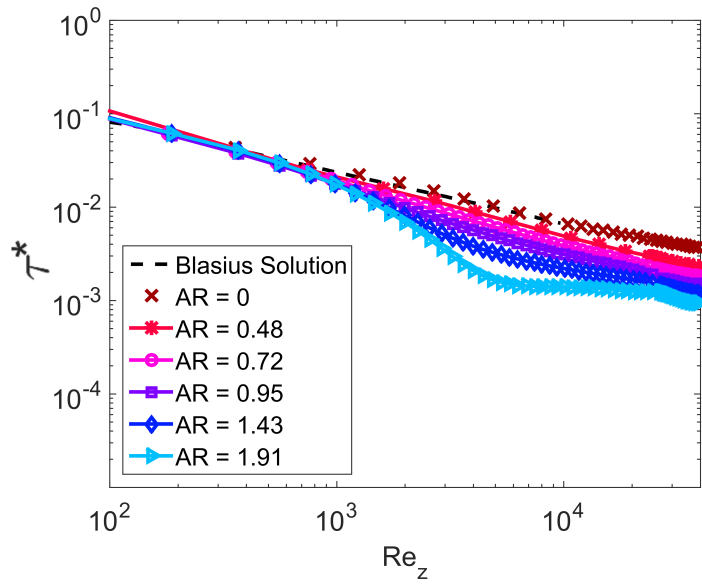
(a)
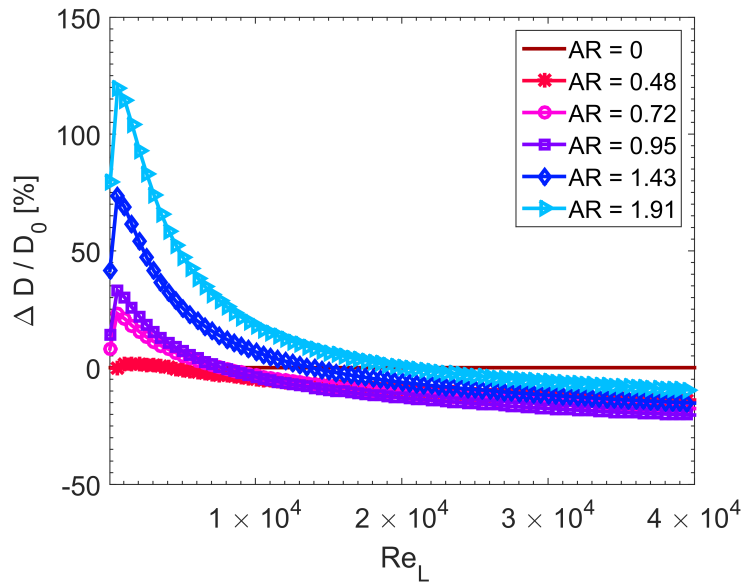
(b)

Figure 3-21: (a) Evolution of the local transverse average of dimensionless wall shear stress distribution (Equation 3.19) for the same inlet velocity and different aspect ratio riblets. (b) Increases ($\Delta D > 0$) and reductions ($\Delta D < 0$) in the total drag force (D) for wrinkled plates of different total length of the range $0 < L/\lambda < 191$ (increasing global Reynolds number Re_L) for various aspect ratio wrinkles $0 < \mathrm{AR} < 2$, keeping the wavelength λ constant.

studied, the case with AR $= 0.95$ was found to provide the highest reduction in the total drag. I can illustrate this most clearly by holding the global Reynolds number Re_L and riblet spacing L/λ constant and calculating the total drag reduction as a function of the aspect ratio of the riblets. I illustrate this in Figure 3-22 for three different values of Re_L showing that for each of the cases there is an optimum aspect ratio providing the largest possible drag reduction. Quite generally I find that the total frictional drag reduction (corresponding to $\Delta D/D_0 < 0$) at a constant global Reynolds number Re_L and L/λ is first enhanced as the aspect ratio of the wrinkles increases, then reaches an optimum and as the aspect ratio increases still further the extent of drag reduction decreases and eventually shifts to a net drag increase. For $\mathrm{Re}_L > 10^4$ the optimum aspect ratio is slightly less than unity, but after that the optimum aspect ratio is close to AR ≈ 1. Previous wind tunnel experiments by Walsh with V-groove riblets of AR $= 1$ and AR $= 2$ at constant free-stream velocity also show that riblets with AR $= 1$ result in a larger drag reduction compared to AR $= 2$ [37].

A similar trend as discussed above can be observed for the other data points presented in Figure 3-20(b) as the plate length is increased. To illustrate that, at a constant aspect ratio of AR $= 1.9$ (which did not show any drag reduction for the case of $L/\lambda = 47.75$) the evolution in the total drag force for plates of various lengths ($1 < L/\lambda < 191$) with different inlet velocities are presented in Figure 3-23. As I discussed in Section 3.5.1, changing the inlet velocity results in a change in the pressure distribution (Figure 3-12(b)) and thus alters the location of the minimum pressure inside the grooves (Figure 3-13). For short plates, the presence of the wrinkles leads to an overall increase in the frictional drag, but in each case a net drag reduction is observed when the length of the plate exceeds a critical value. However, due to the differences in the pressure distribution among the cases with different inlet velocities, the cross over from drag increase to drag decrease occurs at a longer plate length as the free-stream velocity (and thus Re_λ) is increased. Points A, B and C indicated on the figure correspond to the points A, B and C noted in Figure 3-20(b) ($\mathrm{Re}_L = 1 \times 10^4$, 2.4×10^4, and 5.9×10^4 respectively) where for a fixed plate length
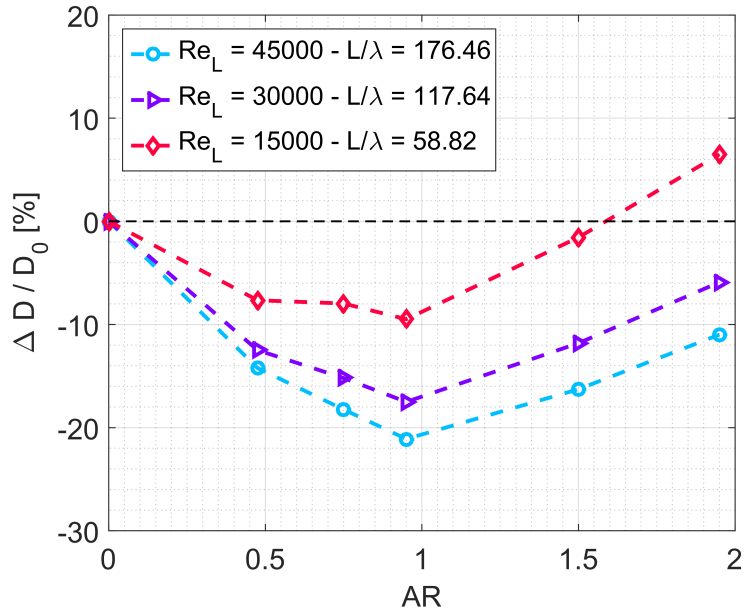
Figure 3-22: Drag reduction curve for plates with global Reynolds number of $\text{Re}_L = 15000$ and plate length $L/\lambda = 58.82$, global Reynolds number $\text{Re}_L = 30000$ and plate length $L/\lambda = 117.64$, and global Reynolds number $\text{Re}_L = 45000$ and plate length $L/\lambda = 176.46$ (same inlet velocity $W_{\text{in}} = 1$ m/s and the same wavelength $\lambda = 2\pi/3 \times 10^{-1}$ mm) as a function of the aspect ratio of the riblets.

of $L/\lambda = 47.75$ only a net drag increase was observed.

3.6   Conclusions

In this chapter I have examined in detail the effects of sinusoidal riblets on the spatial structure and evolution of a steady viscous boundary layer. The presence of the riblets results in a local flow retardation inside the valleys of the riblets and even the possibility of a local flow reversal. Riblets increase the average thickness of the boundary layer as well, resulting in an increase in the shape factor of the boundary layer. The presence of riblets also changes the pressure distribution close to the leading edge of the plate when compared with the flat boundary layer. This flow retardation creates a cushion of almost stagnant fluid inside the riblets upon which the fluid flowing above the plate can slide. This creates a non-uniform shear stress distribution laterally across the plate and a local average shear stress lower than the
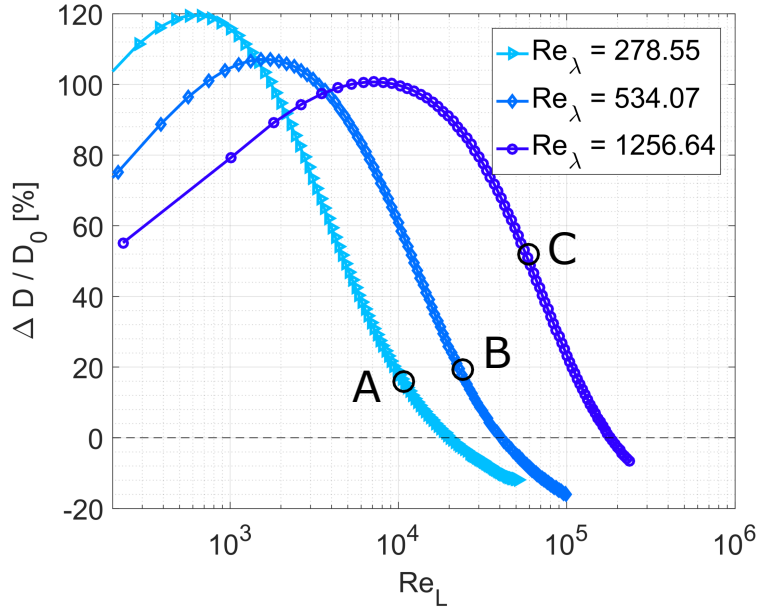
Figure 3-23: Reduction in total drag for wrinkled plates of different length Re_L, AR $= 1.9$ and inlet velocities of $W_{\mathrm{in}} = 1, 2$ and 5 m/s corresponding to $\mathrm{Re}_\lambda = 278.55$, 534.07 and 1256.64. Points A, B and C correspond to the same points in Figure 3-20(b).

corresponding flat plate. For sufficiently long plates, this can result in a reduction of the total viscous drag force acting on the surface compared with flat surfaces, provided the aspect ratio of the wrinkles is not so large that the increase in wetted area offsets the local reduction in local wall shear stress $\tau_{\mathrm{w}}(x_{\mathrm{s}}, y_{\mathrm{s}})$ at each point. By careful computation of the local skin friction coefficient $C_f(x_{\mathrm{s}}, y_{\mathrm{s}})$ as well as the total integrated frictional drag force D, I have shown that the reduction in drag is a function of the aspect ratio of the riblets. For each Re_L and L/λ there is an optimum aspect ratio where the highest drag reduction can be achieved. For fully-developed viscous boundary layers at $\mathrm{Re}_L \gtrsim 10^4$ (so that leading edge effects are not important), it appears that aspect ratios of order unity produce the maximum reduction in drag, which can be as large as $\Delta D/D_0 \approx -20\%$ at $\mathrm{Re}_L \approx 4 \times 10^4$.

The drag reduction results presented in Figure 3-21(b) which have been plotted as a function of the Reynolds number (based on the total length of the plate) can now be replotted based on the scaled Reynolds number as defined in Chapter 2

and compared with the results in Figure 2-13. The re-scaled results are shown in Figure 3-24. The results here agree very well with the trend previously presented in Figure 2-13 showing that for riblets to be drag reducing, the scaled Reynolds number. $\text{Re}_L(\lambda/L)^2$, needs to be less than a maximum threshold. The accompanying results shown in Figure 3-22 also confirm the non-monotonic behaviour that was shown in Chapter 2. However, the full numerical simulations presented in this chapter are able to capture drag reductions larger than those the theory predicts. In addition, these simulations show that riblets with AR > 1.5 are also able to reduce the drag force while the theoretical calculations were not able to capture this.
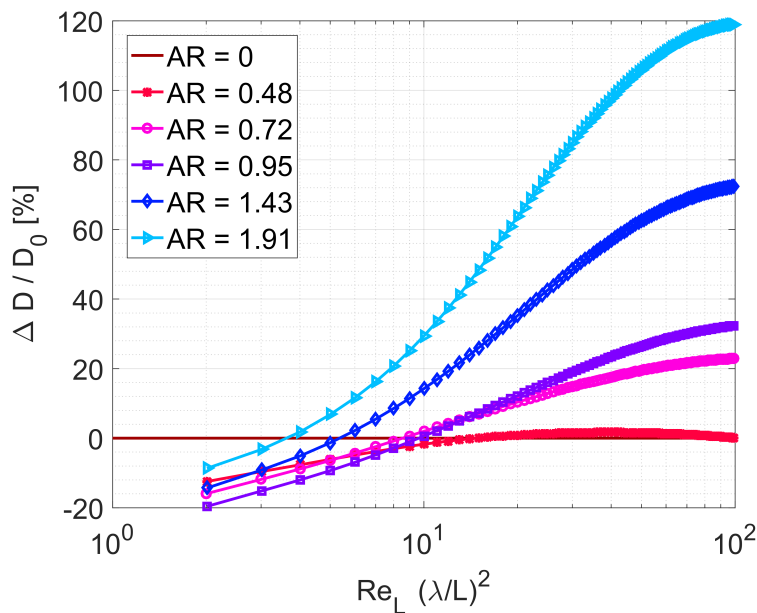
Figure 3-24:   Increases ($\Delta D > 0$) and reductions ($\Delta D < 0$) in the total drag force (D) for wrinkled plates of different total length of the range $0 < L/\lambda < 191$ plotted as a function of the scaled Reynolds number $\text{Re}_L(\lambda/L)^2$ as defined in Chapter 2 for various aspect ratio wrinkles $0 < \text{AR} < 2$, keeping the wavelength λ constant.

Thus, one can see that the asymptotic theory in itself is able to predict the trends in the changes in the frictional drag force due to presence of the riblets, however the trends and ranges are very conservative compared to the results that full three dimensional numerical simulations of steady viscous flow over riblet surfaces can offer. Also, these detailed computations as well as the trends captured in the theoretical calculations presented in the previous chapter, help rationalize why previous experi-

161

mental measurements have reported conflicting conclusions regarding drag increases or decreases and will provide guidance for selecting optimal riblet sizes and spacings for specific design applications requiring minimized frictional drag.

Chapter 4

Taylor-Couette Flow with Riblet Covered Rotors in the Laminar (Couette) Regime

4.1   Introduction

In the previous chapters, the concept of drag reduction using riblet surfaces was considered in the context of flat plate boundary layers. The effect of the riblets were discussed theoretically using an extension of classical boundary layer theory to three dimensions. Since this asymptotic theory has its own limitations discussed in Chapters 2, the flow was also explored numerically using wrinkled textures as a model riblet covered surface in Chapter 3.

In both Chapters 2 and 3, I showed that in boundary layer flows (whether over smooth plates or riblet-textured plates) velocity profiles, the pressure distribution as well as the shear stress distribution are a function of the stream-wise position along the plate and ultimately the total drag reduction is directly dependent on the total length of the plate considered, as well as the wavelength of the riblets, and their aspect ratio AR. In addition, the extension of classical boundary layer theory to riblet surfaces, neglecting the role of the pressure gradient, offers a starting point in

understanding the possibility of achieving drag reduction in high Reynolds number laminar boundary layer flows. However, considering the full Navier-Stokes equations (through a comprehensive numerical calculations) shows that the leading edge of the plate and the additional favourable pressure gradient close to the leading edge can help enhance the drag reduction achieved by creating a nearly stagnant cushion of fluid inside the grooves where fluid slides on itself, thus resulting in a much smaller local shear stress inside the grooves and hence a reduction in the total integrated drag force on a plate of length of length, L.

However, due to this dependence on the stream-wise location, it is difficult to design experiments that would allow for robust and unambiguous measurement of flow profiles, local shear stress, and frictional drag. Thus in this chapter, I consider a well defined and fully developed flow in which the velocity and frictional drag can be accurately measured in the lab. While channel or pipe geometries can offer a fully developed flow, the Reynolds number dependence of the entrance length results in difficulty in making accurate measurements of the total frictional drag. Therefore, here I employ the flow between two rotating concentric cylinders, famously known as Taylor-Couette flow [105]. I use this flow to investigate the effect of riblets geometry on the changes of the frictional drag (in this case in the form of frictional torque on the inner rotor) and compare the results of experiments with a numerical model of the flow and discuss the physics behind the changes in the torque due to the change in geometry.

The Taylor-Couette set-up has previously been used for studying drag reduction using a number of different passive and active methods, specifically in the turbulent regime. Hall and Joseph used riblets on the inner cylinder of the Taylor-Couette cell to study the effect of riblets with $AR = 2$ and $\lambda = 114$ μm with different Taylor Couette set-ups and were able to observe up to 5.1% reduction in drag [106]. Greidanus and co-workers [107] used a Taylor-Couette cell with riblets of $\lambda/d = 0.012$ and $AR = 0.92$ to study the reduction in the shear stress on the cylinders with $10^3 < \mathrm{Re}_d < 10^5$ and were able to observe a reduction in the shear stress similar to the drag reduction reported previously by Bechert [40] in channel flow setting as well has those reported by Hall
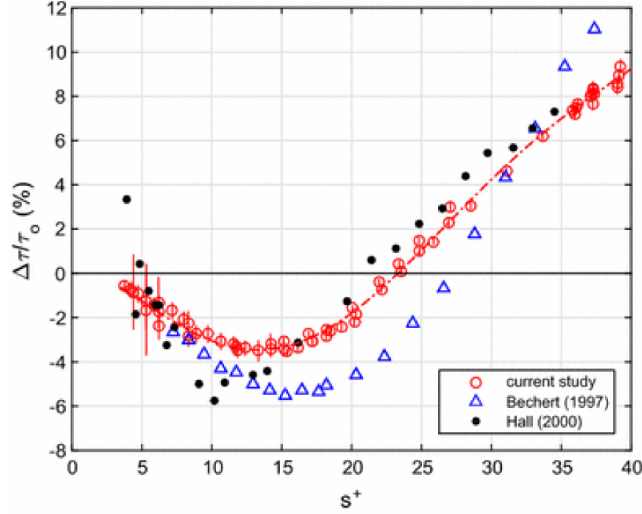
Figure 4-1: Experimental results of Greidanus et. al ($10^3 <$ Re $< 10^6$) [107] (symbols marked by "current study"), and Hall and Joseph ($10^3 <$ Re $< 10^5$) [106] of drag reduction using riblets in Taylor-Couette flow compare with the results drag reduction tests of Bechert et. al [40] using riblets in the Berlin oil channel with zero pressure gradient and driven by a drive shaft corresponding to $500 <$ Re$_\tau < 5000$ where Re$_\tau$ is the shear Reynolds number defined as Re$_\tau = \rho u^* H/\mu$ where H is the channel height [58]. s^+ is the riblet spacing (wavelength) in the wall units which was defined earlier in Chapter 1. The figure is reproduced from Reference [107].

and Joseph [106] as reprinted in Figure 4-1. Zhu and co-workers also performed a set of direct numerical simulation to understand the changes in the turbulent Taylor-Couette flow in presence of riblets [108]. They reports that the presence of the riblets in the Taylor Couette flow enhanced the transport of momentum through plume ejections happening at the tip of the riblets. In their calculations, the riblet surfaces increased the value of torque compared with the smooth case. However, they foresee the possibility of seeing a reduction in torque, if there are no plume ejections from the tips and the grooves impeding the Taylor vortices [108].

More recently, Rosenberg and co-workers used a Taylor-Couette setup with a radius ratio of 0.93 with a rotating outer cylinder and fixed inner cylinder with $6000 <$ Re < 9000 to study the effect of liquid infused surfaces on drag reduction using grooved textures on the inner cylinder with spacing of 100 μm and height of about 80 μm which were filled with various oils and they were able to see a maximum drag reduction of 14% [109].

In this chapter, I will use the Taylor-Couette flow especially in the laminar (Couette regime) to discuss the change in the frictional torque on the inner cylinder as a result of the stream-wise V-groove riblets as a function of the speed of rotation. First, I will take a look at the historical and theoretical background of Taylor-Couette flow as well as how the riblets are added to the flow geometry. Then the experimental setup used is discussed in Section 4.5. Subsequently in Section 4.6, the results of experiments in the laminar (Couette regime) are presented and compared with axisymmetric periodic simulations of the riblets in the Taylor-Couette flow. Lastly, in Sections 4.7 and 4.8 I will discuss the effect of the changes in the geometry of the riblets and the Taylor-Couette cell on the changes observed in the torque and provide a theoretical explanation for the experimental and numerical results.

4.2 Taylor-Couette Flow: Historical Background

The original effort in studying the flow between two rotating concentric cylinders can be traced back to Newton when he considered the circular motion of the fluids [105]. But Max Margules, an Austrian physicist, is one of the first people to propose using rotating cylinders as a method of measuring the viscosity of fluids by determining the torque on the inner cylinder of the set-up as a function of rotation rate (assuming the fluid adheres to the walls of the cylinders) [110, 105].

Then, nearly at the same time, French physicist Maurice Couette and British Scientist Henry Reginald Arnulph Mallock independently made similar viscometers, with the difference that Couette's set-up consisted of a rotating outer cylinder and fixed inner cylinder, while Mallock's set-up allowed for both the inner and outer cylinder to rotate. Couette seems to have known about Margules work and inspired by it tried to measure the viscosity of fluid by using a similar set-up with various configurations, first rotating the outer cylinder and keeping the inner cylinder stationary, and then rotating the inner cylinder and keeping the outer cylinder stationary [105, 111, 112].

Mallock originally used his device to measure the viscosity of water and then, in a later work, he used the device to investigate the stability of the fluid motion between
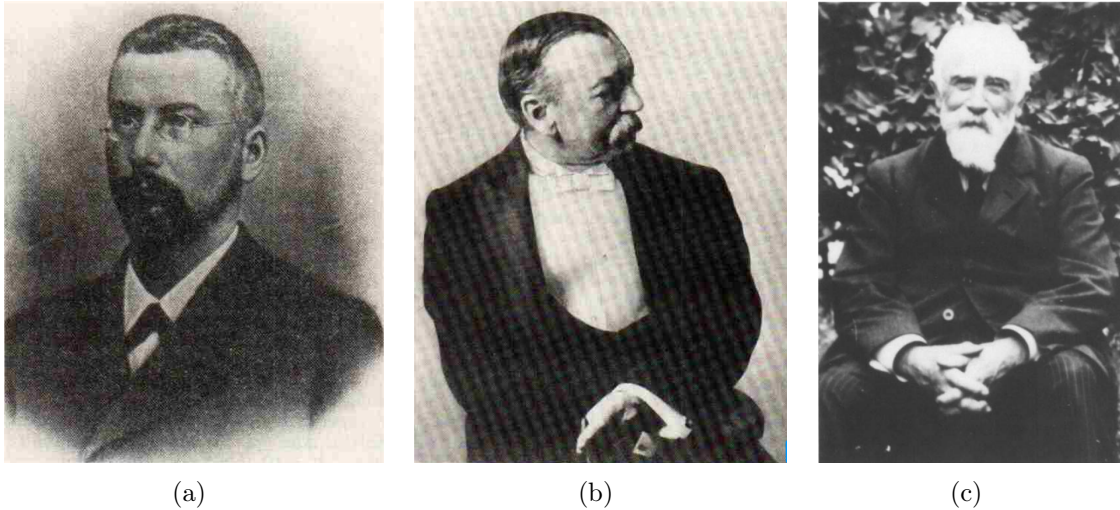
Figure 4-2: Early scientists pioneering the study of flow between concentric cylinders; (a) Max Margules [105], (b) Henry Reginald Arnulph Mallock [105], (c) Maurice Couette [113].

the two concentric cylinders [111, 112]. There he noticed that when the inner cylinder is rotating and the outer cylinder is stationary, the flow cannot sustain a laminar behaviour and the torque on the inner rotor did not exhibit a linear relationship with the rotation rate any more [110, 105, 112]. Mallock's experiments were all conducted in the ranges of velocities for which the base unidirectional flow is unstable and thus he incorrectly concluded that the flow is always unstable [105, 112].

The first person who attempted to explain this instability is Rayleigh who considered the stability of fully developed unidirectional motion in absence of the viscosity and showed that the flow is stable as long as the square of the angular momentum per unit mass of the fluid increases outward monotonically [105].

On the other hand, Couette used a set of concentric cylinders as a viscometer to measure the viscosity of different fluids [105, 113]. In Couette's setup, the inner cylinder was kept stationary and the outer cylinder rotating. Due to the configuration, Couette only noticed two flow regimes, one laminar which can be calculated from the integration of the equations of motion (and this solution is now widely known as Couette flow) and another regime where the flow did not match the solution of the steady axisymmetric equations of the motion [105].

167

Later, G.I. Taylor studied the instability of the flow between the concentric cylinders with both cylinders rotating and in his famous paper [114] he proposed a criteria for the transition between the Couette flow and the axisymmetric vortices which are now known as Taylor vortices [114]. Taylor solved the equations for the flow instability in the limit of a small gap Taylor-Couette cell (the ratio of the radius of the inner cylinder to the radius of the outer cylinder close to 1) to simplify the equations and compared the results of the analysis with his experiment [114].

Later, other scientists such as Goldstein [115] and Chandrasekhar [116, 117, 118] theoretically and numerically studied the instability of the flow between rotating cylinders and Davey [119] extended the studies to the growth of the Taylor vortices and later, jointly with DiPrima and Stuart [120], investigated instability of the Taylor vortices that would lead to initiation of other forms of instabilities. Donnelly and Schwarz [121] performed experimental investigations on the stability of flow between two cylinders and discussed the results based on the observed wavelengths and amplitudes of the instabilities as well as the wave forms observed in the experiments. In their experimental work, they noticed that using a wider gap Taylor-Couette cell ensured stability of the flow over a wider ranges of Taylor numbers [121]. As an appendix to the paper published by Donnelly and Schwarz, Roberts offered a mathematical method to predict the location of transition from Couette flow to Taylor vortex regime and the table provided there covers a wide range of Taylor-Couette set-ups and will be referred to later in this chapter [122]. Others, such as Nickerson [123], Bligen and Boulos [124], and Eagles [125] studied the evolution in the torque in Taylor-Couette cells in Taylor vortex and wavy Taylor vortex regimes. In addition, Swinney and co-workers [126, 127, 128, 129, 130, 131] throughout the years have performed experiments in various regimes of Taylor-Couette flow, offering a phase map of the flow types in their 1986 paper as a function of the Reynolds number based on the rotation of the inner and outer cylinder as defined in the section 4.3 [132] as well as discussions on the physics behind the forms of instability. Grossmann, Lohse and other co-workers have also been extending the work on the turbulent Taylor-Couette flow both numerically and experimentally [133, 134, 135, 108, 136].

(a)

(b)
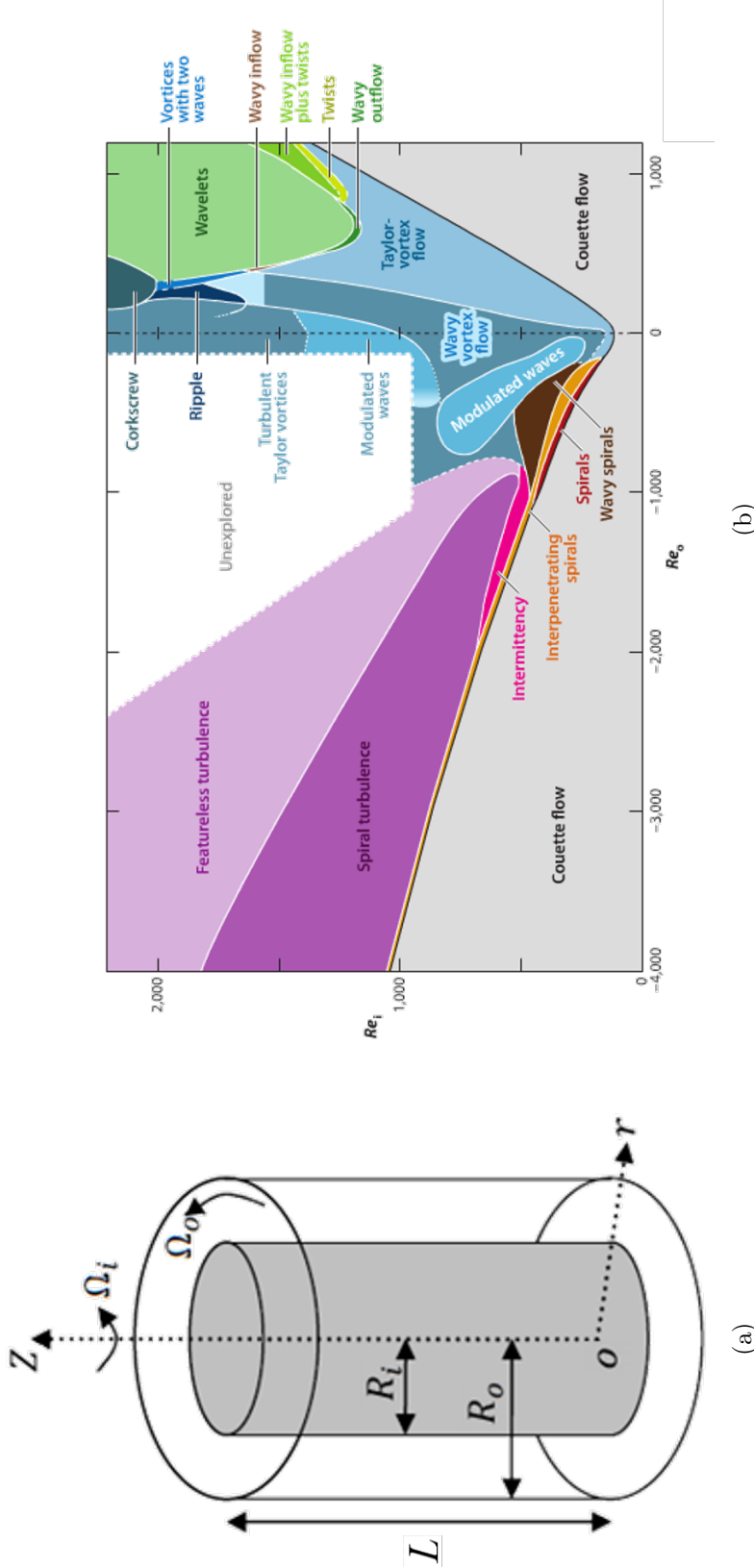
Figure 4-3: (a) Schematic of a Taylor-Couette cell. Here R_i is the radius of the inner cylinder, R_o is the radius of the outer cylinder, L is the length of the cell, and Ω_i and Ω_o are the angular velocity of the inner cylinder and outer cylinder respectively. This coordinate system used in this chapter is a cylindrical polar coordinate system where the radial direction is shown by r, the circumferential direction is shown by ϕ, and the axial direction is denoted by z [137]. (b) Phase map of the different flow types in the Taylor-Couette flow (between two concentric cylinders) as a function of the Reynolds number based on the rotation rate of the inner cylinder and the outer cylinder [132, 135].

4.3 Taylor-Couette Flow: Theory

Schematic of the geometry bounding this flow is shown in figure 4-3(a), where both cylinders can rotate independently. Depending on how the cylinders rotate with respect to each other, various types of flow and instabilities can be observed and have been reported in literature using phase maps such as the one shown in Figure 4-3(b) as a function of the Reynolds number based on the inner and outer cylinders [132, 135]. If the radius and the angular velocity of the inner cylinder and the outer cylinder are R_i, Ω_i, R_o, and Ω_o respectively, then the Reynolds number for the flow based on the inner and outer cylinders and the gap size are defined as

$$\mathrm{Re}_{d,i} = \frac{\rho R_i \Omega_i (R_o - R_i)}{\mu} \tag{4.1}$$

$$\mathrm{Re}_{d,o} = \frac{\rho R_o \Omega_o (R_o - R_i)}{\mu} \tag{4.2}$$

where $d = R_o - R_i$ is the gap between the two cylinders. (In some of the previous literature, the Reynolds number is defined based on the radius of the inner and outer cylinders instead of the gap size) Using these two Reynolds numbers one can determine the type of the flow using the Taylor-Couette flow phase map as originally put together by Andereck et al. [132, 135].

In addition to the Reynolds number which defines the dynamics of the flow, two purely geometric dimensionless groups are used to define the geometry of the cell. The first one, the radius ratio, η, is defined as

$$\eta = \frac{R_i}{R_o} \tag{4.3}$$

and offers a measure of the curvature of the geometry of the Taylor-Couette cell. The second one, is the dimensionless length, Γ, (also known as aspect ratio in the previous literature) which is calculated as

$$\Gamma = \frac{L}{R_{\mathrm{o}} - R_{\mathrm{i}}} \tag{4.4}$$

where L is the axial height of the cell. Here to avoid confusion with the riblets aspect ratio, I will call Γ the length ratio. In the ideal Taylor-Couette flow $\Gamma \to \infty$.

To take the effects of curvature into account, sometimes instead of a Reynolds number, one defines another dimensionless group, called the Taylor number which is a combination of the square of the Reynolds number, $\mathrm{Re}_{d,\mathrm{i}}$, and the radius ratio, η, and defined as [122]:

$$\mathrm{Ta} = \frac{2(1 - \eta)}{1 + \eta} \mathrm{Re}_{d,\mathrm{i}}^2 \tag{4.5}$$

At Reynolds numbers lower than the critical Reynolds number $\mathrm{Re}_d < \mathrm{Re}_{d,\mathrm{crit}}$, before the flow experiences any form of instabilities, flow between the two rotating cylinders is laminar and the velocity profile can be found using the equations of creeping flow theory. The geometry of the flow is shown in Figure 4-3(a) in the cylindrical coordinate system (r, ϕ, z) representing the radial, azimuthal, and axial directions. The inner and outer cylinder are rotating at Ω_{i} and Ω_{o} in the counter clockwise direction respectively. At the inner and outer cylinders $(r = R_{\mathrm{i}}$ and $r = R_{\mathrm{o}})$ I have no slip boundary conditions and I assume the length of the cylinders is infinitely long. Starting from the Navier-Stokes equation in cylindrical polar coordinate system in the ϕ direction, at steady state, I have

$$\rho \left(v_r \frac{1}{r} \frac{\partial r v_\phi}{\partial r} + \frac{v_\phi}{r} \frac{\partial v_\phi}{\partial \phi} + v_z \frac{\partial v_\phi}{\partial z} \right) = \mu \left(\frac{\partial}{\partial r} \left(\frac{1}{r} \frac{\partial (r v_\phi)}{\partial r} \right) + \frac{1}{r^2} \frac{\partial^2 v_\phi}{\partial \phi^2} + \frac{\partial^2 v_\phi}{\partial z^2} \right) - \frac{1}{r} \frac{\partial p}{\partial \phi}. \tag{4.6}$$

Thus, assuming the velocity is unidirectional $(v_\phi(r))$ and not in radial and axial direction, I can postulate a velocity profile of the form

$$\boldsymbol{v} = \begin{bmatrix} v_r \\ v_\phi \\ v_z \end{bmatrix} = \begin{bmatrix} 0 \\ v_\phi(r) \\ 0 \end{bmatrix} \tag{4.7}$$

for a swirling flow in which the circumferential velocity is only a function of radial position. Also, due to axi-symmetry, all the derivatives with respect to ϕ disappear, thus

$$\frac{\partial v_\phi}{\partial \phi} = 0 \quad \& \quad \frac{\partial p}{\partial \phi} = 0 \tag{4.8}$$

and the equation of motion in the ϕ direction (Equation 4.6) can be simplified to

$$\frac{\partial}{\partial r} \left(\frac{1}{r} \frac{\partial}{\partial r} (r v_\phi) \right) = 0. \tag{4.9}$$

The integration of Equation 4.9, gives that the circumferential velocity has a functional form of

$$v_\phi(r) = \frac{C_1}{r} + C_2 \, r \tag{4.10}$$

where C_1 and C_2 are coefficients to be found using two boundary conditions. For the case of two independently rotating cylinders with arbitrary rotation rates, I have

$$r = R_\mathrm{i} \quad \rightarrow \quad v_\phi = R_\mathrm{i} \Omega_\mathrm{i} \tag{4.11}$$

on the inner wall and

$$r = R_\mathrm{o} \quad \rightarrow \quad v_\phi = R_\mathrm{o} \Omega_\mathrm{o} \tag{4.12}$$

on the outer wall. Now, using Equations 4.11 and 4.12, for the general case with both cylinders rotating, the coefficients can be calculated

$$C_1 = R_\mathrm{o} \frac{\eta}{1 - \eta^2} \left(R_\mathrm{i} \Omega_\mathrm{i} - \eta R_\mathrm{o} \Omega_\mathrm{o} \right) \tag{4.13}$$

$$C_2 = -\frac{1}{R_o}\frac{1}{1-\eta^2}\left(\eta R_i \Omega_i - R_o \Omega_o\right) \tag{4.14}$$

and thus the velocity profile can be written in the general form

$$v_\phi = \frac{\eta}{1-\eta^2}\left(R_i \Omega_i - \eta R_o \Omega_o\right)\frac{R_o}{r} - \frac{1}{1-\eta^2}\left(\eta R_i \Omega_i - R_o \Omega_o\right)\frac{r}{R_o} \tag{4.15}$$

in dimensional form. If the velocity is non-dimensionalized by the velocity of the inner cylinder then

$$\frac{v_\phi}{R_i \Omega_i} = \frac{\eta}{1-\eta^2}\left(1 - \frac{\Omega_o}{\Omega_i}\right)\frac{R_o}{r} - \frac{1}{1-\eta^2}\left(\eta - \frac{1}{\eta}\frac{\Omega_o}{\Omega_i}\right)\frac{r}{R_o} \tag{4.16}$$

and if non-dimensionalized by the velocity of the outer cylinder, I have

$$\frac{v_\phi}{R_o \Omega_o} = \frac{\eta^2}{1-\eta^2}\left(\frac{\Omega_i}{\Omega_o} - 1\right)\frac{R_o}{r} - \frac{1}{1-\eta^2}\left(\eta^2\frac{\Omega_i}{\Omega_o} - 1\right)\frac{r}{R_o}. \tag{4.17}$$

Either non-dimensional form can be useful depending on the flow that is being analysed. When both cylinders are rotating another dimensionless groups, consisting of the ratio of the rotation rates of the cylinders (Ω_i/Ω_o), is sometimes employed as well. As it can be seen from the above equations, the unidirectional velocity profile obtained in cylindrical Couette flow is only a function of the geometry and the ratio of the rotation rates of the two cylinders.

Here, I am only interested in the cases where one of the cylinders is rotating at a time. Since the experimental setup used in this work is attached to a stress-controlled rheometer (discussed in Section 4.5), then I can only measure the angular velocity and torque on the inner cylinder. Similarly one can extend this method to use a strain-controlled rheometer where the angular velocity is measured on the outer cylinder while the torque is measured on the inner cylinder. Therefore, out of the various possibilities for this flow, the cases of rotating inner cylinder (finite $\text{Re}_{d,i}$) with fixed outer cylinder ($\text{Re}_{d,o} = 0$), and rotating outer cylinder (finite $\text{Re}_{d,o}$) with stationary inner cylinder ($\text{Re}_{d,i} = 0$) can be effectively used for conducting experiments on other physical phenomena such as measuring the viscosity of fluids [138], or measuring the

the frictional torque on the rotors and drag reduction tests [109].

These two cases are similar at low Reynolds number, but at high enough Reynolds numbers, the case with rotating inner cylinder (finite $\text{Re}_{d,\text{i}}$) and stationary outer cylinder (corresponding to the vertical line of $\text{Re}_{d,\text{o}} = 0$ on Figure 4-3(b)) experiences instabilities (discussed earlier) that results in flow transition from laminar (Figure 4-4(a)) to Taylor vortices (Figures 4-4(b) and 4-4(c)), then wavy Taylor vortices, afterwards to turbulent Taylor vortices and ultimately to featureless turbulence. On the other hand, when only the outer cylinder is rotating (corresponding to the horizontal line of $\text{Re}_{d,\text{i}} = 0$ on Figure 4-3(b)), no instability is observed until the transition from laminar to featureless turbulent flow occurs [132, 135, 121, 120, 114].

Thus, in the laminar or Couette flow regime when only the inner cylinder is rotating, using Equations 4.16 with $\Omega_\text{o} = 0$, the velocity profile can be written compactly in the form:

$$\frac{v_\phi}{R_\text{i}\Omega_\text{i}} = -\frac{\eta}{1 - \eta^2}\frac{r}{R_\text{o}} + \frac{\eta}{1 - \eta^2}\frac{R_\text{o}}{r} \tag{4.18}$$

and when only the outer cylinder is rotating, using Equation 4.17 with $\Omega_\text{i} = 0$, the velocity profile is simplified to

$$\frac{v_\phi}{R_\text{o}\Omega_\text{o}} = \frac{1}{1 - \eta^2}\frac{r}{R_\text{o}} - \frac{\eta^2}{1 - \eta^2}\frac{R_\text{o}}{r}. \tag{4.19}$$

In this work, I am interested in using the Taylor-Couette flow for the purpose of measuring the total frictional torque exerted by the working fluid on the inner cylinder. Here, I am interested in the total torque on the inner cylinder, since with the experimental setup (discussed in section 4.5), I am able to measure the angular velocity and torque on the inner cylinder and I will use that to discuss the effect of riblets. To find the total torque, first I need to find the stress distribution on the inner cylinder. The shear stress in a Newtonian fluid is found using

(a)
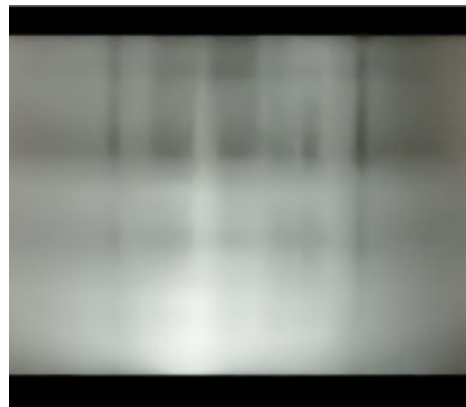
(b)
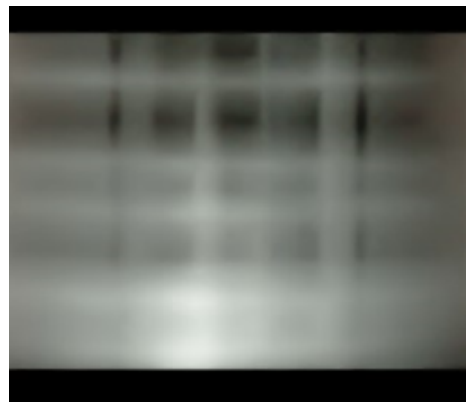
(c)

Figure 4-4: Taylor-Couette flow with $\eta = 0.63$ and $\Gamma = 5.1$ with only the inner cylinder rotating in (a) laminar (Couette flow) regime with $\mathrm{Re}_{d,\mathrm{i}} < 74$, (b) close to transition with $\mathrm{Re}_d \approx 74$ and (c) after transition to Taylor-Vortices with $\mathrm{Re}_{d,\mathrm{i}} > 74$ and prior to transition to the wavy Taylor vortices. Note that all three flow types shown here are axi-symmetric. For this geometry, the critical Reynolds number for transition from laminar to Taylor vortices is $\mathrm{Re}_{d,\mathrm{crit}} = 74$.

$$\boldsymbol{\tau} = \mu\dot{\boldsymbol{\gamma}} \tag{4.20}$$

where $\boldsymbol{\tau}$ is the Cauchy stress tensor in the fluid and $\dot{\boldsymbol{\gamma}}$ is the rate of strain tensor in the fluid which can be found as

$$\dot{\boldsymbol{\gamma}} = [(\boldsymbol{\nabla v}) + (\boldsymbol{\nabla v})^T] \tag{4.21}$$

where $\boldsymbol{\nabla v}$ is the gradient of the velocity profile. So, specifically for the cases where only the inner cylinder is rotating, the strain rate on the inner cylinder (i.e. $r = R_i$) is

$$\dot{\boldsymbol{\gamma}} = \begin{bmatrix} 0 & \dfrac{-2}{1-\eta^2} & 0 \\ \dfrac{-2}{1-\eta^2} & 0 & 0 \\ 0 & 0 & 0 \end{bmatrix} \Omega_i \tag{4.22}$$

and when only the outer cylinder is rotating, the rate of the shear strain (again!) on the inner cylinder ($r = R_i$) is

$$\dot{\boldsymbol{\gamma}} = \begin{bmatrix} 0 & \dfrac{2}{1-\eta^2} & 0 \\ \dfrac{2}{1-\eta^2} & 0 & 0 \\ 0 & 0 & 0 \end{bmatrix} \Omega_o \tag{4.23}$$

Therefore, the deviatoric stress tensor on the inner cylinder ($r = R_i$) for the case with inner cylinder rotating can be written as

$$\boldsymbol{\tau}(r = R_i, \phi, z) = \begin{bmatrix} 0 & \dfrac{-2\mu}{1-\eta^2}\Omega_i & 0 \\ \dfrac{-2\mu}{1-\eta^2}\Omega_i & 0 & 0 \\ 0 & 0 & 0 \end{bmatrix} \tag{4.24}$$

and when only the outer cylinder is rotating is written as

176

$$\boldsymbol{\tau}(r = R_\mathrm{i}, \phi, z) = \begin{bmatrix} 0 & \dfrac{2\mu}{1-\eta^2}\Omega_\mathrm{o} & 0 \\ \dfrac{2\mu}{1-\eta^2}\Omega_\mathrm{o} & 0 & 0 \\ 0 & 0 & 0 \end{bmatrix}. \tag{4.25}$$

As it can be seen, in both cases the deviatoric stress tensor only has one non-zero component $\tau_{r\phi}$.

$$\tau_{r\phi} = \frac{-2\mu}{1-\eta^2}\Omega_\mathrm{i} \tag{4.26}$$

$$\tau_{r\phi} = \frac{2\mu}{1-\eta^2}\Omega_\mathrm{o} \tag{4.27}$$

Thus the traction vector $\boldsymbol{\tau}_\mathrm{w} = \boldsymbol{\tau}(r = R_\mathrm{i}, \phi, z).\boldsymbol{n}_\mathrm{w}$ on the inner cylinder when the inner cylinder is rotating is written as

$$\boldsymbol{\tau}_\mathrm{w} = \begin{bmatrix} 0 & \dfrac{-2\mu}{1-\eta^2}\Omega_\mathrm{i} & 0 \\ \dfrac{-2\mu}{1-\eta^2}\Omega_\mathrm{i} & 0 & 0 \\ 0 & 0 & 0 \end{bmatrix} . \begin{bmatrix} 0 \\ 1 \\ 0 \end{bmatrix} = \begin{bmatrix} 0 \\ \dfrac{-2\mu}{1-\eta^2}\Omega_\mathrm{i} \\ 0 \end{bmatrix} \tag{4.28}$$

and when the outer cylinder is rotating is written as

$$\boldsymbol{\tau}_\mathrm{w} = \begin{bmatrix} 0 & \dfrac{2\mu}{1-\eta^2}\Omega_\mathrm{o} & 0 \\ \dfrac{2\mu}{1-\eta^2}\Omega_\mathrm{o} & 0 & 0 \\ 0 & 0 & 0 \end{bmatrix} . \begin{bmatrix} 0 \\ 1 \\ 0 \end{bmatrix} = \begin{bmatrix} 0 \\ \dfrac{2\mu}{1-\eta^2}\Omega_\mathrm{o} \\ 0 \end{bmatrix} . \tag{4.29}$$

And thus the magnitude of traction vector on the inner cylinder is equivalent to the $r\phi$ component of the stress tensor and in both cases are identical if $\Omega_\mathrm{i} = \Omega_\mathrm{o}$ and only the magnitude of their sign is different (Note that this does not necessary mean the same $\mathrm{Re}_{d,\mathrm{i}}$ and $\mathrm{Re}_{d,\mathrm{o}}$ for both cases). Now to find the total frictional torque on the inner cylinder for either cases I can write

177

$$\boldsymbol{T} = \int_{S_{\mathrm{w}}} \boldsymbol{r}_{\mathrm{w}} \times \boldsymbol{\tau}_{\mathrm{w}} dS_{\mathrm{w}} = \int_0^L \boldsymbol{r}_{\mathrm{w}} \times \boldsymbol{\tau}_{\mathrm{w}} 2\pi r_{\mathrm{w}} dz. \tag{4.30}$$

where $\boldsymbol{r}_{\mathrm{w}}(\phi, z)$ is the local vector and r_{w} is the magnitude of the local radius of the wall on the inner cylinder in the most general form for any textured or un-textured rotor which can be a function of the axial and circumferential direction. For the case of periodic riblets in the circumferential direction then only the local vector is a function of the axial direction, $\boldsymbol{r}_{\mathrm{w}}(z)$. On a smooth rotor $r_{\mathrm{w}} = R_{\mathrm{i}}$, thus, for the case with only the inner cylinder rotating I have

$$\boldsymbol{T} = \int_0^L \begin{bmatrix} r_{\mathrm{w}} \\ 0 \\ 0 \end{bmatrix} \times \begin{bmatrix} 0 \\ \dfrac{-2\mu}{1-\eta^2}\Omega_{\mathrm{i}} \\ 0 \end{bmatrix} 2\pi r_{\mathrm{w}} dz = \dfrac{-4\mu}{1-\eta^2}\Omega_{\mathrm{i}}\pi R_{\mathrm{i}}^2 L \boldsymbol{e}_z \tag{4.31}$$

where $\boldsymbol{e}_z$ is the unit normal in the axial direction and when the outer cylinder is rotating the torque can be written

$$\boldsymbol{T} = \int_0^L \begin{bmatrix} r_{\mathrm{w}} \\ 0 \\ 0 \end{bmatrix} \times \begin{bmatrix} 0 \\ \dfrac{2\mu}{1-\eta^2}\Omega_{\mathrm{o}} \\ 0 \end{bmatrix} 2\pi r_{\mathrm{w}} dz = \dfrac{4\mu}{1-\eta^2}\Omega_{\mathrm{i}}\pi R_{\mathrm{i}}^2 L \boldsymbol{e}_z. \tag{4.32}$$

Thus the magnitude of the frictional torque on the inner cylinder can be simplified and expressed as in equations below for cases when the inner cylinder is rotating and one when the outer cylinder is rotating respectively

$$T = \frac{4\mu}{1-\eta^2}\Omega_{\mathrm{i}}\pi R_{\mathrm{i}}^2 L = 4\pi\nu^2\rho L \frac{\eta}{(1-\eta^2)(1-\eta)}\mathrm{Re}_{d,\mathrm{i}} \tag{4.33}$$

$$T = \frac{4\mu}{1-\eta^2}\Omega_{\mathrm{i}}\pi R_{\mathrm{i}}^2 L = 4\pi\nu^2\rho L \frac{\eta^2}{(1-\eta^2)(1-\eta)}\mathrm{Re}_{d,\mathrm{o}}. \tag{4.34}$$

Note that Equations 4.33 and 4.34 are again identical for both situations as long as $\Omega_{\mathrm{i}} = \Omega_{\mathrm{o}}$ among the two cases. Note that the same Reynolds numbers would not result

in the same torque for both the cases and it needs to be multiplied by a the radius ratio determined from the geometry. Thus the torque can be written as a function of a dimensional pre-factor and two dimensionless groups, one based on the geometry involving the radius ratio and another based on the Reynolds number of the flow. Thus the total torque is non-dimensionalized by $4\pi\rho\nu^2 L$ which is the dimensional pre-factor in both Equations 4.33 and 4.34 as

$$G = \frac{T}{4\pi\rho\nu^2 L} \tag{4.35}$$

where G is the non-dimensional torque [128, 127]. For the case of the smooth rotor in the laminar regime the dimensional torque of Equations 4.33 and 4.34 can be written as the following equations for the cases with inner cylinder rotating and outer cylinder rotating respectively.

$$G = \frac{\eta}{(1-\eta^2)(1-\eta)}\mathrm{Re}_{d,\mathrm{i}} \tag{4.36}$$

$$G = \frac{\eta^2}{(1-\eta^2)(1-\eta)}\mathrm{Re}_{d,\mathrm{o}} \tag{4.37}$$

which only involve two dimensionless groups, the radius ratio, η, and, the appropriate Reynolds number corresponding to the configuration. Note that this is only true in the case of uni-directional flow.

Therefore, using either forms of the flow should result in comparable results for drag reduction. In the current work, I will examine the case where the inner cylinder is rotating and thus from this point forward the Reynolds number (Re_d) will be the Reynolds number using the velocity on the inner cylinder. As mentioned earlier, in case of only inner cylinder rotating, depending on the Taylor number or Reynolds number, four different flow types can be observed, ranging from Couette flow, Taylor vortex flow, wavy Taylor vortex flow, and turbulent flow as shown in Figure 4-3(b) [132, 139, 140].

It has been previously shown that local transition from laminar to Taylor vortices described by a critical Reynolds number (based on the rotation of the inner cylinder) or Taylor number ($\text{Re}_{d,\text{crit}}(\eta)$ or $\text{Ta}_{\text{crit}}(\eta)$) depends on the radius ratio, η, [121, 141]. The height ratio, Γ, and the boundary conditions at the top and bottom of the cell can define how close the system is to the infinitely long, ideal Taylor-Couette flow [132]. Earlier calculations by Roberts [122] has offered a table to determine the critical Taylor number as a function of the radius ratio for infinitely long cells which can be easily used for finding the transition Reynolds number for different geometries. For example, for a Taylor Couette cell with $\eta = 0.63$ (the geometry of the experimental setup used in this thesis), the transition Reynolds number can be found to be $\text{Re}_{d,\text{crit}} = 74$.

4.3.1   Pressure distribution in Taylor-Couette flow

One added level of complexity in the Taylor-Couette flows that does not exist in other flows is the centrifugal effect that creates a pressure gradient in the radial direction of the flow. In the easiest case of cylindrical Couette flow where I have a theoretical solution to the problem, I can calculate this pressure gradient by looking at the Navier-Stokes equation in the radial direction (in the cylindrical polar coordinate system). In cylinder Couette flow after postulating the velocity profile as in equation 4.7, I was able to calculate the velocity profile for the general configuration of both cylinders rotating (Equation 4.15) and the special cases where only one of the cylinders is rotating (Equations 4.16 and 4.17).

The experimental setup (discussed in Section 4.5) used in this work is attached to a stress-controlled rheometer, allowing me to measure the angular velocity and the torque on the inner rotors of the Taylor-Couette cell. Therefore, in this work, I am interested in the case where only the inner cylinder is rotating, thus, I will continue the calculation of the pressure distribution for this case only. Taking Equation 4.16 and 4.7, with the axi-symmetry, I can simplify the Navier-Stokes equation in the radial direction from

$$\rho\left(\frac{v_r}{r}\frac{\partial}{\partial r}(rv_r) + \frac{v_\phi}{r}\frac{\partial v_r}{\partial \phi} + v_z\frac{\partial v_r}{\partial z} - \frac{v_\phi^2}{r}\right) = -\frac{\partial p}{\partial r} + \mu\left(\frac{\partial}{\partial r}\left(\frac{1}{r}\frac{\partial}{\partial r}(rv_r)\right) + \frac{1}{r^2}\frac{\partial^2 v_r}{\partial \phi^2} + \frac{\partial^2 v_r}{\partial z^2}\right)$$

(4.38)

with $v_r = 0$, $v_z = 0$, and v_ϕ only a function of the radial location to

$$-\rho\frac{v_\phi^2}{r} = -\frac{\partial p}{\partial r}.$$

(4.39)

Now substituting for v_ϕ from Equations 4.16 in the above equation gives

$$\frac{\partial p}{\partial r} = \rho\left(\frac{\eta}{1-\eta^2}\right)^2\left(\frac{1}{r}-r\right)^2\frac{1}{r}.$$

(4.40)

Assuming the reference pressure for the atmospheric pressure ($p_{\text{atm}} = 0$) to be at the outer cylinder, the boundary condition can be written as

$$r = R_\text{o} \quad \rightarrow \quad p = 0$$

(4.41)

then I can integrate the differential equation to find the dimensionless fluid pressure distribution as a function of the radial location across the gap

$$\frac{p}{\rho(R_\text{i}\Omega_\text{i})^2} = \left(\frac{\eta}{1-\eta^2}\right)^2\left(-\frac{1}{2}\left(\frac{R_\text{o}}{r}\right)^2 - 2\ln\left(\frac{r}{R_\text{o}}\right) + \frac{1}{2}\left(\frac{r}{R_\text{o}}\right)^2\right) + C_z$$

(4.42)

where C_z is a function of z to be found from the Navier-Stokes equation in the axial z direction. This pressure distribution can directly affect the experiments through changing the shape of the free surface between the external air and the fluid at the top of the Taylor-Couette cell. Taking the Navier-Stokes equation in the axial direction,

$$\rho\left(v_r\frac{\partial v_z}{\partial r} + \frac{v_\phi}{r}\frac{\partial v_z}{\partial \phi} + v_z\frac{\partial v_z}{\partial z}\right) = -\frac{\partial p}{\partial z} + \mu\left(\frac{1}{r}\frac{\partial}{\partial r}\left(r\frac{\partial v_z}{\partial r}\right) + \frac{1}{r^2}\frac{\partial^2 v_z}{\partial \phi^2} + \frac{\partial^2 p_z}{\partial z^2}\right) - \rho g$$

(4.43)

and simplifying the equation using Equation 4.7 gives:

181

$$\frac{p}{\rho(R_i\Omega_i)^2} = -\frac{gL}{(R_i\Omega_i)^2}\frac{z}{L} + C_r \tag{4.44}$$

where $C_r(r)$ is a constant or a function of the radial direction r only. Thus, comparing and combining the Equations 4.42 and 4.44 gives

$$\frac{p}{\rho(R_i\Omega_i)^2} = \left(\frac{\eta}{1-\eta^2}\right)^2\left(-\frac{1}{2}\left(\frac{R_o}{r}\right)^2 - 2\ln\left(\frac{r}{R_o}\right) + \frac{1}{2}\left(\frac{r}{R_o}\right)^2\right) - \frac{gL}{(R_i\Omega_i)^2}\frac{z}{L}. \tag{4.45}$$

On the top surface of the Taylor-Couette cell open to the ambient air, the pressure is atmospheric everywhere. Therefore the free surface (r_s, z_s) of a Newtonian viscous fluid under steady rotation can be found using

$$\frac{p_{\mathrm{atm}}}{\rho(R_i\Omega_i)^2} = \left(\frac{\eta}{1-\eta^2}\right)^2\left(-\frac{1}{2}\left(\frac{R_o}{r_s}\right)^2 - 2\ln\left(\frac{r_s}{R_o}\right) + \frac{1}{2}\left(\frac{r_s}{R_o}\right)^2\right) - \frac{gL}{(R_i\Omega_i)^2}\frac{z_s}{L}. \tag{4.46}$$

Setting $p_{\mathrm{atm}} = 0$ then I have

$$0 = \left(\frac{\eta}{1-\eta^2}\right)^2\left(-\frac{1}{2}\left(\frac{R_o}{r_s}\right)^2 - 2\ln\left(\frac{r_s}{R_o}\right) + \frac{1}{2}\left(\frac{r_s}{R_o}\right)^2\right) - \frac{gL}{(R_i\Omega_i)^2}\frac{z_s}{L}. \tag{4.47}$$

and

$$\frac{z_s}{L} = \mathrm{Fr}^2\left(\frac{\eta}{1-\eta^2}\right)^2\left(-\frac{1}{2}\left(\frac{R_o}{r_s}\right)^2 - 2\ln\left(\frac{r_s}{R_o}\right) + \frac{1}{2}\left(\frac{r_s}{R_o}\right)^2\right) \tag{4.48}$$

where here the Froude number Fr is defined as

$$\mathrm{Fr} = \frac{R_i\Omega_i}{\sqrt{gL}}. \tag{4.49}$$

Therefore, the geometric design of the Taylor-Couette cell (specifically the radius ratio) affects the shape of the free surface of the fluid in the Taylor-Couette flow. The results are plotted for various radius ratios η and it is seen in Figure 4-5. Using a

wider gap Taylor-Couette cell (i.e. $\eta < 0.85$) would result in a deflection of fluid close to the inner cylinder.
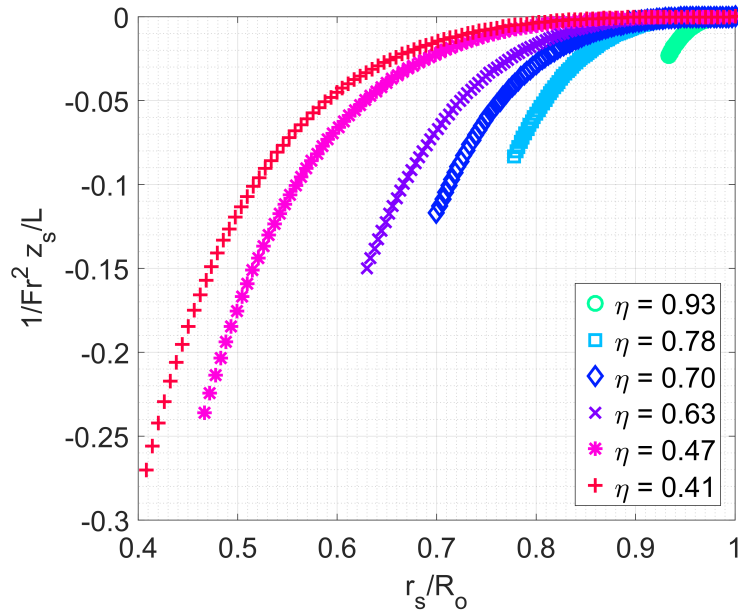
Figure 4-5: Shape of the free surface in a Taylor-Couette cell open to air as a function of the radial location and the radius ratio of the cell. $r_\mathrm{s}/R_\mathrm{o} = 1$ corresponds to the radial location of the outer cylinder.

On the other hand, the location of the free surface of the working fluid is also directly dependent on the Froude number, Fr, of the flow as defined in Equation 4.49 and for a constant radius ratio, increasing the Froude number results in a lower deflection close to the inner cylinder as shown in Figure 4-6.

Hence, from Equation 4.48 I see that the free surface of the fluid will have a curved shape with a deflection toward the inner rotor compared to the outer cylinder. Using a wide gap Taylor-Couette cell (i.e. $\eta < 0.8$) also results in an even enhanced deflection at $r/R_\mathrm{o} = \eta$. In addition, increasing the velocity of the inner cylinder, which results in an increase in the Reynolds number as well as the Froude number, also changes the shape of the free surface. As Froude number increases, then the local depression close to the rotor increases, possibly resulting in part of the rotor not being in contact with fluid. This causes added errors to the torque measurements as well as helping air bubbles to be entrained in the experimental setup and causing added errors to
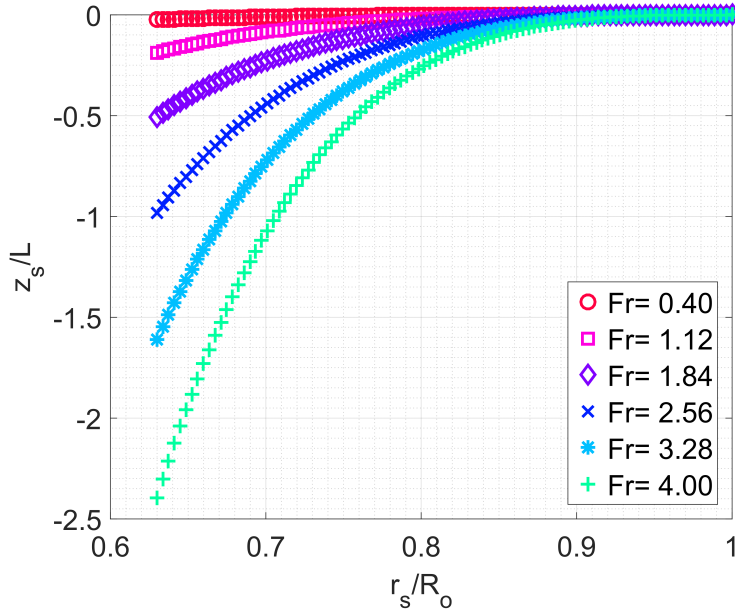
Figure 4-6: Shape of the free surface in a Taylor-Couette cell open to air as a function of the radial location and the Froude number of the flow for a cell with $\eta = 0.63$.

the measured torque. Therefore, only a limited range of velocities can be employed to avoid the errors due to the changes in the surface height. However, one can easily change the ranges of Reynolds number by changing the viscosity of the working fluid, while not changing the Froude number of the flow. This method was employed here to cover a wider range of Reynolds numbers in the experiments.

4.4 Riblets in Taylor-Couette flow

In order to study the effect of the riblets on the changes in torque measured in Taylor-Couette flows, I consider the case of Taylor-Couette flow when only the inner cylinder is rotating. Since I am using a stress-controlled rheometer with my experimental setup, I am only able to measure the rotation rate and the torque on the inner rotor. For that, the inner rotor is covered with V-groove riblets that are aligned in the circumferential direction (flow direction) and cover the entire length of the rotor. Here I am again using V-grooves which are the simplest riblet geometry and allow me to theoretically discuss the changes in the total frictional torque on the inner rotor

in section 4.8. This study can easily be extended to other forms of riblet shapes. Again, to understand the effect of the riblets similar to the previous chapters, I need to define additional non-dimensional variables that characterize dimensions of the riblets in this study. Figure 4-8 shows a schematic of the cross section of a Taylor-Couette cell with riblets on the inner rotor. For V-groove riblets, two parameters fully define the shape of the riblets, the wavelength or spacing of the riblets, denoted by λ and the amplitude of the riblets, defined using A similar to the definitions used in the previous chapters (Figure 4-8).
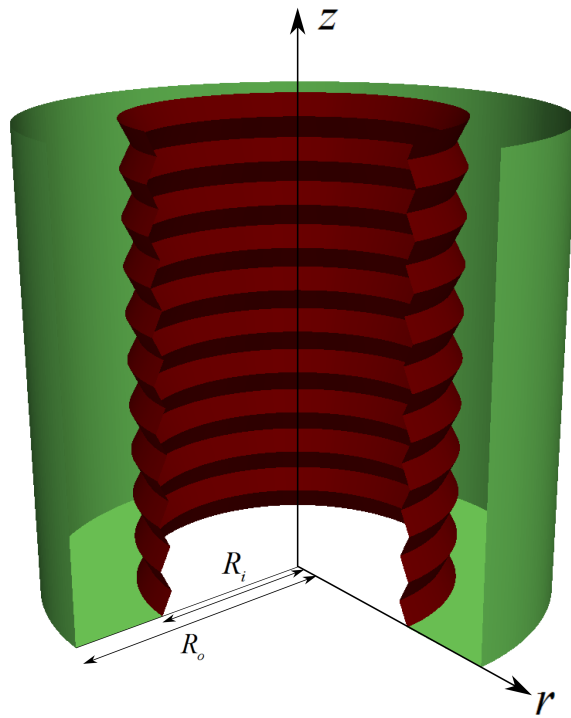
Figure 4-7: Schematic of a Taylor-Couette cell with a riblet covered inner rotor. The inner radius R_i here corresponds to the distance from the center of the coordinate system to the furthest point on the riblets (riblet peaks) and R_o is the radius of the outer cylinder. Again, a cylindrical polar coordinate system has been used for the analysis (r, ϕ, z).

As noted earlier, Taylor Couette flow involves three distinct length scales, the radii of the inner and outer cylinders, R_i and R_o, as well as the gap size, d, which can easily be related to each other through the definition of the gap size, $d = R_o - R_i$, as well as the radius ratio η. Thus, only one dimensionless group is sufficient to describe
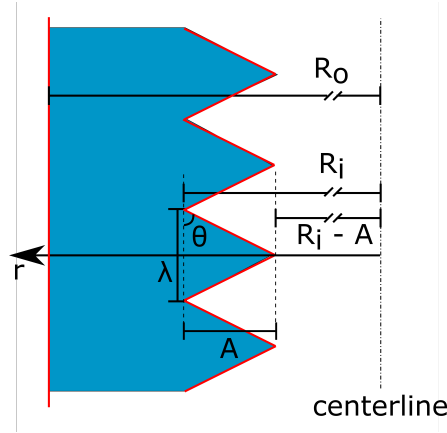
Figure 4-8: (b) Enlarged schematic of the riblet geometry on the Taylor Couette cell wall showing the inner and outer radius R_i and R_o as well as the geometry of the riblets. The blue region corresponds to the fluid domain that is analysed throughout this chapter.

the geometry of the Taylor-Couette cell in the laminar (Couette) regime. Based on the definitions I always have $R_\mathrm{o} > R_\mathrm{i}$ and from the definition of the radius ratio I have

$$\frac{d}{R_\mathrm{i}} = \frac{1 - \eta}{\eta} \qquad (4.50)$$

and hence the gap could be smaller, the same or larger than the radii of either of the cylinders. On the other hand, the riblet geometry is defined by the amplitude and the wavelength of the riblets, which are usually smaller than the characteristic length scales of the flow they are used in. For example the riblets used in the investigation by Hall and Joseph [106], Bechert and coworkers [40], and Greidanus and coworkers [107], as shown in Figure 4-1, as well as the dimensions of natural surface textures such as ribs on shark denticles, as shown in Figure 1-4, are much smaller than the characteristic length scales of the flow. Hence, even in Taylor-Couette flow $A, \lambda < R_\mathrm{i}, d$. While both radii of the cylinders are important length scales in the problem, diffusion of vorticity from the rotating inner cylinder occurs within the distance of the gap and therefore, to non-dimensionalize the wavelength of the riblets, I use the size of the gap as λ/d, which serves as a connection between the riblets dimension and the general dimensions of the Taylor-Couette problem. Unlike a boundary layer

flow in which the location along the plate played an important role as discussed in Chapters 2 and 3 and was used for non-dimensionalizing the wavelength, here the direction of the viscous diffusion in the radial direction (i.e. across the gap) is the more appropriate length scale to be used.

However, it should be noted that the ratio λ/d can easily be translated to λ/R_i using Equation 4.50. While I report my data as a function of λ/d, the group λ/R_i can be effectively used to simplify the equations of motion and boundary conditions at the riblet wall to find appropriate scaling for the torque as a function of the geometry and this will be discussed in the latter sections.

As a measure of the sharpness of the V-groove, I also use the dimensionless aspect ratio, AR, defined as

$$ \text{AR} = \frac{2A}{\lambda} = \tan \theta \tag{4.51} $$

which is also the tangent of the side angle θ as shown in Figure 4-8. Note that for a smooth rotor $\text{AR} = 0$ and the radius of the wall on the inner cylinder is $r_w = R_i$ for every axial location z.

Now for the case of the riblet covered inner rotor the total torque can be calculated using equations 4.30, but it should be noted that now r_w is not a constant and will change along the axial direction, same with the shear stress distribution. For the case of the V-groove riblets the radius of the wall on the inner cylinder can be written as

$$ 0 < z < \frac{\lambda}{2} \quad : \quad r_w = (R_i - \text{AR } z) \tag{4.52} $$

and due to symmetry about the line of $z = \lambda/2$:

$$ \frac{\lambda}{2} < z < \lambda \quad : \quad r_w = (R_i - \text{AR } (\lambda - z)) \tag{4.53} $$

and this definition of r_w is used in Equation 4.30 for riblet covered rotors.

4.5   Experimental Setup

A custom designed wide gap Taylor-Couette with radius ratio of $\eta = 0.63$ was built and used in this work. The setup is shown schematically in Figure 4-9. The fixed part of the setup is built using a CNC mill and sits on the fixed Peltier plate of a stress-controlled rheometer (TA Instruments AR-G2).

The top and bottom plates of the Taylor-Couette cell as shown in Figure 4-11 are made of Delrin blocks of 6" $\times$ 6" $\times$ 0.5" inches and 6" $\times$ 6" $\times$ 1" respectively, and the outer cylinder is cut from an acrylic cylinder with an inner diameter of 1.75" and the outer diameter of 2" and brought to the required size by turning.
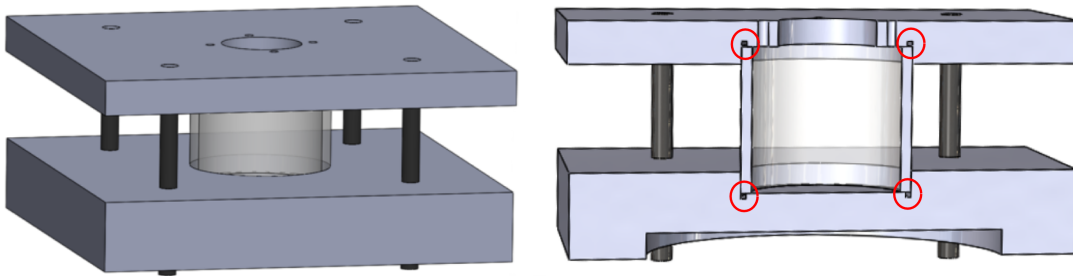
Figure 4-9:   Schematic of the fixed part of the Taylor-Couette cell design used in the current experiments. The top and bottom parts are 6" $\times$ 6" $\times$ 0.5" and 6" $\times$ 6" $\times$ 1" respectively. The cylinder has a 2" outer diameter and 1.75" inner diameter. The four 1/4" screws are for applying pressure on the O-rings to seal the set up. The location of the O-ring slots are shown with red circles.
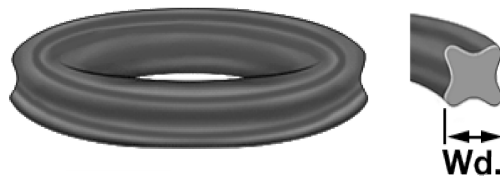
Figure 4-10:   Schematic of the cross section of an X-profile O-ring used in the Taylor-Couette cell design to ensure a tight seal. The nominal width of the O-ring used is 1/16" with an outer diameter of 2".

The Delrin blocks were manually squared on a mill using a 2" face mill. Then the closed and open holes were made using a pocketing operation with a 3/8" end mill. To seal the setup from any leakage, two O-rings were used, one on each of the

blocks. The O-ring slots (designated by the red circles on Figure 4-9) were made using a profiling operation with a 1/16" end mill. The O-rings chosen were X-profile O-rings as shown in Figure 4-10 (also known as Quattro seals [142]) and have four points of contact which can offer a better seal in dynamic systems. To put pressure on the O-rings the entire setup is assembled using four 1/4" socket screws as seen in Figure 4-9. To be able to constantly monitor the effect of pressure and changes in the height of the free surface as discussed in section 4.3.1 and avoid the entrance of air bubbles into the working fluid, four additional holes were drilled on the top surface. In addition, to control the effect of the height, the Reynolds number of the flow was changed by both changing the angular velocity within a range of $1 \leqslant \Omega_i \leqslant 120$ rad/s as well as the viscosity of the working fluid by using different mixtures of glycerol and DI water. The engineering drawing of the top and bottom blocks are shown in Figures 4-12 and 4-13.
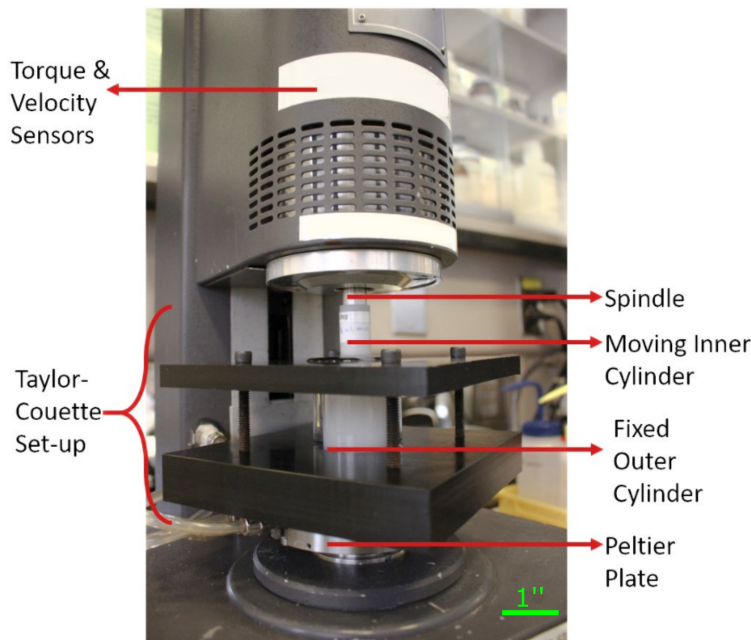
Figure 4-11: Experimental setup of the custom-designed and built Taylor Couette cell used in this study. The Taylor-Couette cell mounted on the stress-controlled rheometer (TA Instruments AR-G2).

Stream-wise-aligned Riblet covered rotors with V-grooves were 3D printed using a Form 1+ 3D printer. A snapshot of the rotor configuration in addition to the added
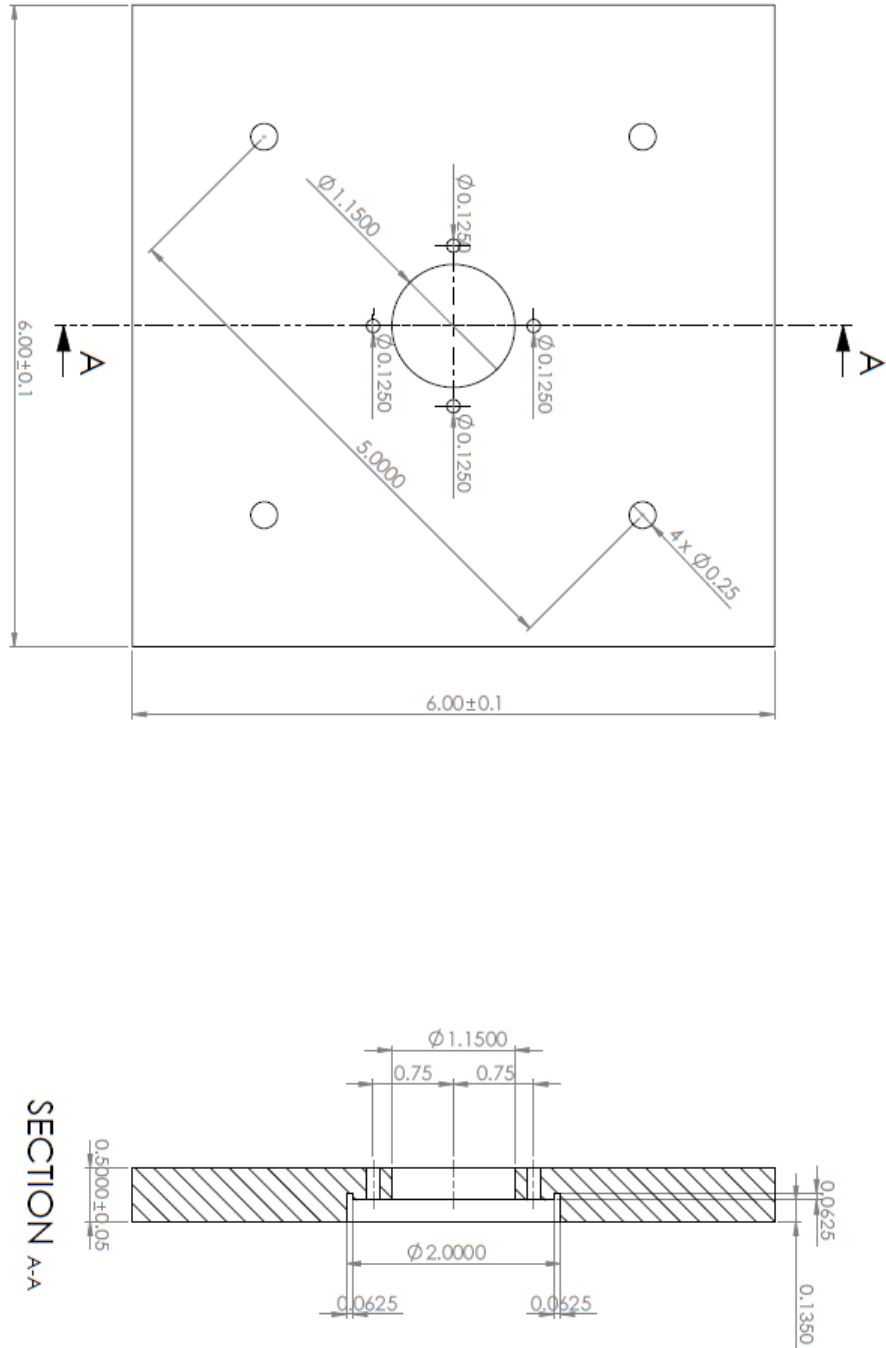
Figure 4-12: Engineering drawings of the top block of the Taylor-Couette cell. All dimensions are shown in inches.
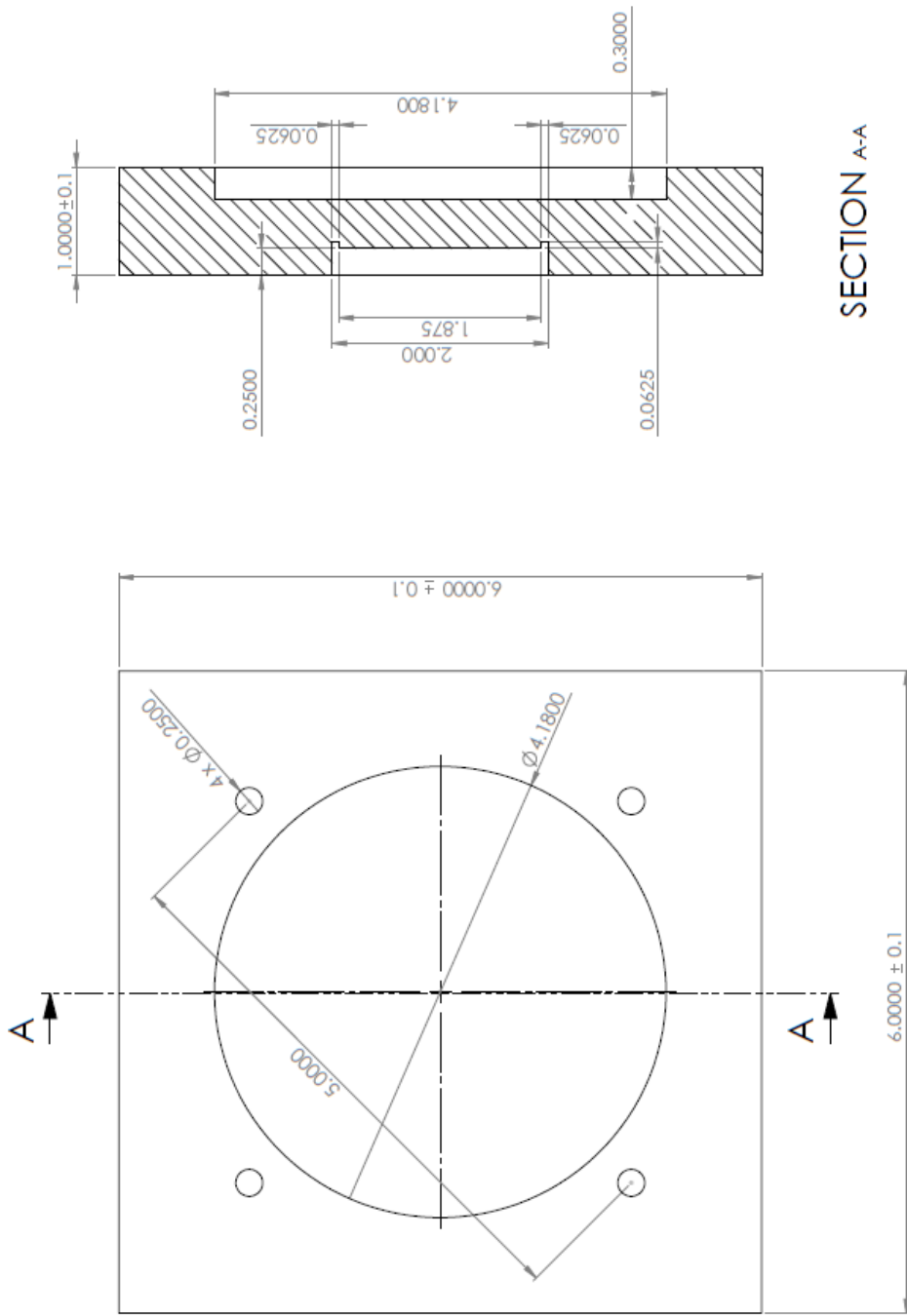
Figure 4-13: Engineering drawings of the bottom block of the Taylor-Couette cell. All dimensions are shown in inches.

(a)

(b)
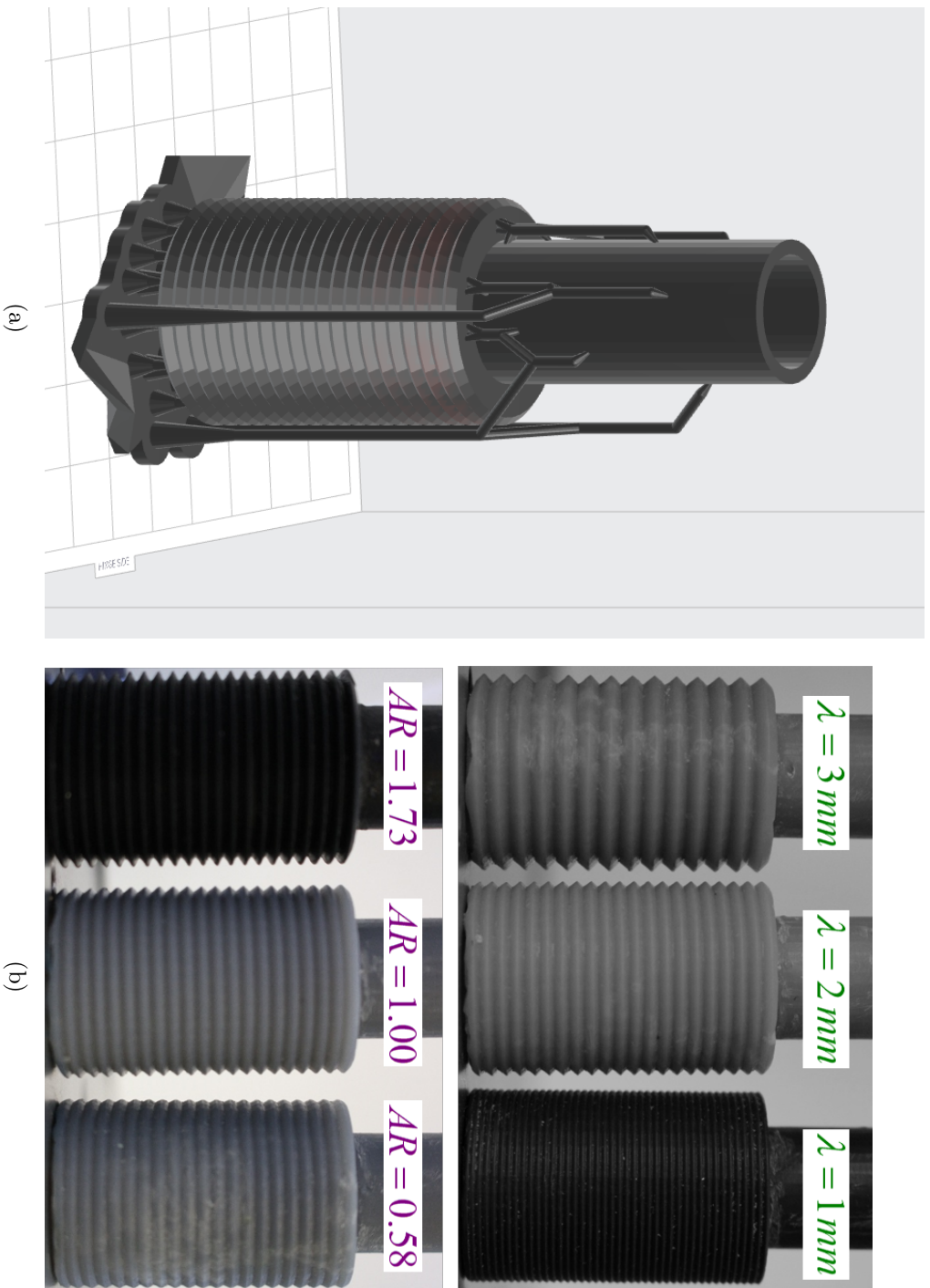
Figure 4-14: (a) A screen shot of the 3D model of the riblet covered rotors with the needed supports prior to printing using a Form 1+ 3D printer. The supports were created using Formlabs software preForm. (b) 3D printed riblet covered rotors with different wavelengths $\lambda = 1$ mm, 2 mm, and 3 mm and aspect ratios AR = 0.58, 1, and 1.73.

supports needed for 3D printing in the corresponding software preForm is shown in Figure 4-14(a). The rotor was intentionally printed in the shown configuration to avoid cracking and chipping the surface of the riblets as well as top of the rotor (which gets connected to the spindle of the rhometer) while removing the supports. The finish of the bottom is of least importance as the effect on the measured torque is always subtracted through a calibration process. The calibration method will be discussed in more detail in Section 4.5.1. To allow for comparison, a smooth rotor was also 3D printed. The rotors can be mounted to the moving spindle of the rheometer and thus the angular velocity and torque on the inner rotor are measured using the sensors located in the rheometer head. The overall assembled Taylor-Couette cell and the rotors as attached to the rheometer are shown in Figure 4-11 and a few of the printed rotors are shown in Figure 4-14(b).

All these Taylor-Couette configurations (the fixed cell and the rotors together) have a radius ratio of $\eta = 0.63$ with $R_i = 14$ mm and $R_o = 1.75" = 22.23$ mm and a dimensionless height of $\Gamma = 5.1$ and $L = 42$ mm . The riblets of the rotors are aligned in the circumferential direction (flow direction) and they are printed with three different wavelengths of $\lambda = 1$ mm, 2 mm, and 3 mm (The minimum resolution mentioned in the specifications of the Form 1+ printer is 300 μm), and with three different aspect ratios of AR $= 0.58$, 1, and 1.73 corresponding to side angles of $\theta = 30°, 45°$ and $60°$ (9 different rotors + 1 smooth rotor).

4.5.1 Calibrating the Effect of the Closed Ends

With the limitations of the real life experiments compared with the idealized theoretical models, there is a need to calibrate the experimental results for the effects rising from the non-ideal setups used in the experiments. Taylor-Couette flow is not an exception to this fact and various methods can be used to deduct these effects from the measurement. The most common issue with a Taylor-Couette setup is arisen from the added torque due to the no-slip boundary condition on the bottom enclosure of the cell and the bottom of the rotor. Depending on the setup used, similar condition can arise for the top of the cell as well.

In the current setup, the rotors are connected to the head of the rheometer through the spindle and they get suspended in the fluid inside the Taylor-Couette flow and the rotor does not come into contact with the bottom of the Taylor-Couette cell. A schematic of a two dimensional cross section of the assembled Taylor Couette setup used here is shown in Figure 4-15(a) with the radii of the inner and outer cylinder and the axial height of the rotor marked. As it can be seen on the figure, while the Taylor-Couette cell has a top plate, the opening on this plate has a diameter larger than the diameter of the rotors used. Therefore, top of the rotor is only in contact with fluid and no walls above this portion of the working fluid. Thus no additional frictional effect is sensed from the top of the rotors and the only difficulty comes from the pressure effect which was discussed earlier.
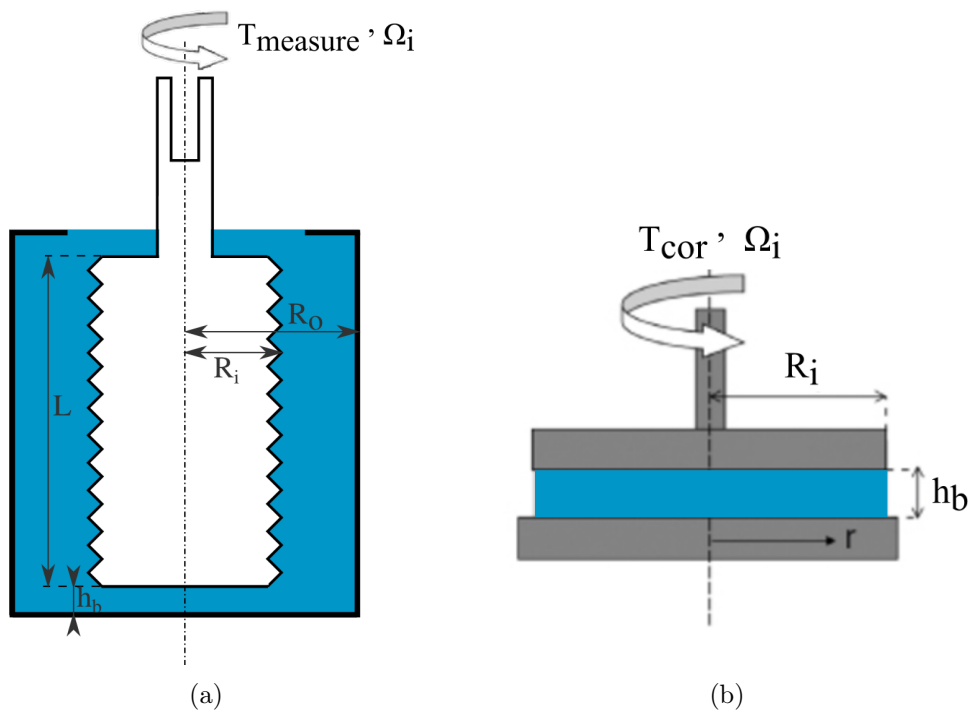
Figure 4-15: (a) Schematic of the geometry of the Taylor-Couette setup with closed bottom gap with height h_b from Equation 4.55.(b) Schematic of the flow between the bottom of the Taylor-Couette cell and the bottom of the rotor.

But the bottom of the Taylor-Couette setup is closed and this results in the torque measurements to be larger compared to the calculations of the creeping flow theory as shown in Equation 4.33 in the laminar or Couette regime (when only the inner

cylinder is rotating). Therefore, one can decompose the measured torque (call it T_{measure}) into two components, a theoretical part (T_{th} which is the same as Equation 4.33) and a correction term, T_{cor}.

$$T_{\text{measure}} = T_{\text{th}} + T_{\text{cor}} \qquad (4.54)$$

Different methods can be employed to find T_{cor}. For example, Rosenberg and co-workers first make their measurements using a Taylor-Couette cell completely filled with the fluid as shown with the schematic A in the Figure 4-16 and this corresponds to the measured torque T_{measure}. Then they repeated the experiments, with the same Taylor-Couette cell, but this time filled with fluid only up to the bottom of the rotor as shown in Schematic B and use the results as T_{cor}. Ultimately, they subtracted the results of the measurements T_{cor} from the original torque measurements T_{measure} to find the torque associated with the schematic C. The results are shown in Figure 4-16 [109]. With this method they were able to achieve a good agreement between the friction coefficient previously reported (Figure 4-16).
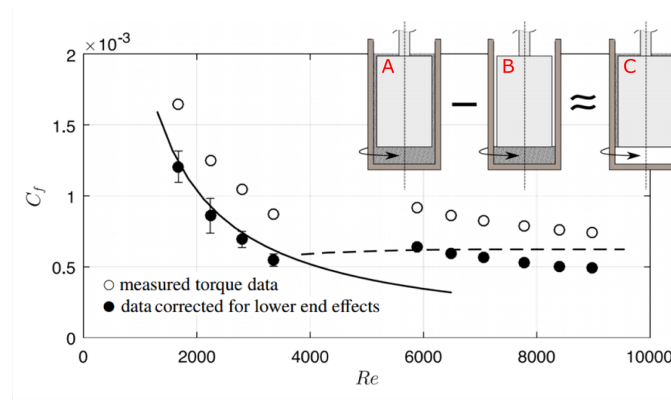
Figure 4-16: Schematic of the calibration method for the effect of the bottom gap as employed by Rosenberg et. al and plot of the measured friction coefficients and corrected friction coefficients as a function of the Reynolds number [109].

Here, to find the correction term T_{cor}, I model the effect of the viscous flow in between the bottom of the Taylor-Couette cell and the bottom of the rotor as shear flow between two parallel plates, as shown in the schematic in Figure 4-15(b).Therefore, this correction term can be analytically calculated and written as [138]

$$T_{\text{cor}}(h_{\text{b}}) = 2\pi\mu \frac{R_{\text{i}}^4}{4h_b}\Omega_{\text{i}} \tag{4.55}$$

where for a Taylor-Couette cell with a fixed geometry, the term T_{cor} is a function of the bottom gap size denoted by h_{b}. Now with the above equation, one can calibrate the experimental setup for the h_{b} that would result in the equality shown in Equation 4.54. In the calibration, using the case of a small Reynolds number of $\text{Re}_d = 4$, torque on the inner rotor was measured while changing the bottom gap h_{b} and then the results were compared with the calculated torque using $T_{\text{calc}} = T_{\text{th}} + T_{\text{cor}}$. The difference between the measured and calculated torques can be presented as an error defined as

$$E(h_{\text{b}}) = \frac{T_{\text{measure}} - T_{\text{calc}}}{T_{\text{calc}}} \times 100 \tag{4.56}$$

as a function of the gap height h_{b} and the results are shown in Figure 4-17. As shown in the figure, the bottom gap of $h_{\text{b}} = 520$ μm gives almost no error (0.02%) and hence this gap height has been used for the rest of the measurements. For the range of $3 < \text{Re}_d < 60$ the infinity norm of the error for the measurements shown later in Figure 4-18 is found to be 0.9% and for $60 < \text{Re}_d < 80$ which is in the transition region, the norm of the error increases to 3.5% and keeps increasing as Re_d is increased and the flow transitions to the Taylor vortex flow (Infinity norm returns the largest value in an array).

4.5.2 Characterisation of the Smooth Rotor Taylor-Couette Flow

As a baseline for comparison, the torque on a smooth base rotor is measured for a range of Reynolds numbers and Figure 4-18 shows the measured torque for the Reynolds number $4 < \text{Re}_d < 110$ using a mixture of 75% volume in glycerol and 25% DI water as the working fluid (The viscosity of the mixture is measured with a 40 mm cone and plate setup to be $\mu = 0.0366$ Pa.s and the density of the mixture
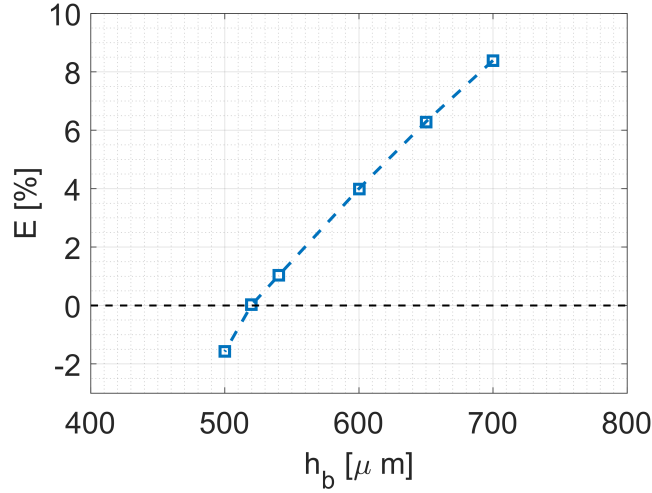
Figure 4-17: The calibration plot, showing the error as defined in Equation 4.56 as a function of the bottom gap height h_b.

can be calculated to be $\rho = 1190$ kg/m^3 [143]). As seen in the figure the result of the experiments match very well with the theoretical torque plus the correction arising from the bottom plate. For the rest of the work, to allow for comparison between numerical calculations and the experimental results, the correction term will be subtracted from the measured torque to omit the effect of the bottom gap from the results.

To find the location of transition from the laminar regime (Couette flow) to the Taylor vortex regime from the experimental results, I follow a similar method to the one used by Lathrop et. al [128, 127]: The exponent α for local torque scaling ($G \sim \mathrm{Re}^\alpha$ where G is the dimensionless measured torque after subtracting the correction term) is calculated as follows using Equation 4.57

$$\alpha = \frac{\partial \, \log_{10} G}{\partial \, \log_{10} \mathrm{Re}_d} \tag{4.57}$$

and the results of the calculations are presented in Figure 4-19.

As it can be seen in the figure, for $\mathrm{Re}_d < 60$ the exponent remains $\alpha = 1$ as it is expected from the theory (equation 4.36) and then between a range of Reynolds number of $60 < \mathrm{Re}_d < 110$ the exponent goes through a sudden change up to $\alpha \approx 2$ and down to $\alpha \approx 1.53$. In this range the flow is transitional. The vertical line at
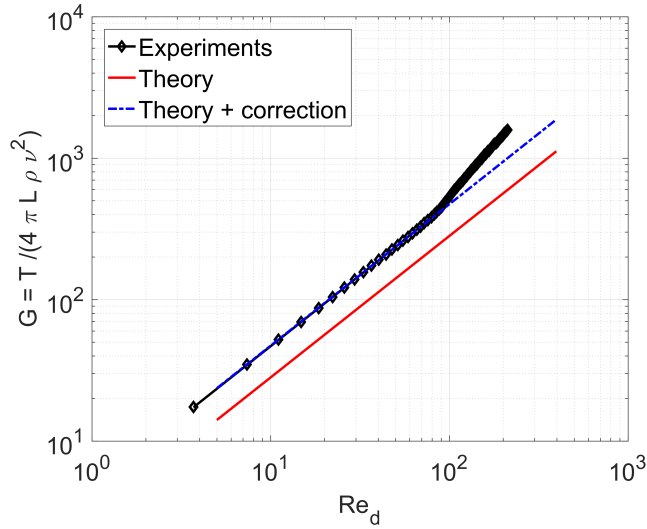
Figure 4-18: Experimental data of non-dimensional torque as a function of the Reynolds number Re_d for a smooth rotor in Taylor-Couette cell with $\eta = 0.63$ and $\Gamma = 5.1$ in addition to the theoretical results from the creeping flow calculations incorporating the added correction term from Equation 4.55 for the effect of the bottom gap with $h_b = 520$ μm.
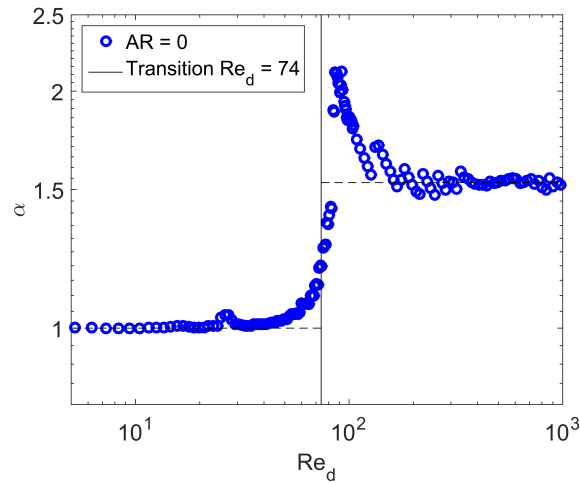
Figure 4-19: Exponent of the local torque scaling for $G \sim Re_d^\alpha$ as a function of the Reynolds number, calculated using Equation 4.57.

$Re_d = 74$ (corresponding to $Ta_{crit} = 2480$) is the location of the theoretical transition from laminar to Taylor Vortices for $\eta = 0.63$ [122] sits within an intermediate location in this region and points to the onset of the jump in the magnitude of the exponent. Thus, the theoretical transition predicts the transition in the experimental results

very well. In addition, for the range of $400 < \text{Re}_d < 10^4$, Wendth has previously reported an exponent of $\alpha = 1.5$ for the torque scaling [144] which matches very well with the exponent $\alpha \approx 1.53$ found here.

4.6 Experimental Results

Since I am interested in understanding the effect of the riblet geometry on the changes in the total frictional torque on the inner cylinder, the results presented are in the form of the changes in torque as a function of the various dimensionless variables introduced earlier in the chapter. First, I present the results of the experiments over a range of Reynolds numbers of $4 < \text{Re}_d < 1000$ in Figure 4-20. Here changes in torque are defined as equation 4.58

$$\frac{\Delta G}{G_0} = \frac{G - G_0}{G_0} \times 100 \tag{4.58}$$

where G is the non-dimensional torque measured for the riblet covered rotors and corrected using the correction term in Equation 4.55, and G_0 is the non-dimensional torque of the smooth rotor after correction. The results are presented in the three plots as a function of the Reynolds number Re_d, the aspect ratio of the riblets, AR, as well as λ/d. The vertical dashed line shows the location of the theoretical transition point $\text{Re}_d = 74$ which was also discussed earlier. The horizontal dashed line shows the line of no changes in torque and based on the definition of the torque change, a negative torque change corresponds to a drag reducing case and a positive torque change corresponds to a drag increasing case. Each experimental data point were repeated at least 2-3 times to confirm repeatability as well as to obtain the error bars shown in the figures. The range of data between $4 < \text{Re}_d < 105$ were measured using a working fluid composed of 75% by volume glycerol and 25% DI water and the mixture viscosity was measured for each test and this value was subsequently used for the data analysis. The range of data between $100 < \text{Re}_d < 1000$ were measured using a working fluid with 50% by volume of glycerol and 50% DI water and again for each test the viscosity of the fluid was measured and used for the analysis.
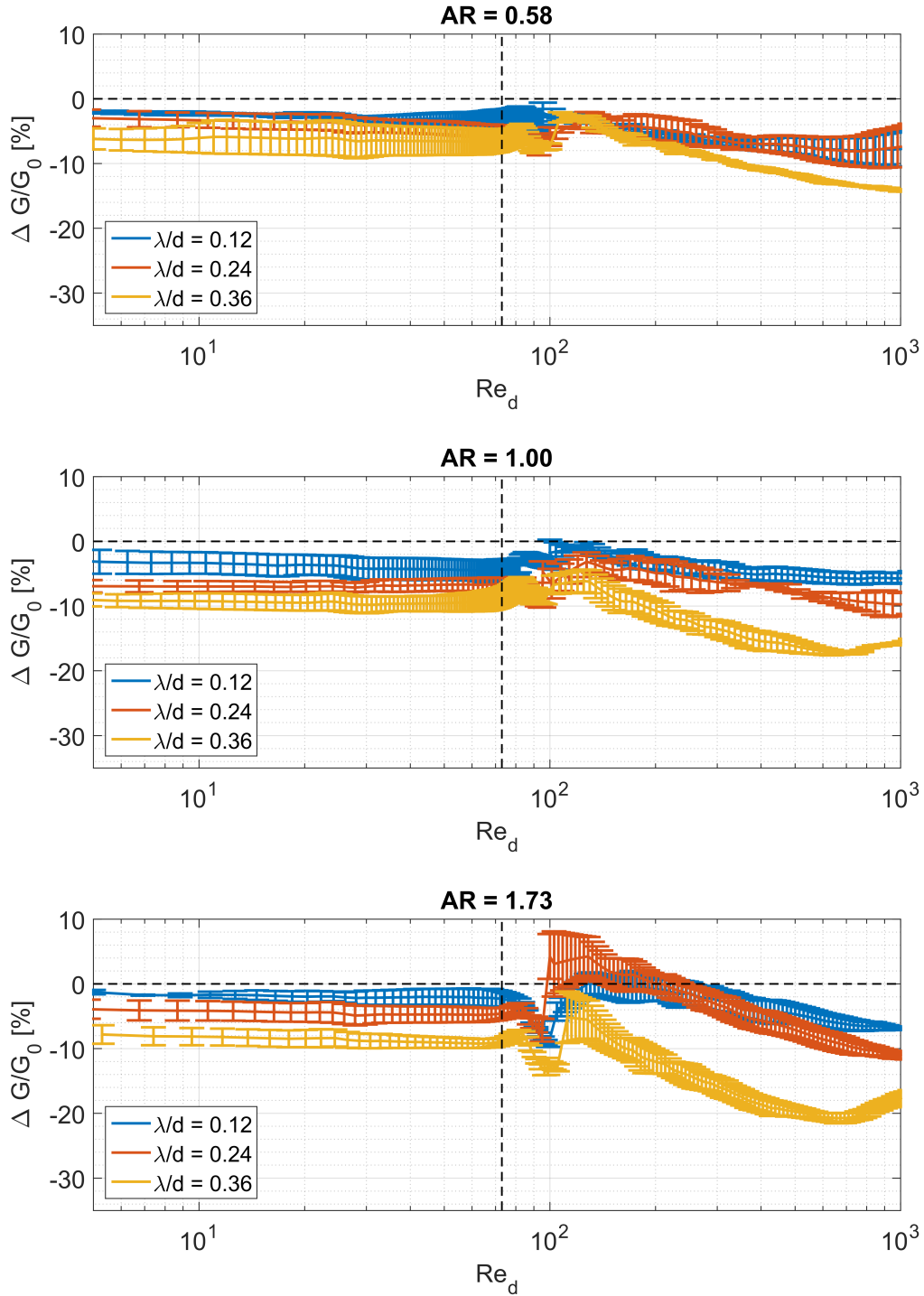
Figure 4-20: Results of reduction in torque measured for riblet covered rotors compared with smooth rotors as a function of the Reynolds number and λ/d for (a) AR = 0.58, (b) AR = 1.00 and (c) AR = 1.73.

4.7 Comparison with Numerical Simulations

In the laminar steady two dimensional flow where only the inner cylinder is rotating, prior to transition to a Taylor Vortex state (TV), the velocity profile is only a function of the geometry of the Taylor-Couette cell and not a function of the Reynolds number (Equation 4.18). A similar behaviour is expected in the presence of riblets and therefore, it is expected that the resulting change in the torque due to riblets will not be a function of the Reynolds number prior to transition to the Taylor vortices (TVs). Figure 4-20 also shows that before approaching the critical Reynolds number, the changes in the torque is nearly constant with respect to Re_d. While all cases show a drag reducing effect, the results seem to be only dependent on changes in the riblet geometry and not in the dynamics of the flow (as captured by Re_d).

To confirm this, axi-symmetric and periodic models of a single riblet in a Taylor-Couette setup with the same λ/d and a range of $0 < \mathrm{AR} < 2.5$ were created and the numerical simulations were performed using OpenFOAM finite volume solver. Similar to the boundary layer simulations mentioned in Chapter 3, the steady state algorithm SIMPLE was used. To compare the effect of the Reynolds number, two cases with $\mathrm{Re}_d = 23$ and $\mathrm{Re}_d = 58$ were modelled to calculate the changes in torque for a range of $0 < \mathrm{AR} < 2.5$ and λ/d similar to the values used in the experiments. The experimental results are overlaid for comparison. As seen in Figures 4-21, the measured and calculated changes in torque are identical between the two Reynolds numbers presented as long as the geometric variables are kept constant. This can also be seen in the experimental results shown in Figures 4-20.

However, changing the geometry of the riblets by either changing the AR or changing λ/d has a direct effect on the torque changes measured. First consider the case where the wavelength of the riblets are kept constant (constant λ/d) and the amplitude of the riblets are varied (changing AR). As seen in the experimental results in Figure 4-20, the results do not show a clear trend across the figure, but if the results are replotted as in Figures 4-21, it can be seen that for a constant value of λ/d the change in torque is a non-monotonic function of the aspect ratio AR of the riblets.
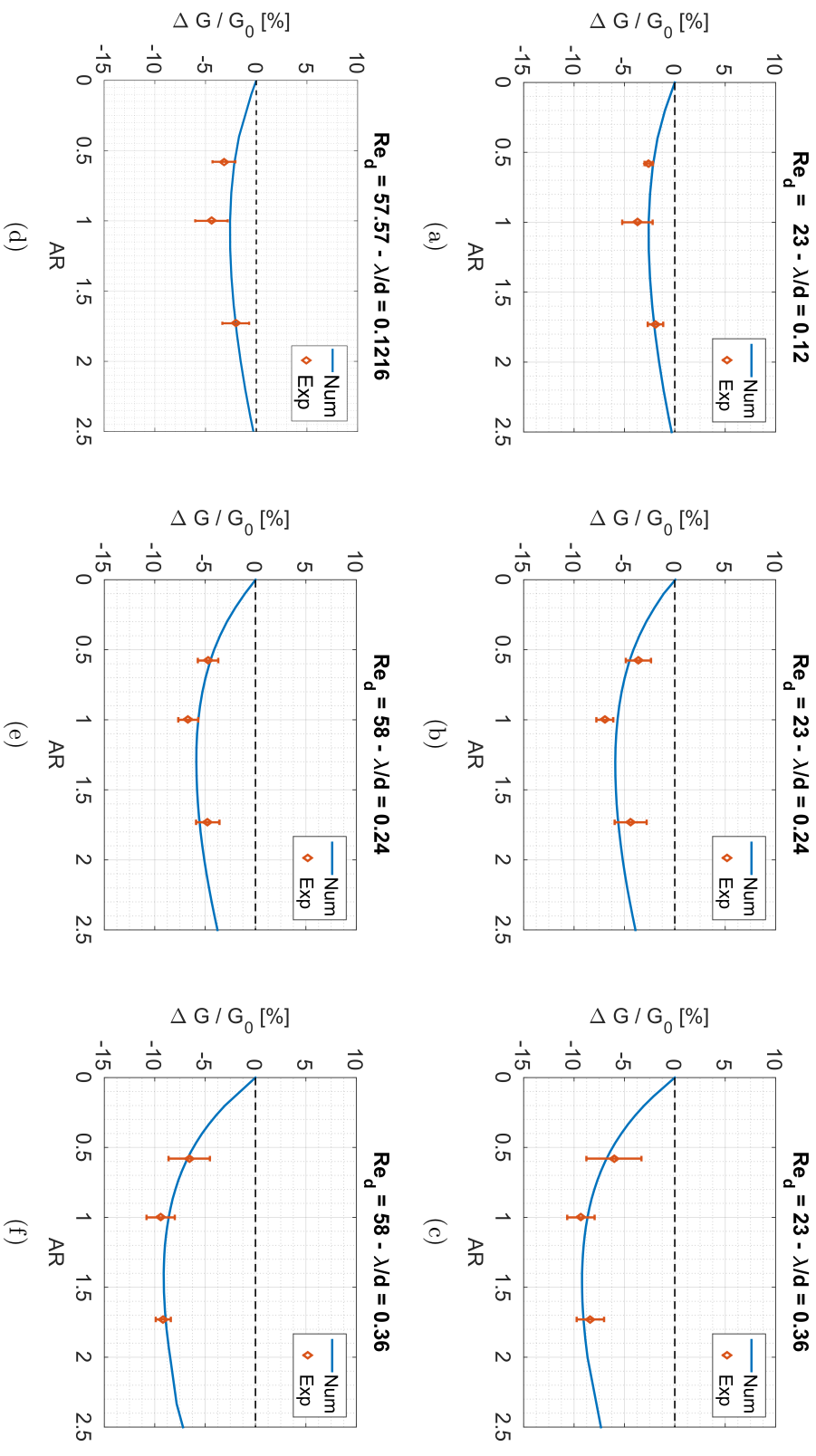
Figure 4-21: Numerical and experimental results of changes in the non-dimensional torque G as a function of the AR for (a) $\mathrm{Re}_d = 23$ and $\lambda/d = 0.12$, (b) $\mathrm{Re}_d = 23$ and $\lambda/d = 0.24$, (c) $\mathrm{Re}_d = 23$ and $\lambda/d = 0.36$, (d) $\mathrm{Re}_d = 58$ and $\lambda/d = 0.12$, (e) $\mathrm{Re}_d = 58$ and $\lambda/d = 0.24$ and (f) $\mathrm{Re}_d = 58$ and $\lambda/d = 0.36$.

In addition, the maximum torque reduction happens at an intermediate aspect ratio which is dependent on the wavelength, and as λ/d is increased a wider range of aspect ratios offer torque reduction. In these sets of experiments in the laminar Couette regime up to 10% torque reduction was observed.

The non-monotonic behaviour of the change in torque as a function of the aspect ratio can be discussed in more detail, by considering the component of the traction vector normal to the wall of the inner cylinder. If I denote the shear stress tensor in the fluid by $\boldsymbol{\tau}$ then the shear stress at the wall or the so-called traction vector, $\boldsymbol{\tau}_\mathrm{w}$, can be found as

$$\boldsymbol{\tau}_\mathrm{w} = \boldsymbol{\tau}.\boldsymbol{n}_\mathrm{w} \tag{4.59}$$

and when the riblets are present, the normal vector to the wall can be written as

$$\boldsymbol{n}_\mathrm{w} = \begin{bmatrix} \cos\theta \\ 0 \\ -\sin\theta \end{bmatrix} = \begin{bmatrix} \dfrac{1}{\sqrt{1+\mathrm{AR}^2}} \\ 0 \\ -\dfrac{\mathrm{AR}}{\sqrt{1+\mathrm{AR}^2}} \end{bmatrix} \tag{4.60}$$

where for a smooth rotor with $\mathrm{AR} = 0$, the wall normal is back to $\boldsymbol{e}_r$. Therefore, the component of the traction vector in the circumferential direction which contributes to the frictional torque can be found to be

$$\tau_{\mathrm{w},\phi} = (\boldsymbol{\tau}.\boldsymbol{n}_\mathrm{w}).\boldsymbol{e}_\phi = \tau_{r\phi}\cos\theta - \tau_{z\phi}\sin\theta \tag{4.61}$$

and thus

$$\tau_{\mathrm{w},\phi} = \tau_{r\phi}\frac{1}{\sqrt{1+\mathrm{AR}^2}} - \tau_{z\phi}\frac{\mathrm{AR}}{\sqrt{1+\mathrm{AR}^2}}. \tag{4.62}$$

In the presence of riblets, in addition to $\tau_{r\phi}$ the stress tensor will also have a non-zero value of $\tau_{z\phi}$ and both of the shear stress components $\tau_{r\phi}$ and $\tau_{z\phi}$ vary across the riblet length and they follow a distribution shown as in Figures 4-22(a) and 4-22(b) with the highest stress at the peaks of the riblets and the lowest stress at the trough

203
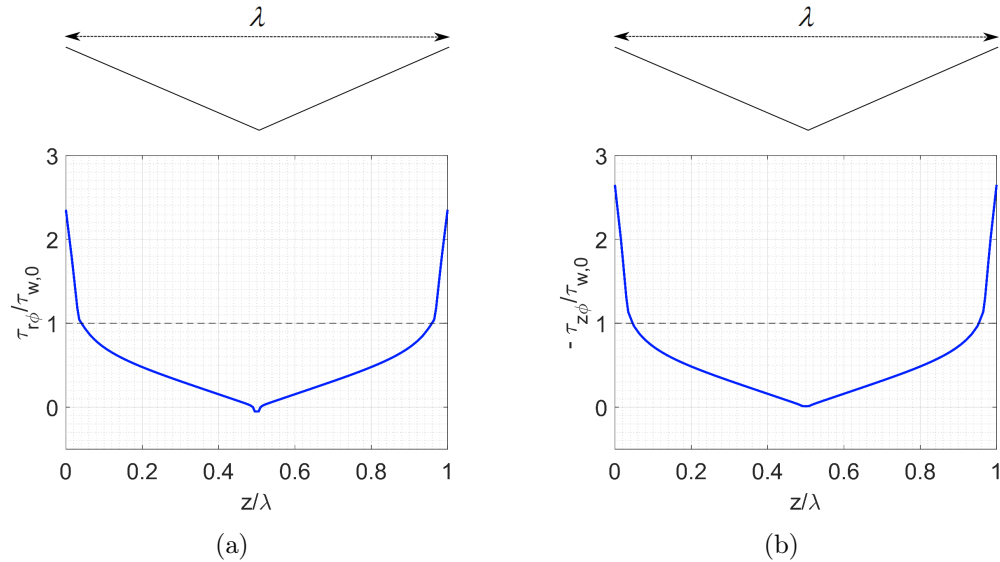
of the riblets.

Figure 4-22: Distribution of shear stress components (a) $\tau_{r\phi}$ and (b) $\tau_{z\phi}$ normalized by the shear stress in the case of a smooth rotor as a function of the axial location on the riblet surfaces with $\lambda/d = 0.12$ and AR $= 1$, and $\mathrm{Re}_d = 58$ (is the same for any other Reynolds number prior to transition to Taylor vortices. Here $\tau_{\mathrm{w},0}$ is the shear stress in the case of a smooth rotor with AR $= 0$.

Therefore, the circumferential components of the traction vector $\tau_{\mathrm{w},\phi}$ acting on each riblet is calculated from the numerical simulations for the case of $\lambda/d = 0.12$ and $\mathrm{Re}_d = 58$ (which is similar to any other Re_d prior to transition to Taylor vortex flow) and are plotted non-dimensionalized by the value of $\tau_{\mathrm{w},0}$ as shown in Equation 4.26 for the smooth rotor and as a function of the axial direction z, non-dimensionalized by λ and shown in Figure 4.7.

As shown in the figure, the introduction of the riblets results in a varying shear stress distribution on the wall. Close to the trough of the riblets the shear stress is lower than the shear stress in the case of the smooth rotor and near the peaks of the riblets, the shear stress is higher than the smooth rotor. Similar behavior has been previously reported in flows over riblets in channel flows and boundary layer flows [47, 70] and also was observed in my numerical simulation of the boundary layer flow over riblets as noted in Section 3.5.2 of chapter 3 along the velocity decomposition as well.
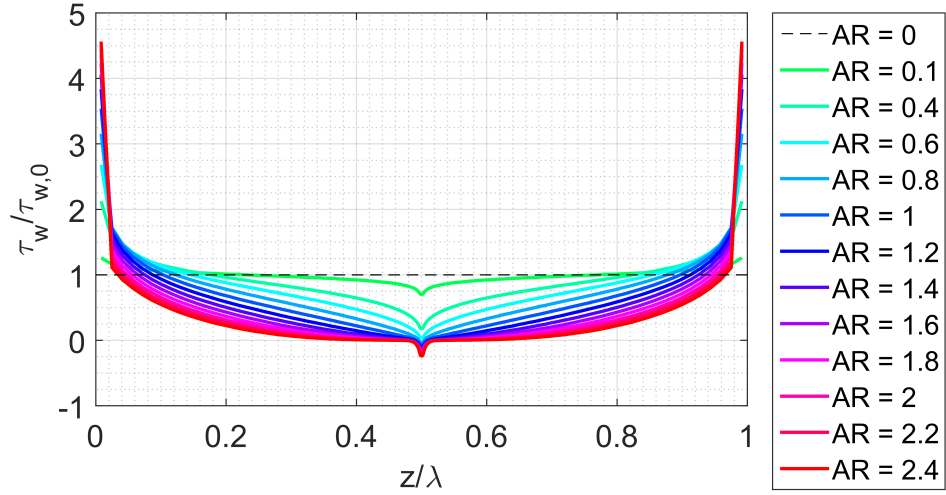
Figure 4-23: Distribution of shear stress normalized by the shear stress of the case with a smooth rotor (Equation 4.26) for riblets of $\lambda/d = 0.12$ within one riblet at $\mathrm{Re}_d = 58$ as a function of the AR corresponding to figure 4-21(b).

As seen in Figure 4.7, as the aspect ratio, AR, of the riblets is increased, the shear stress distribution expands so that a wider area of the riblet surface experiences a shear stress which is lower than the shear stress on a smooth rotor and a smaller portion of the riblet wall locally experiences a shear stress that is larger than the shear stress on a smooth rotor. Therefore, upon integration, the riblet surface will experience an average shear stress that is lower than the smooth rotor, and increasing the aspect ratio AR of the riblets results in a constant decrease in the average shear stress $< \tau_\mathrm{w} >$ distribution as is shown in Figure 4.7.

However, adding riblets and increasing the aspect ratio of the riblets also results in a constant increase in the total wetted area of the inner cylinder. The increasing trend in the wetted area is also plotted in Figure 4.7. Therefore, the interplay of the decrease in the average shear stress on the wall and the increase in the wetted area as the aspect ratio is increasing results in the non-monotonic behavior (as seen in Figure 4-21(b)) of the total torque as a function of the aspect ratio.

$$T = \int_0^\lambda \boldsymbol{r}_\mathrm{w} \times \boldsymbol{\tau}_w dS = \int_0^\lambda r_\mathrm{w} \tau_{\mathrm{w},\phi} 2\pi r_\mathrm{w} dl = \int_0^\lambda r_\mathrm{w}^2 \tau_{\mathrm{w},\phi} 2\pi \sqrt{1 + \mathrm{AR}^2} dz \qquad (4.63)$$

At lower aspect ratios, the decrease in the shear stress on the wall overcomes the increase in the wetted area (S in Figure 4.7) and the final combination results in a reduction in the total torque. However, from an intermediate aspect ratio forward, the increase in the area given by the last term in the integrand will overcome the decrease in the average shear stress distribution and the total integrated torque will increase, until ultimately the riblets will not be able to offer any reduction in frictional torque. The location of the maximum torque reduction is dependent on the λ/d and for the range of λ/d shown in Figures 4-21, the optimum aspect ratio is between $1.1 < \mathrm{AR} < 1.5$.
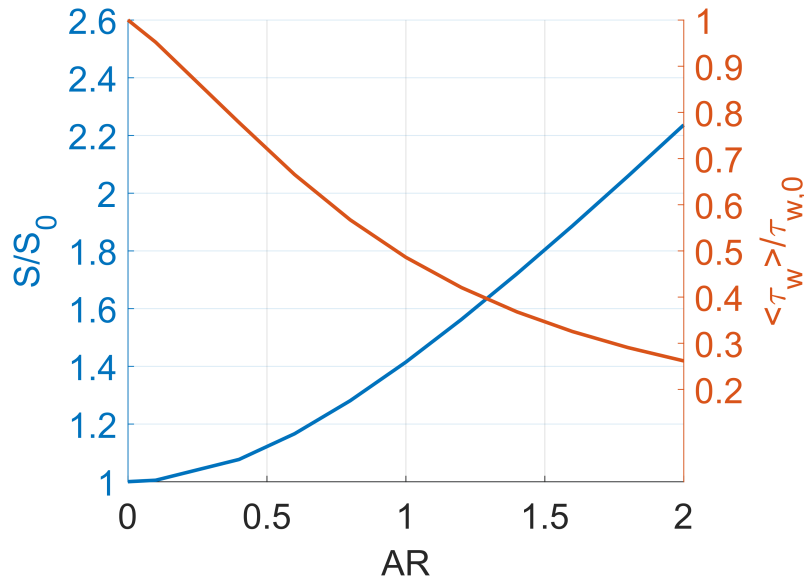
Figure 4-24: Average shear stress for $\mathrm{Re}_d = 58$ and $\lambda/d = 0.12$ as a function of the AR and the change in the wetted area of the riblets as a function of the AR. Increasing the AR of the riblets results in a decrease in the average shear stress within one riblet while the wetted area S increases. Here S_0 is the wetted surface area of a smooth rotor in cylindrical Couette flow.

On the other hand, when the aspect ratio of the riblets is kept constant, the torque reduction achieved is directly dependent on wavelength of the riblets and as λ/d increases, the torque reduction achieved is enhanced as seen in Figures 4-20 and 4-21. If the torque reduction at a constant AR is plotted as a function of the λ/d (shown in Figure 4-25), it can be seen that the torque reduction follows a linear trend with the λ/d.
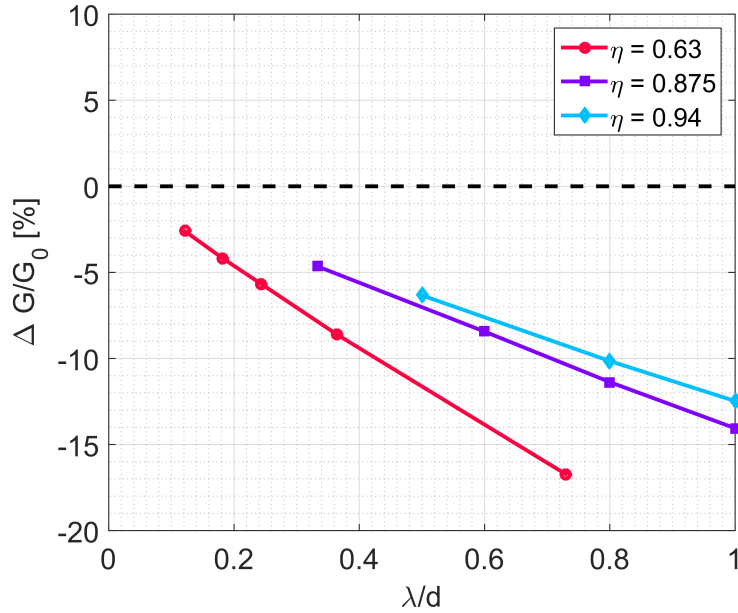
Figure 4-25: Torque reduction as a function of the wavelength of the riblets at fixed value of the aspect ratio, AR = 1.00.

4.8   Theoretical Modelling

To understand the effect of the size of the riblets, I can expand my theoretical calculations of the cylindrical Couette flow to higher order terms for small riblets with amplitudes smaller than the radius of the inner cylinder ($A \ll R_i$). To consider this small parameter and be able to compare with the rest of the dimensionless groups introduced throughout this chapter, I can write

$$\frac{A}{R_i} = \frac{\text{AR}}{2} \frac{\lambda}{R_i} \tag{4.64}$$

and hence I can think of two small parameters in the problem. One is the aspect ratio of the riblets $\text{AR} = 2A/\lambda$ (meaning very shallow riblets) as well ε

$$\varepsilon = \frac{\lambda}{R_i}. \tag{4.65}$$

where at the limit of $A/R_i \to 0$, the results of the torque calculations would go back to the results from a smooth cylinder in steady Taylor-Couette flow and at a constant

aspect ratio increasing the wavelength would result in an increase in ε and similar to the schematic shown in Figure 4-26.

(a)   (b)
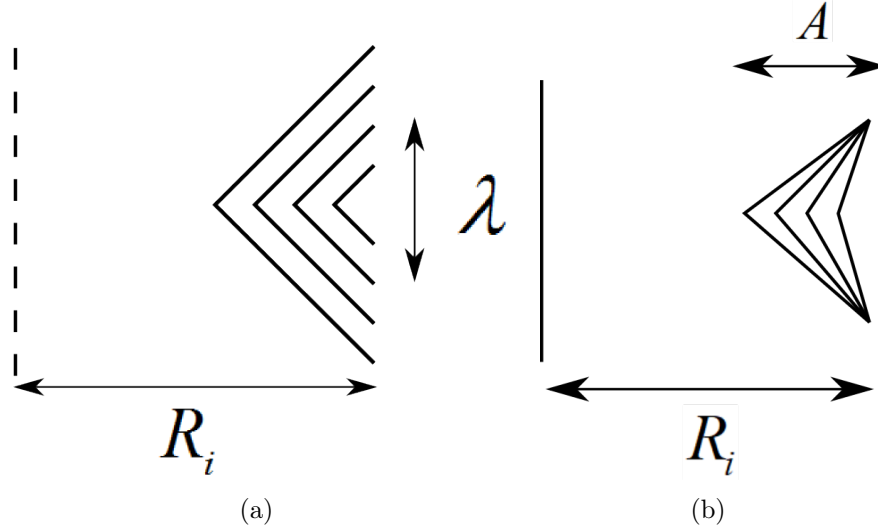
Figure 4-26:   Schematic of the small parameters (a) $\varepsilon = \lambda/R_{\mathrm{i}}$ and (b) $\mathrm{AR} = 2A/\lambda$ to use for the higher order terms in the Taylor-Couette solution.

Then, assume the azimuthal velocity (v_ϕ) profile in presence of the riblets can be written in the below form, which has a zeroth order and a first order term, with the zeroth order being the same profile as the solution for smooth laminar Couette setup. Any effect of higher order terms is neglected here,

$$v_\phi = v_\phi^{(0)} + \mathrm{AR} \ \varepsilon \ v_\phi^{(1)} + O(\mathrm{AR}^2 \ \varepsilon^2)... \tag{4.66}$$

and the zeroth order Couette solution is only a function of the radial direction r.

$$v_\phi^{(0)} = \frac{\eta}{1 - \eta^2} \left(\frac{R_{\mathrm{o}}}{r} - \frac{r}{R_{\mathrm{o}}} \right) \tag{4.67}$$

Also, Here it is assumed that v_r is of second and higher order and thus does not show up in the current analysis and v_z of the first order and is only a function of the radial direction. More details about this assumption can be found in Appendix A. Therefore

208

$$\begin{bmatrix} v_r \\ v_\phi \\ v_z \end{bmatrix} = \begin{bmatrix} 0 \\ v_\phi^{(0)} \\ 0 \end{bmatrix} + \text{AR } \varepsilon \begin{bmatrix} 0 \\ v_\phi^{(1)} \\ v_z^{(1)}(r) \end{bmatrix} + O(\varepsilon^2) \tag{4.68}$$

Thus, the radial and axial velocity do not show up in the equations of motion and the governing equation for flow between concentric cylinders simplifies to only the azimuthal component of the Navier-Stokes equation and can be written as

$$\frac{\partial}{\partial r}\left(\frac{1}{r}\frac{\partial}{\partial r}(rv_\phi)\right) + \frac{\partial^2 v_\phi}{\partial z^2} = 0 \tag{4.69}$$

And substituting for v_ϕ from Equation 4.66 I have (again neglecting the second and higher order terms):

$$\frac{\partial}{\partial r}\frac{1}{r}\frac{\partial}{\partial r}\left(r(v_\phi^{(0)} + \text{AR } \varepsilon \ v_\phi^{(1)})\right) + \frac{\partial^2}{\partial z^2}\left(\text{AR } \varepsilon \ v_\phi^{(1)}\right) = 0 \tag{4.70}$$

which can be divided into two separate equations

$$\frac{\partial}{\partial r}\frac{1}{r}\frac{\partial}{\partial r}\left(r(v_\phi^{(0)})\right) = 0 \tag{4.71}$$

$$\frac{\partial}{\partial r}\frac{1}{r}\frac{\partial}{\partial r}\left(r(v_\phi^{(1)})\right) + \frac{\partial^2}{\partial z^2}\left(v_\phi^{(1)}\right) = 0 \tag{4.72}$$

Since Equation 4.67 satisfies the equations for motion for smooth Taylor-Couette flow, then, Equation 4.71 is already satisfied and thus, the equation of motion for the first order term simplifies to Equation 4.72.

Now to solve this equation, let's make some simplifying assumption. Since the boundary condition on the inner cylinder is a constant rotation rate of Ω_i. Therefore, the velocity boundary condition on the riblets is not uniform and is dependent on the local position on the riblets wall. If $r_w(z)$ is the local radial location on the riblet inner cylinder, then the boundary condition for v_ϕ is written as

$$0 < z < \frac{\lambda}{2} \quad : \quad v_{\phi,\text{BC}} = r_w\Omega_i = (R_i - \text{AR } z)\Omega_i \tag{4.73}$$

and due to symmetry about the line of $z = \lambda/2$:

$$\frac{\lambda}{2} < z < \lambda \quad : \quad v_{\phi,\mathrm{BC}} = r_\mathrm{w}\Omega_\mathrm{i} = (R_\mathrm{i} - \mathrm{AR}\,(\lambda - z))\Omega_\mathrm{i}. \tag{4.74}$$

Thus for the first order term in azimuthal velocity, the boundary condition for $0 < z < \lambda/2$ can be written as

$$\mathrm{AR}\ \varepsilon\ v_{\phi,\mathrm{BC}}^{(1)} = v_{\phi,\mathrm{BC}} - v_\phi^{(0)}\Big|_{r=R_\mathrm{i}-\mathrm{AR}z} \tag{4.75}$$

and in the non-dimensional form as

$$\mathrm{AR}\ \ \varepsilon\ \frac{v_{\phi,\mathrm{BC}}^{(1)}}{R_\mathrm{i}\Omega_\mathrm{i}} = (1 - \mathrm{AR}\frac{z}{R_\mathrm{i}}) - \frac{v_\phi^{(0)}\Big|_{r=R_\mathrm{i}-\mathrm{AR}z}}{R_\mathrm{i}\Omega_\mathrm{i}}. \tag{4.76}$$

Now substituting for the zeroth order term from Equation 4.67 at $r = R_\mathrm{i}$, I get

$$\varepsilon\ \mathrm{AR}\ \frac{v_{\phi,\mathrm{BC}}^{(1)}}{R_\mathrm{i}\Omega_\mathrm{i}} = (1 - \mathrm{AR}\frac{z}{R_\mathrm{i}}) - \frac{\eta}{1-\eta^2}\left(\frac{R_\mathrm{o}}{Ri - ARz} - \frac{Ri - ARz}{R_\mathrm{o}}\right) \tag{4.77}$$

and by replacing $R_\mathrm{i}/R_\mathrm{o}$ with η I have

$$\varepsilon\ \mathrm{AR}\ \frac{v_{\phi,\mathrm{BC}}^{(1)}}{R_\mathrm{i}\Omega_\mathrm{i}} = (1 - \mathrm{AR}\frac{z}{R_\mathrm{i}}) - \frac{\eta}{1-\eta^2}\left(\frac{1}{\eta\left(1 - \mathrm{AR}\dfrac{\lambda}{R_\mathrm{i}}\right)} - \eta\left(1 - \mathrm{AR}\frac{\lambda}{R_\mathrm{i}}\right)\right). \tag{4.78}$$

Then substituting for

$$\mathrm{AR}\frac{z}{R_\mathrm{i}} = \mathrm{AR}\frac{\lambda}{R_\mathrm{i}}\frac{z}{\lambda} = \mathrm{AR}\ \varepsilon\ \frac{z}{\lambda} \tag{4.79}$$

and hence

$$\varepsilon \text{ AR } \frac{v_{\phi,\text{BC}}^{(1)}}{R_i\Omega_i} = (1 - \text{AR } \varepsilon\frac{z}{\lambda}) - \frac{1}{1-\eta^2}\frac{1}{\left(1 - \text{AR } \varepsilon\frac{z}{\lambda}\right)} + \frac{\eta^2}{1-\eta^2}\left(1 - \text{AR } \varepsilon\frac{z}{\lambda}\right). \quad (4.80)$$

So, now for shallow riblets with amplitude much smaller than R_i

$$\varepsilon \text{ AR} \ll 1, \quad (4.81)$$

I can use the Taylor series expansion

$$\frac{1}{\left(1 - \text{AR } \varepsilon \frac{z}{\lambda}\right)} = 1 + \text{AR } \varepsilon \frac{z}{\lambda} + O(\varepsilon^2\text{AR}^2)... . \quad (4.82)$$

Thus the boundary condition (neglecting the second and higher order terms) can be written as

$$\varepsilon \text{ AR } \frac{v_{\phi,\text{BC}}^{(1)}}{R_i\Omega_i} = (1 - \text{AR}\varepsilon\frac{z}{\lambda}) - \frac{1}{1-\eta^2}\left(1 + \text{AR}\varepsilon\frac{z}{\lambda}\right) + \frac{\eta^2}{1-\eta^2}\left(1 - \text{AR}\varepsilon\frac{z}{\lambda}\right) \quad (4.83)$$

and simplified to

$$\varepsilon \text{ AR } \frac{v_{\phi,\text{BC}}^{(1)}}{R_i\Omega_i} = \frac{-2}{1-\eta^2} \text{ AR } \varepsilon \frac{z}{\lambda} + O(\varepsilon^2\text{AR}^2)... \quad (4.84)$$

or equivalently

$$\frac{v_{\phi,\text{BC}}^{(1)}}{R_i\Omega_i} = \frac{-2}{1-\eta^2}\frac{z}{\lambda} + O(\varepsilon\text{AR})... . \quad (4.85)$$

In the limit of shallow grooves and small ε, the Equation 4.72 can be solved analytically with boundary conditions of $\Omega_o = 0$ at $r = R_o$ and Equation 4.84 at $r = R_i$. The solution can be written as

$$\frac{v_{\phi}^{(1)}}{R_i\Omega_i} = \frac{-2\eta}{(1-\eta^2)^2}\left(\frac{R_o}{r} - \frac{r}{R_o}\right)\frac{z}{\lambda}. \quad (4.86)$$

Now similarly to find the change in the torque due to the geometry, the torque

can also be expanded in terms of a zeroth and first order term as

$$T = T^{(0)} + \text{AR } \varepsilon \; T^{(1)} + O(\text{AR}^2 \varepsilon^2)... \tag{4.87}$$

where the torque on a smooth rotor $(T^{(0)})$ is as in Equation 4.33. Thus to calculate the first order term of torque, I use the first order term in velocity to calculate the additional contribution to shear rate on the wall. Since I am assuming $\text{AR} \ll 1$ then I can approximate the shear rate on the riblet wall as the shear rate calculated at $r = R_i$. Thus

$$\dot{\gamma}_{r\phi}^{(1)} = r \frac{\partial}{\partial r} \left(\frac{v_\phi^{(1)}}{r} \right) \tag{4.88}$$

which can be found to be

$$\dot{\gamma}_{r\phi}^{(1)} = \frac{-2\eta}{(1-\eta^2)^2} \frac{-2R_o}{r^2} \frac{z}{\lambda} R_i \Omega_i \tag{4.89}$$

and at $r = R_i$ then the shear stress on $r = R_i$ can be written as

$$\tau_{r\phi}^{(1)} = \mu \frac{4\eta}{(1-\eta^2)^2} \frac{R_o}{R_i^2} \frac{z}{\lambda} R_i \Omega_i. \tag{4.90}$$

Hence the first order correction term in torque can be calculated as

$$T^{(1)} = 2 \int_0^{\lambda/2} \tau_{r\phi}^{(1)} 2\pi R_i^2 dz. \tag{4.91}$$

Since the riblets are symmetric about each peak or trough, I calculate the integral on half of the riblet and then multiply the results by two. Thus substituting for the shear stress and simplifying I get

$$T^{(1)} = 16\pi\mu \frac{\eta}{(1-\eta^2)^2} \frac{R_o}{R_i} R_i^2 \Omega_i \int_0^{\lambda/2} \frac{z}{\lambda} dz. \tag{4.92}$$

Gathering terms and simplifying

$$T^{(1)} = 4(4\pi\rho\nu^2\lambda) \frac{\rho R_i \Omega_i d}{\mu} \frac{R_i}{\lambda d} \frac{1}{(1-\eta^2)^2} \int_0^{\lambda/2} \frac{z}{\lambda} dz \tag{4.93}$$

and then re-writing in terms of the different dimensional and dimensionless groups (such as $\rho R_\mathrm{i} \Omega_\mathrm{i} d/\mu = \mathrm{Re}_d$) from earlier definitions I have

$$T^{(1)} = 2(4\pi\rho\nu^2\lambda) \left(\frac{R_\mathrm{i}}{d\lambda} \frac{1}{(1-\eta^2)^2} \frac{\lambda^2}{4\lambda} \right) \mathrm{Re}_d \tag{4.94}$$

which simplifies to

$$T^{(1)} = \frac{1}{2}(4\pi\rho\nu^2\lambda) \frac{1}{(1-\eta^2)^2} \frac{R_\mathrm{i}}{d} \mathrm{Re}_d. \tag{4.95}$$

and in dimensionless form

$$G^{(1)} = \frac{T^{(1)}}{(4\pi\rho\nu^2\lambda)} = \frac{1}{2} \frac{1}{(1-\eta^2)^2} \frac{R_\mathrm{i}}{d} \mathrm{Re}_d. \tag{4.96}$$

Now to find the change in torque compared to a smooth rotor, I have

$$\frac{\Delta G}{G_0} = \frac{\left(G^{(0)} + \mathrm{AR}\ \varepsilon\ G^{(1)} \right) - G^{(0)}}{G^{(0)}}. \tag{4.97}$$

From Equation 4.33 and the earlier discussions I know that

$$G^{(0)} = -\frac{\eta}{(1-\eta^2)(1-\eta)} \mathrm{Re}_d \tag{4.98}$$

where the negative sign arises naturally from the definition of the rate of shear strain and torque. Therefore, Equation 4.97 can be written as

$$\frac{\Delta G}{G_0} = \frac{\dfrac{1}{2} \dfrac{1}{(1-\eta^2)^2} \dfrac{R_\mathrm{i}}{d}\ \mathrm{AR}\ \varepsilon \mathrm{Re}_d}{-\dfrac{\eta}{(1-\eta^2)(1-\eta)} \mathrm{Re}_d} \tag{4.99}$$

or

$$\frac{\Delta G}{G_0} = -\frac{1}{2} \mathrm{AR} \left(\varepsilon \frac{R_\mathrm{i}}{d} \right) \left(\frac{1}{\eta(1+\eta)} \right). \tag{4.100}$$

Using the definition of $\varepsilon = \lambda/R_\mathrm{i}$, I can write

$$\varepsilon \frac{R_\mathrm{i}}{d} = \frac{\lambda}{d} \tag{4.101}$$

213

and now substituting this back into the above, I have

$$\frac{\Delta G}{G_0} = -\frac{1}{2}\text{AR} \left(\frac{\lambda}{d}\right)\left(\frac{1}{\eta(1+\eta)}\right) = -\left(\frac{A}{d}\right)\left(\frac{1}{\eta(1+\eta)}\right). \qquad (4.102)$$

Therefore, for a shallow riblet with small ε the reduction in torque is proportional to the aspect ratio of the riblet, the size of the riblets λ/d, as well as the geometry of the Taylor Couette cell (from the term $1/(\eta(1+\eta))$). I can compare this expression with the results presented in Figure 4-21. The figures are re-plotted with the theoretical line from Equation 4.102 for $\eta = 0.63$. As can be seen in Figures 4-27, the theoretical result captures the slope when AR $\to 0$ for all three cases of $\lambda/d = 0.12$, 0.24, and 0.36 at $\text{Re}_d = 58$. However, at aspect ratios larger than 0.1 (AR < 0.1) the theory fails to predict the progressive torque increase seen from the numerical and experimental results at high AR.

The above results were generated by keeping the radius ratio, η, and the gap size, d/λ, constant and only changing the wavelength of the riblets. Figure 4-28 shows the results of numerical simulation where the wavelength of the riblets and the radius of the inner cylinder were kept constant at $\lambda/R_\text{i} = 0.07$ and the radius of the outer cylinder and the gap were changed and therefore, both η and λ/d were changed. The results presented here also shows a similar non-monotonic relationship with the aspect ratio for the reduction in torque, but as it can be seen again the higher order theory can capture the slope of the curves at AR $\to 0$. Thus the theory and the supporting presented experimental and numerical data show that the torque reduction is initially directly dependent on the size of the riblets with respect to the size of the Taylor-Couette geometry (i.e. $\varepsilon\text{AR} = 2A/R_\text{i}$, as well as the radius ratio η of the Taylor-Couette cell used.

However, by comparing the above theory to the computational results, the theory fails to capture the non-monotonic evolution in torque reduction measured at higher aspect ratios. To solve this perturbation problem, I encounter two separate small parameters, first λ/R_i and second the AR. The discussion so far was for the situation where both λ/d and AR, are small for the riblets and hence the problem was solved
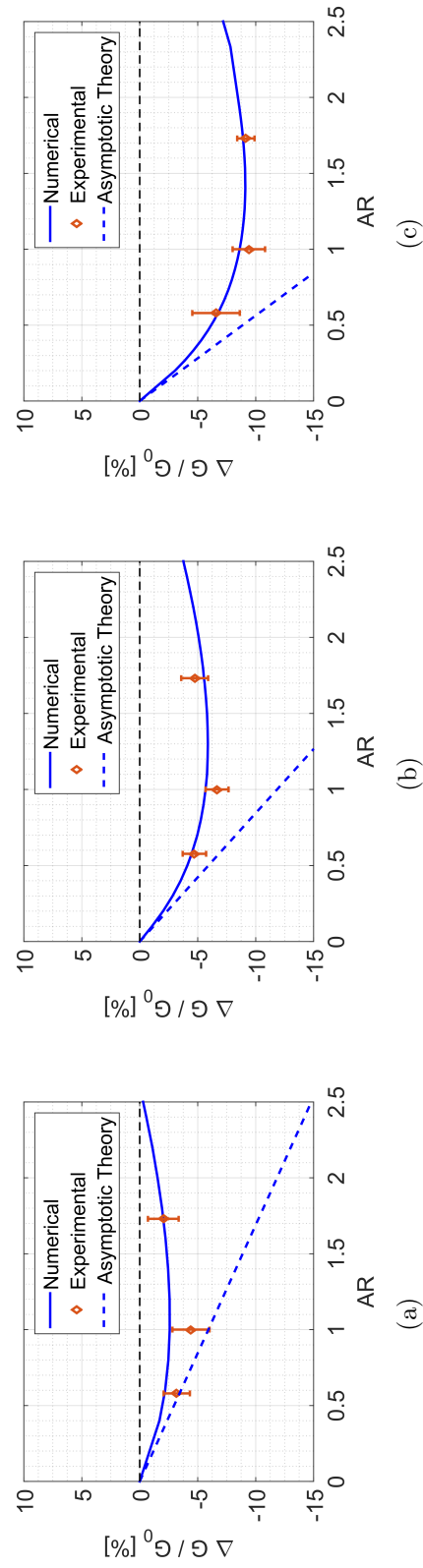
Figure 4-27: Results of numerical calculations, experiments and asymptotic perturbation theory for cylindrical Couette flow near riblet-coated inner radius(for shallow riblets with small λ/R_i) showing the torque change as a function of the aspect ratio AR, at $Re_d = 58$ and for (a) $\lambda/d = 0.12$, (b) $\lambda/d = 0.24$, and (c) $\lambda/d = 0.36$. The perturbation theory results captures the slope at small AR. For all cases $\lambda/R_i < 0.22$.
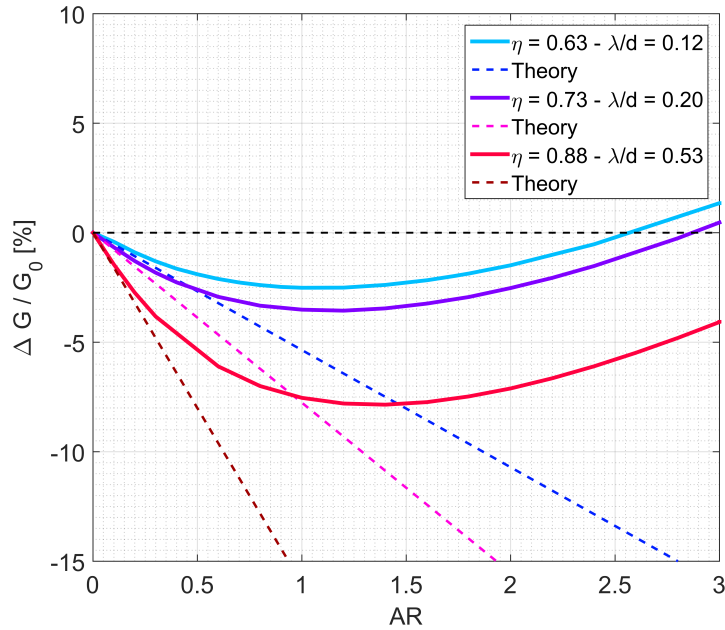
Figure 4-28: Torque reduction results from numerical simulation of Taylor-Couette flow with riblet covered rotors with $\lambda/R_i = 0.07$ and different radius ratio, η, and λ/d as a function of the aspect ratio, AR. Theoretical results for shallow riblets are also shown in the figure with dashed lines.

using a domain perturbation method where the boundary conditions at the riblet wall was replaced by a series expansion based on the the small parameters introduced.

The earlier discussion about the reduction in the average shear stress distribution and the increase in wetted area explains the trend in the torque reduction as a function of the aspect ratio. But for a larger value of AR and small $\varepsilon = \lambda/R_i$ the domain perturbation method cannot capture the trend in the torque reduction presented in the experimental and numerical results in Figure 4-21. To tackle this problem, where only ε is the small parameter, one can employ an integral approach to relate the torque reduction measured or numerically calculated to the size of the riblets and the geometry of the Taylor-Couette cell.

I assume a constant aspect ratio AR (not necessarily small), but still a small value of $\varepsilon = \lambda/R_i$. Thus in the limit of $\varepsilon \ll 1$, I can expand the velocity profile into a zeroth and first order term as

$$v_\phi = v_\phi^{(0)} + \varepsilon v_\phi^{(1)} \tag{4.103}$$

Again, $v_\phi^{(0)}$ can be written as in Equation 4.67 and the equations of motion can be again written as in Equations 4.71 and 4.72. The boundary condition on the riblet surface is again the same as in Equation 4.75 and can be expanded with the same Taylor expansion and written as

$$\frac{v_{\phi,\mathrm{BC}}^{(1)}}{R_\mathrm{i}\Omega_\mathrm{i}} = \frac{-2}{1-\eta^2}\,\mathrm{AR}\,\frac{z}{\lambda} \tag{4.104}$$

However, since the aspect ratio is no longer very small, instead of assuming that the above boundary condition holds on $r = R_\mathrm{i}$, I assume that for each aspect ratio the boundary condition on the inner cylinder can be defined as an average of the boundary condition over one period in the z direction. If I consider a purely geometric averaging, I have

$$\frac{\int_0^{\lambda/2} z\,dz}{\frac{\lambda}{2}} = \frac{\frac{\lambda^2}{8}}{\frac{\lambda}{2}} = \frac{\lambda}{4}. \tag{4.105}$$

However due to the complexity of the problem and the fact that such an average needs to be dependent on the aspect ratio, I assume that instead of the above boundary condition, I can satisfy the boundary condition only at one intermediate location $z = K\lambda/4$ where K is only dependent on the aspect ratio and apply this boundary condition

$$\frac{v_{\phi,\mathrm{BC}}^{(1)}}{R_\mathrm{i}\Omega_\mathrm{i}} = \frac{-2}{1-\eta^2}\,\mathrm{AR}\,\frac{K}{4} \tag{4.106}$$

at $r = R_\mathrm{i}$. Note that for AR $\to$ 1, $K = 1$. With this assumption, Equation 4.72 simplifies back to the one dimensional version which is only a function of the radial location. Thus, with this boundary condition at $r = R_\mathrm{i}$ and $\Omega_\mathrm{o} = 0$ at $r = R_\mathrm{o}$ the velocity profile can be found to be

$$\frac{v_\phi^{(1)}}{R_i \Omega_i} = \frac{-2\eta}{(1-\eta^2)^2} \, \text{AR} \left(\frac{R_o}{r} - \frac{r}{R_o} \right) \frac{K}{4}. \tag{4.107}$$

Again, calculating the rate of shear strain and the shear stress at the rotor will follow the same method and the first order shear stress at $r = R_i$ is written as

$$\tau_{r\phi}^{(1)} = \mu \frac{4\eta}{(1-\eta^2)^2} \, \text{AR} \, \frac{R_o}{R_i^2} \frac{K}{4} R_i \Omega_i. \tag{4.108}$$

Again for this expansion in Equation 4.103, the torque can be written as

$$T = T^{(0)} + \varepsilon T^{(1)} \tag{4.109}$$

and the first order correction term in torque can be found to be

$$T^{(1)} = \frac{K \text{AR}}{2} (4\pi \rho \nu^2 \lambda) \frac{1}{(1-\eta^2)^2} \frac{R_i}{d} \text{Re}_d. \tag{4.110}$$

Hence the non-dimensional torque and the torque reduction can be written as

$$G^{(1)} = \frac{K \text{AR}}{2} \frac{1}{(1-\eta^2)^2} \frac{R_i}{d} \text{Re}_d \tag{4.111}$$

and

$$\frac{\Delta G}{G_0} = -\frac{K \text{AR}}{2} \frac{\lambda}{d} \frac{1}{\eta(1+\eta)} \tag{4.112}$$

where as mentioned earlier, K is only a function of the AR. Note that for $\text{AR} \ll 1$ I expect that $K \to 1$ as per Equation 4.102.

Therefore, at a constant aspect ratio, AR, the reduction in torque due to the riblets is again proportional to the size of the riblets compared to the gap of the cell λ/d, confirming the behaviour presented in Figure 4-25 and also in the experimental and numerical results shown earlier in Figures 4-20 and 4-21.

In addition, the geometry of the Taylor-Couette cell plays an additional role in the total torque reduction achieved. As shown in Figures 4-25 and 4-28, keeping λ/d constant alone is does not guarantee the same torque reduction across all the possible

Taylor-Couette geometries. However, using Equation 4.112, one can see that as long as $(\lambda/d)(\eta(1+\eta)^{-1})$ is kept constant, the results of the torque reduction should be the same. Therefore, one can plot the torque reduction at a constant AR as a function of this new combination $(\lambda/d)(\eta(1+\eta)^{-1})$ as shown in Figures 4-29(a), 4-30(a), and 4-31(a). In these figures, the torque reduction is plotted for various scenarios in which λ/d was kept constant and only the radius ratio of the Taylor-Couette cell was changed. To ensure that the parameter $\varepsilon = \lambda/R_i$ is small, only the cases with $\varepsilon < 0.3$ were considered. Different symbols correspond to different cases of λ/d for fixed AR = 0.58 and the data are plotted against $\lambda/d(\eta(1+\eta)^{-1})$ for all the cases. In addition to the numerical data, the experimental results from Figure 4-20 are also added for comparison. It should be noted that in the experiments, $\eta = 0.63$ was kept constant and λ/d was changed by changing λ. The results shown in all the figures collapse on one line, confirming the linear relationship predicted by Equation 4.112. In addition, a line can be fitted through the data and the slope of the line can be used to find the parameter K in the equation using

$$\frac{K}{2}\text{AR} \times 100 = \text{slope} \tag{4.113}$$

and the values of K can be found to be $K = 0.61$ for AR = 0.58, $K = 0.46$ for AR = 1, and $K = 0.27$ for AR = 1.73. On the other hand, looking back at Figure 4-28, one can see that the ratio of the torque reduction calculated numerically compared with the theory for small aspect ratio corresponds very well with the values of $K = 1$. For larger aspect ratios the values of K found above correspond well with the non-monotonic behaviour in the figure where the torque reduction calculated is less than what the asymptotic theory predicts in Equation 4-28.

Table 4.1 shows the calculated values of the coefficient K and the multiplication of KAR for the cases presented in Figures 4-29, 4-30, and 4-31. In addition, the results are plotted in Figures 4-32 as a function of the aspect ratio as well as the values of K calculated from the results of torque reduction for riblets with $\lambda/d = 0.24$ in a Couette cell with $\eta = 0.63$ corresponding to Figure 4-27(b). As it is seen, K
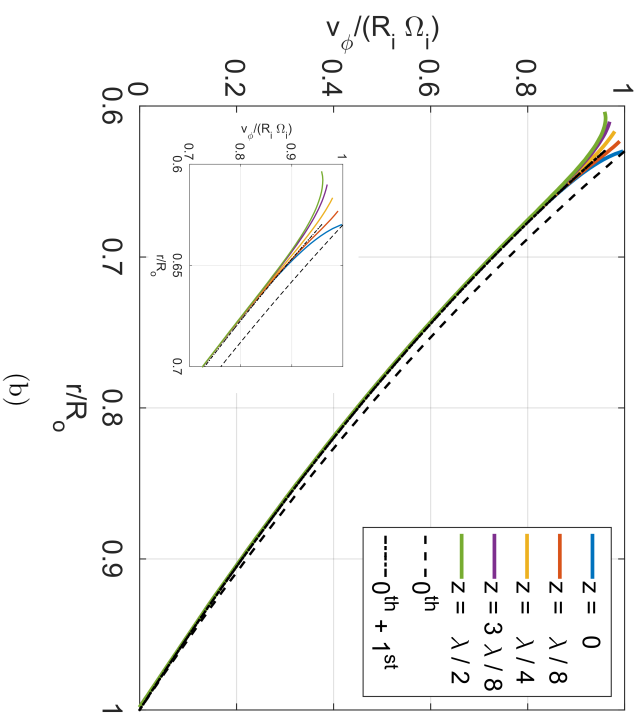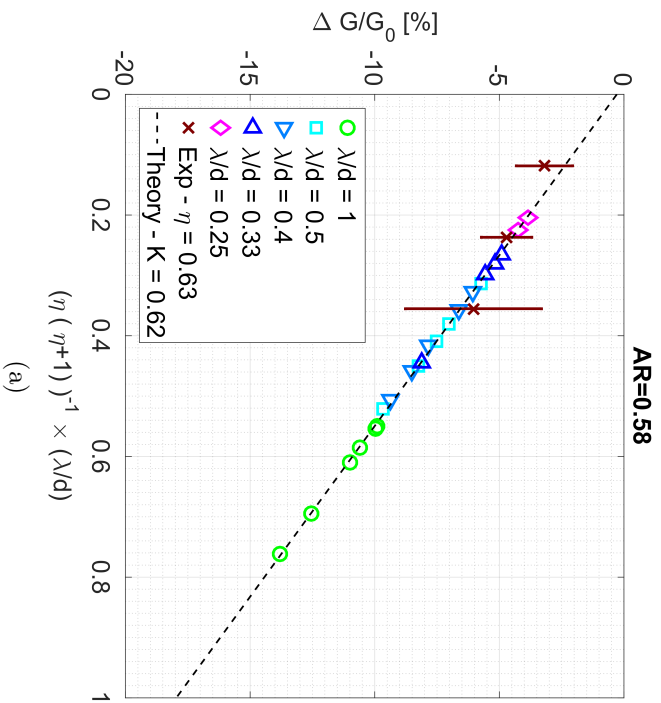
Figure 4-29: (a) Collapse of the experimental and numerical torque reduction date for riblets of $AR = 0.58$ and various λ/d in Taylor-Couette flow with various η when plotted as a function of $(\lambda/d)(\eta(1+\eta))^{-1}$. The data collapse on a line with $K = 0.62$ corresponding to Equation 4.112. (b) The zeroth and first order correction terms of the velocity profile calculated using K from figure 4-29(a) on top of the velocity profile at different axial location within one period of the riblet with AR = 0.58, $\lambda/d = 0.24$, and $\eta = 0.63$.
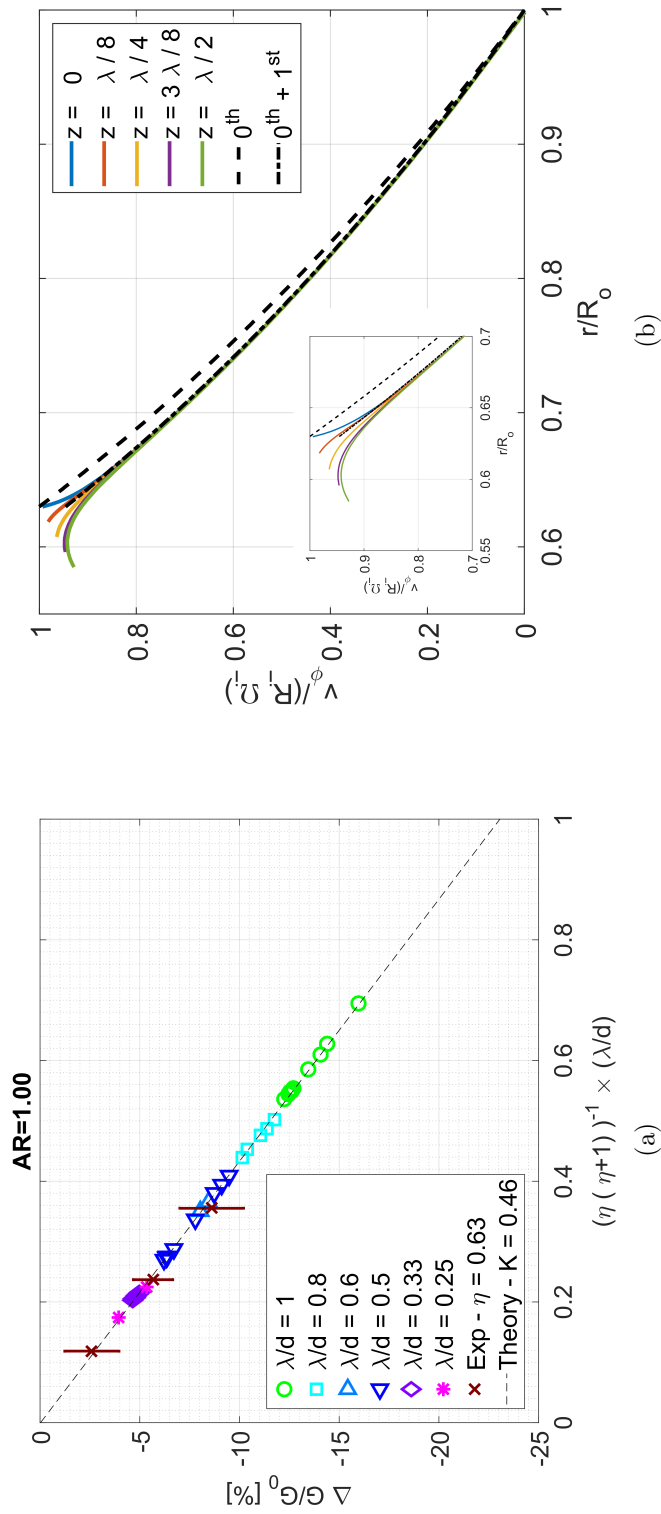
Figure 4-30: (a) Collapse of the experimental and numerical torque reduction date for riblets of AR = 1 and various λ/d in Taylor-Couette flow with various η when plotted as a function of $(\lambda/d)(\eta(1+\eta))^{-1}$. The data collapse on a line corresponding to Equation 4.112 with $K = 0.46$. (b) The zeroth and first order correction terms of the velocity profile calculated using K from figure 4-30(a) on top of the velocity profile at different axial location within one period of the riblet with AR = 1, $\lambda/d = 0.24$, and $\eta = 0.63$.
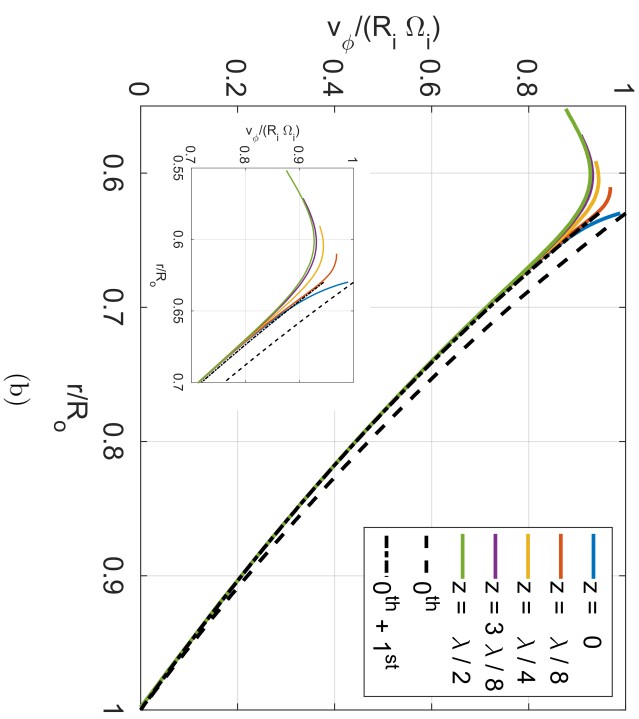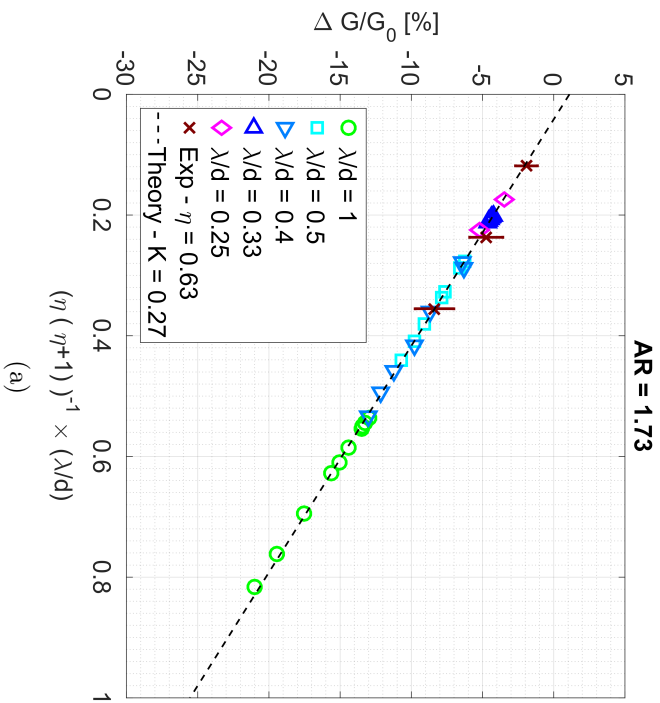
Figure 4-31: (a) Collapse of the experimental and numerical torque reduction date for riblets of AR = 1.73 and various λ/d in Taylor-Couette flow with various η when plotted as a function of $(\lambda/d)(\eta(1+\eta))^{-1}$. The data collapse on a line corresponding to Equation 4.112 with $K = 0.27$. (b) The zeroth and first order correction terms of the velocity profile calculated using K from figure 4-31(a) on top of the velocity profile at different axial location within one period of the riblet with AR = 1.73, $\lambda/d = 0.24$, and $\eta = 0.63$.

has a decreasing trend as aspect ratio increases, however the ARK reveals the non-monotonic behaviour of the torque reduction as a function of the aspect ratio of the riblets.

Table 4.1:   List of the calculated values of coefficient K and AR K for various aspect ratios.

AR	K	AR K
0	1.00	0
0.58	0.62	0.36
1.00	0.47	0.47
1.73	0.27	0.47

(a)   (b)
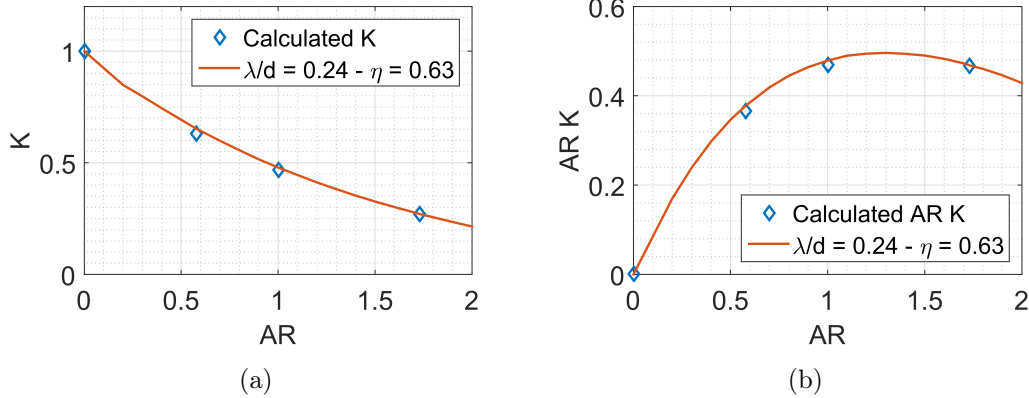
Figure 4-32:   Variation of the (a) coefficient K and (b) AR K with aspect ratio A calculated from data presented in Figures 4-29(a),4-30(a), and 4-31(a). The results are compared with K calculated for results of the numerical calculations of torque reduction shown in Figure 4-27(b) for Couette cell with $\eta = 0.63$ and $\lambda/d = 0.58$ prior to transition to the Taylor vortex state.

Lastly, I can use the fitting parameter K to go back to the velocity profile calculated earlier in Equation 4.107 and compare the results with the velocity profiles calculated for one case for each of the aspect ratios presented in Figures 4-29(a), 4-30(a), and 4-31(a). The velocity profiles for the Taylor Couette cell with $\eta = 0.63$ and riblets of $\lambda/d = 0.24$ with AR $= 0.58$, AR $= 1$, and AR $= 1.73$ are shown in Figures 4-29(b), 4-30(b), and 4-31(b) respectively. The velocity profiles are shown for 5 different lines within a riblet at locations $z = 0$, $z = \lambda/8$, $z = \lambda/4$, $z = 3\lambda/8$, and $z = \lambda/2$. In addition the zeroth order velocity profile and the zeroth plus the

first order velocity profiles with the corresponding K found from the torque reduction plots are also shown in the figures.

As it is seen in the velocity profiles, for all three cases, adding the first order correction to the zeroth order solution helps align this average velocity profile to all the velocity profiles in the gap far away from the rotating inner cylinder and only close to the riblet wall the difference be observed. However, as shown earlier, this average velocity profile can capture the shear stress distribution that the riblets create on the wall.

4.9   Conclusion

In this chapter, I used the flow between concentric cylinders known as Taylor-Couette flow to study the effect of riblets on the flow and the torque change they can offer. The experimental setup was designed and built using various manufacturing methods. The inner cylinders were 3D printed using a Form 1+ 3D printer with various V-groove riblet sizes in both aspect ratio and wavelengths. The fixed outer cylinder was built using a CNC mill as discussed earlier. The setup was mounted on a stress controlled rheometer to allow for measurement of the velocity and torque on the inner cylinder.

To understand the results of the experiments, axi-symmetric and periodic numerical simulations were performed on the laminar cylindrical Couette flow with riblet surfaces and the results were compared with experimental results. Lastly, using a higher order expansion and domain perturbation method, I provide a framework for explaining the effect of changing the size of the riblets on the total torque change observed.

The experimental and numerical results confirmed that using riblet surfaces confer an ability to reduce the frictional torque exerted by the fluid on the rotor. In addition, it was seen that the presence of riblets results in a decrease in the average shear stress on the riblet walls and as the aspect ratio, AR, of the riblets were increased, the average shear stress decreased. However, the increase in the aspect ratio also results in an increase in the wetted surface area. Hence the interplay of the shear stress

reducing effect of the riblet surfaces and increase in the wetted area, results in the total torque reduction presenting a non-monotonic behaviour with the increase in the aspect ratio, AR, of the riblets.

In addition, the experimental and numerical results show that at a fixed aspect ratio AR, the torque reduction achieved is directly proportional to the wavelength of the riblets and increasing λ/d, enhances the drag reduction achieved. Also, the geometry of the Taylor-Couette cell affects the total torque reduction achieved. Using a higher order perturbation theory for the steady viscous flow over riblet surfaces I was able to confirm that for riblets with small λ/R_i the reduction in torque is linearly proportional to the λ/d and inversely proportional to $\eta(\eta + 1)$; while at very small aspect ratios AR, it is linearly proportional to the aspect ratio. However, the linear relationship with aspect ratio starts to break down after AR $\approx$ 0.1. For higher values of AR, the effect of aspect ratio takes a more complicated turn which can be rationalized using the shear stress distributions presented earlier. However, for constant AR I was able to collapse the results of the experimental and numerical simulations with various λ/d and η.

The above discussions were all in the laminar regime where the effect of the Reynolds number on either the smooth cases or the riblet covered rotors is linear and thus in comparison, it drops out of the problem. In the next chapter, I will discuss the case of riblets in the Taylor vortex flow regime where the dynamics of the flow affect the results and dependent on the Reynolds number.

THIS PAGE INTENTIONALLY LEFT BLANK

Chapter 5

Taylor-Couette Flow with Riblet Covered Rotors in the Taylor Vortex Regime

5.1 Introduction

In the previous chapter, I explored the effect of riblets in Taylor-Couette flow and specifically discussed the changes that riblets induce in the flow and in the total frictional torque exerted by the fluid on the inner rotor in the laminar (Couette) Flow. I showed that similar to the case of the boundary layers, discussed in Chapters 2 and 3, the torque reduction in laminar Taylor-Couette flow is a non-monotonic function of the aspect ratio of the riblets. While the introduction of the riblets results in a decrease in the average shear stress on the scale of one riblet period, the increase in the wetted surface area of the inner cylinder counteracts this decreasing effect and hence the interplay of the two phenomena results in a non-monotonic behaviour in the total integrated frictional drag or torque reduction in the flows discussed so far.

In this chapter, I will discuss the extended effect of the geometry of the riblets in the Taylor vortex regime and how the riblets interact with the larger-scale Taylor vortex structures that occur due to the instability of the flow, in addition to the

viscous dominated effect of the riblets on the flow (similar to the case of the laminar Taylor-Couette flow discussed in Chapter 4).

In Chapter 4 the history of the Taylor-Couette flow and the theoretical formulations of the Couette flow were discussed. The theoretical background of the Taylor vortex flow is mostly built around the instability itself and how to mathematically and physically predict the critical conditions and dynamical structure of the transition. Lord Rayleigh was the first person to discuss this instability using an energy argument for inviscid flow and showed that a necessary and sufficient condition for stability to axisymmetric disturbances in flow between concentric cylinders with both cylinders rotating is that

$$\frac{d}{dr}\left(\Omega r^2\right)^2 \geqslant 0. \tag{5.1}$$

Later, in the early 1920s, G.I. Taylor was the first person to formulate the equations of motion to understand the instability of the flow. He simplified the eigenvalue problem for small gap Taylor-Couette cell and compared the results with experimental observations [114]. The results of Taylor's experiments and calculations asymptotically approach the Rayleigh's criteria at larger Reynolds numbers (based on the velocity of the inner and outer cylinders) [114] .

Later, others such as Goldstein [115] and Chandrasekhar [116, 117, 118], Davey alone [119] and in collaboration with DiPrima and Stuart [120], Donnelly and Schwarz [121], Roberts [122], Nickerson [123], Swinney and co-workers [126, 127, 128, 129, 130, 131], and Grossmann, Lohse, and other co-workers [133, 134, 135, 108, 136] investigated the spatial structures of this instability throughout the years.

Here, I am only interested in the effect of the riblet geometry on the Taylor vortices and in this chapter I will specifically examine the results of the flow at $\mathrm{Re}_d = 230$ with riblets of $\lambda/d = 0.24$ with a range of AR, where the flow is above the first transition point ($\mathrm{Re}_{d,\mathrm{crit}} = 74$) before wavy Taylor vortices develops.

5.2 Methods

The data presented and discussed in this chapter is a combination of experimental results collected and shown in Chapter 4 and time dependent numerical simulations of the Taylor-Couette flow in the Taylor vortex regime, well before any wavy Taylor vortices can be observed ($74 < \mathrm{Re}_d \lesssim 300$).

5.2.1 Experimental

The experimental method is the same as explained in Chapter 4 and to be able to increase the Reynolds number without the effect the associated radial pressure gradient, a mixture of 50% glycerol and 50% DI water was used as the working fluid. The rest of the details are unchanged.

5.2.2 Numerical Method

To understand the effect of the presence of the riblets on the Taylor vortex flow and visualize the changes in the vortices and flow dynamics, axi-symmetric simulations of Taylor-Couette cells with both smooth and riblet rotors were performed. To be able to capture the Taylor vortices, the length of the Taylor-Couette cells were adjusted so that at least two or three vortex pairs would be visible inside the gap. To capture the added details that the Taylor vortices, instead of a laminar model for the flow, I use a large eddy simulation with a dynamic one equation model for the sub-grid level. Large eddy simulation is one form of the simulation developed for tackling the challenging problem of the Turbulent flow.

For modelling turbulent flows, different methods have been introduced to approximate the complex phenomenon. There are three levels of approximations used. First one is called the Reynolds Averaged Numerical Simulations or RANS where the solution for the velocity vector ($\boldsymbol{u}$) and pressure (p) is decomposed into a statistical average and fluctuations term ($\boldsymbol{u} = \overline{\boldsymbol{u}} + \boldsymbol{u}'$ and $p = \overline{p} + p'$). Therefore, using the statistical averages and solving for the terms does not allow for a fine description of the flow to be achieved, thus this approach is not well suited for the studies of the

fundamentals of the turbulent flow. In other words, in the energy spectrum of the flow, the entire flow is modelled and not resolved at all the scales [145].

The second type of simulation is known as Large Eddy Simulation or LES, where only the low frequency part (or large scale structures) of the solution is solved for while the large frequencies (small scales) are modelled. For this the Navier Stokes equations are filtered explicitly or implicitly by either spectral cut-off or numerical discretizations. In this method, the smaller scales are modelled using various sub-grid scale methods [145, 146].

The third method is known as Direct Numerical Simulations or DNS, where all the scales of the flow is solved for, therefore this method is the most appropriate for the fundamental studies of the turbulence, however it is the most expensive method compared to the other two.

Here I am using the Large Eddy Simulation which is more detailed than RANS simulations and less costly compared to the Direct Numerical Simulations. Below a short introduction to the Large Eddy Simulations is presented.

5.2.3   Large Eddy Simulations

As mentioned, in large eddy simulations, the problem is divided into a sub-grid problem and large scale problem. For this cut-off various filters have been introduced and used. Filters used in Large Eddy Simulations are high pass filters (in terms of of scales) or low pass filters (in terms of the frequencies). A general definition of a filter used in LES is as shown below, using a convolution integral [145, 146, 147]

$$\overline{\phi} = \int_{-\infty}^{\infty} \int_{-\infty}^{\infty} \phi(\xi, t') G(x - \xi, t - t') dt' d\xi^3 \tag{5.2}$$

where ϕ can be any scalar, vector, or tensor field, G is the filter kernel, and the over-bar represents the filtered quantity. Filters used in LES have three properties which are important as they make it possible to manipulate the Navier-Stokes equations

resolved

subgrid

Δ

PHYSICAL SPACE

resolved

subgrid

Log(E(k))

$k_c = \pi / \overline{\Delta}$

Log(k)

FOURIER SPACE
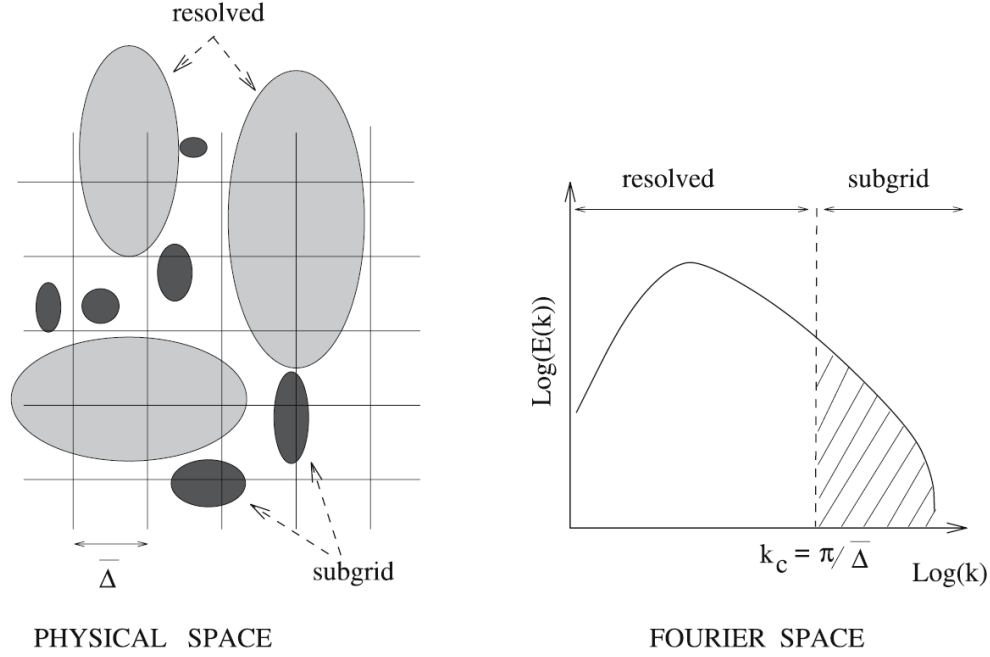
Figure 5-1: Schematic of the filtering operation in the simplest form when the mesh is identical to the filter in the problem. Here the cut-off wave-number is called k_c which can be calculated directly from the cut-off length (length scale of the filter) $\overline{\Delta}$ shown in the physical space [145].

[145]. The first one is that they conserve constants, i.e.

$$1 = \int_{-\infty}^{\infty} \int_{-\infty}^{\infty} G(x - \xi, t - t')dt'd\xi^3 \qquad (5.3)$$

Second, they are linear meaning $\overline{\phi + \psi} = \overline{\phi} + \overline{\psi}$, and third, they commutate with derivation as shown below.

$$\overline{\frac{\partial \phi}{\partial x}} = \frac{\partial \overline{\phi}}{\partial x}. \qquad (5.4)$$

If the Navier-Stokes and the continuity equations are written in the form

$$\frac{\partial u_i}{\partial t} + \frac{\partial (u_i u_j)}{\partial x_j} = -\frac{1}{\rho}\frac{\partial p}{\partial x_i} + \nu(\frac{\partial u_i}{\partial x_j} + \frac{\partial u_j}{\partial x_i}) \qquad (5.5)$$

$$\frac{\partial u_i}{\partial x_i} = 0 \qquad (5.6)$$

231

(where u_i are the components of the velocity vector and p the pressure), when a filter with earlier properties is applied to each of these equations, I have [145, 148]

$$\frac{\partial \overline{u_i}}{\partial t} + \frac{\partial (\overline{u_i u_j})}{\partial x_j} = -\frac{1}{\rho}\frac{\partial \overline{p}}{\partial x_i} + \nu\left(\frac{\partial \overline{u_i}}{\partial x_j} + \frac{\partial \overline{u_j}}{\partial x_i}\right) \tag{5.7}$$

$$\frac{\partial \overline{u_i}}{\partial x_i} = 0. \tag{5.8}$$

Thus the only term that is not clearly defined is the non-linear term on the left hand side. I can decomposed the non-linear term $\overline{u_i u_j}$ using a decomposition for the velocity vector $\mathbf{u}$ into a filtered velocity $\overline{\mathbf{u}}$ (resolved scale) and $\mathbf{u}'$ (sub-grid scale) as [145]

$$\mathbf{u} = \overline{\mathbf{u}} + \mathbf{u}' \quad \rightarrow \quad u_i = \overline{u_i} + u_i' \tag{5.9}$$

and substituting Equation 5.9 into the non-linear term from Equation 5.7 and expanding the terms gives

$$\overline{u_i u_j} = \overline{(\overline{u_i} + u_i')(\overline{u_j} + u_j')} = \overline{\overline{u_i}\,\overline{u_j}} + \overline{\overline{u_i}u_j'} + \overline{u_i'\,\overline{u_j}} + \overline{u_i'u_j'}. \tag{5.10}$$

The second and third term in Equation 5.10 can be combined as

$$C_{ij} = \overline{\overline{u_i}u_j'} + \overline{u_i'\,\overline{u_j}} \tag{5.11}$$

which represents the interaction between the small (unresolved scale) and large scales (resolved scale). Last term in Equation 5.10 is written as

$$R_{ij} = \overline{u_i'u_j'} \tag{5.12}$$

which is called the Reynolds sub-grid tensor, showing the interactions between the sub-grid scales. Therefore, the full non-linear term can be rewritten as:

$$\overline{u_i u_j} = \overline{\overline{u_i}\,\overline{u_j}} + (\overline{u_i}\,\overline{u_j} - \overline{\overline{u_i}\,\overline{u_j}}) = \overline{u_i}\,\overline{u_j} + C_{ij} + R_{ij} = \overline{u_i}\,\overline{u_j} + \tau_{ij} \tag{5.13}$$

232

where $\tau_{ij} = C_{ij} + R_{ij}$. Substituting the above terms back into Equation 5.7, I have

$$\frac{\partial \overline{u_i}}{\partial t} + \frac{\partial (\overline{u_i}\,\overline{u_j})}{\partial x_j} = -\frac{1}{\rho}\frac{\partial \overline{p}}{\partial x_i} + \nu\Big(\frac{\partial \overline{u_i}}{\partial x_j} + \frac{\partial \overline{u_j}}{\partial x_i}\Big) - \frac{\partial \tau_{ij}}{\partial x_j} \qquad (5.14)$$

Equation 5.14 is the filtered Navier-Stokes equation for the resolved scales and τ_{ij} is known as the Sub-Grid Tensor and it comprises of the C_{ij} which is the interactions between the sub-grid scale and the resolved scale, and R_{ij} which presents the interactions within the sub-grid scale. Thus, now in addition to the three components of the velocity vector and one pressure, the nine elements of the sub-grid tensor are also unknown. Thus, the three momentum equations and the continuity equation are not enough to solve for all the unknowns in the problem. This requires a model to connect τ_{ij} to the rest of the known and unknown parameters in the problem.

In order to introduce the sub-grid models, it is beneficial to derive the sub-grid scale kinetic energy equation as well. To derive the sub-grid scale kinetic energy equation, first, I need to multiply each of the Navier Stokes equations with their corresponding velocity component and sum all the equations, which can be written as: [145, 148]

$$u_i \frac{\partial u_i}{\partial x_i} + u_i \frac{\partial}{\partial x_j}(u_i u_j) = -\frac{u_i}{\rho}\frac{\partial p}{\partial x_i} + \nu u_i \frac{\partial^2 u_i}{\partial x_j \partial x_j} \qquad (5.15)$$

and then filtering the entire equation gives

$$\overline{u_i \frac{\partial u_i}{\partial x_i}} + \overline{u_i \frac{\partial}{\partial x_j}(u_i u_j)} = -\overline{\frac{u_i}{\rho}\frac{\partial p}{\partial x_i}} + \overline{\nu u_i \frac{\partial^2 u_i}{\partial x_j \partial x_j}}. \qquad (5.16)$$

To simplify Equation 5.16, I need to multiply each of the filtered Navier Stokes equations by the corresponding filtered velocity and sum them all as shown below.

$$\overline{u_i}\frac{\partial \overline{u_i}}{\partial t} + \overline{u_i}\frac{\partial (\overline{u_i}\,\overline{u_j})}{\partial x_j} = -\overline{u_i}\frac{1}{\rho}\frac{\partial \overline{p}}{\partial x_i} + \overline{u_i}\,\nu\Big(\frac{\partial \overline{u_i}}{\partial x_j} + \frac{\partial \overline{u_j}}{\partial x_i}\Big) - \overline{u_i}\frac{\partial \tau_{ij}}{\partial x_j} \qquad (5.17)$$

Then, subtracting equation 5.17 from 5.16 and defining the kinetic energy $k = \frac{1}{2}\overline{u_i u_i}$, and the kinetic energy on the filtered level $\overline{k} = \frac{1}{2}\overline{u_i}\,\overline{u_i}$, and the kinetic energy of the sub-grid scale as $k_{\text{sgs}} = k - \overline{k}$, I can find an equation for the k_{sgs} as

$$\frac{\partial k_{\text{sgs}}}{\partial t} + \frac{\partial (\overline{u_i} k_{\text{sgs}})}{\partial x_j} = -\frac{\partial \overline{u_i}}{\partial x_j} \tau_{ij} - \frac{\partial}{\partial x_j} (\frac{1}{2} \overline{u_i u_i u_j} - \frac{1}{2} \overline{u_i u_i u_j} + \frac{1}{\rho} \overline{u_j p} - \frac{1}{\rho} \overline{u_j} \overline{p} - \overline{u_i} \tau_{ij})$$

$$+\nu \frac{\partial^2 k_{\text{sgs}}}{\partial x_j \partial x_j} - \nu \overline{\frac{\partial u_i}{\partial x_j} \frac{\partial u_i}{\partial x_j}} - \frac{\partial \overline{u_i}}{\partial x_j} \frac{\partial \overline{u_i}}{\partial x_j} \tag{5.18}$$

This sub-grid kinetic energy equation as shown in Equation 5.18 is used in the models for the subgrid scale. When used, instead of the four equations, five equations and five unknowns are solved for with the additional unknown being k_{sgs} [145, 148].

Various sub-grid models have been proposed to define the sub-grid stress tensor. For example, the Smagorinsky model is one of the algebraic models which tries to define the sub-grid stress tensor terms in the momentum equation. The model is based on the assumption of equilibrium in the sub-grid level and thus the production and dissipation on this level being equal. In this model, the deviatoric part of the sub-grid tensor is defined as a sub-grid scale kinematic viscosity multiplied by the stress tensor in the resolved scale, $\overline{S_{ij}}$, as shown below [145, 99, 149, 150]

$$\tau_{ij} - \frac{2}{3} k_{\text{sgs}} \delta_{ij} = -\nu_{\text{sgs}} \overline{S_{ij}} \tag{5.19}$$

and to define the sub-grid scale kinematic viscosity, ν_{sgs}, an algebraic equation is used as

$$\nu_{\text{sgs}} = C_{\text{s}}^2 \Delta^2 < 2\overline{S_{ij}} \; \overline{S_{ij}} > \tag{5.20}$$

where Δ is the cut-off length scale that is dependent on the filter used in the equations. The constant C_{s} takes a number in the range of 0.1-0.45 and there are different theoretical approaches to finding it [145, 99, 149, 150]. The normal part of the sub-grid stress tensor, which corresponds to $\frac{2}{3} k_{\text{sgs}} \delta_{ij}$ can be added as an isotropic term to the pressure term and solved with the pressure gradient as a modified pressure term [145].

While Smagorinsky's model is simple to apply, it has its own limitation of not having a tunable coefficient. It has been seen that the coefficient is lower in shear flows

compared to the isotropic turbulence, and similarly close to the wall the coefficient needs to be lower, but setting it as constant does not correspond with the physics of the flow in various regions [99].

Another form of sub-grid scale model is known as One Equation Eddy Viscosity Model which uses a differential equation to close the sets of differential equation to be solved using LES. In this model, the differential equation of the sub-grid scale kinetic energy is added to the rest of the equations. For this model, Equation 5.18 is rewritten as [145]:

$$\frac{\partial k_{\text{sgs}}}{\partial t} - \frac{\partial}{\partial x_j}(\overline{u_j} k_{\text{sgs}}) = \frac{\partial}{\partial x_j}(\nu_{\text{sgs}} \frac{\partial k_{\text{sgs}}}{\partial x_j}) - G - \varepsilon \tag{5.21}$$

where G is known as production term and ε is known as the dissipation terms. Here, in the sub-grid scale kinetic energy, the dissipation and the production terms are modelled using equations below

$$G = 2\nu_{\text{sgs}}|\overline{S}|^2 \tag{5.22}$$

$$\varepsilon = \frac{C_{\text{e}} k_{\text{sgs}}^{3/2}}{\Delta} \tag{5.23}$$

$$\nu_{\text{sgs}} = C_{\text{s}}^2 \Delta^2 < 2\overline{S_{ij}} \ \overline{S_{ij}} > \tag{5.24}$$

$$C_{\text{s}} = \sqrt{C_{\text{K}}\sqrt{\frac{C_{\text{K}}}{C_{\text{e}}}}} \tag{5.25}$$

where again, the coefficients C_{K} and C_{e} need to be chosen and are not tunable according to the flow type. Thus the dynamic version of the one equation eddy viscosity model was introduced in the 1990s. The main idea behind the dynamic viscosity model is to offer a way to tune the constants defining the eddy viscosity and not use a fixed value throughout the domain and over time.

Therefore, instead of the assumption of the local equilibrium at the sub-grid level, in this model it is assumed that there is an equilibrium between the sub-grid and the resolved scales. Therefore one can find an equation to dynamically find the coefficient.

In this model, the equation of the kinetic energy at the resolved scale is again filtered with another filter of wider bandwidth (shown by the over-hat sign) and thus written as [148, 151]:

$$\frac{\partial K}{\partial t} - \frac{\partial}{\partial x_j}(\widehat{\overline{u_j}} K) = \frac{\partial}{\partial x_j}(\nu_{\text{sgs}} \frac{\partial K}{\partial x_j}) - G_{\text{K}} - \varepsilon_{\text{K}}. \tag{5.26}$$

On the sub-grid scale I have [148, 151]:

$$\frac{\partial k_{\text{sgs}}}{\partial t} - \frac{\partial}{\partial x_j}(\overline{u_j} k_{\text{sgs}}) = \frac{\partial}{\partial x_j}(\nu_{\text{sgs}} \frac{\partial k_{\text{sgs}}}{\partial x_j}) - G_{\text{sgs}} - \varepsilon_{\text{sgs}}. \tag{5.27}$$

Now, with the equilibrium assumption between the two scales I can write that [148, 151]:

$$G_{\text{K}} - \varepsilon_{\text{K}} = \widehat{G_{\text{sgs}} - \varepsilon_{\text{sgs}}} \tag{5.28}$$

and using a definition similar to Equation 5.23 for the dissipation term at each level I have [148, 151]

$$G_{\text{K}} - \frac{C_{\text{e}} K^{3/2}}{\widehat{\Delta}} = \widehat{G_{\text{sgs}}} - \frac{\widehat{C_* k_{\text{sgs}}^{3/2}}}{\Delta} \tag{5.29}$$

which results in [148, 151]

$$C_*^{n+1} = (G_{\text{K}} - \widehat{G_{\text{sgs}}} + \frac{\widehat{C_*^n k_{\text{sgs}}^{3/2}}}{\Delta}) \frac{\widehat{\Delta}}{K^{3/2}}. \tag{5.30}$$

Dynamic model is attracting more attention as it has the ability to tune the coefficient depending on the flow type and other circumstances which models such as Smagorinsky were not able to do. Due to this tunability, in this work, the dynamic model is used for the sub-grid scale model.

5.3 Results

After transition to the Taylor-vortex and the wavy Taylor-vortex regime, the behaviour of the velocity profiles becomes dependent on the Reynolds number and thus the resulting measurements in the torque reduction show a slight dependence on the Reynolds number. As shown in Figures 4-20 in the previous chapter, immediately after transition, between $74 < \mathrm{Re}_d < 110$ the results of the torque reduction show a combination of irregular decrease and increase which is due to the hysteresis in the vicinity of transition. From Figure 4-19 it can also be seen that transition region covers a wider range of Reynolds numbers than just one Reynolds number of $\mathrm{Re}_d = 74$. Similar hysteresis in the behaviour of the Taylor-Vortex flow have been reported previously by [132].

In the Taylor vortex regime, in addition to the size of the gap (which is the characteristic length scale in the Couette flow calculations), the wavelength of the vortex turns into another important length scale in the problem. Various researchers have indicated that this wavelength does not have a fixed value and can not be uniquely determined [152, 153, 154]. Groman and Swinney have reported observing a variation of between 16 and 20 vortices in a Taylor-Couette apparatus of $\Gamma = 20$ [155].

In the current experimental setup, with $\Gamma = 5.1$ nearly all the times, at steady state, three vortex pairs can be identified, but in some cases, right after the transition, initially, four vortex pairs are seen and as the flow evolves, they ultimately collapses into three pairs in the steady-state case. Similar behaviour was observed in the results of the numerical simulation with $\mathrm{Re}_d = 230$, $\eta = 0.63$, and $\Gamma = 3.4$ (2/3 of the length of the experimental setup to reduce the cost of the simulations) where first three vortex pairs are initiated and during the transient time, the vortices interact to adjust their wavelengths and collapse into two vortex pairs by the time the flow reaches the steady state. Snapshots of the velocity profiles are presented in the coming section.

Therefore, in the presence of the riblets in the Taylor vortex flow, the changes in the flow and hence the torque is a combination of the viscous dominated process

similar to the case of the Couette flow discussed in Chapter 4 and the interaction of the riblets (especially their peaks) with the larger Taylor vortices in the flow. Below I will discuss this interaction in more detail and how the different contributions to the shear stress distribution results in changes in the total frictional torque on the inner rotor when changing the aspect ratio of the riblets.

5.3.1   Interaction of Taylor Vortices with Riblets

After the Taylor-Couette flow has transitioned to the Taylor vortices, the flow that was only a function of the radial direction is now a function of both radial and axial direction and new vortical structures appear in the flow due to the instabilities that were discussed earlier.

As it was shown in the previous chapter, the introduction of the riblets resulted in changes in the velocity profile, shear stress distribution, and hence the total torque. Since the flow was fully viscous and none of the inertial effects were important, the changes were independent of the Reynolds number of the flow and they were all dictated by the changes in the aspect ratio, AR, of the riblets as well as the changes in the size of the riblet with respect to the gap size λ/d. In addition, the changes observed in the torque were also dependent on the geometry of the Taylor-Couette cell as well, specifically the radius ratio of the cell η.

However, in Taylor-vortex flow with riblet covered rotors, in addition to the changes in the viscous flow, the riblets interact with the larger Taylor vortices in the flow and result in additional changes in the flow and the torque. The interaction of the riblets and Taylor vortices can be best demonstrated using the in plane streamlines for the radial and axial velocity, contours of the azimuthal velocity, as well as the Q criteria introduced in Chapter 3. The results below are presented at two different Reynolds number. First at $\text{Re}_d = 115$ which is at the ending edge of the transition region as shown in Figure 4-19 and then at $\text{Re}_d = 230$ which is in the Taylor vortex region.

Figure 5-2 shows the early stages of the evolution of the velocity profiles in Taylor-Couette flow with $\text{Re}_d = 115$, $\eta = 0.63$, and $\Gamma = 5.1$. The figures show a planar cut

within the concentric cylinder system and the cut plane on the left shows the evolution in $v_\phi/R_i\Omega_i$ while the cut plane on the right shows the in plane streamlines, calculated using v_r and v_z overlaid on the contour plots of the azimuthal velocity (The azimuthal velocity have been normalized by the velocity of the inner cylinder). Figure 5-2(a) shows the time of only 3×10^{-3} times the diffusion time after the start of the flow. Diffusion time, t_d is defined as $t_d = d^2/\nu$ where d is the gap of the Taylor Couette cell and ν is the kinematic viscosity of the fluid in the cell. At $t = 3 \times 10^{-3}$ t_d, the azimuthal velocity is diffusing in a similar manner as in the Couette flow. However, in this case, the axial and radial velocity are both non-zero and the streamlines of the in-plane flow (streamlines with only v_r and v_z) create two larger flow structures as it is seen on the slice on the right. These two structures which are rotating, grow over time and lead to the creation of two vortices on the two ends of the cell as it is shown in Figure 5-2(b). Again, at this stage with $t = 7.4 \times 10^{-2}$ t_d the azimuthal flow does not show any difference from what is expected of the Couette flow, but now the two rotating structures are taking the form of two vortices on the two ends of the cells.
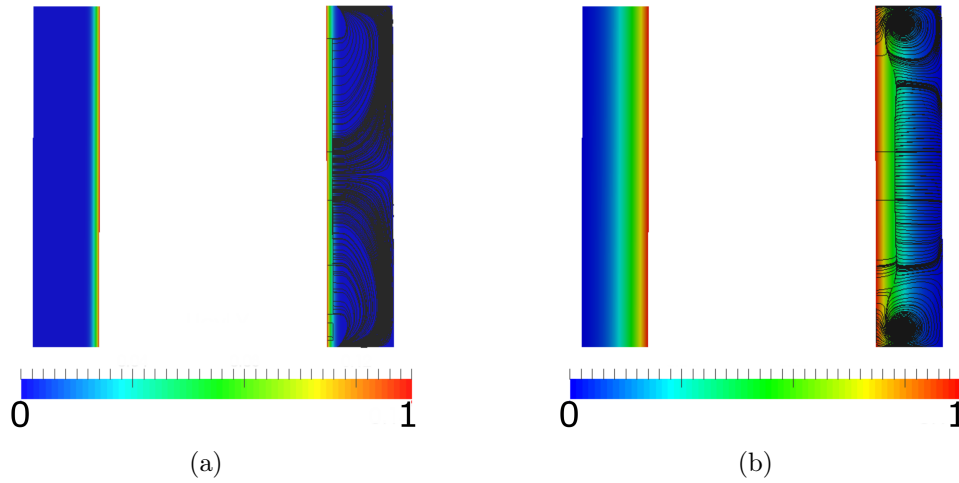
Figure 5-2: Contours of azimuthal velocity (left cut) and streamlines of the in plane axial and radial velocity (right cut) presented on a planar cut within the Taylor-Couette flow at (a) $t = 3 \times 10^{-3}$ t_d, (b) $t = 7.4 \times 10^{-2}$ t_d for $\text{Re}_d = 115$, $\eta = 0.63$, and $\Gamma = 5.1$.

By the time $t = 1.2 \times 10^{-2}$ t_d (see Figure 5-3(a)) the two vortices on the two ends are fully formed and each of the two initiate another vortex (counter-rotating with

respect to themselves). However, still the azimuthal velocity does not see any effects from the radial and axial velocities. Afterwards, at $t = 1.5 \times 10^{-2}\ t_{\mathrm{d}}$ then the two new vortices each start to initiate another counter rotating vortex, filling the entire length of the cell with three pairs of counter-rotating vortices as seen in Figure 5-3(b).
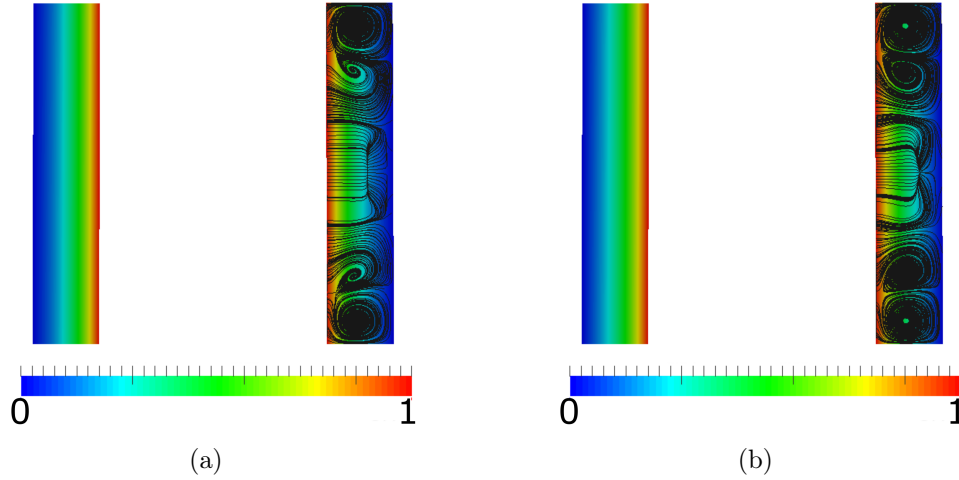
Figure 5-3: Contours of azimuthal velocity (left cut) and streamlines of the in plane axial and radial velocity (right cut) presented on a planar cut within the Taylor-Couette flow at (a) $t = 1.2 \times 10^{-2}\ t_{\mathrm{d}}$, (b) $t = 1.5 \times 10^{-2}\ t_{\mathrm{d}}$ for $\mathrm{Re}_d = 115$, $\eta = 0.63$, and $\Gamma = 5.1$.

Then at $t = 2.2 \times 10^{-2}\ t_{\mathrm{d}}$, the last two vortices in the middle are still taking their form (Figure 5-4(a)) and then by $t = 3.0 \times 10^{-2}\ t_{\mathrm{d}}$ as seen in Figure 5-4(b) the three vortex pairs are completely formed and they cover the entire length of the cell. Then for a while the azimuthal velocity diffuses toward the outer cylinder while the vortices keep this pattern until the time around $t = 4.1 \times 10^{-2}\ t_{\mathrm{d}}$ where a slight instability becomes visible in the contour plots of the circumferential velocity profile as seen in Figure 5-4(c). Then this instability goes through a modulation as shown in Figure 5-4(d) at time $t = 4.6 \times 10^{-2}\ t_{\mathrm{d}}$ and then the instabilities grow as shown in Figures 5-4(e) ($t = 5.2 \times 10^{-2}\ t_{\mathrm{d}}$) and by $t = 5.9 \times 10^{-2}\ t_{\mathrm{d}}$ as shown in Figure 5-4(f) the three vortex pairs are all formed and the radial, azimuthal and axial velocities have reached the steady state. The wavelength of each vortex pairs comes out to be $\Lambda/d = 1.7$ and each of the two vortices in the pair cover a distance of $0.85\ d$.

However, in presence of the riblets the grooves give rise to a three-dimensional flow
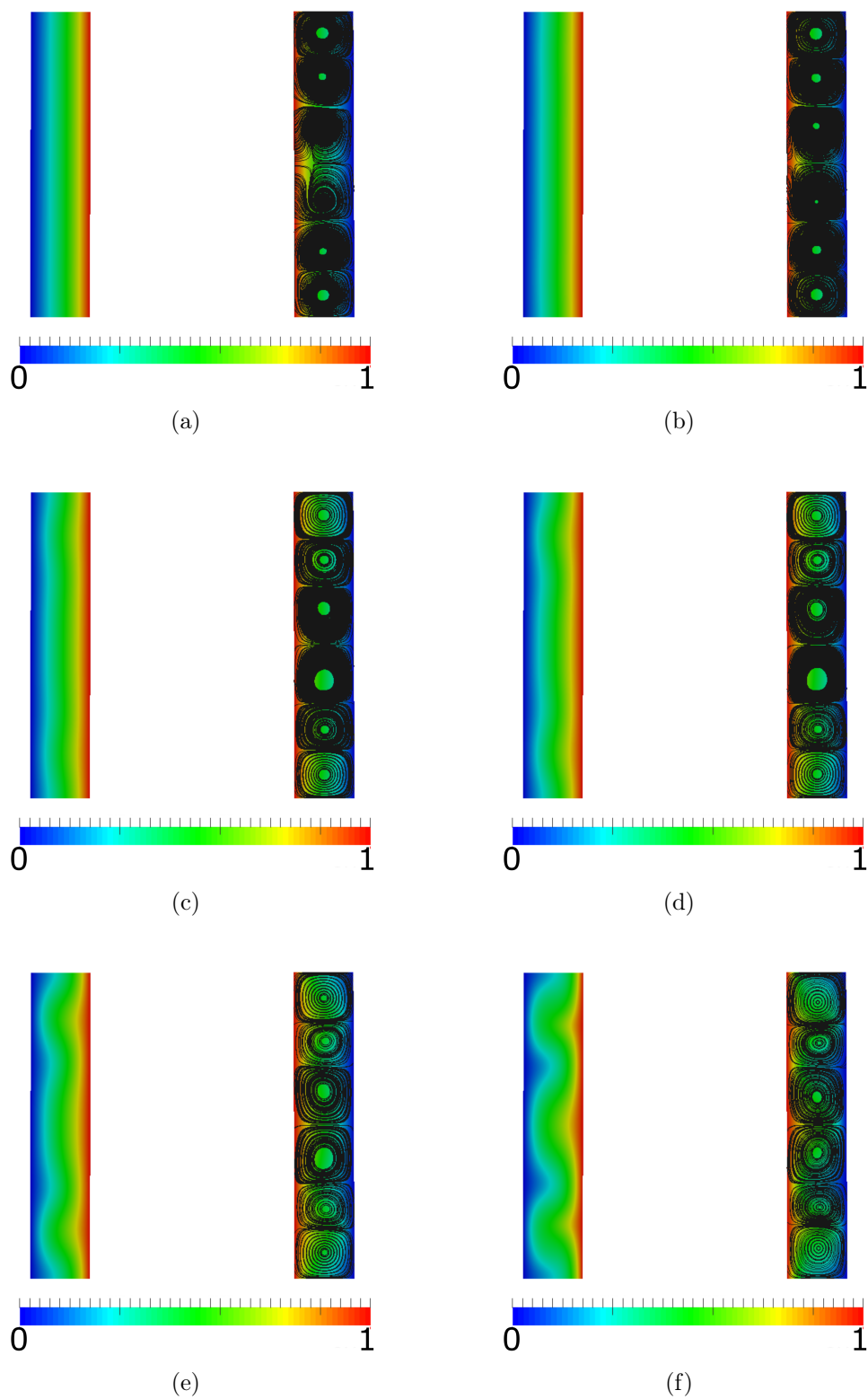
Figure 5-4: Contours of azimuthal velocity and streamlines of the in plane axial and radial velocity at (a) $t = 2.2 \times 10^{-2} \, t_{\mathrm{d}}$, and (b) $t = 3.0 \times 10^{-2} \, t_{\mathrm{d}}$, (c) $t = 4.1 \times 10^{-2} \, t_{\mathrm{d}}$, (d) $t = 4.6 \times 10^{-2} \, t_{\mathrm{d}}$, (e) $t = 5.2 \times 10^{-2} \, t_{\mathrm{d}}$, and (f) $t = 5.9 \times 10^{-2} \, t_{\mathrm{d}}$, for $\mathrm{Re}_d = 115$, $\eta = 0.63$, and $\Gamma = 5.1$.

241

inside each of them that result in initially observing two closed sets of streamlines inside each of the riblets as shown in Figure 5-5(a) at $t = 3 \times 10^{-3}\ t_\mathrm{d}$, while toward the outer cylinder I observe larger vortical structures taking shape, but they are not directly communicating with the riblet wall on the inner cylinder. Then this three dimensional flow inside the grooves starts to affect the larger flow structures within the gap and the difference is easily seen between Figures 5-2(b) and 5-5(b) at $t = 7.4 \times 10^{-2}\ t_\mathrm{d}$ while the first set of recirculating regions on the two ends of the Taylor-Couette cell are becoming visible. Comparing the two figures, one can see that in presence of the riblets, the initial Taylor-vortices are not as smoothly round as the ones that are initiated when the inner cylinder is smooth and the rest of the streamlines in the rest of the length of the cell are under direct influence of the riblets.
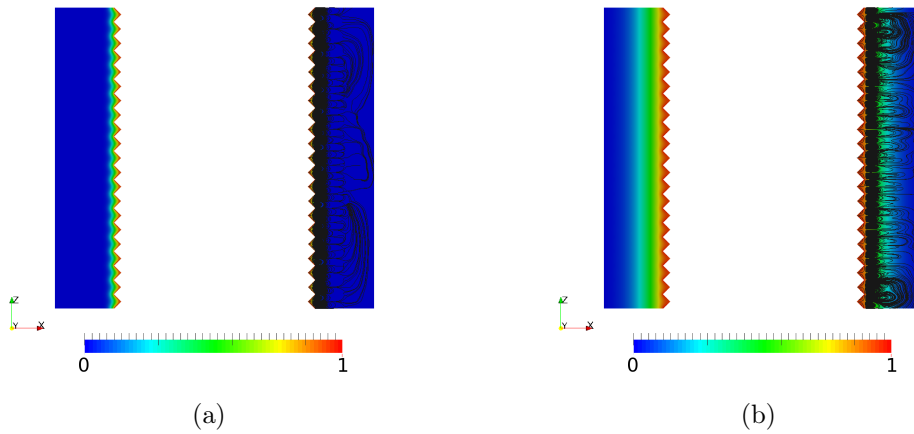
Figure 5-5: Contours of azimuthal velocity and streamlines of the in plane axial and radial velocity at (a) $t = 3 \times 10^{-3}\ t_\mathrm{d}$, (b) $t = 7.4 \times 10^{-2}\ t_\mathrm{d}$, for $\mathrm{Re}_d = 115$, $\eta = 0.63$, and $\Gamma = 5.1$ and riblets of $\lambda/d = 0.24$, and aspect ratio $\mathrm{AR} = 1$.

Then at $t = 1.2 \times 10^{-2}\ t_\mathrm{d}$ the second set of the vortices start to grow and become visible. But in the case of the riblet wall shown in Figure 5-6(a), one can see that the initial vortices are starting to form smoother streamlines while the smaller regions of closed streamlines right above the riblet wall, these smaller vortices, and the larger Taylor vortices are directly interacting with each other. Then at $t = 1.5 \times 10^{-2}\ t_\mathrm{d}$ (shown in Figure 5-6(b) the second set of the vortices have been formed and leading

the way for the final ones to initiate and grow in the central region of the Taylor Couette cell. Again, the smaller vortices due to the riblets are constantly interacting with the new and older Taylor vortices. But on the two ends, the larger Taylor vortices seem to be taking over the entire region and absorbing the small vortices from the riblets region, while the other Taylor-vortices are still interacting with the smaller vortices in the flow.

<div align="center">(a)   (b)</div>
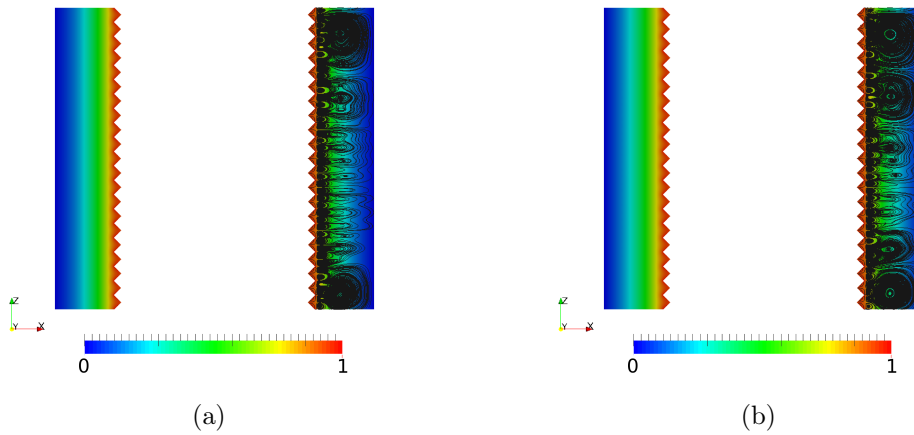
Figure 5-6: Contours of azimuthal velocity and streamlines of the in plane axial and radial velocity at (a) $t = 1.2 \times 10^{-2} \ t_\mathrm{d}$, (b) $t = 1.5 \times 10^{-2} \ t_\mathrm{d}$, for $\mathrm{Re}_d = 115$, $\eta = 0.63$, and $\Gamma = 5.1$ and riblets of $\lambda/d = 0.24$, and aspect ratio $\mathrm{AR} = 1$.

Then by $t = 2.2 \times 10^{-2} \ t_\mathrm{d}$ (as shown in Figure 5-7(a)), the three pairs of the Taylor vortices completely cover the entire gap and the length of the Taylor-Couette cell, while the azimuthal velocity is still not sensing any effect of the radial and axial velocities. The two Taylor vortices at the two ends have completely taken over the smaller vortices, but the other four vortices are still interacting with the smaller vortices and only a few of them are still left in the riblet boundary. Note that throughout this evolution, none of the Taylor vortices are able to penetrate into the grooves and the flow inside the grooves is a completely viscous dominated one. By $t = 3.0 \times 10^{-2} \ t_\mathrm{d}$ the smaller vortices due to the riblets have completely vanished into the larger Taylor vortices and the three vortex pairs have filled the entire cell (Figure 5-7(b)).
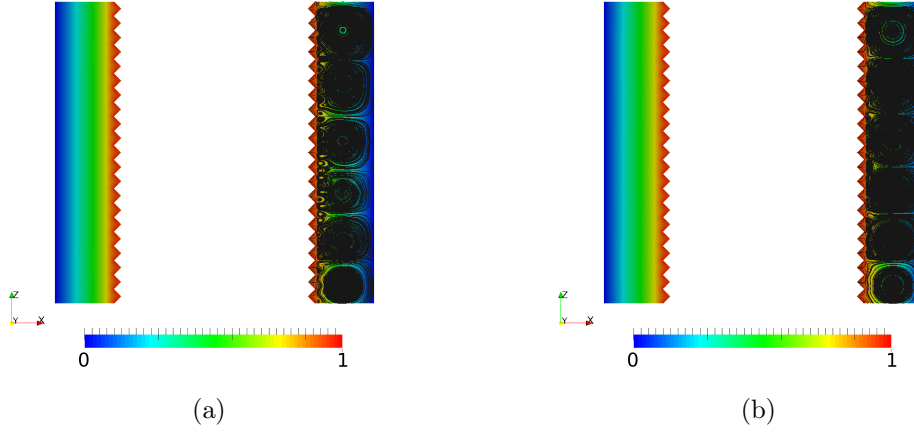
Figure 5-7: Contours of azimuthal velocity and streamlines of the in plane axial and radial velocity at (a) $t = 2.2 \times 10^{-2} \ t_{\mathrm{d}}$, and (b) $t = 3.0 \times 10^{-2} \ t_{\mathrm{d}}$, for $\mathrm{Re}_d = 115$, $\eta = 0.63$, and $\Gamma = 5.1$ and riblets of $\lambda/d = 0.24$, and aspect ratio $\mathrm{AR} = 1$.

Afterwards at $t = 4.1 \times 10^{-2} \ t_{\mathrm{d}}$, while no sign of the smaller riblets is left in the cell, the azimuthal velocity starts to sense the effect of the instability (Figure 5-8(a)) and by $t = 4.6 \times 10^{-2} \ t_{\mathrm{d}}$ the instability is becoming modulated and the velocity profile is not the same everywhere in the axial direction. From this point you can also see the Taylor vortices attempting to penetrate inside the grooves and more streamlines are visible inside the grooves (Figure 5-8(b)).

The modulation of the instability continues through to time $t = 5.2 \times 10^{-2} \ t_{\mathrm{d}}$, similar to the form in the case with the smooth rotor (Figures 5-9(a) and 5-4(e)), and finally the flow reaches to its steady state form as shown in Figures 5-9(b) and 5-9(b). The Taylor vortices have a similar form as to the ones in case with smooth rotors, however, close to the riblet wall the Taylor vortices slightly penetrate inside the grooves and especially peaks of the grooves are in contact with the high momentum fluid which results in sensing a higher shear stress at the peaks. The shear stress distribution will not be the same for all the riblets as the flow is now dependent on the axial direction as well. The wavelength of the vortex pairs and the length of a single vortex are again $1.7 \ d$ and $0.85 \ d$ respectively.

After reaching the steady state point, the riblet surface shown above with $\lambda/d =$
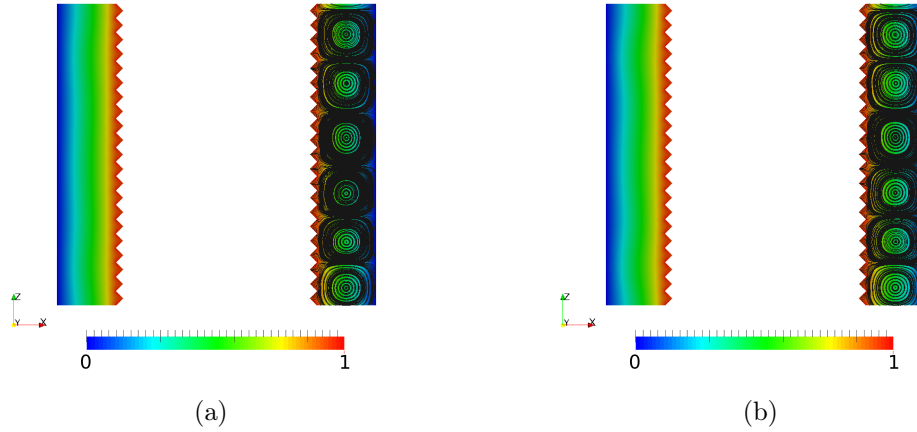
Figure 5-8:   Contours of azimuthal velocity and streamlines of the in plane axial and radial velocity at for Taylor vortex flow in presence of riblets with $AR = 1$ and at $Re_d = 115$ (a) $t = 4.1 \times 10^{-2} \ t_d$, (b) $t = 4.6 \times 10^{-2} \ t_d$, where t_d, for $Re_d = 115$, $\eta = 0.63$, and $\Gamma = 5.1$ and riblets of $\lambda/d = 0.24$, and aspect ratio $AR = 1$.
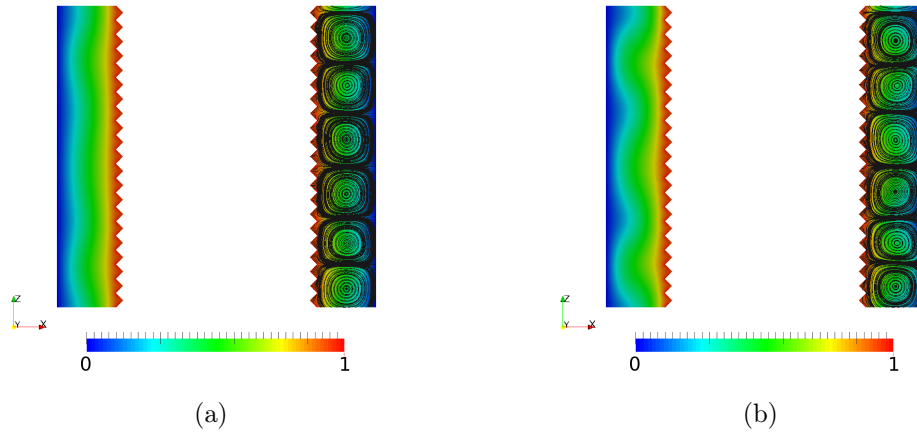
Figure 5-9:   Contours of azimuthal velocity and streamlines of the in plane axial and radial velocity at for Taylor vortex flow in presence of riblets with $AR = 1$ and at $Re_d = 115$ (a) $t = 5.2 \times 10^{-2} \ t_d$, and (b) $t = 5.9 \times 10^{-2} \ t_d$, for $Re_d = 115$, $\eta = 0.63$, and $\Gamma = 5.1$ and riblets of $\lambda/d = 0.24$, and aspect ratio $AR = 1$.

0.24 and $AR = 1$ shows a total torque reduction of 4.6% compared to the case with the smooth rotor numerically which is consistent with the results of the measurement presented in Figure 4-20 in Chapter 4.

For the case of the Reynolds number of $Re_d = 230$, the transient steps in the

245

growth of the Taylor vortices are presented below. In $\text{Re}_d = 230$, the original insta-bility gives rise to three vortex pairs initially, but the vortices combine to settle into two vortex pairs over a length of $\Gamma = 3.4$ (2/3 of the length in the previous case; to reduce the costs of the simulations).

The time evolution of the Taylor vortices at $\text{Re}_d = 230$, for Taylor Couette cells with no riblets (AR = 0) are shown in Figures 5-10 and 5-11 and 5-12, for riblets with aspect ratios of AR = 1 are shown in Figures 5-13 and 5-14, and for AR = 2 are shown in Figures 5-15 and 5-16. The evolution is shown using the scalar Q which is defined as in Equation 3.4 and discussed in chapter 3. Here Q is non-dimensionalized by the square of the rate of shear strain and specifically here by using the rate of shear strain in a laminar Taylor Couette flow with smooth rotors, as written in Equation 4.22. Thus the color bar of the figures is presenting $Q/\dot{\gamma}_{r\phi}^2$. As shown in Figures 5-10, first the flow develops in the same manner as the laminar flow, but by 0.12 t_d the flow starts to undergo an instability which is modulated and gives rise to three vortex pairs in the entire length. However, the three vortex pairs are not stable and they oscillate back and forth and it can be seen in the bottom figures in Figure 5-10

The oscillation continues as shown in Figures 5-11 until the three pairs of vortices fill the entire region. The two vortex pairs toward the top of the cell are smaller in wavelength compared with the one toward the bottom.

But these vortices cannot sustain their shape and ultimately, as shown in Figures 5-12, the two vortex pairs on the top move toward each other and collapse into one pair (at about 0.52 t_d) and the two remaining vortex pairs adjust their wavelengths to cover the entire length of the cylinder (Note that periodic boundary condition is used for the top and bottom of the cell). After the time of 0.6 t_d the Taylor vortex flow over smooth rotor reaches a steady state and no changes are seen in the flow. Again the final wavelength of the Taylor vortex pairs is calculated to be 1.7 d. Mullin, Heise and Pfister discuss such collapse of N vortices to $N - 2$ vortices in terms of a pitchfork bifurcation [156].

For the case of the riblets with AR = 1, the process of the evolution of the vortices is similar to the case of the smooth rotor. However, in the case of the riblets
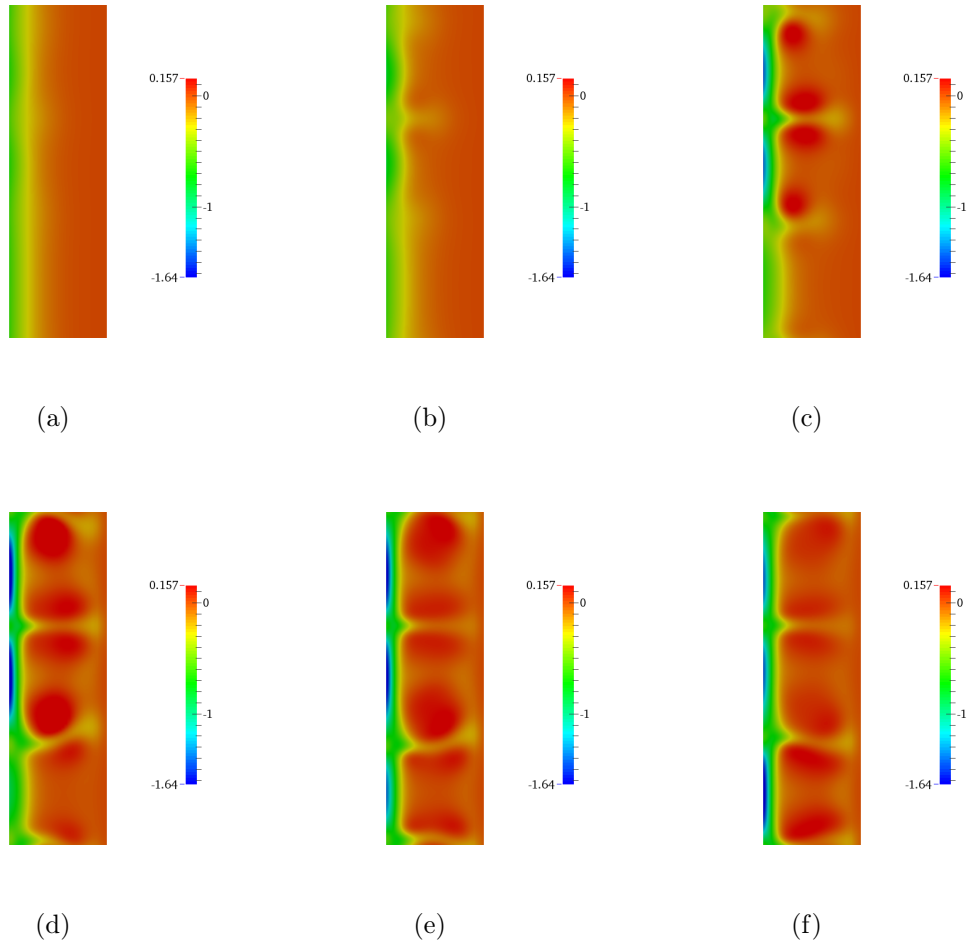
Figure 5-10:   Time lapse of Q criteria of the initiation of the Taylor vortices in flow with $\mathrm{Re}_d = 230$, $\eta = 0.63$, and $\Gamma = 3.4$ for t/t_d (a) 1.03×10^{-1}, (b) 1.18×10^{-1}, (c) 1.33×10^{-1}, (d) 1.48×10^{-1}, (e) 1.64×10^{-1}, and (f) 1.77×10^{-1} over a smooth rotor.

of AR $= 1$, the first sign of instability is visible slightly later than the smooth case at $0.13\ t_\mathrm{d}$ and again three pairs of vortices are initiated along the length of the cell with one having a larger wavelength than the others (See Figure 5-13).

However, this time there is no oscillation visible in the Taylor vortices as it was observed in the case with the smooth rotor. Again the presence of three pairs of vortices is unstable and the two vortex pairs with smaller wavelengths move toward each other and ultimately collapse into one larger Taylor vortex. Afterwards the two Taylor vortices adjust their wavelengths to be the same and fill the entire length of the cell (shown in Figures 5-14).
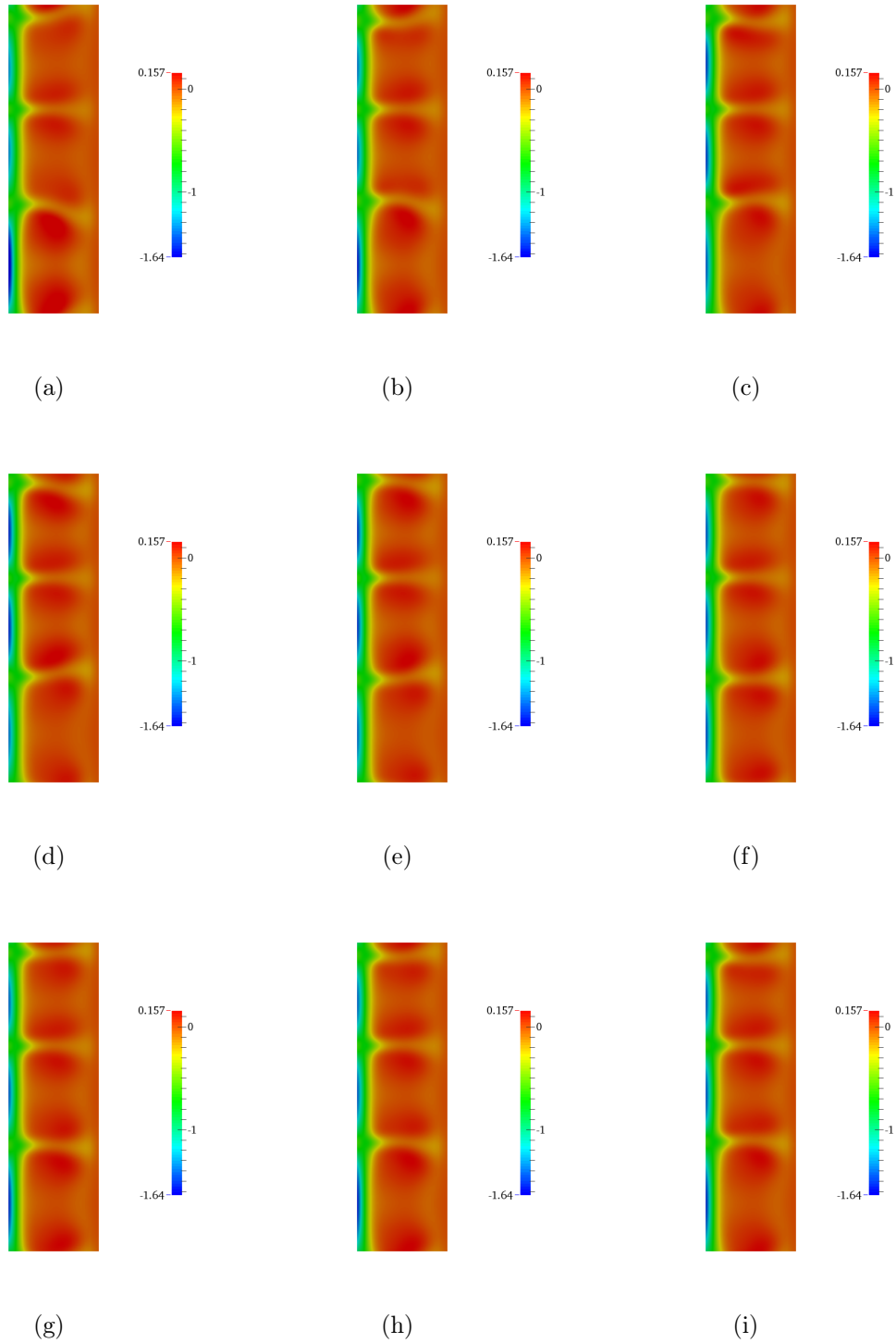
Figure 5-11: Time lapse of Q criteria of the initiation and growth of the Taylor vortices in flow with $\mathrm{Re}_d = 230$, $\eta = 0.63$, and $\Gamma = 3.4$ for t/t_d (a) 1.92×10^{-1}, (b) 2.09×10^{-1}, (c) 2.24×10^{-2}, (d) 2.37×10^{-1}, (e) 2.51×10^{-1}, (f) 2.66×10^{-1}, (g) 2.81×10^{-1}, (h) 2.96×10^{-1}, and (i) 3.10×10^{-1} over a smooth rotor.
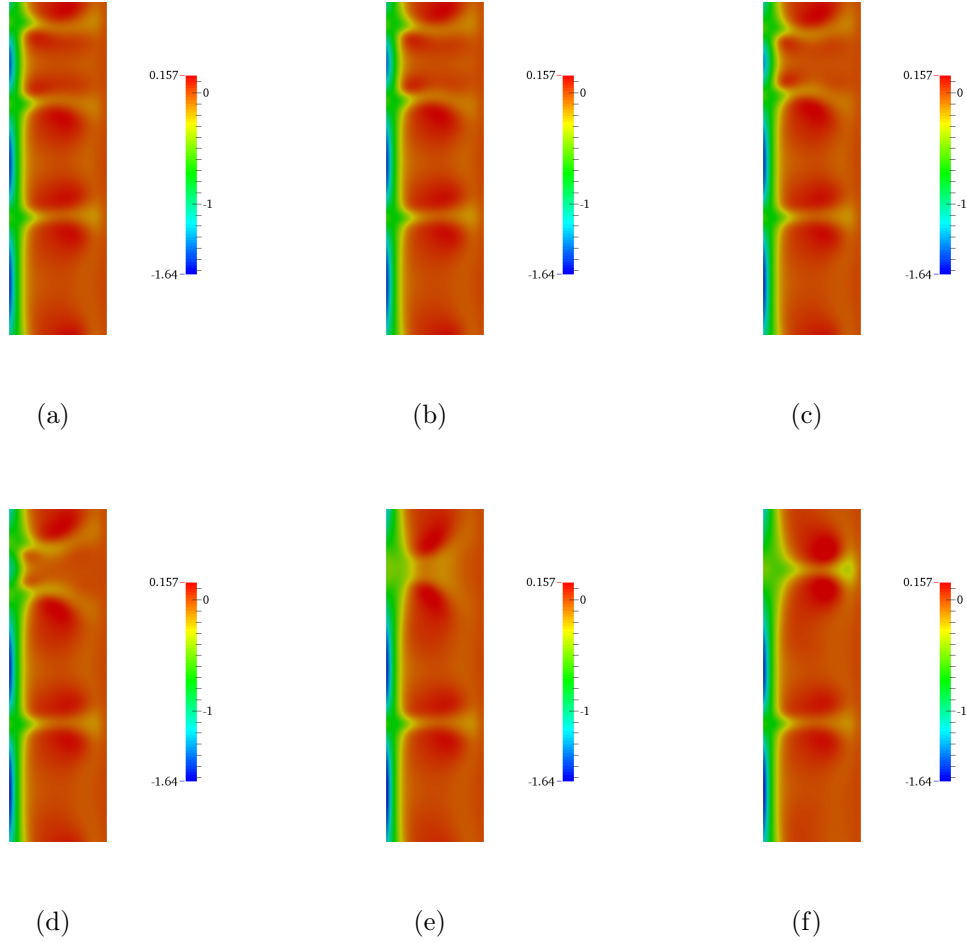
Figure 5-12:   Time lapse of Q criteria of the initiation and growth of the Taylor vortices in flow with $\text{Re}_d = 230$, $\eta = 0.63$, and $\Gamma = 3.4$ for t/t_d (a) 4.58×10^{-1}, (b) 4.73×10^{-1}, (c) 4.88×10^{-1}, (d) 5.03×10^{-1}, (e) 5.18×10^{-1}, and (f) 5.32×10^{-1} over a smooth rotor.

Similar behaviour is also seen when riblets with AR $= 2$ are put in the Taylor-Couette flow at $\text{Re}_d = 230$. First signs of the instability is visible at $t = 0.13$ t_d (slightly later than what was seen in the case with the smooth rotor) and again three pairs of Taylor vortices show up in the cell.

Afterwards, unlike the smooth case, no visible oscillations are seen among the vortices, however the top two vortex pairs move toward each other and combine into one vortex pair. The two vortex pairs cover the entire length of the cell with each pair having a wavelength of $\Lambda/d = 1.7$ and each of the separate counter rotating cells have a length of 0.85 d. This wavelength is similar across all the cases of smooth and
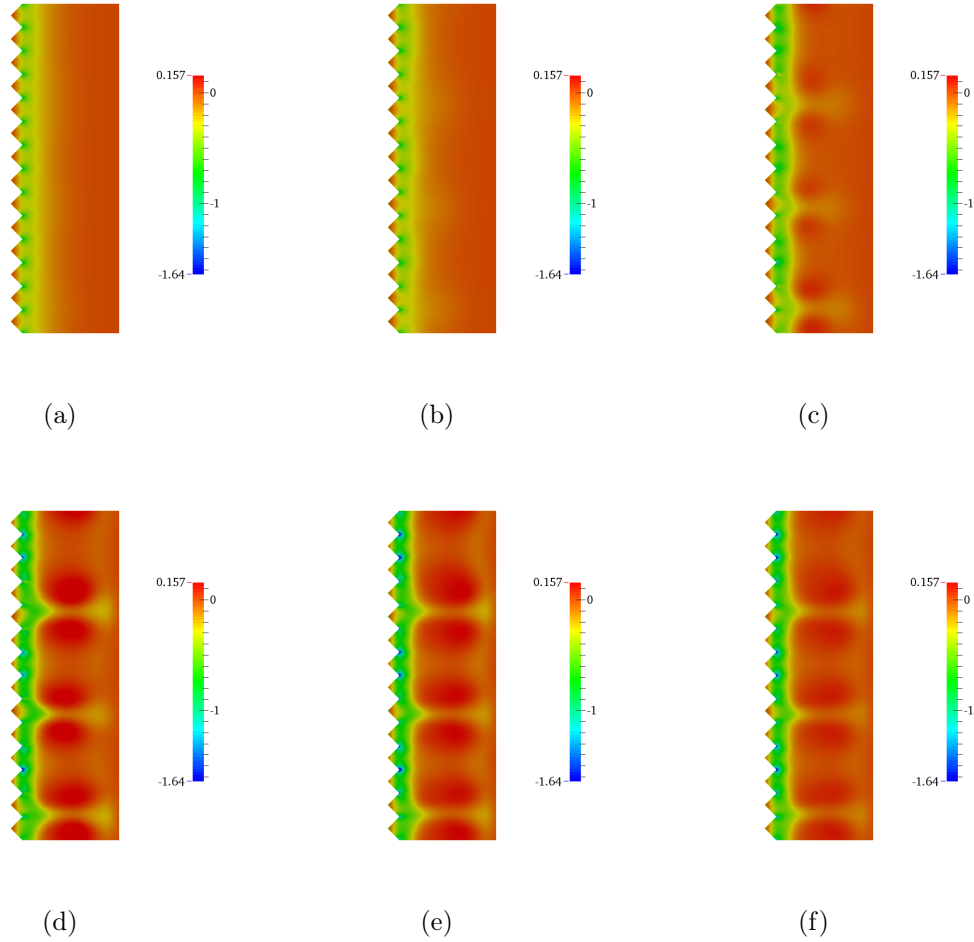
Figure 5-13: Time lapse of Q criteria of the initiation and growth of the Taylor vortices in flow with $\mathrm{Re}_d = 230$, $\eta = 0.63$, and $\Gamma = 3.4$ for t/t_{d} (a) 1.18×10^{-1}, (b) 1.33×10^{-1}, (c) 1.48×10^{-1}, (d) 1.64×10^{-1}, (e) 1.77×10^{-1}, and (f) 1.92×10^{-1} over a riblet covered rotor with aspect ratio of $\mathrm{AR} = 1$.

riblet surfaces.

So, while the overall behaviour of the Taylor vortices and their evolution seems to be similar with slight difference between the cases with smooth rotor and the riblets with $\mathrm{AR} = 1$ and $\mathrm{AR} = 2$, the most prominent difference that is clear among all the time instances is that the contours of Q close to the inner cylinder for the case with the smooth rotor are on the lower side of the color bar corresponding to flow being dominated by the rate of strain tensor and in this case specifically the rate of the shear strain. Hence the entire length of the inner cylinder is in contact with flow with
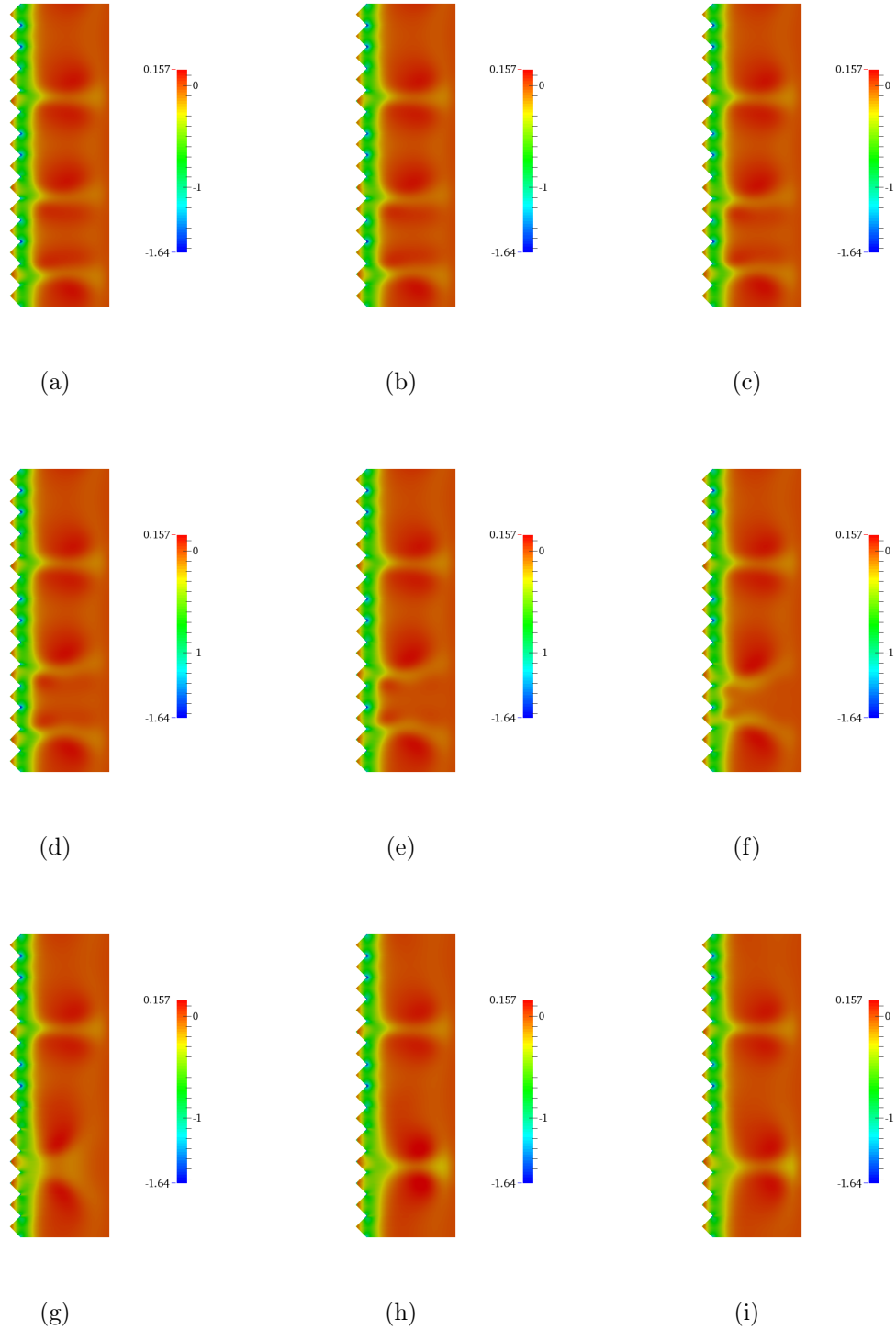
Figure 5-14: Time lapse of Q criteria of the initiation and growth of the Taylor vortices in flow with $\mathrm{Re}_d = 230$, $\eta = 0.63$, and $\Gamma = 3.4$ for t/t_d (a) 3.40×10^{-1}, (b) 3.58×10^{-1} , (c) 3.70×10^{-1}, (d) 3.85×10^{-1}, (e) 3.99×10^{-1}, (f) 4.14×10^{-1}, (g) 4.29×10^{-1}, (h) 4.44×10^{-1}, and (i) 4.59×10^{-1} over a riblet covered rotor with aspect ratio of AR = 1.
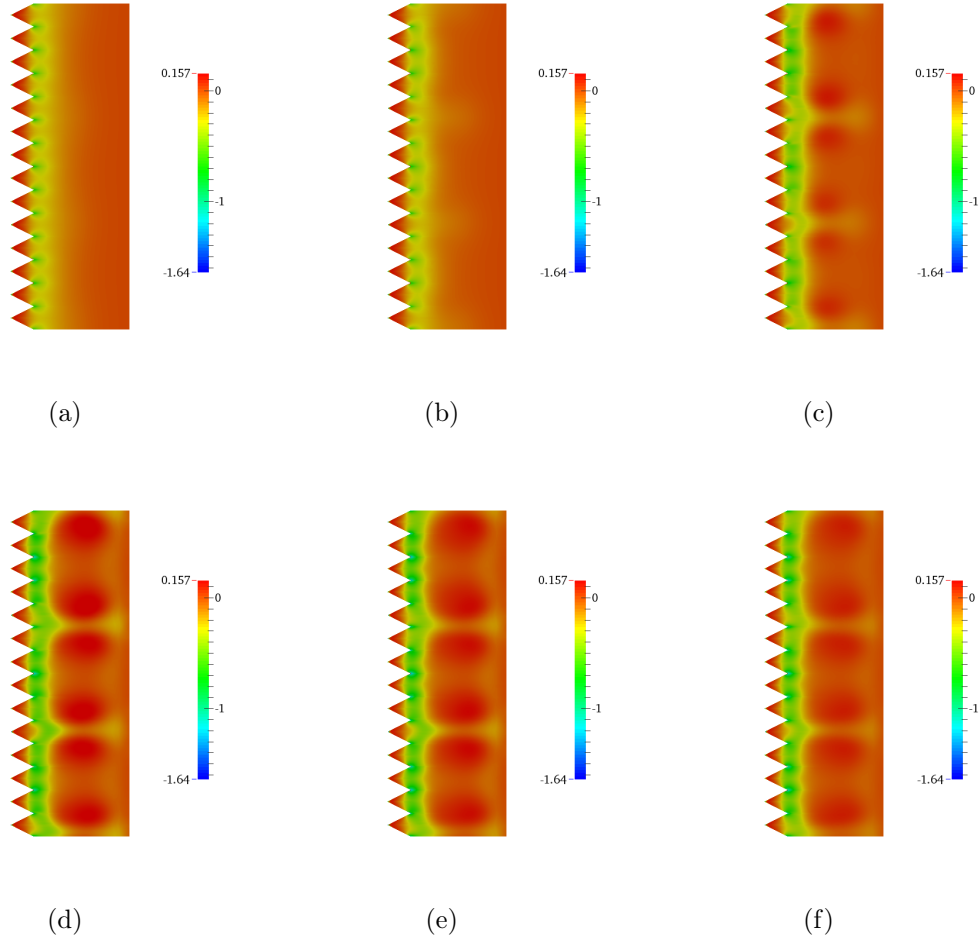
Figure 5-15: Time lapse of Q criteria of the initiation and growth of the Taylor vortices in flow with $\text{Re}_d = 230$, $\eta = 0.63$, and $\Gamma = 3.4$ for t/t_{d} (a) 1.18×10^{-1}, (b) 1.33×10^{-1}, (c) 1.48×10^{-1}, (d) 1.64×10^{-1}, (e) 1.77×10^{-1}, and (f) 1.92×10^{-1} over a riblet covered rotor with aspect ratio of $\text{AR} = 2$.

a high rate of shear strain.

However, moving to the case with riblets of $\text{AR} = 1$ and $\text{AR} = 2$, it can be seen that only parts of the riblets, especially in the vicinity of the peaks of the riblets, are in contact with flow with high rates of shear strain and as one moves toward the inside of the grooves, the flow moves toward a higher rate of rotation (or the anti-symmetric part of the velocity gradient tensor). Since the total torque is directly dependent on the shear rate and not the rotation in the flow, inside the grooves experiences a lower shear stress compared to the case of the smooth rotor. Thus, only a portion of
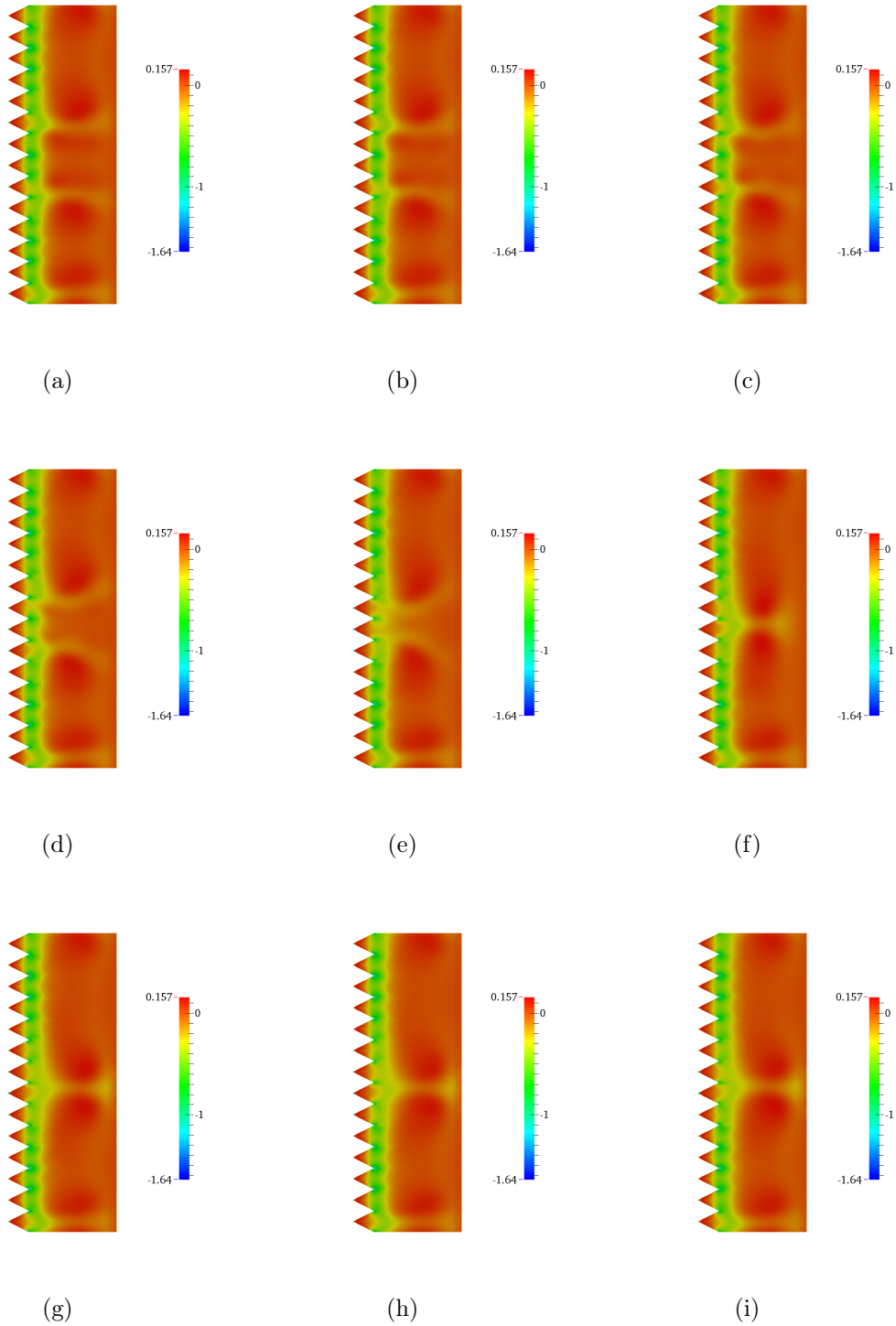
Figure 5-16: Time lapse of Q criteria of the initiation and growth of the Taylor vortices in flow with $\mathrm{Re}_d = 230$, $\eta = 0.63$, and $\Gamma = 3.4$ for t/t_d (a) 8.73×10^{-1}, (b) 8.88×10^{-1}, (c) 9.02×10^{-1}, (d) 9.17×10^{-1}, (e) 19.32×10^{-1}, (f) 9.47×10^{-1}, (g) 9.61×10^{-1}, (h) 9.76×10^{-1}, and (i) 9.91×10^{-1} over a riblet covered rotor with aspect ratio of AR = 2.

the length of the inner rotor will be in contact with high momentum fluid when the riblets are present. Note that this is a local discussion of the distribution of the rate of shear strain on the wall and does not take into account the increase in the wetted surface area. This will be discussed in more detail in the next section.

The evolution of the frictional torque on the inner cylinder for Taylor-Couette flow with $\mathrm{Re}_d = 230$ and riblet covered rotors with aspect ratios of $0 \leqslant \mathrm{AR} \leqslant 2$ are plotted in Figure 5-17. As seen in the figure, the evolution of the torque up to the steady state value goes through different paths with different jumps at different times depending on the geometry used. However, the over all transient process is very similar across the different cases.
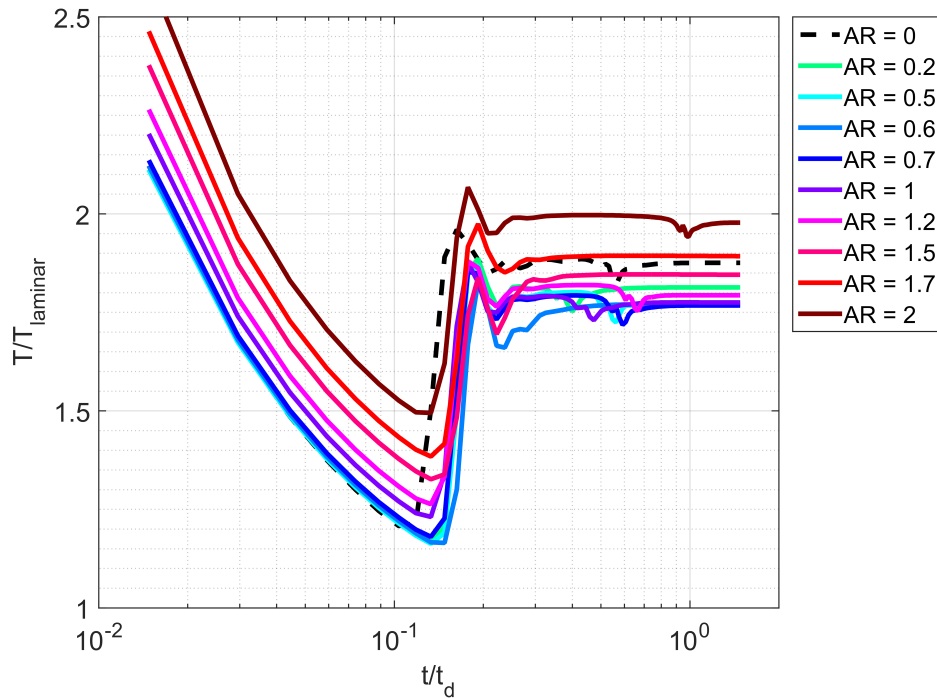
Figure 5-17: Evolution of frictional torque over time for Taylor Couette flow at $\mathrm{Re}_d = 230$, $\eta = 0.63$, and $\Gamma = 3.4$ for riblet covered rotors with aspect ratios $0 \leqslant \mathrm{AR} \leqslant 2$. The torque is normalized by the torque defined in the laminar case and the time is normalized by the diffusion time.

Figure 5-18 shows the torque evolution for the case of $\mathrm{AR} = 1.5$ from the cases shown in Figure 5-17. In addition at different times, especially at local minima and maxima of the curve, the contour plots of the circumferential velocity as well as the

streamlines of the axial and radial velocity are shown in the figure as well. At first while toward the outer cylinder the larger vortex structures start to get formed, inside each groove smaller vortex pairs are also created. As time goes forward, without the azimuthal velocity feeling any difference, the four pairs of Taylor vortices start to interact with the smaller vortices inside the grooves.

Afterwards, as the azimuthal velocity starts to show signs of the instability, the larger Taylor vortices take over the smaller vortices inside the grooves and then a wave showing the four vortex pairs becomes visible on the velocity contour. Then a sudden jump in the torque is observed and the velocity contour now shows the instability, but still the vortex pairs are interacting and mixing with each other to form three vortex pairs at the torque maximum.

At the next local minimum, the mixing continues and the vortex pairs are down to two, but still remnants of older vortices are seen. In addition, the velocity contour also shows an unusual, non-periodic shape and ultimately when the flow reaches steady state, only two pairs of vortices are visible in the entire cell with $\Gamma = 3.4$ and the velocity contours turn into a periodic shape also showing two cells corresponding to two vortex pairs.

5.3.2 Effect of Riblet Geometry in Torque Changes

Similar to the Couette flow, riblets are capable of changing the total frictional torque on the inner cylinder. The change in torque is not only a function of the viscous flow retardation inside the grooves, but also the interaction of the riblets with the Taylor vortices will affect the total torque reduction achieved.

The results presented in Figure 4-20 show that in the Taylor vortex regime, the total torque reduction is again a function of the aspect ratio of the riblets and similar non-monotonic behaviour is observed in the torque change as a function of the aspect ratio. I can compare the results at $\text{Re}_d = 230$ which is well above the transition region from Couette flow to the Taylor vortex region, but still no wavy Taylor vortices are observed in this region. The results of the torque evolution over time for various aspect ratios were presented in Figure 5-17. Note that no theoretical results for the
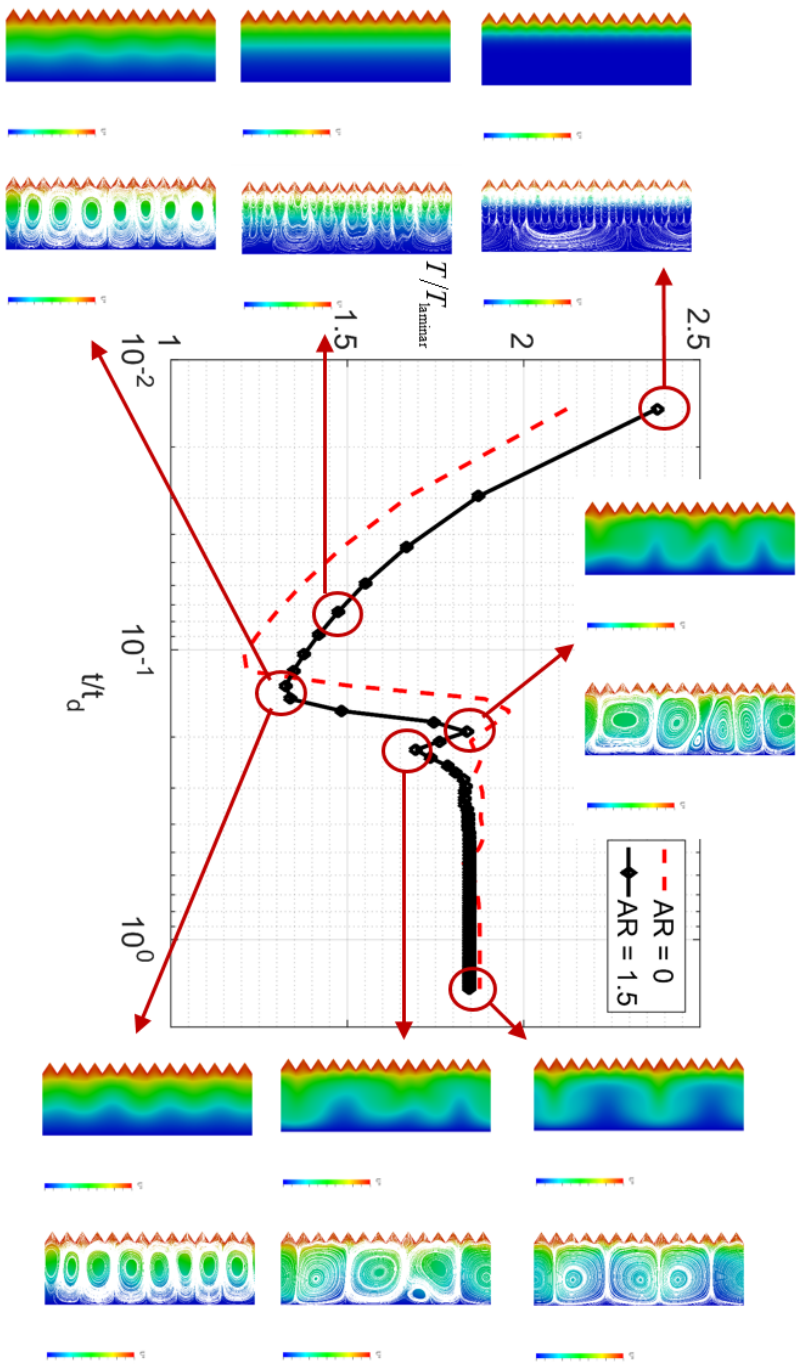
Figure 5-18: Time evolution of torque for riblet covered rotors with AR = 1.5 at Re_d = 230 compared with the smooth rotor. Corresponding contour plots of the azimuthal velocity profile as well as in-plane streamlines with axial and radial velocities are shown for distinct times where various changes occur in the flow. This riblet surface can reduce the total drag by about 1%.

torque in the Taylor vortex region has been reported, however, in different Reynolds number regimes various functional forms such as power law scaling have been suggested throughout the years. As mentioned in the previous chapter, in the Taylor vortex regime, torque is dependent on $\mathrm{Re}_d^{1.53}$ which is very close to the exponent of 1.5 reported by Wendt [144].

The results of the change in torque for $\mathrm{Re}_d = 230$, $\eta = 0.63$, and riblets of $\lambda/d = 0.24$ as a function of the aspect ratio, AR, is plotted in Figure 5-19. In the figure, the computational results are plotted for various aspect ratios and the results of the experiments are added for comparison. The results show a non-monotonic behaviour for the torque reduction as a function of the aspect ratio. On this plot, an additional curve shows the results of the torque reduction in the laminar flow for $\mathrm{Re}_d < 75$ with the same riblet geometry, over a range of the aspect ratios, similar to the one presented in Chapter 4.
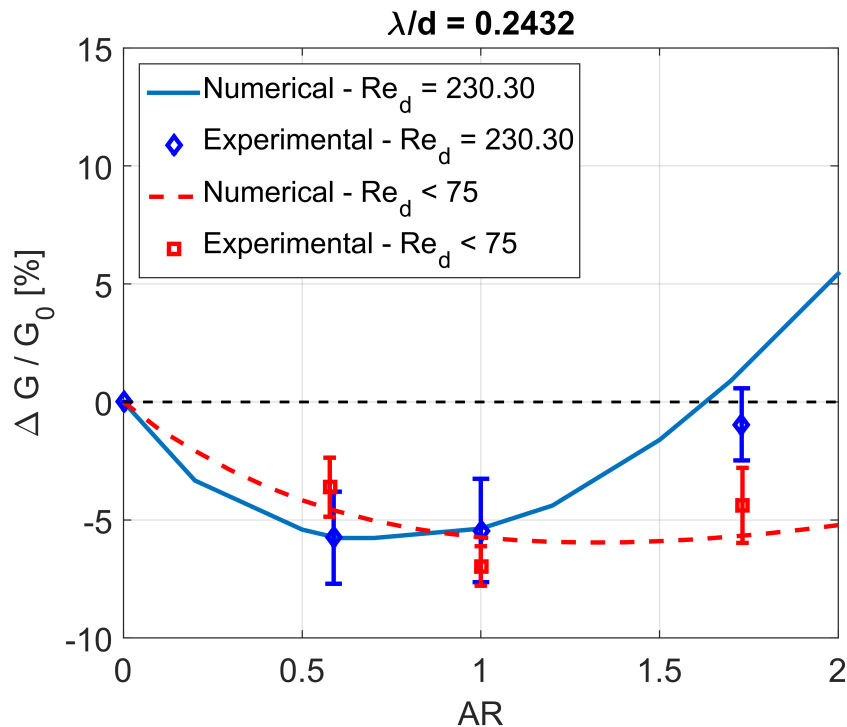
Figure 5-19: Frictional torque change in the Taylor vortex regime with riblets of $\lambda/d = 0.24$ at $\mathrm{Re}_d = 230$ over a range of aspect ratios. The results of the torque change for the laminar Taylor Couette flow for $\lambda/d = 0.24$ as a function of the AR is also shown here for comparison.

Comparing the drag reduction in the Taylor vortex flow compared with the laminar flow shows that in the Taylor vortex regime the torque reduction is achieved over a smaller range of aspect ratios, AR compared with the reduction in the laminar region. The maximum reduction is nearly similar between the two cases, however, this maximum happens at a lower aspect ratio (AR $\approx 0.6 - 0.7$) for the Taylor vortex case, compared with the laminar one which is happening at AR $\approx 1.2 - 1.3$.

This trend in the torque change can again be explained by shear stress distribution on the riblet wall. Here with the Taylor vortices present, instead of plotting the shear stress distribution for only one riblet, the shear stress distribution within two Taylor vortex pair wavelengths is presented in Figure 5-20 to capture the details of the shear stress profiles. The shear stress is normalized by the shear stress distribution on a smooth wall in the laminar flow.

First it can be seen that the presence of the riblets definitely changes the shear stress distribution and the shear stress felt inside the grooves is smaller than the shear stress close to the peaks of the riblets. On the other hand, due to the dependence of the velocity profiles on the axial direction, then the shear stress is not similar for each and every riblet, therefore, the maxima and minima of the shear stress on the curves follow the overall shape of the shear stress distribution due to the Taylor vortices while it goes through maxima and minima due to the presence of the riblets. This shows that both riblets and the Taylor-Couette vortices play a role in the changes seen in the torque.

Due to the distribution of the shear stress on riblet covered rotors, I notice that a wide area of each riblet is experiencing shear stresses lower than the shear stress on the smooth surface. However, increasing the aspect ratio, results in a wider and wider area experiencing a lower shear stress inside the grooves. Therefore, the average shear stress distribution (averaged over one wavelength of the vortex pair) in Taylor-vortex flow over the riblets decreases as the aspect ratio of the riblets increase. But, due to the Taylor vortices the peaks of the riblets experience a modulated increase in the shear stress compared to the case of the laminar flow. Especially in higher AR cases, the minimum of the shear stress profiles are rather constant throughout the length

258
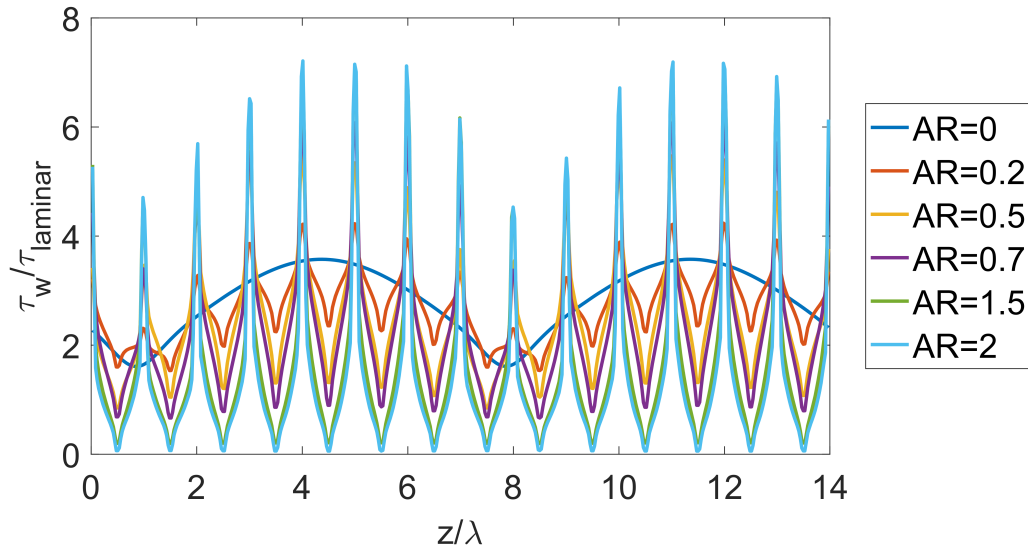
Figure 5-20: Shear stress distribution on the riblet wall in Taylor-Couette flow with riblet covered inner cylinders. The shear stress is plotted for 2 Taylor vortex pair wavelengths and for various aspect ratios at $\mathrm{Re}_d = 230$. The shear stress is non-dimensionalized with the shear stress in the laminar Taylor-Couette flow with smooth rotors $\tau_{\mathrm{laminar}} = 2\mu/(1 - \eta^2)$.

while the maxima change throughout the length following the distribution of shape of the shear stress due to the Taylor vortices. The average shear stress distribution as a function of the aspect ratio of the riblets are presented in Figure 5-21. Similar to the laminar flow, the average shear stress is decreasing with aspect ratio while the total wetted area is increasing. Therefore, the total torque reduction which is the interplay of the reduction in the average shear stress distribution and the increase in the area, goes through a non-monotonic behaviour as a function of the aspect ratio of the riblets.

However, it should be noted that due to the modulation in the shear stress felt on the peaks of the riblets, the decrease in the average shear stress is not as substantial as in the laminar case and therefore, comparing Figures 5-21 and 4.7, it can be seen that this reduction in the average shear stress in the case of the Taylor vortices can only counteract the effect of the area increase to only a smaller range of aspect ratios compared to the laminar Taylor-Couette flow and hence the torque reduction can be achieved over a smaller range of aspect ratios compared with the laminar case.
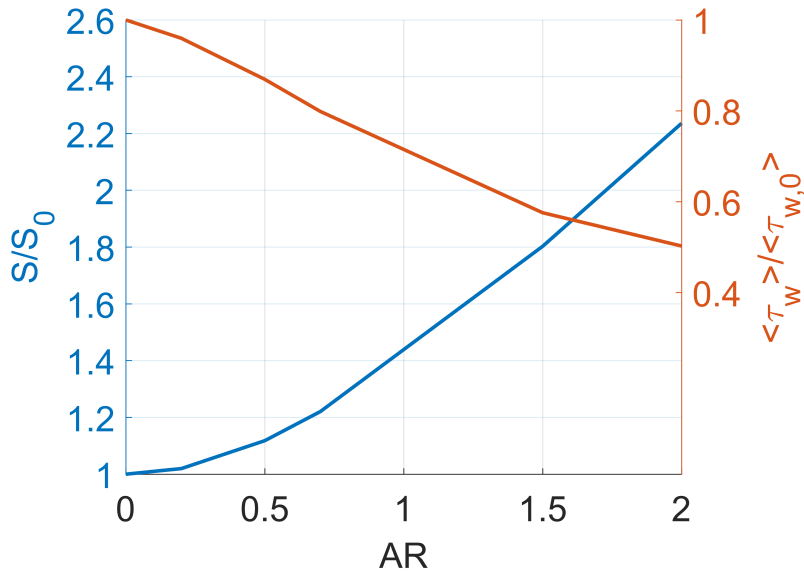
Figure 5-21:   Average shear stress in Taylor vortex flow over riblet covered rotors compared with the average shear stress on a smooth rotor as a function of the AR for the case of $\lambda/d = 0.24$ and $\mathrm{Re}_d = 230$ as well as the change in the wetted area as a function of the AR.

5.4   Conclusion

In this chapter, the case of the Taylor Couette flow at $\mathrm{Re}_d = 230$ in the Taylor vortex regime with $\eta = 0.63$, and $\Gamma = 3.4$ was employed to investigate the effect of the riblet covered rotors on the changes in the frictional torque on the inner cylinder. Time dependent numerical simulations of the flow over riblets with $\lambda/d = 0.24$ and aspect ratio of ranges between 0 and 2 were discussed in terms of the interactions of the riblets with the Taylor vortices.

The time dependent interaction of the geometry of riblets with the Taylor vortices were presented for smooth and various riblet walls and discussed in terms of the velocity distribution and the Q criteria in the flow.

Later, the evolution of the torque over time were presented and compared with the flow structure at various time stamps prior to reaching the steady state. As it was seen the riblet peaks are directly in contact with the final Taylor vortices and the Taylor vortices tend to try to penetrate inside the grooves and hence the region in the vicinity of the peaks is in contact with high momentum fluid and experiences

a higher shear stress compared to the rest of the grooves.

In the end, the changes in torque were presented as a function of the aspect ratio and compared with the corresponding laminar situation. Similar to the laminar case, the riblets reduce the average shear stress distribution over the wall as the AR of the riblets is increased. However, the presence of the Taylor vortices and interactions with the riblets result in an additional increase in the total frictional torque and hence the decrease in the average shear stress distribution is smaller than the decrease in the laminar case. Therefore, the non-monotonic behaviour observed in the torque change as a function of AR can be extended in the Taylor vortex flow, however, only a smaller ranges of the aspect ratios are able to provide a reduction in the total frictional drag force.

With the complexity of the Taylor vortex flow and the various bifurcations that are possible for this flow, it is intriguing to model additional cases with different riblet geometries and other Reynolds numbers. The simulations for larger Reynolds number should be performed for the full geometry of the concentric cylinders, since the rest of flow behaviours are not axisymmetic. However, such simulations can be expensive and would require larger computational memories than available in the current study.

THIS PAGE INTENTIONALLY LEFT BLANK

Chapter 6

Conclusion and Future Directions

In the previous chapters, a comprehensive study of the riblet surfaces in a model external and internal flow were presented; Boundary layers as the external flow and Taylor-Couette flow as the internal flow. In both cases we showed that riblet surfaces have the ability to reduce the frictional drag force on the corresponding surfaces that were analysed. However, it was also shown that the dynamics of the flow through a Reynolds number, as well as the geometry of the riblets, and the overall flow play direct roles in the final changes in the frictional drag force.

In this chapter, an overall summary of the findings of the previous chapters are presented based on the dynamics of the flow and the geometry of the riblets. Then in a later section, a list of suggestions for future research on this method of passive drag reduction and applications of the method in different industries will be discussed.

6.1 Effect of the Flow Dynamics - Reynolds Number

Dependence of the changes in the frictional drag using riblet surfaces on the dynamics of the flow defined in terms of the Reynolds number varies based on the flow type being analysed. One can clearly see the difference by comparing the case of the boundary layers over riblet covered surfaces in Chapters 2 and 3 and a closed system such as the Taylor-Couette flow in the laminar regime where the flow is axi-symmetric and fully developed as shown in Chapter 4. As it was shown, in a fully developed laminar

Taylor-Couette flow the torque over a smooth and riblet surface scales linearly with the Reynolds number and hence the changes in torque due to riblets is not dependent on the Reynolds number. Hence the experimental and numerical results, and the accompanying theory all confirm this. It should be noted that in this flow, the velocity profile and the shear stress profiles are only dependent on the geometry of Taylor-Couette cell and the riblets and the Reynolds number does not present itself in them. Therefore, torque is only dependent on Re_d linearly.

On the other hand, in the boundary layers, the local velocity profiles and the local shear stress distribution are directly dependent on the Reynolds number. Therefore, the total frictional drag will be dependent on the total length of the plate as it was shown in Chapters 2 and 3. Therefore, with the shear stress dependence on the local Reynolds number based on the stream-wise direction in both smooth and riblet surfaces as shown in Figure 3-21(a), then the total frictional drag as calculated by the integral of the local shear stress will be dependent on the Reynolds number based on the length of the plate as shown in Figure 3-21(b). On the other hand, the theoretical model and scaling introduced in Chapter 2 allows us to described the total frictional drag reduction as a function of a scaled form of Reynolds number based on the total length and use that to adjust the design of the riblet surfaces based on the length of the plate or the velocity of the free-stream (The size of the riblets will be discussed later in section 6.3).

Calculations of the reduction in the total frictional drag force using conformal mapping for the V-groove riblets and the numerical simulations for the wrinkled surfaces show that for a riblet surface to be drag reducing the scaled Reynolds number $\mathrm{Re}_L(\lambda/L)^2$ of a surface needs to be smaller than a threshold. This means that at a constant riblet wavelength and constant flow velocity, the length of the plate needs to be larger than a minimum threshold for it to be drag reducing. On the other hand, at a constant plate length and a constant riblet wavelength, then the velocity of the flow needs to be lower than a threshold to offer drag reduction.

6.2 Effect of the Riblet Sharpness - Aspect Ratio

While both boundary layer flow and Taylor-Couette flow are different in many ways, their response to changes in aspect ratio, AR, of the riblet were very similar. In both boundary layer flow and Taylor Couette flow, at a constant Reynolds number and a constant non-dimensional riblet wavelength (depending on the flow λ is non-dimensionalized with different length scales), the changes in the total frictional drag (or torque) measured or calculated on the surfaces showed a non-monotonic behaviour. First at lower aspect ratios riblets results in a reduction in drag/torque and this reduction was enhanced up to an optimum aspect ratio. Then the trend was reversed and as the aspect ratio was increased more, drag/torque reduction diminishes and after an aspect ratio, only drag increase in observed.

This behaviour can be explained by the shear stress distribution inside the riblets and how the presence of the riblets results in a non-uniform distribution of the shear stress inside the grooves with the peaks of the riblets experiencing a larger shear stress compared to their equivalent smooth wall while the trough of the riblets experience a lower shear stress compared to the smooth wall. Therefore, the average of the shear stress distribution (whether in boundary layers or in Taylor-Couette flows) will encounter a decreasing trend as the aspect ratio of the riblets is increased. However, no matter the shape of the riblets chosen, increasing the aspect ratio directly results in an increase in the wetted surface area. Therefore, observing a reduction in total drag is ultimately dependent on the interplay of the decreasing trend in the shear stress distribution as the aspect ratios are increased and the increasing trend in the wetted surface area. Hence this interplay results in a non-monotonic behaviour in the total reduction achieved in each of the cases.

6.3 Effect of the Size of the Riblets - Wavelength

As it was shown throughout the previous chapters, the changes in frictional drag due to the presence of the riblet surfaces is directly dependent on the size of the riblets

used in both external and internal flows.

In the boundary layers, through the scaling of the extended three dimensional boundary layer equations, it was shown that the total torque reduction is dependent on the λ/z and it is best to be used in a scaled form of the local and global Reynolds number as $\mathrm{Re}_z(\lambda/z)^2$ and $\mathrm{Re}_L(\lambda/L)^2$ respectively. Using the scaled Reynolds number, the results of the calculations with conformal mapping shown in Chapter 2 showed that the reduction in the total frictional drag force is directly dependent on the scaled Reynolds number and for a ribelt surface to be drag reducing, the plate should have a scaled Reynolds number smaller than a threshold depending on the aspect ratio of the riblets. Therefore, with the definition of the scaled Reynolds number, at a constant velocity and constant length, then the wavelength of the riblets should be smaller than a limit for the plate to be drag reducing.

On the other hand, for the case of the Taylor-Couette flow, the wavelength was non-dimensionalized by the size of the gap of the Taylor-Couette cell which is the length scale where the diffusion of vorticity happens. Experimental results presented in Chapter 4 showed that increasing the wavelength at constant Taylor-Couette geometry and riblet aspect ratio results in a an enhancement in the torque reduction achieved. The relationship of the torque reduction with the wavelength of the riblets were also analysed using a higher order expansion of the velocity profile and using a perturbed boundary condition to solve the equations for the first order term of the azimuthal velocity. The model at small aspect ratios and small λ/R_i captures the slope of the torque reduction curves from the numerical simulations. The simplified model used later in the chapter, can capture the relationship of the torque reduction as a function of both λ/d and the geometry of the Taylor-Couette cell through $(\eta(1+\eta))^{-1}$ and the results were shown for three different aspect ratios.

Therefore, depending on the type of the flow, the size of the riblets in terms of the wavelength chosen can play a role in different ways and the drag change achieved (whether increase or decrease) would show different scaling behaviours with the wavelength. In addition, in both cases shown above, the results were dependent on a combination of the non-dimensional wavelength, geometry of the overall flow, and in

the case of the boundary layer on the dynamics of the flow. Therefore, while the torque reduction with aspect ratio takes a universal trend, the dependence on the wavelength needs to be mapped separately for the specific flow type needed and used solely for that flow.

6.4 Future Directions

The ability of reducing frictional drag force using passive methods, such as riblet surfaces can have spectacular implications for different industries. Understanding the effect of riblets on external and internal flows in different regimes allows for innovative designs of external and internal surfaces which could offer lower frictional losses, hence reducing the energy losses associated with the frictional drag between the fluid and the solid surfaces.

In terms of the external flows, with the understanding form this study for the laminar boundary layer flow and the literature for the riblet drag reduction in the turbulent boundary layers, one can design surfaces tailored to offer the best response in different locations along the length of the surface and hence a better total reduction in drag. This can be applied to ship halls, surface of the airplanes, as well as the body of Unmanned Underwater Vehicles (UUVs) where close to the leading edge of the vehicle the flow is laminar and further down the length the flow naturally or forcibly transitions to turbulent.

On the other hand, there is still room for additional investigation in the effect of the riblets within the transition region of the boundary layer flow, between laminar and turbulent regimes. While it is very important to understand the frictional response of the riblets in the transition, the question of whether the riblets can delay the transition or not is still open for further investigation.

In terms of the internal flows, the flow in presence of the riblets at the entrance length prior to becoming fully developed can be analysed in the same manner as the boundary layer flow discussed here. In the fully developed case before transitioning to turbulence, similar method as the one used in the Taylor-Couette flow can be em-

ployed to understand the effect of the riblets as well. While experimental methods involving the pipe flow or channel flow can be difficult, especially in terms of fabrication methods, the advances in 3D printing methods can offer a new avenue in overcoming the difficulties of such experiments.

Lastly, as a physical exploration, it is of interest to understand how the change in the geometry of the riblets can affect the Taylor-Couette flow in the regimes where the symmetry of the flow is broken as well as in regions where both cylinders are rotating. Taylor-Couette flow as a model flow for physical studies can offer additional insight into the mechanisms of how riblets affect the flow in different circumstances and use those insights to analyse other cases.

Appendix A

Matched Asymptotic Expansion for Cylindrical Couette Flow over V-groove Riblet Rotors

To solve the equations of motion for steady cylindrical Couette flow over V-groove riblet surfaces, we can start by decomposing the solution for the velocity and pressure distribution as a base solution and a first order perturbation for small riblets with

$$\frac{A}{R_\mathrm{i}} \ll 1 \tag{A.1}$$

and calling $\lambda/R_\mathrm{i} = \varepsilon$, Equation A.1 can be rewritten as

$$\mathrm{AR}\frac{\lambda}{R_\mathrm{i}} = \mathrm{AR}\varepsilon \ll 1. \tag{A.2}$$

Here the base flow is the cylindrical Couette flow over smooth rotors discussed in chapter 4 and the perturbation term is due to the presence of the riblets. Therefore, we can expand the pressure and velocity profiles in the forms

$$p = p^{(0)} + \mathrm{AR}\varepsilon\; p^{(1)} + O(\mathrm{AR}^2\; \varepsilon^2)... \tag{A.3}$$

$$\boldsymbol{v} = \begin{bmatrix} v_r \\ v_\phi \\ v_z \end{bmatrix} = \begin{bmatrix} 0 \\ v_\phi^{(0)} \\ 0 \end{bmatrix} + \mathrm{AR}\varepsilon \begin{bmatrix} v_r^{(1)} \\ v_\phi^{(1)} \\ v_z^{(1)} \end{bmatrix} + O(\mathrm{AR}^2\,\varepsilon^2)... \tag{A.4}$$

First the component of the steady axisymmetric Navier Stokes equation in the ϕ direction is written as

$$\rho \left(\frac{v_r}{r} \frac{\partial v_\phi}{\partial r} + v_z \frac{\partial v_\phi}{\partial z} \right) = \mu \left(\frac{\partial}{\partial r} \left(\frac{1}{r} \frac{\partial}{\partial r}(rv_\phi) \right) + \frac{\partial^2 v_\phi}{\partial z^2} \right). \tag{A.5}$$

With the no-slip boundary condition on the inner and outer cylinders, i.e. $v_r^{(1)}(r = R_{\mathrm{i}}) = v_r^{(1)}(r = R_{\mathrm{o}}) = 0$, it is assumed that $v_r^{(1)} = 0$ (note that this ansatz will be supported in Equations A.15 - A.20). Thus, substituting the above expansion for the velocity and gathering the first order terms with the assumption that $v_r^{(1)} = 0$ gives

$$\frac{\partial}{\partial r} \left(\frac{1}{r} \frac{\partial}{\partial r}(rv_\phi^{(1)}) \right) + \frac{\partial^2 v_\phi^{(1)}}{\partial z^2} = 0 \tag{A.6}$$

with the boundary condition of

$$\frac{v_{\phi,BC}^{(1)}}{R_{\mathrm{i}}\Omega_{\mathrm{i}}} = \frac{-2}{1 - \eta^2} \frac{z}{\lambda} + O(\varepsilon \mathrm{AR}).... \tag{A.7}$$

as explained in Chapter 4 using a Taylor series expansion for V-grooves in the range $0 \le z/\lambda \le 1/2$ (due to symmetry the problem is solved for half of a V-groove). Now one can solve Equation A.6 to get

$$\frac{v_\phi^{(1)}}{R_{\mathrm{i}}\Omega_{\mathrm{i}}} = \frac{-2\eta}{(1 - \eta^2)^2} \left(\frac{R_{\mathrm{o}}}{r} - \frac{r}{R_{\mathrm{o}}} \right) \frac{z}{\lambda}. \tag{A.8}$$

Now, using the axisymmetric Navier Stokes equation in the radial direction

$$\rho \left(v_r \frac{\partial v_r}{\partial r} + v_z \frac{\partial v_r}{\partial z} - \frac{v_\phi^2}{r} \right) = \frac{\partial p}{\partial r} + \mu \left(\frac{\partial}{\partial r} \left(\frac{1}{r} \frac{\partial}{\partial r}(rv_r) \right) + \frac{\partial^2 v_r}{\partial z^2} \right) \tag{A.9}$$

and again, substituting the expansion and gathering the first order terms

$$\rho \frac{2v_\phi^{(0)} v_\phi^{(1)}}{r} = \frac{\partial p^{(1)}}{\partial r} \tag{A.10}$$

and thus

$$\frac{\partial p^{(1)}}{\partial r} = \rho \frac{2\eta^2}{(1-\eta^2)^3} \frac{1}{r} \left(\frac{R_o}{r} - \frac{r}{R_o} \right)^2 \frac{z}{\lambda} (R_i \Omega_i)^2. \tag{A.11}$$

Integrating this equation, one gets an equation for the pressure distribution as

$$p^{(1)} = \frac{2\eta^2}{(1-\eta^2)^3} \frac{z}{\lambda} \left(-\frac{1}{2} \left(\frac{R_o}{r} \right)^2 - 2\ln \left(\frac{r}{R_o} \right) + \frac{1}{2} \left(\frac{r}{R_o} \right)^2 \right) \rho \left(R_i \Omega_i \right)^2. \tag{A.12}$$

Therefore, the pressure gradient in the z direction is written as

$$\frac{\partial p^{(1)}}{\partial z} = \frac{2\eta^2}{(1-\eta^2)^3} \frac{1}{\lambda} \left(-\frac{1}{2} \left(\frac{R_o}{r} \right)^2 - 2\ln \left(\frac{r}{R_o} \right) + \frac{1}{2} \left(\frac{r}{R_o} \right)^2 \right) \rho \left(R_i \Omega_i \right)^2 \tag{A.13}$$

which is only a function of the radial direction, r. To simplify, I denote the right hand side of above equation $f(r)$ and use the component of the steady axisymmetric Navier-Stokes equation in the axial direction

$$\rho \left(v_r \frac{\partial v_z}{\partial r} + v_z \frac{\partial v_z}{\partial z} \right) = -\frac{\partial p}{\partial z} + \mu \left(\frac{1}{r} \frac{\partial}{\partial r} \left(r \frac{\partial v_z}{\partial r} \right) + \frac{\partial^2 v_z}{\partial z^2} \right) \tag{A.14}$$

Substituting for the pressure and velocity expansion, and collecting the first order terms, simplifies the above equation to

$$\mu \left(\frac{1}{r} \frac{\partial}{\partial r} \left(r \frac{\partial v_z^{(1)}}{\partial r} \right) + \frac{\partial^2 v_z^{(1)}}{\partial z^2} \right) = \frac{\partial p^{(1)}}{\partial z} = f(r) \tag{A.15}$$

Therefore, the solution to v_z has a form of

$$v_z^{(1)} = g(r) + C_1 z + D \tag{A.16}$$

and with the boundary condition of

$$\frac{\partial v_z^{(1)}}{\partial z}\bigg|_{z=0} = -\frac{\partial v_z^{(1)}}{\partial z}\bigg|_{z=\lambda/2}, \tag{A.17}$$

one thus finds that $C_1 = 0$. Therefore, using the continuity equation (at this order)

$$\frac{1}{r}\frac{\partial}{\partial r}(rv_r^{(1)}) + \frac{\partial v_z^{(1)}}{\partial z} = 0 \tag{A.18}$$

and substituting the above form for the first order terms, one gets

$$\frac{1}{r}\frac{\partial}{\partial r}(rv_r^{(1)}) = 0 \tag{A.19}$$

which can be solved as

$$v_r^{(1)} = \frac{D_1}{r} \tag{A.20}$$

and with boundary condition of no-slip at the inner and outer walls, $D_1 = 0$ and thus $v_r^{(1)} = 0$, confirming the assumption that was made earlier to solve the equations. Any radial/ recirculating velocity that is induced by the riblets thus develops only at higher orders $O(\varepsilon^2 AR^2)$ and beyond.

A.1 Cases With larger Aspect Ratios

For finite aspect ratio cases, the first order velocity and pressure terms can be expanded using an inner and outer expansion where the outer expansion is valid for radial locations outside the grooves and the inner expansion is valid for $y = r - R_i \ll d$ (as shown in Figure A-1), close to the riblet textured wall.

A.1.1 Outer Expansion

Here, assume the outer expansion is valid for radial locations outside the riblet surface. Therefore, I assume that the first order velocity and pressure distributions will only be a function of the radial direction. Hence
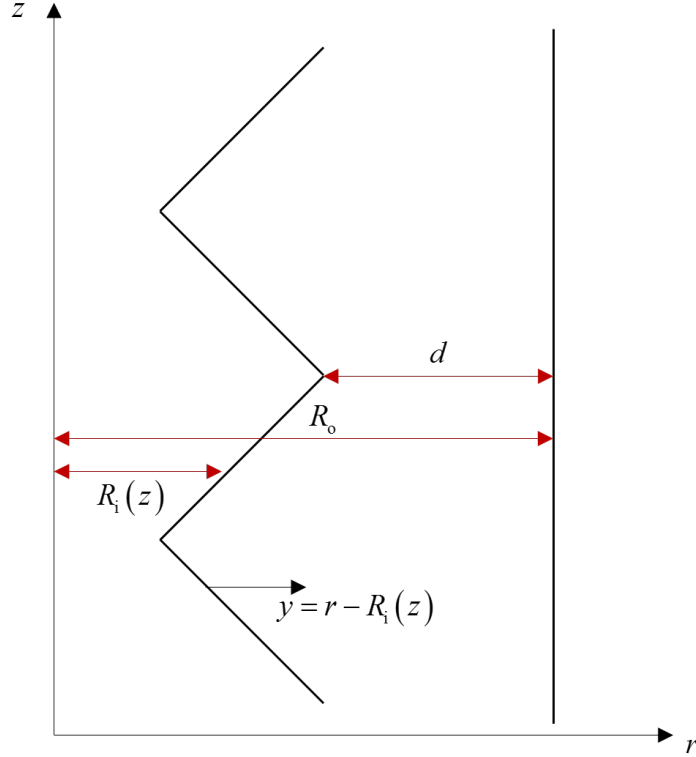
Figure A-1: Schematic of the V-groove riblets with arbitrary aspect ratio on the inner cylinder of a cylindrical Couette flow geometry. To solve the equations of motion for Couette flow in this geometry, the solution is expanded using an inner and an outer expansion, with the inner solution valid close to the inner cylinder, i.e. $y \ll d$, and the outer solution valid outside the grooves.

$$p = p^{(0)} + \varepsilon p_O^{(1)} + O(\varepsilon^2)... \tag{A.21}$$

neglecting terms of second order and higher with

$$\frac{\partial p_O^{(1)}}{\partial z} = 0. \tag{A.22}$$

Substituting the above equation into the axial component of the steady axisymmetric cylindrical Navier-Stokes equation

$$\rho \left(v_r \frac{\partial v_z}{\partial r} + v_z \frac{\partial v_z}{\partial z} \right) = \frac{\partial p}{\partial z} + \mu \left(\frac{1}{r} \frac{\partial}{\partial r} \left(r \frac{\partial v_z}{\partial r} \right) + \frac{\partial^2 v_z}{\partial z^2} \right) \tag{A.23}$$

and substituting for the pressure and velocity, and collecting the first order terms,

simplifies the above equation to

$$\mu \left(\frac{1}{r} \frac{\partial}{\partial r} \left(r \frac{\partial v_{z,O}^{(1)}}{\partial r} \right) + \frac{\partial^2 v_{z,O}^{(1)}}{\partial z^2} \right) = 0 \tag{A.24}$$

with boundary conditions of $v_{z,O} = 0$ on the inner and outer cylinder and

$$\left. \frac{\partial v_z^{(1)}}{\partial z} \right|_{z=0} = - \left. \frac{\partial v_z^{(1)}}{\partial z} \right|_{z=\lambda/2} \tag{A.25}$$

This equation with the above boundary conditions has a trivial solution of $v_{z,O}^{(1)} = 0$.
Now using the continuity equation

$$\frac{1}{r} \left(\frac{\partial}{\partial r} (r v_r) \right) + \frac{\partial v_z}{\partial z} = 0 \tag{A.26}$$

and substituting for the velocity profile and gathering the first order terms of the outer solution gives

$$\frac{1}{r} \left(\frac{\partial}{\partial r} \left(r v_{r,O}^{(1)} \right) \right) + \frac{\partial v_{z,O}^{(1)}}{\partial z} = 0 \tag{A.27}$$

with similar boundary conditions of of $v_{r,O}^{(1)} = 0$ on the inner and outer cylinder and

$$\left. \frac{\partial v_r^{(1)}}{\partial z} \right|_{z=0} = - \left. \frac{\partial v_r^{(1)}}{\partial z} \right|_{z=\lambda/2} \tag{A.28}$$

With $v_{z,O}^{(1)} = 0$ and the given boundary conditions, $v_{r,O}^{(1)} = 0$. Therefore, the velocity profile can be written as

$$\boldsymbol{v} = \begin{bmatrix} v_r \\ v_\phi \\ v_z \end{bmatrix} = \begin{bmatrix} 0 \\ v_\phi^{(0)} \\ 0 \end{bmatrix} + \mathrm{AR}\varepsilon \begin{bmatrix} 0 \\ v_{\phi,O}^{(1)}(r) \\ 0 \end{bmatrix} \tag{A.29}$$

with the pressure as in Equation A.21. Hence this form of steady velocity profile was used in the integral solutions proposed in Chapter 4. Therefore, the equations of motion at the leading order are written as

$$\rho \frac{\left(v_\phi^{(0)}\right)^2}{r} = \frac{\partial p^{(0)}}{\partial r} \tag{A.30}$$

$$\frac{\partial}{\partial r} \frac{1}{r} \left(\frac{\partial}{\partial r} (r v_\phi^{(0)}) \right) = 0 \tag{A.31}$$

with boundary condition of $v_\phi^{(0)}(r = R_i) = R_i \Omega_i$ and $v_\phi^{(0)}(r = R_o) = 0$ on the inner and outer cylinder and for pressure $p^{(0)}(r = R_0) = 0$. These equations can be solved as to give:

$$v_\phi^{(0)} = \frac{1}{1 - \eta^2} \left(\frac{R_o}{r} - \frac{r}{R_o} \right) R_i \Omega_i, \tag{A.32}$$

and

$$p^{(0)} = \left(\frac{\eta}{1 - \eta^2} \right)^2 \left(-\frac{1}{2} \left(\frac{R_o}{r} \right)^2 - 2 \ln \left(\frac{r}{R_o} \right) + \frac{1}{2} \left(\frac{r}{R_o} \right)^2 \right) \rho \left(R_i \Omega_i \right)^2 . \tag{A.33}$$

For the first order correction induced by the presence of the riblets, one has

$$\rho \frac{2 v_\phi^{(0)} v_{\phi,O}^{(1)}}{r} = \frac{\partial p_O^{(1)}}{\partial r} \tag{A.34}$$

$$\frac{\partial}{\partial r} \frac{1}{r} \left(\frac{\partial}{\partial r} (r v_{\phi,O}^{(1)}) \right) = 0 \tag{A.35}$$

The boundary condition on the riblet surface is again the same as in Equation A.7. However, since the aspect ratio is no longer very small and I am using the outer expansion valid far from the riblets ($y/d \sim O(1)$), instead of assuming that the above boundary condition holds on $r = R_i$, I assume that for each aspect ratio riblet the effective boundary condition on the inner cylinder can be defined as an average of the boundary condition over one period in the z direction. If I consider a purely geometric averaging, one has

$$\frac{\int_0^{\lambda/2} z\,dz}{\frac{\lambda}{2}} = \frac{\frac{\lambda^2}{8}}{\frac{\lambda}{2}} = \frac{\lambda}{4}. \tag{A.36}$$

However due to the complexity of the problem and the fact that such an average needs to be dependent on the aspect ratio, I assume that instead of the above boundary condition, one can satisfy the boundary condition exactly at one intermediate location $z = K\lambda/4$ where K is only dependent on the aspect ratio and apply this boundary condition

$$\frac{v_{\phi,\text{BC}}^{(1)}}{R_{\text{i}}\Omega_{\text{i}}} = \frac{-2}{1 - \eta^2}\,\text{AR}\,\frac{K}{4} \tag{A.37}$$

at $r = R_{\text{i}}$. Note that for $\text{AR} \to 1$, $K = 1$. Now solving the equation for the azimuthal velocity one gets

$$v_{\phi,\text{O}}^{(1)}(r) = \frac{-2\eta}{(1 - \eta^2)^2}\left(\frac{R_{\text{o}}}{r} - \frac{r}{R_{\text{o}}}\right)\frac{1}{4}\,(R_{\text{i}}\Omega_{\text{i}}) \tag{A.38}$$

and for the pressure

$$p_{\text{O}}^{(1)}(r) = -\left(\frac{\eta^2}{(1 - \eta^2)}\right)^2\left(-\frac{1}{2}\left(\frac{R_{\text{o}}}{r}\right)^2 - 2\ln\left(\frac{r}{R_{\text{o}}}\right) + \frac{1}{2}\left(\frac{r}{R_{\text{o}}}\right)^2\right)\rho\,(R_{\text{i}}\Omega_{\text{i}})^2. \tag{A.39}$$

A.1.2 Inner Expansion

In case of the inner expansion, I assume the solution is applicable to radial locations close to the riblet wall ($y \ll d$) and therefore velocity and pressure are a function of both radial and axial directions and hence:

$$p = p^{(0)} + \varepsilon p_{\text{I}}^{(1)} + O(\varepsilon^2)... \tag{A.40}$$

$$\boldsymbol{v} = \begin{bmatrix} v_r \\ v_\phi^{(0)} \\ v_z \end{bmatrix} = \begin{bmatrix} 0 \\ v_\phi \\ 0 \end{bmatrix} + \varepsilon \begin{bmatrix} v_{r,\mathrm{I}}^{(1)}(r,z) \\ v_{\phi,\mathrm{I}}^{(1)}(r,z) \\ v_{z,\mathrm{I}}^{(1)}(r,z) \end{bmatrix} + O(\varepsilon^2)... \tag{A.41}$$

Thus the continuity equation for the first order term in the inner expansion can be written as

$$\frac{1}{r}\frac{\partial}{\partial r}(r v_{r,\mathrm{I}}^{(1)}) + \frac{\partial}{\partial z} v_{z,\mathrm{I}}^{(1)} = 0. \tag{A.42}$$

To satisfy the continuity equation, one can define a stream-function $(\psi^{(1)})$ for the first order radial and axial velocities as

$$v_{r,\mathrm{I}}^{(1)} = \frac{\partial \psi^{(1)}}{\partial z} \tag{A.43}$$

$$v_{z,\mathrm{I}}^{(1)} = -\frac{1}{r}\frac{\partial}{\partial r}(r\psi^{(1)}) \tag{A.44}$$

On the other hand, the Navier-Stokes equations for the radial and axial direction are written as

$$-\rho\frac{2 v_\phi^{(0)} v_{\phi,\mathrm{I}}^{(1)}}{r} = -\frac{\partial p_\mathrm{I}^{(1)}}{\partial r} + \mu\left(\frac{\partial}{\partial r}\left(\frac{1}{r}\frac{\partial}{\partial r}\left(r v_{r,\mathrm{I}}^{(1)}\right)\right) + \frac{\partial^2 v_{r,\mathrm{I}}^{(1)}}{\partial z^2}\right) \tag{A.45}$$

$$0 = -\frac{\partial p_\mathrm{I}^{(1)}}{\partial z} + \mu\left(\frac{1}{r}\frac{\partial}{\partial r}\left(r\frac{\partial}{\partial r}\left(v_{z,\mathrm{I}}^{(1)}\right)\right) + \frac{\partial^2 v_{z,\mathrm{I}}^{(1)}}{\partial z^2}\right) \tag{A.46}$$

Now differentiating Equation A.45 with respect to z and Equation A.46 with respect to r and eliminating the pressure term, and substituting for the definition of the stream function from above, I get:

$$-\rho\frac{\partial v_{\phi,\mathrm{I}}^{(1)}}{\partial z} = \mu\left(\frac{r}{2 v_\phi^{(0)}}\nabla^2\nabla^2\psi^{(1)}\right) \tag{A.47}$$

where

$$\nabla^2 = \frac{\partial}{\partial r}\left(\frac{1}{r}\frac{\partial}{\partial r}r\right) + \frac{\partial^2}{\partial z^2}. \tag{A.48}$$

Now for the Navier-Stokes equation in the ϕ direction we have

$$\rho v_{r,\mathrm{I}}^{(1)}\frac{1}{r}\frac{\partial}{\partial r}\left(rv_\phi^{(0)}\right) = \mu\left(\frac{\partial}{\partial r}\left(\frac{1}{r}\frac{\partial}{\partial r}\left(rv_{\phi,\mathrm{I}}^{(1)}\right)\right) + \frac{\partial^2 v_{\phi,\mathrm{I}}^{(1)}}{\partial z^2}\right) \tag{A.49}$$

Now, differentiating Equation A.49 with respect to z and taking the ∇^2 of Equation A.47 and eliminating the azimuthal velocity gives

$$-\frac{1}{r}\frac{\partial}{\partial r}\left(rv_\phi^{(0)}\right)\frac{\partial v_{r,\mathrm{I}}^{(1)}}{\partial z} = \nu^2\nabla^2\left(\frac{r}{2v_\phi^{(0)}}\nabla^2\nabla^2\psi^{(1)}\right) \tag{A.50}$$

or equivalently using Equation A.43

$$-\frac{1}{r}\frac{\partial}{\partial r}\left(rv_\phi^{(0)}\right)\frac{\partial^2\psi^{(1)}}{\partial z^2} = \nu^2\nabla^2\left(\frac{r}{2v_\phi^{(0)}}\nabla^2\nabla^2\psi^{(1)}\right) \tag{A.51}$$

with no slip boundary conditions at the inner and outer cylinder for both radial and axial velocities

$$v_{r,\mathrm{I}}^{(1)}(r = R_\mathrm{i}, z) = \left.\frac{\partial\psi^{(1)}}{\partial z}\right|_{(r=R_\mathrm{i},z)} = 0, \tag{A.52}$$

$$v_{r,\mathrm{I}}^{(1)}(r = R_\mathrm{o}, z) = \left.\frac{\partial\psi^{(1)}}{\partial z}\right|_{(r=R_\mathrm{o},z)} = 0, \tag{A.53}$$

$$v_{z,\mathrm{I}}^{(1)}(r = R_\mathrm{i}, z) = \left.-\frac{1}{r}\frac{\partial}{\partial r}(r\psi^{(1)})\right|_{(r=R_\mathrm{i},z)} = 0, \tag{A.54}$$

and

$$v_{z,\mathrm{I}}^{(1)}(r = R_\mathrm{o}, z) = \left.-\frac{1}{r}\frac{\partial}{\partial r}(r\psi^{(1)})\right|_{(r=R_\mathrm{o},z)} = 0 \tag{A.55}$$

and from Equations A.25 and A.28

$$\frac{\partial}{\partial z}\left(\frac{1}{r}\frac{\partial(r\psi^{(1)})}{\partial r}\right)\bigg|_{(r,z=0)} = -\frac{\partial}{\partial z}\left(\frac{1}{r}\frac{\partial(r\psi^{(1)})}{\partial r}\right)\bigg|_{(r,z=\lambda/2)}, \qquad (A.56)$$

and

$$\frac{\partial}{\partial z}\left(\frac{\partial\psi^{(1)}}{\partial z}\right)\bigg|_{(r,z=0)} = -\frac{\partial}{\partial z}\left(\frac{\partial\psi^{(1)}}{\partial z}\right)\bigg|_{(r,z=\lambda/2)}. \qquad (A.57)$$

Thus to solve the equation for the inner expansion, one needs to solve the above linear partial differential equation for the stream-function $\psi^{(1)}$ and then find the rest of the velocities by substituting the stream-function into the previous equations.

THIS PAGE INTENTIONALLY LEFT BLANK

Bibliography

[1] Micehal J Walsh. Riblets. *Viscous drag reduction in boundary layers*, 1:203–261, 1990.

[2] Preston Lowrey and Jeff Harasha. A preliminary assessment of the feasibility of using riblets in internal flows to conserve energy. *Energy*, 16(3):631–642, 1991.

[3] Riblets for Stars & Stripes. `http://ntrs.nasa.gov/archive/nasa/casi.ntrs.nasa.gov/20020087761.pdf`. [Accessed 5-March-2016].

[4] NASA riblets for Stars & Stripes. `http://www.nasa.gov/centers/langley/news/factsheets/Riblets.html`, October 1993. [Accessed 5-March-2016].

[5] BMW Oracle racing: 3M. `https://www.youtube.com/watch?v=8w4BwhTvEr8`, March 2010. [Accessed 5-March-2016].

[6] Ricardo García-Mayoral and Javier Jiménez. Drag reduction by riblets. *Philosophical Transactions of the Royal Society A: Mathematical, Physical and Engineering Sciences*, 369(1940):1412–1427, 2011.

[7] Agrim Sareen, Robert Deters, Steven Henry, and Michael Selig. Drag reduction using riblet film applied to airfoils for wind turbines. *Journal of Solar Energy Engineering*, 136(2):021007, 2013.

[8] Kwing-So Choi. Drag-reduction test of riblets using ares high-speed buoyancy propelled vehicle-moby-d. *Aeronautical Journal*, 94(933):79–85, 1990.

[9] Kwing-So Choi. Cost-effective production of microgrooves for drag reduction on the surface of aircraft in situ. *SPIE-The International Society for Optical Engineering, Proceedings Volume*, 1573:136–144, 1992.

[10] Kwing-So Choi. Smart flow control with riblets. In *Advanced Materials Research*, volume 745, pages 27–40. Trans Tech Publ, 2013.

[11] S Sundaram, PR Viswanath, and S Rudrakumar. Viscous drag reduction using riblets on naca 0012 airfoil to moderate incidence. *AIAA Journal*, 34(4):676–682, 1996.

[12] JM Caram and A Ahmed. Effects of riblets on the wake characteristics of an airfoil. *AIAA Journal*, 1989.

[13] JM Caram and A Ahmed. Effect of riblets on turbulence in the wake of an airfoil. *AIAA Journal*, 29(11):1769–1770, 1991.

[14] JM Caram and A Ahmed. Development of the wake of an airfoil with riblets. *AIAA Journal*, 30(12):2817–2818, 1992.

[15] PR Viswanath. Aircraft viscous drag reduction using riblets. *Progress in Aerospace Sciences*, 38(6-7):571–600, 2002.

[16] Michael J Walsh, William L Sellers III, and Catherine B Mcginley. Riblet drag reduction at flight conditions. *AIAA Journal*, 1988.

[17] Michael J Walsh, William L Sellers, III, and Catherine B Mcginley. Riblet drag at flight conditions. *Journal of Aircraft*, 26(6), 1989.

[18] DW Bechert, G Hoppe, and W-E Reif. On the drag reduction of the shark skin. In *1985 AIAA Shear Flow Control Conference*, 1985.

[19] A Dinkelacker, P Nitschke-Kowsky, and W-E Reif. On the possibility of drag reduction with the help of longitudinal ridges in the walls. In *Turbulence Management and Relaminarisation*, pages 109–120. Springer, 1988.

[20] DW Bechert, M Bruse, and W Hage. Experiments with three-dimensional riblets as an idealized model of shark skin. *Experiments in Fluids*, 28(5):403–412, 2000.

[21] Li Wen, James Weaver, and George Lauder. Biomimetic shark skin: design, fabrication and hydrodynamic function. *The Journal of Experimental Biology*, 217(10):1656–1666, 2014.

[22] Kenneth Chung, James Schumacher, Edith Sampson, Robert Burne, Patrick Antonelli, and Anthony Brennan. Impact of engineered surface microtopography on biofilm formation of staphylococcus aureus. *Biointerphases*, 2(2):89 – 94, 2007.

[23] Shabnam Raayai-Ardakani, Jose Yague, Karen Gleason, and Mary Boyce. Mechanics of graded wrinkling. *Journal of Applied Mechanics*, 83(12), 2016.

[24] Yuehao Luo, Lu Yuan, Jianhua Li, and Jianshe Wang. Boundary layer drag reduction research hypotheses derived from bio-inspired surface and recent advanced applications. *Micron (Oxford, England)*, 79:59–73, Dec 2015.

[25] DC Chu and GE Karniadakis. A direct numerical simulation of laminar and turbulent flow over riblet-mounted surfaces. *Journal of Fluid Mechanics*, 1993.

[26] Haecheon Choi, Parviz Moin, and John Kim. Direct numerical simulation of turbulent flow over riblets. *Journal of Fluid Mechanics*, 255:503–539, 1993.

[27] D Goldstein, R Handler, and L Sirovich. Direct numerical simulation of turbulent flow over a modeled riblet covered surface. *Journal of Fluid Mechanics*, 302:333–376, 1995.

[28] S-J Lee and S-H Lee. Flow field analysis of a turbulent boundary layer over a riblet surface. *Experiments in Fluids*, 30(2), 2001.

[29] John Kim, Parviz Moin, and Robert Moser. Turbulence statistics in fully developed channel flow at low reynolds number. *Journal of Fluid Mechanics*, 177:133–166, 1987.

[30] H Kim, S Kline, and W Reynolds. The production of turbulence near a smooth wall in a turbulent boundary layer. *Journal of Fluid Mechanics*, 50(01):133, 1971.

[31] Roger L Simpson. *An investigation of the spatial structure of the viscous sublayer*. Max-Planck-Institut für Strömungsforschung, 1976.

[32] Yoshimasa Furuya, Ikuo Nakamura, Masafumi Miyata, and Yasuhiro Yama. Turbulent boundary-layer along a streamwise bar of a rectangular cross section placed on a flat plate. *Bulletin of JSME*, 20(141):315–322, 1977.

[33] John F Kennedy, Sheng-Tien Hsu, and Jung-Tai Lin. Turbulent flows past boundaries with small streamwise fins. *Journal of the Hydraulics Division*, 99(Pap n 9664), 1973.

[34] Sedat F Tardu. Coherent structures and riblets. *Applied Scientific Research*, 54:349–385, 1995.

[35] Baron, Quadrio, and Vigevano. On the boundary layer/riblets interaction mechanisms and the prediction of turbulent drag reduction. *International Journal of Heat and Fluid Flow*, 14(4), 1993.

[36] Micheal J Walsh and L Weinstein. Drag and heat-transfer characteristics of small longitudinally ribbed surfaces. *AIAA Journal*, 17(7):770–771, 1979.

[37] Micheal J Walsh. Drag characteristics of v-groove and transverse curvature riblits. *AIAA Prog. Astronaut. Aeronaut.*, 1980.

[38] Michael J Walsh. Riblets as a viscous drag reduction technique. *AIAA Journal*, 21(4):485–486, 1983.

[39] Micheal J Walsh and AM Lindemann. *Optimization and application of riblets for turbulent drag reduction*. American Institute of Aeronautics and Astronautics, 1984.

[40] DW Bechert, M Bruse, W Hage, JG Th Van der Hoeven, and G Hoppe. Experiments on drag-reducing surfaces and their optimization with an adjustable geometry. *Journal of Fluid Mechanics*, 338:59–87, 1997.

[41] H Schlichting, E Krause, HJ Oertel, and K Gersten. *Boundary-Layer Theory.* Springer Berlin Heidelberg, 2014.

[42] FM White. *Fluid Mechanics.* McGraw-Hill series in mechanical engineering. McGraw Hill, 2011.

[43] PK Kundu and IM Cohen. *Fluid Mechanics.* Elsevier Science, 2010.

[44] AF Mills. *Heat Transfer.* Prentice Hall International Series in. Prentice Hall, 1999.

[45] Marc Perlin, David R Dowling, and Steven L Ceccio. Freeman scholar review: Passive and active skin-friction drag reduction in turbulent boundary layers. *Journal of Fluids Engineering*, 138(9):091104, 2016.

[46] SB Pope. *Turbulent Flows.* Cambridge University Press, 2000.

[47] D Hooshmand, R Youngs, JM Wallace, and JL Balint. An experimental study of changes in the structure of a turbulent boundary layer due to surface geometry changes. *AIAA Paper*, 83:0230, 1983.

[48] P Vukoslavcevic, JM Wallace, and J-L Balint. Viscous drag reduction using streamwise-aligned riblets. *AIAA Journal*, 30(4):1119–1122, 1992.

[49] Seong-Ryong Park and James M Wallace. Flow alteration and drag reduction by riblets in a turbulent boundary layer. *AIAA Journal*, 32(1):31–38, 1994.

[50] Kwing-So Choi. Near-wall structure of a turbulent boundary layer with riblets. *Journal of Fluid Mechanics*, 1989.

[51] B Lazos and SP Wilkinson. Turbulent viscous drag reduction with thin-element riblets. *AIAA Journal*, 26(4), 1987.

[52] ZY Wang and J Jovanovic. Drag characteristics of extra-thin-fin-riblets in an air flow conduit. *Journal of Fluids engineering*, 115(2):222–226, 1993.

[53] E Coustols and J Cousteix. Experimental investigation of turbulent boundary layers manipulated with internal devices: riblets. In *Structure of Turbulence and Drag Reduction*, pages 577–584. Springer, 1990.

[54] J Gallagher and A Thomas. Turbulent boundary layer characteristics over streamwise grooves. *2nd Applied Aerodynamics Conference*, 1984.

[55] EV Bacher and CR Smith. Turbulent boundary-layer modification by surface riblets. *AIAA Journal*, 24(8):1382–1385, 1985.

[56] Laurel Reidy and Greg Anderson. Drag reduction for external and internal boundary layers using riblets and polymers. *26th Aerospace Sciences Meeting*, 1988.

[57] Jianfeng Hou, Babak Vajdi Hokmabad, and Sina Ghaemi. Three-dimensional measurement of turbulent flow over a riblet surface. *Experimental Thermal and Fluid Science*, 85:229–239, 2017.

[58] DW Bechert, G Hoppe, J Hoeven, and R Makris. The berlin oil channel for drag reduction research. *Experiments in Fluids*, 12-12(4-5):251–260, 1991.

[59] Kwing-So Choi, GE Gadd, HH Pearcey, AM Savill, and S Svensson. Tests of drag-reducing polymer coated on a riblet surface. *Applied Scientific Research*, 46(3):209–216, 1989.

[60] Rohr, Andersen, Reidy, and Hendricks. A comparison of the drag-reducing benefits of riblets in internal and external flows. *Experiments in Fluids*, 13(6), 1991.

[61] Francis H Clauser. Turbulent boundary layers in adverse pressure gradients. *Journal of the Aeronautical Sciences*, 1954.

[62] AE Perry and PN Joubert. Rough-wall boundary layers in adverse pressure gradients. *Journal of Fluid Mechanics*, 1963.

[63] Itiro Tani. Drag reduction by riblet viewed as roughness problem. *Proceedings of the Japan Academy. Ser. B: Physical and Biological Sciences*, 64(2):21–24, 1988.

[64] JM Wallace and J-L Balint. Viscous drag reduction using streamwise aligned riblets: Survey and new results. In *Turbulence Management and Relaminarisation*, pages 133–147. Springer, 1988.

[65] Mark Drela. *Flight Vehicle Aerodynamics*. MIT Press, 2014.

[66] K N Liu, C Christodoulou, O Riccius, and D D Joseph. Drag reduction in pipes lined with riblets. *AIAA*, 28(10), Oct 1990.

[67] DB Goldstein and TC Tuan. Secondary flow induced by riblets. *Journal of Fluid Mechanics*, 1998.

[68] OA El-Samni, HH Chun, and HS Yoon. Drag reduction of turbulent flow over thin rectangular riblets. *International Journal of Engineering âĂ¸*, 2007.

[69] Amaury Bannier, Eric Garnier, and Pierre Sagaut. *Riblets Induced Drag Reduction on a Spatially Developing Turbulent Boundary Layer*. Springer, 2016.

[70] M Khan. A numerical investigation of the drag reduction by riblet-surfaces. *4th Joint Fluid Mechanics, Plasma Dynamics and Lasers Conference*, 1986.

[71] DW Bechert and M Bartenwerfer. The viscous flow on surfaces with longitudinal ribs. *Journal of Fluid Mechanics*, 1989.

[72] BE Launder and S Li. A numerical study of riblet effects on laminar flow through a plane channel. *Applied Scientific Research*, 1989.

[73] L Djenidi, J Liandrat, F Anselmet, and L Fulachier. Numerical and experimental investigation of the laminar boundary layer over riblets. *Applied Scientific Research*, 46(3):263–270, 1989.

[74] Seong-Ryong Park and JM Wallace. Flow alteration and drag reduction by riblets in a turbulent boundary layer. *AIAA Journal*, 32(1):31–38, 1994.

[75] Yuji Suzuki and Nobuhide Kasagi. Turbulent drag reduction mechanism above a riblet surface. *AIAA Journal*, 32(9):17811790, 1994.

[76] AM Savill. Drag reduction by passive devices - a review of some recent developments. In *Structure of turbulence and drag reduction*, pages 429–465. Springer, 1990.

[77] SJ Kline, RC Strawn, and JG Bardina. Correlation of the detachment of two-dimensional turbulent boundary layers. *AIAA Journal*, 21(1):68–73, 1983.

[78] Luciano Castillo, Xia Wang, and William K George. Separation criterion for turbulent boundary layers via similarity analysis. *Journal of Fluids Engineering*, 126(3):297, 2004.

[79] S Nakao. Application of v shape riblets to pipe flows. *Journal of Fluids Engineering*, 1991.

[80] Javier Jimenez. On the structure and control of near wall turbulence. *Physics of Fluids*, 6(2):944–953, 1994.

[81] Gregory Bixler and Bharat Bhushan. Fluid drag reduction with shark-skin riblet inspired microstructured surfaces. *Advanced Functional Materials*, 23(36):4507–4528, 2013.

[82] DW Bechert and W Reif. On the drag reduction of the shark skin. *23rd Aerosp Sci Meet*, 1985.

[83] L Djenidi, LC Squire, and AM Savill. High resolution conformal mesh computations for v, u or l groove riblets in laminar and turbulent boundary layers. In *Recent Developments in Turbulence Management*, pages 65–92. Springer, 1991.

[84] P Viswanath and R Mukund. Turbulent drag reduction using riblets on a supercritical airfoil at transonic speeds. *AIAA Journal*, 33(5):945–947, 1995.

[85] Lian Duan and Meelan M Choudhari. Effects of riblets on skin friction and heat transfer in high-speed turbulent boundary layers. *AIAA Paper*, 1108, 2012.

[86] LC Squire and AM Savill. Drag measurements on planar riblet surfaces at high subsonic speeds. *Applied Scientific Research*, 46(3):229–243, 1989.

[87] John D Anderson. Ludwig prandtl's boundary layer. *Physics Today*, 58(12):42–48, 2005.

[88] WH Hager. Blasius: A life in research and education. *Experiments in Fluids*, 34(5):566–571, 2003.

[89] R Schinzinger and PAA Laura. *Conformal Mapping: Methods and Applications*. Dover books on mathematics. Dover Publications, 2003.

[90] Li Wen, James Weaver, and George Lauder. Biomimetic shark skin: design, fabrication and hydrodynamic function. *Journal of Experimental Biology*, 217(10):1656–1666, 2014.

[91] Yuehao Luo, Yufei Liu, and De Zhang. Hydrodynamic testing of a biological sharkskin replica manufactured using the vacuum casting method. *Surface Review and Letters*, 22(02):1550030, 2015.

[92] Chen and John Hutchinson. Herringbone buckling patterns of compressed thin films on compliant substrates. *Journal of Applied Mechanics*, 71(5):597, 2004.

[93] Jie Yin, Jose Yague, Damien Eggenspieler, Karen Gleason, and Mary Boyce. Deterministic order in surface micro topologies through sequential wrinkling. *Advanced Materials*, 24(40):5441–5446, 2012.

[94] EP Chan, EJ Smith, RC Hayward, and AJ Crosby. Surface wrinkles for smart adhesion. *Advanced Materials*, 20(4):711–716, 2008.

[95] Denis Terwagne, Miha Brojan, and Pedro Reis. Smart morphable surfaces for aerodynamic drag control. *Advanced Materials*, 26(38):6608–6611, 2014.

[96] D Neumann and A Dinkelacker. Drag measurements on v-grooved surfaces on a body of revolution in axial flow. *Applied Scientific Research*, 1991.

[97] HK Versteeg and W Malalasekera. *An Introduction to Computational Fluid Dynamics*. Pearson, 1995.

[98] Suhas V Patankar and D Brian Spalding. A calculation procedure for heat, mass and momentum transfer in three-dimensional parabolic flows. *International Journal of Heat and Mass Transfer*, 15(10):1787–1806, 1972.

[99] Joel H Ferziger and Milovan Perić. *Computational Methods for Fluid Dynamics*, volume 3. Springer Berlin, 2002.

[100] The OpenFOAM Foundation. Openfoam | open source computational fluid dynamics. `https://cfd.direct/openfoam/`. [Accessed 1-August-2017].

[101] Julian CR Hunt, Alan A Wray, and Parviz Moin. Eddies, streams, and convergence zones in turbulent flows. *Center for Turbulence Research - Proceedings of the Summer Program*, 1988.

[102] R Narasimha and SN Prasad. Leading edge shape for flat plate boundary layer studies. *Experiments in Fluids*, 17(5):358–360, 1994.

[103] AI Van De Vooren and D Dijkstra. The navier-stokes solution for laminar flow past a semi-infinite flat plate. *Journal of Engineering Mathematics*, 4(1):9–27, 1970.

[104] James A Blackwell. *Preliminary Study of Effects of Reynolds Number and Boundary-Layer Transition Location on Shock-Induced Separation*. National Aeronautics and Space Administration, 1969.

[105] Russell J Donnelly. Taylor-Couette flow: the early days. *Phys. Today*, 44(11):32–39, 1991.

[106] T Hall and D Joseph. Rotating cylinder drag balance with application to riblets. *Experiments in Fluids*, 29(3):215–227, Sep 2000.

[107] AJ Greidanus, R Delfos, S Tokgoz, and J Westerweel. Turbulent Taylor–Couette flow over riblets: drag reduction and the effect of bulk fluid rotation. *Experiments in Fluids*, 56(5):107, 2015.

[108] Xiaojue Zhu, Rodolfo Ostilla-Mónico, Roberto Verzicco, and Detlef Lohse. Direct numerical simulation of Taylor–Couette flow with grooved walls: torque scaling and flow structure. *Journal of Fluid Mechanics*, 794:746–774, 2016.

[109] Brian J Rosenberg, Tyler Van Buren, Matthew K Fu, and Alexander J Smits. Turbulent drag reduction over air-and liquid-impregnated surfaces. *Physics of Fluids*, 28(1):015103, 2016.

[110] Pascal Chossat and Gérard Iooss. *The Couette-Taylor Problem*, volume 102. Springer Science & Business Media, 2012.

[111] A Mallock. Experiments on fluid viscosity. *Philosophical Transactions of the Royal Society of London. Series A, Containing Papers of a Mathematical or Physical Character*, 187:41–56, 1896.

[112] A Mallock. Determination of the viscosity of water. *Proceedings of the Royal Society of London*, 45(273-279):126–132, 1888.

[113] JM Piau, M Bremond, JM Couette, and M Piau. Maurice Couette, one of the founders of rheology. *Rheologica acta*, 33(5):357–368, 1994.

[114] Geoffrey I Taylor. Stability of a viscous liquid contained between two rotating cylinders. *Philosophical Transactions of the Royal Society of London. Series A, Containing Papers of a Mathematical or Physical Character*, 223:289–343, 1923.

[115] S Goldstein. The stability of viscous fluid flow between rotating cylinders. In *Mathematical Proceedings of the Cambridge Philosophical Society*, volume 33, pages 41–61. Cambridge University Press, 1937.

[116] S Chandrasekhar. The stability of viscous flow between rotating cylinders. In *Proceedings of the Royal Society of London A: Mathematical, Physical and Engineering Sciences*, volume 246, pages 301–311. The Royal Society, 1958.

[117] S Chandrasekhar. The stability of viscous flow between rotating cylinders. *Mathematika*, 1(1):5–13, 1954.

[118] S Chandrasekhar. The stability of spiral flow between rotating cylinders. *Proceedings of the Royal Society of London. Series A, Mathematical and Physical Sciences*, pages 188–197, 1962.

[119] A Davey. The growth of Taylor vortices in flow between rotating cylinders. *Journal of Fluid Mechanics*, 14(3):336–368, 1962.

[120] A Davey, RC Di Prima, and JT Stuart. On the instability of Taylor vortices. *Journal of Fluid Mechanics*, 31(01):17–52, 1968.

[121] RJ Donnelly and KW Schwarz. Experiments on the stability of viscous flow between rotating cylinders. vi. finite-amplitude experiments. In *Proceedings of the Royal Society of London A: Mathematical, Physical and Engineering Sciences*, volume 283, pages 531–556. The Royal Society, 1965.

[122] PH Roberts. Appendix to experiments on the stability of viscous flow between rotating cylinders. vi. finite-amplitude experiments. In *Proc. R. Soc. London A*, volume 238, pages 531–556, 1965.

[123] Everett Clifford Nickerson. Upper bounds on the torque in cylindrical Couette flow. *Journal of Fluid Mechanics*, 38(4):807–815, 1969.

[124] E Bilgen and R Boulos. Functional dependence of torque coefficient of coaxial cylinders on gap width and reynolds numbers. *Journal of Fluids Engineering*, 95(1):122–126, 1973.

[125] PM Eagles. On the torque of wavy vortices. *Journal of Fluid Mechanics*, 62(1):1–9, 1974.

[126] Daniel P Lathrop, Jay Fineberg, and Harry L Swinney. Transition to shear-driven turbulence in Couette-Taylor flow. *Physical Review A*, 46(10):6390, 1992.

[127] Daniel P Lathrop, Jay Fineberg, and Harry L Swinney. Turbulent flow between concentric rotating cylinders at large reynolds number. *Physical review letters*, 68(10):1515, 1992.

[128] Daniel P Lathrop, Jay Fineberg, and Harry L Swinney. Transition to shear-driven turbulence in Couette-Taylor flow. *Physical Review A*, 46(10):6390, 1992.

[129] Li-Hua Zhang and Harry L Swinney. Nonpropagating oscillatory modes in Couette-Taylor flow. *Physical Review A*, 31(2):1006, 1985.

[130] WY Tam and Harry L Swinney. Mass transport in turbulent Couette-Taylor flow. *Physical Review A*, 36(3):1374, 1987.

[131] Gregory S Lewis and Harry L Swinney. Velocity structure functions, scaling, and transitions in high-reynolds-number Couette-Taylor flow. *Physical Review E*, 59(5):5457, 1999.

[132] C David Andereck, SS Liu, and Harry L Swinney. Flow regimes in a circular Couette system with independently rotating cylinders. *Journal of Fluid Mechanics*, 164:155–183, 1986.

[133] Bruno Eckhardt, Siegfried Grossmann, and Detlef Lohse. Scaling of global momentum transport in Taylor-Couette and pipe flow. *The European Physical Journal B-Condensed Matter and Complex Systems*, 18(3):541–544, 2000.

[134] Bruno Eckhardt, Siegfried Grossmann, and Detlef Lohse. Torque scaling in turbulent Taylor–Couette flow between independently rotating cylinders. *Journal of Fluid Mechanics*, 581:221–250, 2007.

[135] Siegfried Grossmann, Detlef Lohse, and Chao Sun. High–Reynolds number Taylor-Couette turbulence. *Annual Review of Fluid Mechanics*, 48:53–80, 2016.

[136] Rodolfo Ostilla, Richard JAM Stevens, Siegfried Grossmann, Roberto Verzicco, and Detlef Lohse. Optimal Taylor–Couette flow: direct numerical simulations. *Journal of Fluid Mechanics*, 719:14–46, 2013.

[137] Nabila Ait-Moussa, Sébastien Poncet, and Abdelrahmane Ghezal. Numerical simulations of co-and counter-Taylor-Couette flows: Influence of the cavity radius ratio on the appearance of Taylor vortices. *American Journal of Fluid Dynamics*, 5(1):17–22, 2015.

[138] Christopher W Macosko. *Rheology: principles, measurements, and applications*. Wiley-vch, 1994.

[139] P Chossat and G Iooss. Primary and secondary bifurcations in the Couette-Taylor problem. *Japan Journal of Applied Mathematics*, 2(1):37–68, 1985.

[140] Steven T Wereley and Richard M Lueptow. Spatio-temporal character of non-wavy and wavy Taylor–Couette flow. *Journal of Fluid Mechanics*, 364:59–80, 1998.

[141] ER Krueger, A Gross, and RC Di Prima. On the relative importance of Taylor-vortex and non-axisymmetric modes in flow between rotating cylinders. *Journal of Fluid Mechanics*, 24(03):521–538, 1966.

[142] McMaster-Carr. X-profile oil-resistant buna-n o-rings. `https://www.mcmaster.com/o-rings/=19bw2tp`. [Accessed 25-August-2017].

[143] Nian-Sheng Cheng. Formula for the viscosity of a glycerol- water mixture. *Industrial & engineering chemistry research*, 47(9):3285–3288, 2008.

[144] Fritz Wendt. Turbulente strömungen zwischen zwei rotierenden konaxialen zylindern. *Archive of Applied Mechanics*, 4(6):577–595, 1933.

[145] Pierre Sagaut. *Large Eddy Simulations for Incompressible Flows*, volume 3. Springer Berlin, 2000.

[146] M Germano. Turbulence: the filtering approach. *Journal of Fluid Mechanics*, 238:325–336, 1992.

[147] Daniele Carati, Gregoire S Winckelmans, and Hervé Jeanmart. On the modelling of the subgrid-scale and filtered-scale stress tensors in large-eddy simulation. *Journal of Fluid Mechanics*, 441:119–138, 2001.

[148] Lars Davidson. Large eddy simulation: a dynamic one-equation subgrid model for three-dimensional recirculating flow. In *11th International Symposium on Turbulent Shear Flow, Grenoble, France*, volume 3, pages 26–1, 1997.

[149] Alberto Scotti, Charles Meneveau, and Douglas K Lilly. Generalized smagorinsky model for anisotropic grids. *Physics of Fluids A: Fluid Dynamics (1989-1993)*, 5(9):2306–2308, 1993.

[150] Johan Meyers and Pierre Sagaut. On the model coefficients for the standard and the variational multi-scale smagorinsky model. *Journal of Fluid Mechanics*, 569:287–319, 2006.

[151] Massimo Germano, Ugo Piomelli, Parviz Moin, and William H Cabot. A dynamic subgrid-scale eddy viscosity model. *Physics of Fluids A: Fluid Dynamics (1989-1993)*, 3(7):1760–1765, 1991.

[152] Donald Coles. Transition in circular Couette flow. *Journal of Fluid Mechanics*, 21(3):385–425, 1965.

[153] CA Jones. Nonlinear Taylor vortices and their stability. *Journal of Fluid Mechanics*, 102:249–261, 1981.

[154] JE Burkhalter and EL Koschmieder. Steady supercritical Taylor vortices after sudden starts. *The Physics of Fluids*, 17(11):1929–1935, 1974.

[155] M Gorman and Harry L Swinney. Spatial and temporal characteristics of modulated waves in the circular Couette system. *Journal of Fluid Mechanics*, 117:123–142, 1982.

[156] T Mullin, M Heise, and G Pfister. Onset of cellular motion in Taylor-Couette flow. *Physical Review Fluids*, 2(8):081901, 2017.